

**EXPERIMENTAL AND THEORETICAL STUDIES OF Hf<sup>+</sup>,  
Ta<sup>+</sup>, AND Ta<sup>2+</sup> REACTING WITH METHANE**

by

Laura Grace Parke

A thesis submitted to the faculty of  
The University of Utah  
in partial fulfillment of the requirements for the degree of

Master of Science

Department of Chemistry

The University of Utah

August 2009

Copyright © Laura Grace Parke 2009

All Rights Reserved

THE UNIVERSITY OF UTAH GRADUATE SCHOOL

## SUPERVISORY COMMITTEE APPROVAL

of a dissertation submitted by

Laura Grace Parke

This dissertation has been read by each member of the following supervisory committee and by majority vote has been found to be satisfactory

Date



Chair:

Peter B. Armentrout



Date



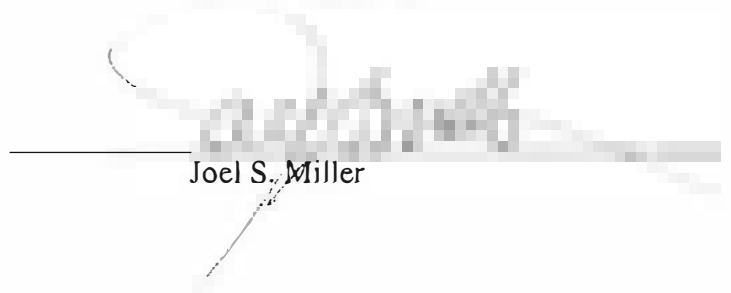
Scott L. Anderson



Date



Joel S. Miller



THE UNIVERSITY OF UTAH GRADUATE SCHOOL

**FINAL READING APPROVAL**

To the Graduate Council of the University of Utah:

I have read the dissertation of                     Laura Grace Parke                     in its final form and have found that (1) its format, citation, and bibliographic style are consistent and acceptable; (2) its illustrative materials including figures, tables and charts are in place; and (3) the final manuscript is satisfactory to the Supervisory Committee and is ready for submission to The Graduate School.



Chair, Supervisory Committee

Approved for the Major Department



Henry S. White  
Chair/Dean

Approved for the Graduate Council



David S. Chapman  
Dean of The Graduate School

## ABSTRACT

Guided-ion-beam tandem mass spectrometer techniques are used to study the activation of methane by the third-row transition metal ions,  $M = \text{Hf}^+$ ,  $\text{Ta}^+$ , and  $\text{Ta}^{2+}$ . In the studies of the third-row transition metals reacting with methane, experimental cross sections are measured as a function of kinetic energy of the reactants and are used to derive the absolute bond dissociation energies of the transition metal complexes,  $\text{MCH}_x^+$  ( $x = 0-3$ ). In addition,  $\text{TaCH}_2^+$  is reacted with  $\text{H}_2$  and  $\text{D}_2$  to examine the rate constants for the reverse reaction. Complementary ab initio calculations are performed to provide the electronic structures of the product species, as well as intermediates and transition states along the reactive potential energy surface. The main goal of this work is to better understand the ability of atomic transition metal ions to activate C-H bonds as well as provide fundamental information regarding metal-ligand bond interactions and provide insight into the role of spin conservation in these heavy-metal systems.

## TABLE OF CONTENTS

ABSTRACT .....	iv
LIST OF TABLES .....	vii
LIST OF FIGURES .....	ix
ACKNOWLEDGMENTS .....	xiii
CHAPTERS	
1. INTRODUCTION AND OVERVIEW .....	1
1.1 Introduction .....	1
1.2 Bond-energy Bond-order Correlation for $M^+CH_x$ Bonds .....	6
1.3 Overview .....	10
1.4 References .....	11
2. EXPERIMENTAL TECHNIQUE AND DATA AND THERMOCHEMICAL ANALYSIS METHODS .....	15
2.1 General .....	15
2.2 Instrumentation .....	17
2.3 Octopole Ion Beam Guide .....	20
2.4 Thermochemical Analysis .....	23
2.5 Theoretical Calculations .....	26
2.6 References .....	27
3. WHY IS HAFNIUM SO UNREACTIVE? EXPERIMENTAL AND THEORETICAL STUDIES OF THE REACTION OF $Hf^+$ WITH METHANE .....	30
3.1 Abstract .....	31
3.2 Introduction .....	31
3.3 Experimental and Theoretical Methods .....	32
3.4 Experimental Results .....	33
3.5 Thermochemical and Theoretical Results .....	34
3.6 Discussion .....	44
3.7 Conclusion .....	44

3.8 Acknowledgement .....	45
3.9 References .....	45
4. EXPERIMENTAL AND THEORETICAL STUDIES OF THE ACTIVATION OF METHANE BY Ta <sup>+</sup> .....	46
4.1 Abstract .....	47
4.2 Introduction .....	47
4.3 Experimental and Theoretical Methods .....	47
4.4 Experimental Results .....	49
4.5 Thermochemical and Theoretical Results .....	51
4.6 Discussion .....	58
4.7 Conclusion .....	60
4.8 Acknowledgement .....	60
4.9 Supporting Information Available .....	60
4.10 References and Notes .....	60
5. ENERGETICS AND MECHANISMS OF C-H BOND ACTIVATION BY A DOUBLY CHARGED METAL ION: GUIDED ION BEAM AND THEORETICAL STUDIES OF Ta <sup>2+</sup> + CH <sub>4</sub> .....	62
5.1 Abstract .....	63
5.2 Introduction .....	63
5.3 Experimental and Theoretical Methods .....	63
5.4 Experimental Results .....	65
5.5 Thermochemical and Theoretical Results .....	67
5.6 Discussion .....	71
5.7 Conclusion .....	73
5.8 Acknowledgement .....	73
5.9 Supporting Information Available .....	73
5.10 References and Notes .....	73

## LIST OF TABLES

Table	Page
1.1. Experimental and theoretical bond energies for $M^+-H$ and $M^+-CH_x$ ( $x = 0-3$ ) .....	8
3.1. Optimized parameters for eq. (1) for $Hf^+ + CH_4$ and $CD_4$ systems .....	34
3.2. B3LYP/HW+/6-311++G(3df,3p) theoretical energies of reactants and products .....	35
3.3. B3LYP/HW+/6-311++G(3df,3p) theoretical structures of reactants and products .....	36
3.4. Experimental and theoretical bond energies for $Hf^+-H$ and $Hf^+-CH_x$ ( $x = 1-3$ ) .....	37
3.5. B3LYP/HW+/6-311++G(3df,3p) theoretical energies of $[Hf,C,4H]^+$ intermediates and transition states .....	40
3.6. B3LYP/HW+/6-311++G(3df,3p) theoretical structures of $[Hf,C,4H]^+$ intermediates and transition states .....	41
4.1. Optimized parameters for equation 1 for $Ta^{2+} + CH_4$ and $CD_4$ System .....	51
4.2. B3LYP/HW+/6-311++G(3df,3p) theoretical energies of reactants and products .....	51
4.3. Experimental and theoretical bond energies for $Ta^+-H$ and $Ta^+-CH_x$ ( $x = 1-3$ ) .....	52
4.4. B3LYP/HW+/6-311++G(3df,3p) theoretical energies of $[Ta,C,4H]^+$ intermediates and transition states .....	55
5.1. Rates ( $10^{-10} \text{ cm}^3 \text{ s}^{-1}$ ) and reaction efficiencies (% , in parentheses) for reaction of $Ta^{2+}$ with methane .....	66
5.2. Optimized parameters for eq 1 for $Ta^{2+} + CH_4$ and $CD_4$ systems .....	68



5.3. Experimental and theoretical bond energies (eV) for Ta <sup>2+</sup> -H and Ta <sup>2+</sup> -CH <sub>x</sub> (x = 0 - 3) .....	68
---	----

## LIST OF FIGURES

Figure	Page
1.1. Variation of product cross sections with translational energy in the center-of-mass frame (lower axis) for the reaction of $M^+$ with $CD_4/CH_4$ . .....	3
1.2. Correlation of $M^+$ -L bond energies with those for organic analogue, L-L. The lines are linear regression fits to the experimental data constrained to pass through the origin to emphasize the bond-order correlations. ....	7
2.1. Schematic of the guided-ion-beam mass spectrometer designed to measure the energy dependences of reactions of thermalized, continuous beams of metal ions. The pumping speeds are given for the individual diffusion pumps, except for the source chamber, which is pumped by a roots blower. ....	16
2.2. Comparison of the $r^6$ effective potential of the octopole to those ( $r^4$ and $r^2$ ) of the hexapole and the quadrupole. ....	22
3.1. Cross sections for reaction of $Hf^+$ ( $^2D$ ) with $CH_4$ as a function of kinetic energy in the laboratory (upper $x$ -axis) and center of mass (lower $x$ -axis) frames. ....	34
3.2. Cross sections for reaction of $Hf^+$ ( $^2D$ ) with $CD_4$ as a function of kinetic energy in the laboratory (upper $x$ -axis) and center of mass (lower $x$ -axis) frames. ....	34
3.3. Correlation of $Hf^+$ -L bond energies with those for the organic analogues, L-L. $Hf^+$ -L values (open circles) are from Table 3.4. Data for $Ti^+$ and $Zr^+$ are listed in the text and shown by squares and triangles, respectively. The lines are linear regression fits to the experimental data constrained to pass through the origin to emphasize the bond-order correlations. ....	39
3.4. $[Hf,C,4H]^+$ potential energy surfaces derived from theoretical results. The energies of all species relative to the $Hf^+$ ( $^2D$ ) + $CH_4$ ground state asymptote are based on ab initio calculations at the	

B3LYP/HW+/6-311++G(3df,3p) level (see Table 3.5). Doublet surfaces are in green ( <sup>2</sup> TS3 and <sup>2</sup> TS4) and blue ( <sup>2</sup> TS2). Quartet surfaces are in pink ( <sup>2</sup> TS3 and <sup>2</sup> TS4) and red ( <sup>2</sup> TS2).	40
3.5. Structures of several intermediates and transition states along the doublet surface of the [Hf,C,4H] <sup>+</sup> system calculated at the B3LYP/HW+/6-311++G(3df,3p) level of theory. Bond lengths shown are in Ångstroms and HHfC bond angles are in degrees.	42
3.6. Structures of several intermediates and transition states along the quartet surface of the [Hf,C,4H] <sup>+</sup> system calculated at the B3LYP/HW+/6-311++G(3df,3p) level of theory. Bond lengths shown are in Ångstroms and HHfC bond angles are in degrees.	43
4.1. Cross sections for reaction of Ta <sup>+</sup> ( <sup>5</sup> F) with CH <sub>4</sub> as a function of kinetic energy in the center-of-mass frame (lower axis) and laboratory frame (upper axis). The full line shows the sum of all product cross sections. The LGS collision cross section is indicated by the dashed line at low energies.	49
4.2. Cross sections for multiple reactions of Ta <sup>+</sup> ( <sup>5</sup> F) with CH <sub>4</sub> as a function of kinetic energy in the center-of-mass frame (lower axis) and laboratory frame (upper axis). Open and closed symbols show results taken at methane pressures of 0.20 and 0.41 mTorr, respectively.	50
4.3. Cross sections for reaction of TaCH <sub>2</sub> <sup>+</sup> with H <sub>2</sub> (open symbols) and D <sub>2</sub> (closed symbols) as a function of kinetic energy in the center-of-mass frame (lower axis) and laboratory frame (upper axis).	50
4.4. Correlation of Ta <sup>+</sup> -L bond energies with those for the organic analogues, L-L. Ta <sup>+</sup> -L values are from Table 4.3 and include both experiment (closed circles) and theory (open circles, BHLYP/HW+/6-311++G(3df,3p) for TaH <sup>+</sup> and TaCH <sub>3</sub> <sup>+</sup> and B3LYP/HW+/6-311++G(3df,3p) for all others). The line is a linear regression fit to the experimental data, constrained to pass through the origin to emphasize the bond-order correlations. Data for VH <sup>+</sup> , VCH <sub>3</sub> <sup>+</sup> , VCH <sub>2</sub> <sup>+</sup> , and VCH <sup>+</sup> (taken from ref 43) are shown by squares, and data for NbH <sup>+</sup> , NbCH <sub>3</sub> <sup>+</sup> , and NbCH <sub>2</sub> <sup>+</sup> (taken from refs 23 and 49) are shown by triangles. The dashed lines are linear regression fits to these data	54
4.5. [Ta,C,4H] <sup>+</sup> potential energy surfaces derived from theoretical results. The relative energies of all species are based on ab initio calculations B3LYP/HW+/6-311++G(3df,3p); see Table 4.4. The singlet surfaces are shown in green, the triplet surfaces in red, and the quintet surfaces in blue	54
4.6. Structures of several intermediates and transition states along the quintet surface of the [Ta,C,4H] <sup>+</sup> system calculated at the	

B3LYP/HW+/6-311++G(3df,3p) level of theory. Bond lengths are given in Å and HTaC bond angles in degrees. ....	56
4.7. Structures of several intermediates and transition states along the triplet surface of the [Ta,C,4H] <sup>+</sup> system calculated at the B3LYP/HW+/6-311++G(3df,3p) level of theory. Bond lengths are given in Å and HTaC bond angles in degrees. ....	56
4.8. Structures of several intermediates and transition states along the singlet surface of the [Ta,C,4H] <sup>+</sup> system calculated at the B3LYP/HW+/6-311++G(3df,3p) level of theory. Bond lengths are given in Å and HTaC bond angles in degrees. ....	57
5.1. Cross sections for reaction of Ta <sup>2+</sup> ( <sup>4</sup> F) with CD <sub>4</sub> as a function of kinetic energy in the center of mass frame (lower axis) and laboratory frame (upper axis). Part a shows products retaining the 2+ charge, whereas part b shows products formed by charge transfer and charge separation. The TaCD <sub>3</sub> <sup>+</sup> cross section has a distinct pressure dependence and the results shown here correspond to P(CD <sub>4</sub> )=0.4 mTorr. ....	65
5.2. Cross Sections for multiple reactions of Ta <sup>2+</sup> ( <sup>4</sup> F) with CH <sub>4</sub> as a function of kinetic energy in the center-of-frame (lower axis) and laboratory frame (upper axis). Open and closed symbols show results taken at methane pressures of 0.20 and 0.41 mTorr, respectively. ....	67
5.3. Structures of ground state products calculated at the B3LYP/HW/6-311++G(3df,3p) level of theory. Bond lengths are given in Å and HTaC and HCH bond angles in degrees. ....	68
5.4. [Ta,C,4H] <sup>2+</sup> potential energy surfaces derived from theoretical results. The relative energy of all species are based on ab initio calculations at the B3LYP/HW+/6-311++G(3df,3p) level, Table S3, relative to the Ta <sup>2+</sup> ( <sup>4</sup> F) + CH <sub>4</sub> ground-state asymptote. ....	69
5.5. Structures of several intermediates and transition states along the quartet surface of the [Ta,C,4H] <sup>2+</sup> system calculated at the B3LYP/HW+/6-311++G(3df,3p) level of theory. Bond lengths are given in Å and HTaC and HTaH bond angles in degrees. ....	70
5.6. Structures of several intermediates and transition states along the doublet surface of the [Ta,C,4H] <sup>2+</sup> system calculated at the B3LYP/HW+/6-311++G(3df,3p) level of theory. Bond lengths are given in Å and HTaC and HTaH bond angles in degrees. ....	71
5.7. Curve crossing model derived from experimental data (full lines) and theoretical results calculated at a B3LYP/HW+/6-311++G(3df,3p)	

level of theory (symbols). The relative energies of the  $\text{TaH}^+ + \text{CH}_3^+$  (part b) and  $\text{TaCH}_3^+ + \text{H}^+$  (part c) theoretical curves have been adjusted so that the asymptotic energies agree with experimental values, hence the potential wells do not match the theoretical value of  $-2.65$  eV. .... 72

## ACKNOWLEDGMENTS

I would like to thank foremost Dr. Peter B. Armentrout for his continual support and guidance. He has been a motivating mentor.

The faculty at the University of Utah, both as an undergraduate and a graduate student, have enriched my education and provided me with insight. Past and present members of the Armentrout group have also been a great help and are thanked for helping to create a positive work environment.

Thanks to the National Science Foundation for providing funding for this work.

## CHAPTER 1

### INTRODUCTION AND OVERVIEW

#### **Introduction**

There are numerous studies of the reactions of atomic first-row, second-row, and third-row transition metal ions ( $M^+$ ) with hydrogen and small hydrocarbons in the gas phase, i.e., in the absence of solvent, stabilizing ligands, and metal supports.<sup>1-22</sup> Such studies provide insight into the electronic requirements for the activation of H-H, C-H, and C-C bonds by single metal centers and the periodic trends in the reactivity of metals. The thermochemistry obtained from these studies is of obvious fundamental interest and also has implications in understanding a variety of catalytic reactions involving transition metal systems.<sup>23,24</sup> In these processes, the transition metal complexes are formed as intermediates in catalytic transformations. A more in-depth understanding of these intermediates could help in the design of more efficient catalysts. The reactivities of these intermediates due to the unfulfilled 18 - electron rule make it difficult to isolate these species. Consequently, little information for these intermediates is available. The reactions of bare transition metal ions with small alkane molecules in the gas phase provide a good starting point for understanding the intrinsic properties of metals in the absence of solvent and stabilizing ligands. In addition, these relatively small systems form an ideal interface between experiment and theory.

Activation of methane is of considerable interest as identification of a convenient catalyst for selective oxidation to methanol would be technologically important by allowing the better use of natural gas.<sup>25,26</sup> Transition metals play an important role in many biological, organic, and inorganic catalytic systems and may play a role in allowing this natural resource to be utilized more widely as a fuel source. Alkane C-H and C-C bond activation is of particular interest to those working in the petroleum industry. The

catalytic conversion of methane to methanol would enable the petroleum industry to tap into these deposits. Not only is methane abundant but it is also a clean burning fuel, having serious implications in helping to save our environment. Further, studies in the gas phase are useful in providing information on the intrinsic properties of bare metal atoms in the absence of solvent and stabilizing ligands or metal support and surface effects. All of these factors contribute and are huge incentives to further our understanding of methane activation.

The differences in reactivity of the third-row transition metal ions compared to each other can be quantitatively addressed by looking at the relative magnitudes of the experimental cross sections for  $M^+ + CH_4 \rightarrow M^+-CH_2 + H_2$  (Figure 1.1).  $La^+$  ( $^3F$ ), a group 3 metal, is moderately reactive. Previous studies in our lab show that  $La^+$  reacts endothermically with methane to form  $LaCH_2^+$ .<sup>16</sup> Sunderlin et al.<sup>16</sup> report that  $La^+$  dehydrogenates ethane by two mechanisms. The first mechanism involves a 1,2-dehydrogenation to form  $M^+$ -ethene at low energy. The second mechanism involves a 1,1-dehydrogenation to form the metal-ethylidene ion at higher energy.

$Lu^+$  ( $^1S$ ), also a group 3 metal, is also among the least reactive. This is a consequence of the  $6s^2$  electronic configuration for ground state  $Lu^+$ . The  $s^2$  configuration is low in energy because of the lanthanide contraction, a consequence of 4f shielding and relativistic effects.<sup>17,27</sup> It was suggested by Irikura and Beauchamp that the reactivity of the transition metal cations with methane can be correlated with the accessibility of the  $s^1d^{n-1}$  electronic configuration. The metal-carbon  $\sigma$  and  $\pi$  bonds have optimal bond lengths that depend on the relative sizes of the metal s and d orbitals. These orbitals are best matched for the third-row metals such that metal carbon bonds can be accommodated without any compromise provided that metal has a  $s^1d^{n-1}$  electronic configuration. Therefore, since the actual bonding involves both s and d orbitals to some extent,  $Lu^+$  ( $^1S_0$ ) will not be reactive.<sup>17,27-30</sup> This corresponds with the endothermic cross section that is observed for  $LuCH_2^+$ . The difference between  $La^+$  (which has no 4f electrons) and  $Lu^+$  (which has a filled 4f shell) is a consequence of the differing 4f orbital occupancy. While the 4f orbitals do not participate directly, the occupation of these orbitals raises the energy of the 5d shell, causing the two valence electrons in the ground state of  $Lu^+$  to both occupy the 6s orbital. To reach a  $s^1d^{n-1}$  electronic configuration,  $Lu^+$



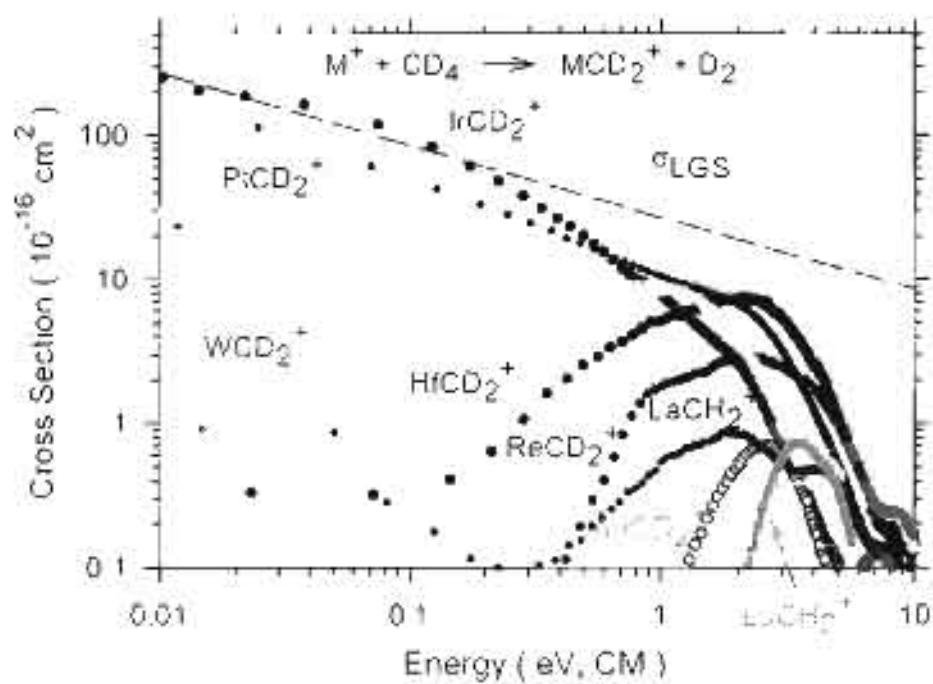


Figure 1.1 Variation of product cross sections with translational energy in the center-of-mass frame (lower axis) for the reaction of  $M^+$  with  $CD_4/CH_4$ .

has a promotion energy of 1.63 eV. For  $\text{La}^+$ , the energy of the 5d and 6s orbitals are closer together, resulting in an open shell electron configuration. To reach a  $s^1 d^{n-1}$  electronic configuration,  $\text{La}^+$  has a promotion energy of only 0.03 eV.<sup>16</sup>

$\text{Hf}^+$  ( $^2\text{D}$ ), a group 4 metal, is also among the least reactive. We find that  $\text{Hf}^+$ , which has a  $^2\text{D}$  ground electronic state with a  $6s^2 5d^1$  configuration, reacts much more like  $\text{Lu}^+$  ( $^1\text{S}, 6s^2$ ) than  $\text{La}^+$  ( $^2\text{D}, 5d^2$ ) because of the closed valence shell. State-specific studies of the reactions of atomic transition metal ions with small molecules have indicated the orbital preferences for efficient reactivity. A simple donor-acceptor model illustrates that reactions are enhanced by electronic configurations where there is an empty acceptor orbital on the metal into which the electrons of the bond to be broken can be donated. If this acceptor orbital is already occupied, a more repulsive interaction occurs that leads to an inefficient reaction. This can take place either by more direct pathways or by introduction of a barrier to the reaction. Conversely, if the acceptor orbital is empty, then the reactants can get close enough so that the metal electrons in orbitals having  $\pi$ -symmetry can back-donate into the antibonding orbital of the bond to be broken. In order to fully activate the bond, both of these acceptor-donor interactions are needed.<sup>3</sup> This corresponds with the endothermic cross section that is observed for  $\text{HfCH}_2^+$ .<sup>31</sup>

$\text{Ta}^+$ , a group 5 metal, is reported to be moderately reactive. It has been found that  $\text{Ta}^+$  ( $^5\text{F}_6, 5d^3 6s^1$ ) reacts four times with methane by sequential dehydrogenations at thermal energies to form  $\text{TaCH}_2^+$  initially, followed by  $\text{TaC}_2\text{H}_4^+$  and  $\text{TaC}_3\text{H}_6^+$ , eventually forming  $\text{TaC}_4\text{H}_8^+$ . Irikura and Beauchamp found that  $\text{Ta}^+$  dehydrogenates  $\text{CH}_4$  with 30% efficiency.<sup>17,27</sup> Studies in our lab also found that  $\text{Ta}^+$  dehydrogenates  $\text{CH}_4$  with relatively low efficiency  $30 \pm 12\%$ .<sup>32</sup> Finally, the C-C coupling reactions intrinsic to Fischer-Tropsch chemistry has been observed to occur for this early third-row transition metal ion.<sup>17,27</sup>

$\text{W}^+$ , a group 6 metal, has been reported to be one of the low to moderately reactive of these elements. We find that  $\text{W}^+$ , which has a  $^6\text{D}_5$  ground electronic state with a  $5d^4 6s^1$  configuration, reacts much more like  $\text{Ta}^+$  ( $^5\text{F}, 5d^3 6s^1$ ) than  $\text{Hf}^+$  ( $^2\text{D}, 5d^1 6s^2$ ) because of the open valence shell. In an ion cyclotron resonance (ICR) mass spectrometry study, Irikura and Beauchamp reported that  $\text{W}^+$  reacts rapidly four times with methane by sequential dehydrogenation to form  $\text{WCH}_2^+$  initially, followed by  $\text{WC}_2\text{H}_4^+$  and  $\text{WC}_3\text{H}_6^+$ , eventually

forming  $\text{WC}_4\text{H}_8^+$  at thermal energies. Subsequent reactions, although slower, lead as far as  $\text{WC}_8\text{H}_{16}^+$ . Irikura and Beauchamp found that  $\text{W}^+$  dehydrogenates  $\text{CH}_4$  with 10% efficiency.<sup>17,27</sup> Studies in our lab found that  $\text{W}^+$  dehydrogenates  $\text{CH}_4$  with low efficiency  $20 \pm 4\%$ .<sup>33</sup> The C-C bond coupling reactions similar to Fischer-Tropsch chemistry have also been observed to occur for this early third-row transition metal ion.<sup>17,27</sup>

$\text{Re}^+$ , a group 7 metal, is also among the least reactive of these elements. This is a consequence of its  $5d^56s^1$  electronic configuration and a  $^7\text{S}_3$  state for  $\text{Re}^+$ . This metal is relatively inactive because of its stable half-filled  $5d^5$  shell electronic configuration. This corresponds with the endothermic cross section that is observed for  $\text{ReCH}_2^+$ . However, despite the stability of the  $\text{Re}^+$  ( $^7\text{S}_3$ ) state, this ion was observed to react with methane to form  $\text{ReCH}_2^+$  when either translationally or electronically excited. Also, it was found that the reverse reaction occurred at thermal energies (0.04 eV). Finally,  $\text{Re}^+$  reacts with cyclopropane to form  $\text{ReCH}_2^+$  at thermal energies.<sup>17,27</sup>

$\text{Os}^+$ , a group 8 metal, is reported to be one of the more reactive third-row transition metal cations.  $\text{Os}^+$  has a  $5d^66s^1$  configuration and a  $^5\text{D}_4$  electronic ground state. In an ion cyclotron resonance (ICR) mass spectrometry study, Irikura and Beauchamp reported that  $\text{Os}^+$  reacts rapidly with methane by dehydrogenation to form  $\text{OsCH}_2^+$  at thermal energies. Irikura and Beauchamp found that  $\text{Os}^+$  dehydrogenates  $\text{CH}_4$  with 30% efficiency.<sup>17,27</sup>

$\text{Ir}^+$ , a group 9 metal, is reported to be the most reactive of the third-row transition metal cations.  $\text{Ir}^+$  has a  $5d^76s^1$  configuration and a  $^5\text{F}_6$  electronic ground state. In an ion cyclotron resonance (ICR) mass spectrometry study, Irikura and Beauchamp reported that  $\text{Ir}^+$  reacts rapidly three times with methane by sequential dehydrogenation to form  $\text{IrCH}_2^+$  initially, followed by  $\text{IrC}_2\text{H}_4^+$  and  $\text{IrC}_3\text{H}_6^+$  at thermal energies. Irikura and Beauchamp found that  $\text{Ir}^+$  dehydrogenates  $\text{CH}_4$  with 70% efficiency.<sup>17,27</sup> Again, studies in our lab found that  $\text{Ir}^+$  dehydrogenates  $\text{CH}_4$  with high efficiency,  $85 \pm 15\%$ . Iridium complexes are good homogeneous C-H bond activation catalysts in solution, reacting by an oxidative addition mechanism at an unsaturated Ir center.<sup>34-38</sup>

$\text{Pt}^+$ , a group 10 metal, is found to be highly reactive with methane over a wide range of kinetic energies.  $\text{Pt}^+$  has a  $5d^9$  configuration and a  $^2\text{D}_1$  ground electronic state. It has been found that  $\text{Pt}^+$  reacts five times with methane by sequential dehydrogenations

at thermal energies to form  $\text{PtCH}_2^+$  initially, followed by  $\text{PtC}_2\text{H}_4^+$ ,  $\text{PtC}_3\text{H}_6^+$ , and  $\text{PtC}_4\text{H}_8^+$ , eventually forming  $\text{PtC}_5\text{H}_{10}^+$ . Irikura and Beauchamp found that  $\text{Pt}^+$  dehydrogenates  $\text{CH}_4$  with 40% efficiency.<sup>17,19,27,35,36</sup> This value can be adjusted to a value of 60% on the basis of a recalibration of the absolute standard used.<sup>36</sup> Heinemann et al. found that  $\text{Pt}^+$  dehydrogenates  $\text{CH}_4$  with 84% efficiency.<sup>35</sup> Achatz et al. found that  $\text{Pt}^+$  dehydrogenates  $\text{CH}_4$  with 47% efficiency.<sup>19</sup> Studies in our lab found that  $\text{Pt}^+$  dehydrogenates  $\text{CH}_4$  with  $76 \pm 17\%$  efficiency.<sup>37</sup> Platinum is one of the most versatile and all-purpose metal catalysts.<sup>23,24</sup>

Finally,  $\text{Au}^+$ , a group 11 metal, is reported to be the least reactive of the third-row transition metals. This is a consequence of its  $5d^{10}$  configuration and a  $^1\text{S}_0$  ground electronic state for  $\text{Au}^+$ . The relative inactivity of  $\text{Au}^+$  can be attributed to the stable, filled  $5d$  shell electronic configuration.<sup>17,27</sup> This corresponds with the endothermic cross section that is observed for  $\text{AuCH}_2^+$ .<sup>38</sup>

### **Bond-energy Bond-order Correlation for $\text{M}^+\text{CH}_x$ Bonds**

One interesting way of investigating the bond order of simple metal–ligand species is to compare with organic analogues, i.e.,  $D_0(\text{M}^+\text{L})$  versus  $D_0(\text{L-L})$ . Such a plot is shown in Figure 1.2. It can be seen that the correlation is remarkably good, which indicates that  $\text{M}^+\text{H}$  and  $\text{M}^+\text{CH}_3$  are single bonds,  $\text{M}^+\text{CH}_2$  is a double bond, and  $\text{M}^+\text{CH}$  is a triple bond, as confirmed by theory. (The linear regression lines in Figure 1.2 are constrained to include the origin to emphasize the bond-order correlation of  $\text{ML}^+$  versus  $\text{L}_2$  species.)

It is also interesting to compare these results across the period for the third-row transition metals,  $\text{La}^+$ ,  $\text{Lu}^+$ ,  $\text{Hf}^+$ ,  $\text{Ta}^+$ ,  $\text{W}^+$ ,  $\text{Re}^+$ ,  $\text{Os}^+$ ,  $\text{Ir}^+$ ,  $\text{Pt}^+$ , and  $\text{Au}^+$  (Figure 1.2). Bond dissociation energies (BDEs) for  $\text{MH}^+$ ,  $\text{MC}^+$ ,  $\text{MCH}^+$ ,  $\text{MCH}_2^+$ , and  $\text{MCH}_3^+$  are given in Table 1.1. From this comparison, we find that group 3, 4, 7, and 11 third-row transition-metal bonded species have the weakest bonds.  $\text{La}^+$  has a promotion energy of 0.03 eV from its ground state, derived from its  $5d^2$  configuration, to its lowest state, derived from the  $6s^1 5d^1$  configuration.<sup>16</sup> For the third-row metals, the bonding involves the  $6s$  metal orbital primarily. Hence, metal ions having a  $5d^n$  ground state must be promoted to the

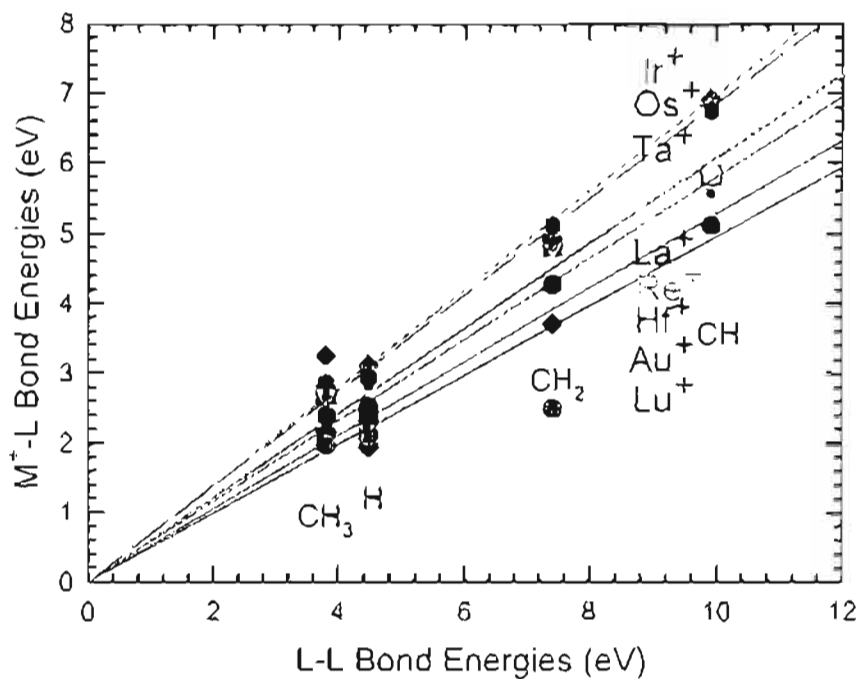


Figure 1.2. Correlation of  $M^+$ -L bond energies with those for organic analogue, L-L. The lines are linear regression fits to the experimental data constrained to pass through the origin to emphasize the bond-order correlations.

TABLE 1.1: Experimental and theoretical bond energies (eV) for  $M^x-H$  and  $M^x-CH_x(x = 0-3)$

	$1s^0$	$1s^1$	$1s^2$	$1s^3$	$W^0$	$Rc^{00}$	Os	$Q^1$	$1s^0$	$Ag^0$
$M^0-H$	$2.52 \pm 0.09$	$2.24 \pm 0.16$	$1.97 \pm 0.13$	$2.39 \pm 0.08$	$2.77 \pm 0.05$	$2.10 \pm 0.04$	2.94	$2.87 \pm 0.06$	$2.81 \pm 0.05$	$2.17 \pm 0.08$
$M^0-CH$	$2.39 \pm 0.15$	$1.97 \pm 0.21$	$2.10 \pm 0.34$	$2.69 \pm 0.14$	$-2.31 \pm 0.10$	$2.77 \pm 0.15$	2.86	$3.25 \pm 0.14$	$2.67 \pm 0.08$	$2.17 \pm 0.14$
$M^0-CH_2$	$4.76 \pm 0.06$	$2.49 \pm 0.03$	$4.27 \pm 0.05$	$4.81 \pm 0.03$	$4.74 \pm 0.03$	$4.14 \pm 0.06$	5.11	$4.92 \pm 0.03$	$4.80 \pm 0.03$	$3.70 \pm 0.07$
$M^0-CH_3$			$5.11 \pm 0.10$	$5.82 \pm 0.10$	$6.01 \pm 0.28$	$5.84 \pm 0.06$	6.75	$6.91 \pm 0.23$	$5.56 \pm 0.10$	
$M^0-C$					$4.90 \pm 0.22$	$5.12 \pm 0.04$		$6.59 \pm 0.05$	$5.42 \pm 0.05$	$2.19 \pm 0.08$

## ERRATUM

Page 8 was assigned twice in this manuscript.

lowest lying  $6s^1 5d^{n-1}$ -type excited state to be prepared for bonding. Because the dissociation limit involves the ground-state atom, it is necessary that the bond energy be reduced by this promotion energy.<sup>39</sup> Because the lowest lying excited state lies only 0.03 eV higher in energy, this results in a slightly more efficient reaction than is otherwise seen for  $\text{Lu}^+$ ,  $\text{Hf}^+$ ,  $\text{Re}^+$ , and  $\text{Au}^+$ .<sup>16</sup> This can help explain why  $\text{La}^+$  has slightly stronger bonds and is more reactive than  $\text{Lu}^+$ ,  $\text{Hf}^+$ ,  $\text{Re}^+$ , and  $\text{Au}^+$ . However, unlike other third-row transition metals,  $\text{La}^+$  is not subject to lanthanide contraction. Consequently, the 6s orbital is diffuse compared to the 5d orbital, reducing bond overlap with the  $\text{CH}_2$  moiety, making it less reactive than  $\text{Ta}^+$  and  $\text{W}^+$ . For  $\text{Lu}^+$  ( $^1\text{S}$ ) and  $\text{Hf}^+$  ( $^2\text{D}$ ), this difference in behavior can again be attributed to the unusual doubly occupied  $6s^2$  orbital. To reach a  $6s^1 5d^{n-1}$  configuration,  $\text{Lu}^+$  and  $\text{Hf}^+$  have promotion energies of 0.17 and 0.45 eV, respectively.<sup>17</sup> For  $\text{Re}^+$  ( $^7\text{S}$ ) and  $\text{Au}^+$  ( $^1\text{S}$ ), the weaker bonds and relative inactivity of the latter two metals can be attributed largely to the stable half-filled and filled 5d shell electronic configurations,  $6s^1 5d^5$  and  $5d^{10}$ , respectively.  $\text{Re}^+$  has a maximum exchange energy of 2.51 eV that is lost upon bonding.  $\text{Au}^+$  also has a promotion energy of 1.86 eV in order to reach a  $6s^1 5d^{n-1}$  configuration.<sup>17</sup> This corresponds with the endothermic cross sections that are observed for  $\text{La}^+$ ,  $\text{Lu}^+$ ,  $\text{Hf}^+$ ,  $\text{Re}^+$ , and  $\text{Au}^+$  carbene.<sup>31,38,40</sup>

Also, from this comparison, it can be seen that  $\text{Ta}^+$  and  $\text{W}^+$  have moderate bond strengths. The reactivities of the  $\text{Ta}^+$  and  $\text{W}^+$  transition metals can be attributed to the open valence shells,  $6s^1 5d^3$  and  $6s^1 5d^4$ , respectively. It is important to note that for  $\text{Ta}^+$  and  $\text{W}^+$  the nonbonding electrons also play an important role in determining bond strengths. Nonbonding electrons control the amount of metal exchange energy that is lost upon bonding. To estimate this change, it is useful to consider the  $(\alpha\beta - \beta\alpha)$  spin function of the bond pair so that the metal orbital is half  $\alpha$  and half  $\beta$ . Consequently, half of the exchange energy between the nonbonding metal orbitals and the metal bonding orbital may be lost. Thus, for group 5 and 6 hydrides, there is a loss of  $3K/2$  and  $4K/2$ , respectively (three and four unpaired nonbonding electrons). Beginning with group 3, there is a gradual increase in exchange loss, eventually reaching a maximum in group 7 (five unpaired nonbonding electrons), in the presence of both  $\alpha$  and  $\beta$  nonbonding orbitals.<sup>39</sup> For  $\text{Ta}^+$  and  $\text{W}^+$ , the amount of exchange energy lost upon forming double



bonds with s and d orbitals is 1.33 and 1.90 eV.<sup>17</sup> This corresponds with bond energies for TaCH<sub>2</sub><sup>+</sup> and WCH<sub>2</sub><sup>+</sup> of 4.81 ± 0.03 and 4.73 ± 0.06 eV.<sup>32,33</sup>

Next, the bond energies of Os<sup>+</sup> and Ir<sup>+</sup> are the strongest among the third-row transition metal cations. For the bare metal cations, the ground states of Os<sup>+</sup> and Ir<sup>+</sup> have 5d<sup>6</sup>6s<sup>1</sup> and 5d<sup>7</sup>6s<sup>1</sup> electronic configurations. Valence shells 6s<sup>1</sup>5d<sup>n-1</sup>, where n > 5, possess a special reactivity due to a decrease in the atomic exchange stabilization, yielding stronger bonds. This extra “reactivity” can be quantified by again taking exchange energy into consideration. Beginning with group 8, there is a gradual decrease in exchange loss, eventually dropping to zero in group 12, in the presence of both α and β nonbonding orbitals.<sup>39</sup> For Os<sup>+</sup> and Ir<sup>+</sup> the exchange energies that are lost upon forming a double bond using s and d orbitals are 1.80 and 1.36 eV.<sup>17</sup> This corresponds with theoretical and experimental bond energies for OsCH<sub>2</sub><sup>+</sup> and IrCH<sub>2</sub><sup>+</sup> of 5.11 and 4.92 ± 0.03 eV.<sup>41</sup>

Finally, Pt<sup>+</sup> has a promotion energy of 0.59 eV,<sup>17</sup> from its ground state, derived from its 5d<sup>9</sup> configuration, to its lowest state, derived from the 6s<sup>1</sup>5d<sup>8</sup> configuration. For the third-row metals, the bonding involves the 6s metal orbital primarily. Hence, metal ions having a 5d<sup>n</sup> ground state must be promoted to the lowest lying 6s<sup>1</sup>5d<sup>n-1</sup>-type excited state to be prepared for bonding. Because the dissociation limit involves the ground-state atom, it is necessary that the bond energy be reduced.<sup>39</sup> This can help explain why Pt<sup>+</sup> has weaker bonds and is less reactive than both Os<sup>+</sup> and Ir<sup>+</sup>.

Another periodic trend that is observed for the transition metals is that there is more electron shielding for the third-row metals than there is for the first- or second-row metals. Relativistic effects lessen the kinetic energy of the inner s orbitals, which allows the s orbitals to contract. Consequently, the d orbitals become more diffuse in going across the period, leading to larger overlap. The overall effect is a significant increase in bonding interaction in going from left to right across the third-row, which leads to much stronger bond energies.<sup>39</sup> This trend in third-row theoretical and experimental bond energies is only offset by promotion and exchange energies.

In this work, we have chosen to study the chemistry of the third-row transition metal cations of Hf<sup>+</sup> and Ta<sup>2+</sup> with CH<sub>4</sub>/CD<sub>4</sub>, and Ta<sup>+</sup> with H<sub>2</sub>/D<sub>2</sub> and CH<sub>4</sub>/CD<sub>4</sub>. The ground states of the three third-row transition metals ions have 5d<sup>1</sup>6s<sup>2</sup>, 5d<sup>2</sup>6s<sup>1</sup>, and 5d<sup>3</sup>6s<sup>1</sup>

electronic configurations, respectively. These studies will help to understand the difference in bond energies, the reactivity of transition-metal complexes, and reaction mechanisms, thereby establishing periodic trends of the three third-row transition metals. In addition, these heavy transition metal containing systems are good examples to study the influence of strong spin-orbit coupling on the reactivity. Theoretical calculations will provide electronic structures, explore potential energy surfaces and possible mechanisms.

## Overview

Chapter 2 gives a detailed description of the guided-ion-beam tandem mass spectrometer as well as the ion source. The endothermic cross sections are modeled by an empirical model and discussed in detail. A detailed description of the theoretical calculations is also given which include the level of theory, basis set, and effective core potentials (ECP).

Chapter 3 discusses the reaction of  $\text{Hf}^+$  with methane. The theoretical calculations are performed to assign electronic structures and explore potential energy surfaces and possible mechanisms.

Chapter 4 discusses the reaction of  $\text{Ta}^+$  with methane, and the reverse reaction of  $\text{TaCH}_2^+$  with  $\text{H}_2/\text{D}_2$  is also discussed. The theoretical calculations are also performed to assign electronic structures and explore potential energy surfaces and possible mechanisms.

Chapter 5 discusses the reaction of  $\text{Ta}^{2+}$  with methane. The theoretical calculations are also performed to assign electronic structures and explore potential energy surfaces and possible mechanisms.

**References**

- (1) Allison, J., *Prog. Inorg. Chem.* **1986**, *34*, 627.
- (2) Freiser, B. S., Ed.; *Organometallic Ion Chemistry*; Kluwer: Dordrecht, 1996; p 1.
- (3) Armentrout, P. B., Gas Phase Organometallic Chemistry. In *Topics in Organometallic Chemistry*; Brown, J. M., Hofmann, P., Eds.; Springer-Verlag: Berlin, 1999; Vol. 4; p 1.
- (4) Zhang, X.-G.; Liyanage, R.; Armentrout, P. B., *J. Am. Chem. Soc.* **2001**, *123*, 5563.
- (5) Zhang, X.-G.; Rue, C.; Shin, S.-Y.; Armentrout, P. B., *JCP* **2002**, *116*, 5574.
- (6) Zhang, X.-G.; Armentrout, P. B., *Organometallics* **2001**, *20*, 4266.
- (7) Schwarz, H., *Book of Abstracts, 211th ACS National Meeting, New Orleans, LA, March 24-28 1996*.
- (8) Schlangen, M.; Schroder, D.; Schwarz, H., *Angew. Chem. Int. Ed.* **2007**, *46*, 1641.
- (9) Schlangen, M.; Schwarz, H., *Angew. Chem. Int. Ed.* **2007**, *46*, 5614.
- (10) Oncak, M.; Cao, Y.; Beyer, M.; Zahradnik, R.; Schwarz, H., *Chem. Phys. Lett.* **2008**, *450*, 268.
- (11) Feyel, S.; Dobler, J.; Schroder, D.; Sauer, J.; Schwarz, H., *Angew. Chem. Int. Ed.* **2006**, *45*, 4681.
- (12) Schlangen, M.; Schroder, D.; Schwarz, H., *Helvetica Chimica Acta* **2007**, *90*, 847.
- (13) Schlangen, M.; Schroder, D.; Schwarz, H., *CHEM. Eur. J.* **2007**, 6810.
- (14) Trage, C.; Diefenbach M.; Schroder, D.; Schwarz, H., *CHEM. Eur. J.* **2006**, 2454.
- (15) Butschke, B.; Schlangen, M.; Schwarz, H.; Schroder, D., *Z. Naturforsch* **2007**, *62b*, 309.
- (16) Sunderlin, L. S.; Armentrout, P. B., *JACS* **1989**, *111*, 3845.

- (17) Irikura, K. K.; Beauchamp, J. L., *J. Phys. Chem.* **1991**, *95*, 8344.
- (18) Pavlov, M.; Blomberg, M. R. A.; Siegbahn, P. E. M.; Wesendrup, R.; Heinemann, C.; Schwarz, H., *JPCA* **1997**, *101*, 1567.
- (19) Achatz, U.; Beyer, M.; Joos, S.; Fox, B. S.; Niedner-Schatteburg, G.; Bondybey, V. E., *JPCA* **1999**, *103*, 8200.
- (20) Buckner, S. W.; MacMahon, T. J.; Byrd, G. D.; Freiser, B. S., *Inorg. Chem.* **1989**, *28*, 3511.
- (21) Ranasinghe, Y. A.; MacMahon, T. J.; Freiser, B. S., *JPC* **1991**, *95*, 7721.
- (22) Achatz, U.; Beyer, M.; Joos, S.; Fox, B. S.; Niedner-Schatteburg, G.; Bondybey, V. E., *Chem. Phys. Lett.* **2000**, *320*, 53.
- (23) Crabtree, R. H., 2nd ed.; Current Ideas and Future Prospects in Metal-Catalyzed Methane Conversion, John Wiley & Sons: New York, 1994.
- (24) Somorjai, G. A., The Surface Science of Heterogeneous Catalysis, John Wiley & Sons: New York, 1994.
- (25) Haggin, J., *Chem. Eng. News*, **1993**, *71*, 27.
- (26) Warren, B. K.; Oyama, S. T., *ACS, Washington, D.C.* **1996**.
- (27) Irikura, K. K.; Beauchamp, J. L., *JACS* **1991**, *113*, 2769.
- (28) Schilling, J. B.; Goddard, W. A.; Beauchamp, J. L., *J. Am. Chem. Soc.* **1987**, *109*, 5565.
- (29) Schilling, J. B.; Goddard, W. A.; Beauchamp, J. L., *J. Phys. Chem.* **1987**, *91*, 5616.
- (30) Ohanessian, G.; Brusich, M. J.; Goddard III, W. A., *JACS* **1990**, *112*, 7179.
- (31) Parke, L. G.; Hinton, C. S.; Armentrout, P. B., *International Journal of Mass Spectrometry and Ion Processes* **2006**, *254*, 168.
- (32) Parke, L. G.; Hinton, C. S.; Armentrout, P. B., *Journal of Physical Chemistry* **2008**, *112*, 10469.
- (33) Armentrout, P. B.; S., S.; Liyanage, R., *J. Phys. Chem. A* **2006**, *110*, 1242.
- (34) Janowicz, A. H.; Bergman, R. G., *J. Am. Chem. Soc.* **1982**, *104*, 352.

- (35) Heinemann, C.; Wesendrup, R.; Schwarz, H., *CPL* **1995**, *239*, 75.
- (36) Schroder, D.; Schwarz, H.; Clemmer, D. E.; Chen, Y. M.; Armentrout, P. B.; Baranov, V. I.; Bohme, D. K., *Int. J. Mass Spectrom. Ion Processes* **1997**, *161*, 175.
- (37) Zhang, X.-G.; Armentrout, P. B., *J. Am. Chem. Soc.* **2001**, *123*, 5563.
- (38) Li, F. -X.; Zhang, X. -G.; Armentrout, P.B., *J. Chem. Phys.* **2006**, *125*, 133114.
- (39) Ohanessian, G.; Goddard, W. A. *Accts. Chem. Res.* **1990**, *23*, 386.
- (40) Armentrout, M. M.; Li, F.-X.; Armentrout, P. B. *JPCA* **2004**, *108*, 9660.
- (41) Li, F.; Zhang, X.-G.; Armentrout, P. B. *International Journal of Mass Spectrometry* **2006**, *255-256*, 279.

## ERRATUM

Page 14 was not assigned in this manuscript.

## CHAPTER 2

### EXPERIMENTAL TECHNIQUE AND DATA AND THERMOCHEMICAL ANALYSIS METHODS

#### **General**

This chapter is intended to provide a general background of the experimental section in each chapter.

The guided-ion-beam tandem mass spectrometer on which these experiments were performed has been described in detail previously.<sup>1,2</sup> Figure 2.1 shows a schematic of this custom-built instrument with a flow-tube ion source. The entire instrument consists of six sections. Briefly, reactant ions are produced in a direct current discharge flow-tube source described below. The ions are extracted from the source, accelerated, and focused by a series of ion optics into a 60° magnetic sector momentum analyzer for mass selection of the primary reactant ions. The mass-selected ions are decelerated to a desired kinetic energy and focused into an octopole ion beam guide, which uses radio-frequency electric fields to trap the ions in the radial direction and ensure complete collection of reactant and product ions.<sup>1,3</sup> The octopole passes through a static gas cell that contains the reaction partner at a low pressure (usually  $\leq 0.3$  mTorr) so that multiple ion-molecule collisions are improbable. The products reported here result from single bimolecular encounters, as verified by pressure dependence studies. Product and unreacted primary ions drift to the end of the octopole where they are extracted, focused, passed through a quadrupole mass filter for mass analysis, and subsequently detected with a secondary electron scintillation ion detector that uses standard pulse counting techniques.<sup>4</sup>

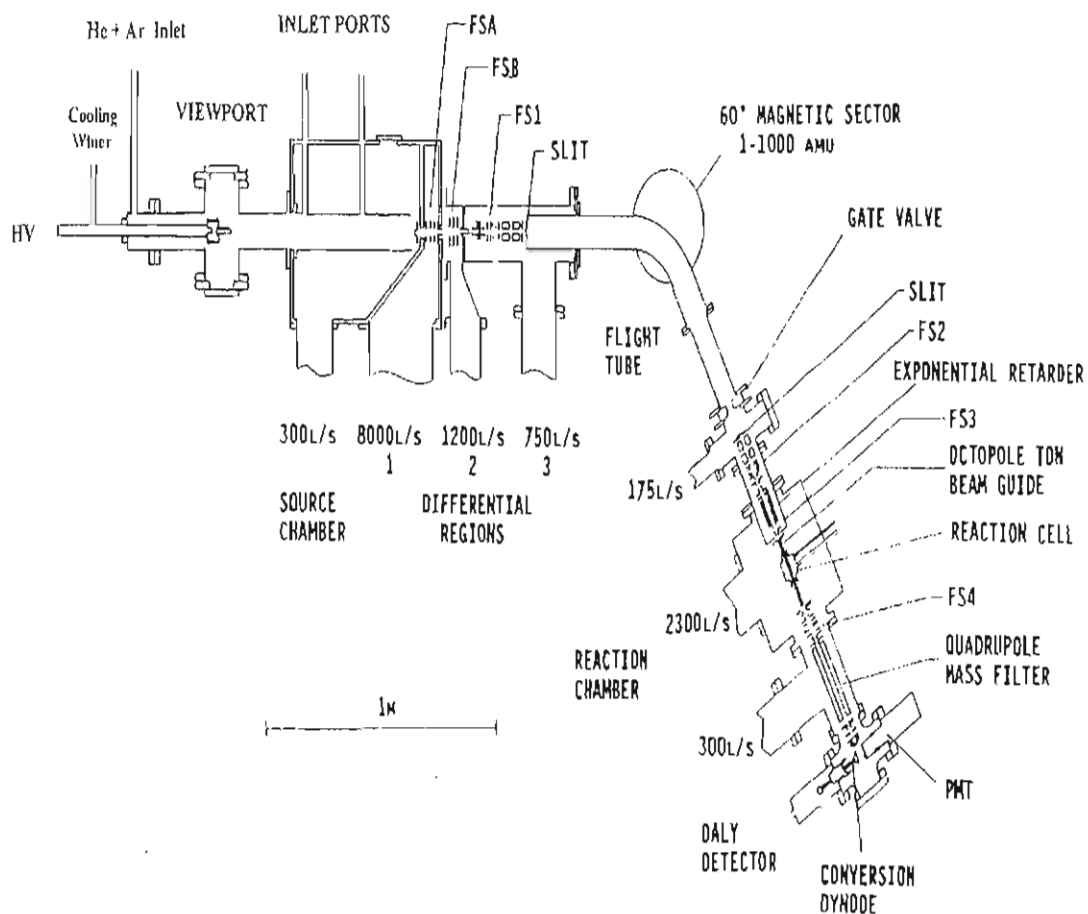


Figure 2.1. Schematic of the guided-ion-beam mass spectrometer designed to measure the energy dependences of reactions of thermalized, continuous beams of metal ions. The pumping speeds are given for the individual diffusion pumps, except for the source chamber, which is pumped by a roots blower.<sup>1</sup>



## Instrumentation

### *Vacuum System*

The guided-ion-beam mass spectrometer (GIBMS) can be divided into six individually pumped regions: (1) ion source chamber (2) differential region (3) first focusing lenses (FS1) region, (4) magnetic sector flight tube, (5) the main chamber that houses the octopole ion beam guide and reaction cell, and (6) the detector chamber. The source region is pumped by a roots blower (285 *l/s* He) backed with a mechanical pump (59 *l/s*) to a pressure of  $\sim 180$  mTorr during operation. The source also has an extra differential pumping region (DR1), which is pumped by a (8000 *l/s*) Varian VHS-400 diffusion pump that is backed by a (25 *l/s*) Sargent-Welch 1398 mechanical pump to typical operating pressures of  $8 \times 10^{-5}$  Torr. To ensure high speed pumping, a gate valve is not used. To increase the effective area of the diffusion pump, the chamber, 7.6 cm in length at the beam line, has an angled backed wall.<sup>1</sup>

Next, ions exit DR1 and enter another differential pumping region (DR2). The chamber is pumped by a (1000 *l/s*) Varian VHS-4 diffusion pump, which operates near  $1 \times 10^{-6}$  Torr. The FS1 region is pumped by a (2400 *l/s*) Varian VHS-6 diffusion pump in order to reduce ion scatter and the flight tube is pumped by a (135 *l/s*) Edwards Diffstak 63M. There is a gate valve that is mounted on the flight tube (and biased at the mass analysis potential during operation), which allows isolation of the source chamber for changing ion sources or for cleaning the ion lenses without venting the entire instrument. Even with frequent venting, the source chamber typically reaches a base pressure of  $\sim 1 \times 10^{-7}$  Torr ( $\sim 1 \times 10^{-5}$  Pa) within several hours. Following the use of contaminating materials in the ion source, the source chamber lenses must be cleaned. Under normal conditions, the instrument can operate for months without requiring cleaning.<sup>1</sup>

The reaction region is continually pumped with an (2000 *l/s*) Edwards Diffstak 250M diffusion pump. The operating pressure is  $2 \times 10^{-6}$  Torr so that the ratio of pressures inside and outside the reaction cell is maintained at 100. The detector chamber, which holds the quadrupole mass filter and the ion detector, is differentially pumped by an Edwards Diffstak model 125, chosen for high pumping speed and low backstreaming rate. This reduces the risk of contamination of the conversion dynode with pump oil.<sup>1</sup>

### *Flow Tube Ion Source*

The GIBMS used in our laboratory utilizes a flow-tube ion source and a detailed description of the flow-tube ion source conditions used in each experiment is found in the corresponding chapters.

One of three ionization sources, microwave discharge, cold cathode dc discharge, or electron impact (EI), can be coupled to the flow-tube ion source. A high pressure plasma (dc discharge) ion source, coupled with the flow tube, is used in these experiments. A carrier gas (helium) is passed through a molecular sieve U-shaped liquid nitrogen trap to remove possible impurities (carbon dioxide, oxygen, and water) and then passed into a 1 meter long, 50 mm inner diameter, stainless steel flow tube (Figure 2.1). An MKS model 1258B flow meter is used to control flow up to 20,000 standard cubic centimeters per min (SCCM), with a typical flow rate of He of about 4,000 – 10,000 SCCM. A 10% flow of argon gas, up to 1000 SCCM, is introduced into the head of a flow tube controlled by an MKS 1258B model flow meter. Both meters are controlled by a MKS 247c 4-channel flow readout controller. A combination of the He/Ar gases flow at a relatively high pressure of 0.3 - 0.7 Torr in the flow tube and is monitored by a MKS baratron capacitance manometer, positioned midway along the flow tube.<sup>1</sup>

A water cooled stainless steel metal rod is insulated from the grounded discharge housing by a quartz glass tube and is maintained at a high negative voltage of about 1 – 3 kV. A boat-like tantalum metal cap, used for holding the various transition metals, covers the end of the metal rod at the cathode. Although the mechanism for ion formation in the cold cathode discharge is not well understood, it is believed that the neutral atoms are sputtered off the metal surface once the Ar<sup>+</sup> ions are accelerated towards the cathode and later ionized by charge transfer or a Penning ionization by the excited Ar molecules. The ions of interest formed in the flow tube are carried down the 1-meter long flow tube by the He/Ar buffer gas prior to entering the ion beam apparatus.

According to the Maxwell-Boltzmann distribution of the mean velocity in a perfect gas, the mean free path,  $\lambda$ , of a molecule between collisions is found using eq. 2.1,

$$\lambda = kT / \sigma P(2)^{1/2} \quad (2.1)$$

where  $\sigma$  is the collision cross section and  $k$  is the Boltzmann constant,  $P$  is the pressure in Pa and  $T$  is the absolute temperature in Kelvin. At room temperature and an operating pressure of 0.3 - 0.7 torr, the mean free path of reactant ions is on the order of  $10^{-5}$  -  $10^{-6}$  meters. After traveling down the 1-meter long flow tube, the atomic ions have undergone over  $\sim 10^5$  thermalizing collisions with He and  $\sim 10^4$  thermalizing collisions with Ar in the room temperature flow tube.

The  $\text{MCH}_2^+$  ions are produced by introducing  $\text{CH}_4$  into the flow tube  $\sim 15$  cm downstream of the discharge zone at a low pressure,  $\sim 2$  mTorr. The ions undergo three-body collisions with the He/Ar flow gas, which both thermalize and stabilize the ions vibrationally and rotationally. Consequently, the internal energy and kinetic energy distributions of these complexes is described by a Maxwell-Boltzmann distribution of rotational and vibrational states corresponding to  $300 \pm 100$  K. Past studies in our laboratory have shown this to be the case for molecular species.<sup>5,6</sup>

#### *Flow Tube Source Ion Extraction*

The ions produced by the flow tube source are gently extracted from the source through a 0.8 mm aperture. After extraction, the ions are passed through a separately pumped differential region which is normally maintained at  $10^{-4}$  -  $10^{-5}$  torr in operation (the corresponding mean free path is about 5 - 100 cm) and a base pressure of about  $10^{-6}$  -  $10^{-7}$  torr in no load condition. The ions are focused and accelerated by low-voltage three-element focusing stages (DLA and DLB). The lens elements, with 1.25 cm diameter apertures, are aligned and spaced 3.2 cm from the beam line by circular stainless steel frameworks. For efficient ion transmission from DR1 to DR2, focusing is necessary. The ion energy distributions are broadened by DLA potentials of 300 V, such that the DLA lens potentials are kept at 25, 0, 25 V, respectively, in a high-low-high fashion. The first element in DLB is grounded. The potential of the other elements can exceed 300 V and does not alter the appearance of the data, ranging anywhere from 37 - 360 V.<sup>1</sup>

#### *Ion Beam Formation*

Ions are extracted from the source, then collimated by a double aperture immersion lens and focused by an einzel lens in focusing stage 1 (FS1), as shown in

Figure 2.1. Before being accelerated to the magnetic momentum analyzer, the ion beam passes through a set of four electrostatic quadrupole doublet lenses in FS1 that are used to focus and to change the ion beam shape from cylindrical to ribbon shape suitable for magnetic momentum analysis. The magnetic momentum analyzer is described in detail in the following passage.<sup>7</sup> The ions of interest are selected and deflected 60° when passing through the flight tube.<sup>1</sup> The object and image distances are 47.6 cm. Upon exiting the flight tube, the ion beam is restored back to a nearly circular cross section by another set of electrostatic quadrupole doublet lenses and refocused by an einzel lens in focusing stage 2 (FS2). Both the entrance and exit slit widths are 1 mm. The analysis potential for the flight tube is about 3 kV. Under this condition, the magnet serves as a mass filter with a mass resolution of  $\sim 100$  ( $m/\Delta m$  FWHM) for ions, with an energy spread of  $< 1$  eV.

The ion beam is positioned by a deflector and passed through the focusing stage 2 (FS2), (Figure 2.1), lens train for transmission through a 0.8 mm aperture. Next, an exponential retarder decelerates the ions from energies of 3 keV to near 40 eV. The retarder consists of 41 evenly spaced plates with exponentially decreasing potentials set by internal resistors. The last six plates are externally controllable, but are typically set near 0-200 V.<sup>1</sup>

### Octopole Ion Beam Guide

The working principle of the octopole is similar to that of the quadrupole and has been used extensively in analytical mass spectrometry. A detailed mathematical derivation of the motion of the ions in inhomogeneous rf fields can be found in the following reference.<sup>11</sup> In general, for the ideal multipole rf only device, the effective potential can be described by eq. 2.2,

$$U_{eff}(r) = 4q^2 V_0^2 / m\omega^2 r_0^2 (r/r_0)^6 \quad (2.2)$$

where  $q$  and  $m$  are the charge of the ion and its mass, respectively,  $r$  is the radial distance from the axis to the pole,  $r_0$  is the maximum value of  $r$  or the inner radius of the octopoles, and  $V_0$  and  $\omega$  are the rms voltage and frequency of the rf, respectively. The potential well

has a flat bottom and steeply rising walls, which enables the octopole to be used as a radial ion trap. By comparison, a schematic diagram of  $U_{eff}$  as a function of  $r/r_0$  is shown in Figure 2.2. The ion translational energy along the axis is not perturbed, such that ions with transverse energies are effectively trapped. Consequently, the effective potential of the octopole has a flat bottom and steeply rising walls, enabling it to be used as a radial ion trap, with the least amount of disturbance on the ion's radial velocity.<sup>1</sup>

An optimum  $V_0$  value 150 V (KEPCO, BHK 1000 – 0.2 MG, 0 –1000 V, 0 – 0.2 A) and 6.3 MHz ( $\omega/2\pi$ ) of resonant frequency are used in all experiments studied here. The DC voltage is applied to the poles by a dipolar supply (KEPCO BOP 500M) in order to enable the study of the kinetic energy dependence of the chemical reaction cross section. The octopole is used as a retarder by scanning the pole's DC voltage from positive to negative. By doing retarding energy analysis, we can find the ion beam's absolute kinetic energy and distribution. The octopole DC bias represents the nominal laboratory ion kinetic energy, because the ion source is held at ground potential. By doing retarding energy analysis, the absolute zero and the full width at half-maximum (fwhm) of the absolute kinetic energy distribution of the reactant ions can be determined. The data distribution is nearly Gaussian. By fitting the  $dI_0/dE_{lab}$  curve of the retarding analysis to a Gaussian distribution function with a full width half maximum (FWHM), we are able to find the mean laboratory ion kinetic energy  $E_{lab}$  using eq. 2.3,

$$\bar{E}_{lab} = \int E \cdot P(E, E_{lab}) \cdot dE / \int P(E, E_{lab}) \cdot dE \quad (2.3)$$

where  $P(E, E_{lab})$  is the Gaussian distribution of ion kinetic energy,  $E$ , and measured laboratory energy,  $E_{lab}$ .

### *Quadrupole Mass Filter*

All products and unreacted ions are analyzed by a commercial (Extrel 150 QC with C60 electronics) quadrupole mass filter. The quadrupole has a mass range ~ 1000 amu and employs large rods (1.59 cm) and a low frequency (880 kHz) in order to maximize ion transmission. The AC-60 controller is used to control the rf and dc voltage on the quadrupole.<sup>1</sup>

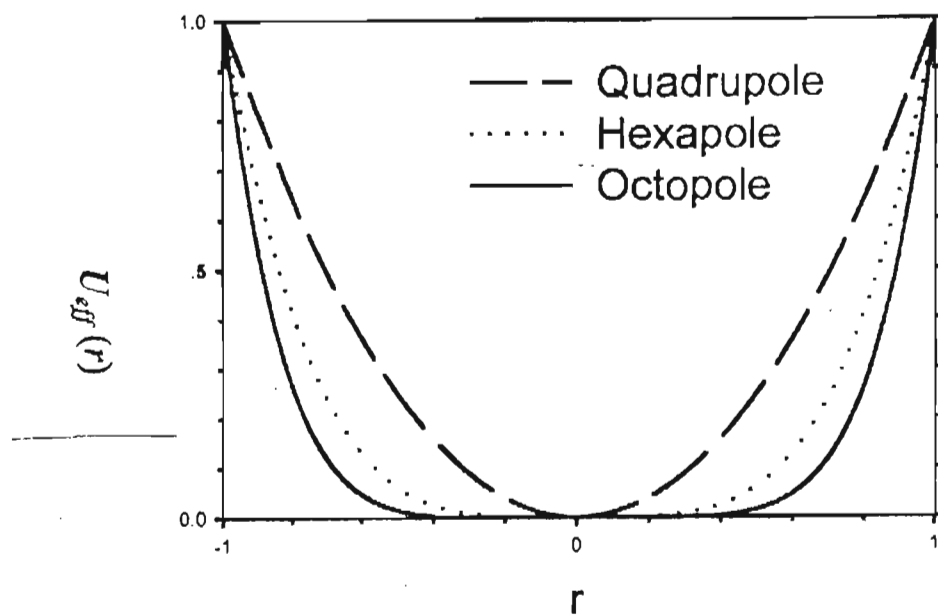


Figure 2.2. Comparison of the  $r^6$  effective potential of the octopole to those ( $r^4$  and  $r^2$ ) of the hexapole and the quadrupole.

### *Detector*

A Daly type ion collector is used to detect the ions after the quadrupole. The conversion dynode on the detector, the doorknob, has an applied potential of -23 kV. The incoming ions are accelerated to the doorknob, causing electrons to be emitted. Electrons ejected from the conversion dynode hit the scintillator, which then fluoresces and emits photons. The photons are collected in a RCA 8850 photomultiplier tube (PMT) and the signal output of the PMT is directly discriminated (Tennelec model 453 discriminator) and counted by a 100 MHz dual counter/timer (Canberra model 2071A), with dwell times of 0.01 s – 0.01 min.<sup>1</sup>

### *Computer Aid Automatic Data Collection*

Most recently, a Lab View program has been developed in our lab to control the programmable magnet power supply for automation of the magnetic mass scan. Prior to this automation, the magnet power supply was manually tuned to find the mass of interest and record its intensity manually. A magnetic gauss meter was used to help identify the mass at a certain flight tube potential. Such automation is useful for conveniently optimizing the ion source conditions and saving the results for future use. An experimental scan consists of setting the collisional energy and then setting the quadrupole to a mass of interest. The timer counts for 0.1- 1 s before the next mass is set. After scanning for the masses of the reactant and the products, a new energy is incremented and the process repeated. Consecutive scans measure reactions that occur with the background chamber pressure. Consequently, these serve as background scans and establish the zero signal level. The background and the foreground scans are repeated until the noise reaches an acceptable level. The two electropneumatic valves, used for setting reactant gas flow, are controlled by digital outputs under software control.<sup>1</sup>

## **Thermochemical Analysis**

### *Ion and Neutral Reactants Energy*

#### Determination of Cross Section

Ion intensities are converted to total absolute cross sections,  $\sigma_{\text{tot}}$ , using eq. 2.4,

$$I_R = (I_R + \Sigma I_P) \cdot \exp(-\sigma_{\text{tot}} n l) \quad (2.4)$$

where  $I_P$  and  $I_R$  are the measured transmitted intensities of the product and reactant ions, respectively,  $n$  is the gas density, and  $l$  is the effective path length (8.26 cm) of the interaction region. The reaction cross section for the individual products,  $\sigma_P$ , is given by eq. 2.5,

$$\sigma_P = \sigma_{\text{tot}} (I_P / \Sigma I_P) \quad (2.5)$$

where  $I_P$  is the measured transmitted product ion intensity. Absolute uncertainties in the cross section magnitude are estimated to be  $\pm 20\%$ , whereas relative magnitudes are more accurate.

By scanning the direct current (dc) bias on the octopole with respect to the potential of the ion source region, we can vary the kinetic-energy dependence of the ions during an experiment. The quadrupole is also scanned over all the products and unreacted parent ions and the intensities are recorded over all the energies. Both the octopole bias and quadrupole are computer-controlled. To allow signal averaging, this process is repeated multiple times and, thus, enables the study of the relatively inefficient chemical reactions.

Because the momentum of the center-of-mass of the collision pair through the laboratory is conserved and is not available to the reaction, the relative energy is in terms of the center of mass (CM) frame instead of the laboratory (LAB) frame. By assuming a stationary target, ion kinetic energies in the laboratory frame,  $E_{\text{lab}}$ , are converted to energies in the center-of-mass frame,  $E_{\text{CM}}$ , according to eq. 2.6

$$E_{\text{CM}} = E_{\text{lab}} m / (m + M) \quad (2.6)$$

where  $m$  and  $M$  are the neutral and ionic reactant masses, respectively. All energies reported below are in terms of the CM frame unless otherwise noted. Two effects broaden the cross section data: the thermal motion of the neutral reactant gas (Doppler broadening)<sup>12</sup> and the kinetic energy distribution of the reactant ions.



The cross sections for exothermic reactions performed in these experiments are well-described by the Langevin-Gioumoussis-Stevenson (LGS) model<sup>13</sup> given by eq. 2.7,

$$\sigma_{\text{LGS}} = \pi e(2\alpha/E)^{1/2} \quad (2.7)$$

where  $e$  is the electron charge,  $\alpha$  is the polarizability of the neutral reactant molecule, and  $E$  is the relative kinetic energy of the reactants. Cross sections for exothermic reactions generally follow this type of energy dependence, although deviations from this behavior are observed.<sup>14</sup> The reaction efficiencies for exothermic reactions are assessed by comparing the experimental cross section measured using GIBMS to the theoretical cross section,  $\sigma_{\text{LGS}}$ .

Many of the cross sections determined in this work are for endothermic reactions, i.e., the cross section is  $\sim 0$  until the kinetic energy reaches the threshold and then increases as the kinetic energy of the ions increases. The kinetic-energy dependence of product cross sections is analyzed to determine  $E_0$ , the energy threshold for product formation at 0 K. Because of the kinetic and internal energy distributions of the reactants, the apparent threshold observed under laboratory conditions can lie below  $E_0$ . To determine  $E_0$ , endothermic reaction cross sections are modeled using an empirical model given in eq. 2.8,<sup>15-17</sup>

$$\sigma(E) = \sigma_0 \times g_i (E + E_i + E_{el} - E_0)^n / E \quad (2.8)$$

where  $\sigma_0$  is an energy-independent scaling factor,  $E$  is the relative kinetic energy of the reactants,  $E_{el}$  is the electronic energy of the transition metal ion ( $M^+$ ) reactant, and  $n$  is an adjustable parameter. There is an explicit sum of contributions from rovibrational states of reactants at 300 K, denoted by  $i$ , having energies  $E_i$  and populations  $g_i$ , where  $\sum g_i = 1$ .

Before comparison with the experimental data, eq. 2.8 is convoluted with the kinetic energy distributions of the ions and neutral reactants at 300 K. The parameters,  $\sigma_0$ ,  $n$ , and  $E_0$ , are then optimized using a nonlinear least-squares analysis to give the best fit to the experimental cross section.<sup>16,17</sup> Error limits for  $E_0$  are calculated from the range of

threshold values for different data sets over a range of acceptable  $n$  values combined with the absolute uncertainty in the kinetic energy scale.

### Theoretical Calculations

All quantum chemistry calculations here are computed with the B3LYP hybrid density functional method<sup>18,19</sup> and performed with the GAUSSIAN 03 suites of programs.<sup>20,21</sup> The B3LYP functional is used for most calculations done here because it provided reasonable results for the analogous  $\text{Pt}^+ + \text{CH}_4$  system.<sup>22</sup> In all cases, the thermochemistry reported here is corrected for zero-point energy effects. Because several of the transition states of interest involve bridging hydrogens, the rather large 6-311++G(3df,3p) basis set is used for carbon and hydrogen. This basis set gives good results for the thermochemistry of methane, with deviations from experiment of less than 0.08 eV for the bond energies of H-CH<sub>3</sub> (4.406 vs. 4.480 eV), H<sub>2</sub>-CH<sub>2</sub> (4.666 vs. 4.713 eV), H-CH (4.332 vs. 4.360 eV), C-H (3.532 vs. 3.465 eV), and H-H (4.505 vs. 4.478 eV) (see Table 1 of reference<sup>22,23</sup> for thermochemistry used for all H, D, CH<sub>x</sub>, and CD<sub>x</sub> species). For most calculations, the 60 core electrons of hafnium and tantalum are described by the relativistic effective core potentials (ECP) of Hay-Wadt (HW),<sup>24</sup> with the valence electrons described by the Los Alamos double- $\zeta$  basis set (LANL2DZ). This basis set is optimized for neutral atoms, whereas the positive charge differentially contracts the  $s$  orbitals compared to the  $d$  orbitals. Hence, we used an altered valence basis set for Hf and Ta as described by Ohanessian et al.,<sup>23</sup> which we designate as HW+.

The most appropriate choice for a level of theory has been investigated for the first- and third-row transition metal methyl cations by Holthausen et al.<sup>25</sup> and for the first-row transition metal methylene cations by Holthausen, Mohr, and Koch.<sup>26</sup> In the first study, these authors used B3LYP, Becke-Half-and-Half-LYP (BHLYP), and QCISD(T) methods with a basis set consisting of a polarized double- $\zeta$  basis on C and H and the Hay/Wadt relativistic ECP with valence electrons added. The symmetries of the metal methyl species were constrained to  $C_{3v}$ . For the first-row  $\text{MCH}_3^+$  species ( $M = \text{Sc} - \text{Cu}$ ), where experimental results are available for all metals, these authors reach the conclusion that the B3LYP functional overbinds severely, with a mean average deviation (MAD) from experiment of 0.41 eV and that the BHLYP functional and the QCISD(T) methods

perform more accurately, with MADs of 0.18 and 0.20 eV, respectively.<sup>27,28</sup> For the third-row elements, the bond energies calculated using B3LYP functional were again higher than those for BHLYP and QCISD(T) functionals. In contrast, for the metal methylene complexes,<sup>26</sup> the BHLYP functional predicts bond energies below experimental values, whereas the performance of the B3LYP functional is quite good. Additionally, these authors found that the results depended on the basis set used for the metal ion with an all-electron basis set providing better results than effective core potential (ECP) methods. On the basis of these results, the present studies performed calculations for the various product ions using the BHLYP functional and the Stuttgart/Dresden (SD) ECP<sup>29</sup> for Hf<sup>+</sup>, Ta<sup>+</sup> and Ta<sup>2+</sup> along with QCISD(T) calculations using the HW+ ECP. Such calculations will be explicitly noted, otherwise, our results will refer to a B3LYP/HW+/6-311++G(3df,3p) level of theory.

## References

- (1) Loh, S. K.; Hales, D. A.; Lian, L.; Armentrout, P. B. *Journal of Chemical Physics* **1989**, *90*, 5466.
- (2) Schultz, R. H.; Armentrout, P. B. *IJMSIP* **1991**, *107*, 29.
- (3) Gerlich, D. *Adv. Chem. Phys.* **1992**, *82*, 1.
- (4) Ervin, K. M.; Armentrout, P. B. *J. Chem. Phys.* **1985**, *83*, 166.
- (5) Dalleska, N. F.; Honma, K.; Sunderlin, L. S.; Armentrout, P. B. *JACS* **1994**, *116*, 3519.
- (6) Rodgers, M. T.; Armentrout, P. B. *J. Phys. Chem. A* **1997**, *101*, 2614.
- (7) Mathews, C. K. v. H., K. E. *Biochemistry; The Benjamin / Cummings Publishing Company* **1990**.
- (8) Li, F. Z., X.-G.; Armentrout, P. B. *International Journal of Mass Spectrometry* **2006**, *255-256*, 279.
- (9) Armentrout, P. B. S., S.; Liyanage, R. *J. Phys. Chem. A* **2006**, *110*, 1242.

- (10) Parke, L. G. H., C. S.; Armentrout, P. B. *International Journal of Mass Spectrometry and Ion Processes* **2006**, *254*, 168.
- (11) Cooks, R. G.; Wong, P. H. *Accounts of Chemical Research* **1998**, *31*, 379.
- (12) Chantry, P. J. *JCP* **1971**, *55*, 2746.
- (13) Gioumousis, G.; Stevenson, D. P. *JCP* **1958**, *29*, 294.
- (14) Armentrout, P. B. *P. Ausloos, S. G. Lias, Eds., D. Reidel* **1987**, 83.
- (15) Chesnavich, W. J.; Bowers, M. T. *JPC* **1979**, *83*, 900.
- (16) Aristov, N.; Armentrout, P. B. *JACS* **1986**, *108*, 1806.
- (17) Armentrout, P. B. Thermochemical Measurements by Guided Ion Beam Mass Spectrometry. In *Advances in Gas Phase Ion Chemistry*; Adams, N. G., Babcock, L. M., Eds.; JAI Press: Greenwich, 1992; Vol. 1; pp 83-119.
- (18) Becke, A. D. *J. Chem. Phys.* **1993**, *98*, 5648.
- (19) Lee, C.; Yang, W.; Parr, R. G. *Phys. Rev. B* **1988**, *37*, 785.
- (20) Frisch, M. J.; Trucks, G. W.; Schlegel, H. B.; Scuseria, G. E.; Robb, M. A.; Cheeseman, J. R.; Zakrzewski, V. G.; Montgomery, J. A., Jr.; Stratmann, R. E.; Burant, J. C.; Dapprich, S.; Millam, J. M.; Daniels, A. D.; Kudin, K. N.; Strain, M. C.; Farkas, O.; Tomasi, J.; Barone, V.; Cossi, M.; Cammi, R.; Mennucci, B.; Pomelli, C.; Adamo, C.; Clifford, S.; Ochterski, J.; Petersson, G. A.; Ayala, P. Y.; Cui, Q.; Morokuma, K.; Salvador, P.; Dannenberg, J. J.; Malick, D. K.; Rabuck, A. D.; Raghavachari, K.; Foresman, J. B.; Cioslowski, J.; Ortiz, J. V.; Baboul, A. G.; Stefanov, B. B.; Liu, G.; Liashenko, A.; Piskorz, P.; Komaromi, I.; Gomperts, R.; Martin, R. L.; Fox, D. J.; Keith, T.; Al-Laham, M. A.; Peng, C. Y.; Nanayakkara, A.; Challacombe, M.; Gill, P. M. W.; Johnson, B.; Chen, W.; Wong, M. W.; Andres, J. L.; Gonzalez, C.; Head-Gordon, M.; Replogle, E. S.; Pople, J. A. *Gaussian 98, Revision A.11*; Gaussian, Inc.: Pittsburgh, PA, 2001.
- (21) Frisch, M. J.; Trucks, G. W.; Schlegel, H. B.; Scuseria, G. E.; Robb, M. A.; Cheeseman, J. R.; Montgomery, J., J. A. ; Vreven, T.; Kudin, K. N.; Burant, J. C.; Millam, J. M.; Iyengar, S. S.; Tomasi, J.; Barone, V.; Mennucci, B.; Cossi, M.; Scalmani, G.; Rega, N.; Petersson, G. A.; Nakatsuji, H.; Hada, M.; Ehara, M.; Toyota, K.; Fukuda, R.; Hasegawa, J.; Ishida, M.; Nakajima, T.; Honda, Y.; Kitao, O.; Nakai, H.; Klene, M.; Li, X.; Knox, J. E.; Hratchian, H. P.; Cross, J. B.; Adamo, C.; Jaramillo, J.; Gomperts, R.; Stratmann, R. E.; Yazyev, O.; Austin, A. J.; Cammi, R.; Pomelli, C.; Ochterski, J. W.; Ayala, P. Y.; Morokuma, K.; Voth, G. A.; Salvador, P.; Dannenberg, J. J.; Zakrzewski, V. G.; Dapprich, S.; Daniels, A. D.; Strain, M. C.; Farkas, O.; Malick, D. K.; Rabuck, A. D.; Raghavachari, K.; Foresman, J. B.; Ortiz, J. V.; Cui, Q.; Baboul, A. G.; Clifford, S.;

Cioslowski, J.; Stefanov, B. B.; Liu, G.; Liashenko, A.; Piskorz, P.; Komaromi, I.; Martin, R. L.; Fox, D. J.; Keith, T.; Al-Laham, M. A.; Peng, C. Y.; Nanayakkara, A.; Challacombe, M.; Gill, P. M. W.; Johnson, B.; Chen, W.; Wong, M. W.; Gonzalez, C.; Pople, J. A. *Gaussian 03, Revision B.02; Revision B.02 ed.*; Gaussian, Inc.: Pittsburgh, PA, 2003.

- (22) Zhang, X.-G.; Armentrout, P. B. *J. Am. Chem. Soc.* **2001**, *123*, 5563.
- (23) Ohanessian, G.; Brusich, M. J.; Goddard III, W. A. *JACS* **1990**, *112*, 7179.
- (24) Hay, P. J.; Wadt, W. R. *JCP* **1985**, *82*, 299.
- (25) Holthausen, M. C. H., C.; Cornehl, H. H.; Koch, W.; Schwartz, H. *J. Chem. Phys.* **1995**, *102*, 4931.
- (26) Holthausen, M. C. M., M.; Koch, W. *Chem. Phys. Lett.* **1995**, *240*, 245.
- (27) Freiser, B. S., Ed.; *Organometallic Ion Chemistry*; Kluwer: Dordrecht, 1996.
- (28) Armentrout, P. B. Gas Phase Organometallic Chemistry. In *Topics in Organometallic Chemistry*; Brown, J. M., Hofmann, P., Eds.; Springer-Verlag: Berlin, 1999; Vol. 4; pp 1.
- (29) Andrae, D.; Haeussermann, U.; Dolg, M.; Stoll, H.; Preuss, H. *Theor. Chim. Acta* **1990**, *77*, 123.

CHAPTER 3

WHY IS HAFNIUM SO UNREACTIVE?  
EXPERIMENTAL AND THEORETICAL  
STUDIES OF THE REACTION  
OF  $\text{Hf}^+$  WITH METHANE

Laura G. Parke, Christopher S. Hinton, P. B. Armentrout

Reprinted from *International Journal of Mass Spectrometry, Volume 254, Issue 3*,  
Laura G. Parke, Christopher S. Hinton, P. B. Armentrout, Why is hafnium so  
unreactive? Experimental and theoretical studies of the reaction of  $\text{Hf}^+$  with methane,  
*Pages 168-182*, 2006, with permission from Elsevier.



## Why is hafnium so unreactive? Experimental and theoretical studies of the reaction of $\text{Hf}^+$ with methane

Laura G. Parke, Christopher S. Hinton, P.B. Armentrout\*

Department of Chemistry, University of Utah, Salt Lake City, UT 84112-0850, USA

Received 19 April 2006; received in revised form 27 May 2006; accepted 29 May 2006  
Available online 7 July 2006

### Abstract

The reaction of atomic hafnium cations with  $\text{CH}_4$  and  $\text{CD}_4$  is studied using a guided ion beam tandem mass spectrometer. In contrast to most third-row transition metal ions, the dehydrogenation reaction to form  $\text{HfCH}_2^+ + \text{H}_2$  is endothermic. At higher energies, other products,  $\text{HfCH}^+$ ,  $\text{HfCH}_3^+$ , and  $\text{HfH}^+$ , the latter being the predominant species, are observed. Implicit in the behavior of the cross sections for  $\text{HfH}^+$ ,  $\text{HfCH}_2^+$ , and  $\text{HfCH}_3^+$  is a  $\text{H}-\text{Hf}^+-\text{CH}_3$  intermediate. Modeling of the endothermic cross sections provides for 0 K bond dissociation energies (in eV) of  $D_0(\text{Hf}^+-\text{CH}) = 5.10 \pm 0.15$ ,  $D_0(\text{Hf}^+-\text{CH}_2) = 4.37 \pm 0.07$ ,  $D_0(\text{Hf}^+-\text{CH}_3) = 2.12 \pm 0.26$ , and  $D_0(\text{Hf}^+-\text{H}) = 1.97 \pm 0.11$ . These experimental bond energies are in good agreement with density functional calculations at the B3LYP/HW+6-311++G(3df,3p) level of theory. Theoretical calculations reveal the mechanism of the reaction and illustrate the geometric and electronic structures of the individual products and intermediates. Unlike its first and second-row congeners, which have quartet ground states and must change spin to dehydrogenate methane,  $\text{Hf}^+$  retains its ground state doublet configuration throughout the dehydrogenation reaction, demonstrating that spin-restrictions are not responsible for the relatively low reactivity of  $\text{Hf}^+$ . Instead, this can be attributed to the unfavorable doubly occupied 6s orbital in the  $^2\text{D}$  ground state of  $\text{Hf}^+$ .

© 2006 Elsevier B.V. All rights reserved.

**Keywords:** Bond dissociation energies; C–H bond activation; Guided ion beam mass spectrometry; Hafnium; Methane

### 1. Introduction

In understanding catalysis, it is useful to consider not only which systems are reactive but also which systems are not. If the underlying reasons for the differences can be quantitatively assessed, the results can lend considerable insight into the electronic and geometric details that enhance (or suppress) reactivity. A case in point is the reactions of atomic metal ions with methane. Activation of methane is of considerable interest as identification of a convenient catalyst for selective oxidation to methanol would be technologically important by allowing better use of natural gas [1,2]. Further, the C–C coupling reactions intrinsic to Fischer-Tropsch chemistry have been observed to occur for the two early third-row transition metal ions,  $\text{Ta}^+$  and  $\text{W}^+$ , in the gas phase [3,4]. Oddly,  $\text{Hf}^+$ , the other early third-row transition metal ion, fails to react with methane at thermal ener-

gies, even though its second-row analogue,  $\text{Zr}^+$ , is probably the most reactive second-row transition metal ion [5,6], and  $\text{Ti}^+$ , its first-row congener, is certainly one of the more reactive first-row transition metal ions [7,8].

The ground state of  $\text{Hf}^+$  is  $^2\text{D}$  with a  $6s^25d^1$  electronic configuration, whereas the ground states of  $\text{Ta}^+$  ( $^3\text{F}$ ,  $6s^15d^3$ ),  $\text{W}^+$  ( $^6\text{D}$ ,  $6s^15d^4$ ),  $\text{Zr}^+$  ( $^4\text{F}$ ,  $5s^14d^2$ ), and  $\text{Ti}^+$  ( $^4\text{F}$ ,  $4s^13d^2$ ) all have half-filled valence s orbitals. Indeed, hafnium is one of only two transition metal cations to have such an  $s^2$  configuration as its ground state,  $\text{Lu}^+$  being the other. For all other transition metal cations, the  $s^2d^{n-2}$  configuration has a relatively high energy compared to the  $s^1d^{n-1}$  or  $d^n$  states. For lutetium and hafnium, the  $s^2$  configuration is low in energy because of the lanthanide contraction, a result of relativistic effects. Because of this closed shell configuration,  $\text{Lu}^+$  ( $^1\text{S}$ ,  $6s^2$ ) has long been known to be very unreactive with methane [9]. On the basis of similar observations for the other third-row metal ions, Irikura and Beauchamp suggested that the reactivity of the transition metal cations with methane can be correlated with the accessibility of the  $s^1d^{n-1}$  configuration [3,4], such that  $\text{Hf}^+$  ( $^2\text{D}$ ) will not be reactive, in good

\* Corresponding author. Tel.: +1 801 581 7885; fax: +1 801 581 8433.  
E-mail address: [armentrout@chem.utah.edu](mailto:armentrout@chem.utah.edu) (P.B. Armentrout).

correspondence with reactivity rules thoroughly evaluated for the first-row transition metal cations [7,10]. However, the question remains why  $\text{Hf}^+$  does not react more efficiently by coupling to its  $^4\text{F}$  ( $6s^1 5d^2$ ) excited state, which lies only 0.56 eV higher in energy [11], especially as spin–orbit coupling effects are large for the third-row metals.

Previous experimental studies concerning the reaction of  $\text{Hf}^+$  with methane were performed at thermal energies by Irikura and Beauchamp using a Fourier transform ion cyclotron resonance (FTICR) mass spectrometer [3,4]. They did not observe a reaction for thermal  $\text{Hf}^+$ , although residual excited states did react. Furthermore, they found that  $\text{HfCH}_2^+$  is readily reduced back to  $\text{Hf}^+$  by dihydrogen, verifying that the dehydrogenation reaction with methane is endothermic. To further explore why  $\text{Hf}^+$  is so unreactive, a more quantitative characterization of the thermochemistry and a thorough exploration of the potential energy surface would be desirable. In the present study, we investigate the reactions of  $\text{Hf}^+$  with  $\text{CH}_4$  and  $\text{CD}_4$  over a wide range of kinetic energies such that several  $\text{HfCH}_x^+$  species are formed. All processes observed are endothermic, thereby allowing the determination of the bond energies of these species and providing mechanistic information about the reactions. Complementing these experimental studies is a thorough theoretical examination of the potential energy surface and all intermediates and products.

## 2. Experimental and theoretical methods

### 2.1. General procedures

These experiments were carried out using a guided ion beam tandem mass spectrometer described in detail elsewhere [12,13]. Ions are generated in a source described below, extracted from the source, accelerated and focused into a magnetic sector momentum analyzer for mass analysis. The  $^{180}\text{Hf}$  isotope (35.2% natural abundance) is selected, decelerated to a desired kinetic energy and then focused into an octopole ion beam guide. Radio frequency electric fields trap the ions in the radial direction for complete collection of reactant and product ions [14,15]. As the ions travel down the octopole, they pass through a static gas cell that holds the neutral reactant at low pressures ( $<0.3$  m Torr) to ensure single collision reaction conditions. This was confirmed through the examination of the pressure dependence of the cross sections measured.

The unreacted parent and product ions drift to the end of the octopole where they are extracted and focused into a quadrupole mass filter for mass separation. A secondary electron scintillation detector is used to detect ions using standard pulse counting techniques. After accounting for background signals, reaction cross sections are calculated from product ion intensities as compared to reactant ion intensities [16]. Uncertainties in absolute cross sections are estimated to be  $\pm 20\%$ .

The octopole is used as a retarding energy analyzer to determine the absolute zero and distribution of the ion kinetic energy by varying the dc bias on the octopole rods relative to the potential of the ion source region [16]. Laboratory (lab) ion energies are converted to energies in the center-of-mass frame (CM) using

$E_{\text{CM}} = E_{\text{lab}} \times m/(m+M)$ , where  $m$  and  $M$  are the neutral and ionic reactant masses, respectively. Reaction cross sections are broadened by the kinetic energy distribution of the reactant ion and the random thermal motion of the reactant molecules in the gas cell (Doppler broadening) [17]. The distributions of ion kinetic energies are independent of energy and are close to Gaussian with a typical fwhm of 0.6–0.9 eV (lab).

### 2.2. Ion source

$\text{Hf}^+$  ions are generated in a direct-current discharge flow tube (DC/FT) source that uses a hafnium cathode held at a high negative voltage (0.7–1.5 kV) over which a flow of approximately 90% He and 10% Ar passes at an average pressure of 0.3–0.4 Torr [13].  $\text{Ar}^+$  ions created in the discharge are accelerated toward the hafnium cathode creating atomic metal ions. Subsequently, the ions undergo  $\sim 10^3$  collisions with He and  $\sim 10^4$  collisions with Ar as they travel down the 1-m long flow tube prior to entering the ion beam apparatus. In previous studies, it has been demonstrated that the electronic temperature of atomic metal ions produced in the flow tube source ranges between 300 and 1100 K [18–22]. Thus, even at the maximum likely temperature, 98.9% of the hafnium ions are in the  $^2\text{D}$  ground state, and 96.2% in the  $^2\text{D}_{3/2}$  ground level (99.9 and 99.7%, respectively, at the average temperature of 700 K). The average electronic energy,  $E_{\text{el}}$ , for  $\text{Hf}^+$  at a temperature of  $700 \pm 400$  K is  $0.006 + 0.010/-0.006$  eV.

### 2.3. Data analysis

Data analysis of the kinetic energy dependence of product cross sections is performed to determine the energy threshold for product formation,  $E_0$ . The apparent threshold observed under laboratory conditions is shifted from this  $E_0$  because of the Maxwell–Boltzmann velocity distribution of the neutral reactants, as well as the kinetic and internal energy distributions of the reactant ions. These effects cause reactions to take place at energies below  $E_0$ . It has been shown in previous theoretical and experimental work that endothermic cross sections can be modeled using Eq. (1) [23–25],

$$\sigma(E) = \frac{\sigma_0 \sum g_i (E + E_i + E_{\text{el}} - E_0)^n}{E} \quad (1)$$

where  $\sigma_0$  is an energy-independent scaling parameter,  $E$  the relative kinetic (translational) energy of the reactants,  $E_0$  the reaction threshold at 0 K, and  $n$  an adjustable parameter that determines the shape of the cross section. The summation is over all possible rovibrational states of the neutral reactant with populations  $g_i$  ( $\sum g_i = 1$ ) and energies  $E_i$ . The vibrational frequencies and rotational constants used in determining  $E_i$  are taken from the literature for  $\text{CH}_4$  and  $\text{CD}_4$  [26]. The electronic energy of the  $\text{Hf}^+$  reactant is  $0.006 + 0.010/-0.006$  eV, as noted above. The model of Eq. (1) is convoluted over the neutral and ion kinetic energy distributions prior to comparison with the data [16,24,25]. The adjustable parameters are then optimized using a nonlinear least-squares analysis to give the best reproduction of the data. Values reported for  $E_0$ ,  $\sigma_0$ , and  $n$  are the average values obtained for



each parameter over a range of best fits to several independent data sets. The corresponding uncertainties are one standard deviation. Uncertainties in the absolute energy scale ( $\pm 0.05$  eV, lab) and the uncertainty in the electronic energy of  $\text{Hf}^+$  are included in the uncertainties reported for  $E_0$ .

As discussed below, the reaction channels observed probably compete with one another, which could have an influence on the thresholds of the higher energy channels. Although we have developed a simple statistical approach to model competition [27], this approach is not sufficient for the present system as some channels (including the entrance channel, see below) have tight transition states that will influence the competition. Ideally, a phase space approach in which angular momentum is explicitly considered is needed to accurately model these bimolecular reactions, but again the presence of a barrier in the entrance channel in addition to the transition states for some channels makes such an approach too difficult to obtain accurate results.

#### 2.4. Theoretical calculations

Most quantum chemistry calculations here are computed with the B3LYP hybrid density functional method [28,29] and performed using the Gaussian 03 suite of programs [30]. This level of theory was chosen because it provides reasonable results for reactions of methane with  $\text{Pt}^+$  [31],  $\text{Re}^+$  [32],  $\text{W}^+$  [33], and  $\text{Ir}^+$  [34]. The relatively large 6-311++G(3df,3p) set is used for carbon and hydrogen because of the bridging hydrogens that occur for many of the transition states of interest. This basis set yields bond dissociation energies (BDEs) for the hydrocarbon species in close correspondence (within 0.08 eV) with experimental BDEs:  $\text{H}-\text{CH}_3$  (4.406 versus 4.480 eV),  $\text{H}_2-\text{CH}_2$  (4.666 versus 4.713 eV),  $\text{H}-\text{CH}$  (4.332 versus 4.360 eV),  $\text{C}-\text{H}$  (3.532 versus 3.465 eV) and  $\text{H}-\text{H}$  (4.505 versus 4.478 eV) [31]. The relativistic effective core potential (ECP) of Hay-Wadt (HW) [35] is used to describe the 60 core electrons of hafnium and the Los Alamos double- $\zeta$  basis set (LANL2DZ) is used to describe the valence electrons. This basis set is optimized for neutral atoms, whereas the charge differentially contracts the 6s orbitals compared to the 5d orbitals. This is accounted for in an altered valence basis set described by Ohanessian et al. [36], designated as HW+, which is used for most of our calculations.

First- and third-row transition metal methyl cations have been thoroughly investigated by Holthausen et al. [37], and first-row transition metal methylene cations by Holthausen et al. [38]. In the first study, calculations were performed using B3LYP, Becke-half-and-half-LYP (BHLYP), and QCISD(T) levels of theory along with a polarized double- $\zeta$  basis on C and H and the Hay-Wadt relativistic ECP with valence electrons added for the metals. For metal methyl cations, the symmetries were constrained to  $C_{3v}$ . It was determined that for first-row  $\text{MCH}_3^+$  species ( $\text{M} = \text{Sc}-\text{Cu}$ ) the B3LYP functional overbinds, with a mean absolute deviation (MAD) from experiment of 0.41 eV. Better estimates are calculated using the BHLYP functional and the QCISD(T) methods, with MADs of 0.18 and 0.20 eV, respectively. For third-row elements, the BDEs calculated using B3LYP were again higher than those obtained using BHLYP and QCISD(T). In contrast, the second study finds that BDEs calcu-

lated for metal methylene cations using the BHLYP functional gave estimates below experimental values, whereas those calculated with the B3LYP functional were comparable. Also, these authors concluded that the results were dependent upon the basis set used for the metal ion with an all electron basis yielding more accurate results than effective core potential (ECP) methods. Drawing from these results, the present study carried out calculations for various product ions using the BHLYP functional and QCISD(T)/B3LYP method and the Stuttgart-Dresden (SD) ECP [39] for  $\text{Hf}^+$  in addition to the B3LYP/HW+ results. Calculations of this sort will be indicated explicitly, otherwise, the calculations have been performed at the B3LYP/HW+/6-311++G(3df,3p) level of theory.

We calculate a  $^2\text{D}$  ground state for  $\text{Hf}^+$  using the HW+ basis set and B3LYP level of theory, with a quartet state at 0.298 eV. Using B3LYP/SD, BHLYP/HW+, and BHLYP/SD combinations of functional and basis sets, the quartet excitation energies are 0.281, 0.283, and 0.239 eV, demonstrating that atomic excitation energies are essentially independent of the basis set and DFT method used. These values are somewhat lower than the 0.563 eV experimental excitation energy between properly weighted spin-orbit levels of the  $^2\text{D}$  ( $6s^25d^1$ ) and  $^4\text{F}$  ( $6s^15d^2$ ) states [11]. At the QCISD(T)/HW+ level of theory, we calculate an excitation energy of 0.774 eV, somewhat above the experimental value.

For calculations of the potential energy surfaces, the B3LYP/HW+/6-311++G(3df,3p) level of theory was used. Transition states were located using the synchronous transit-guided quasi-Newton method (QST2 and QST3) [40,41], followed by geometry optimizations and frequency calculations to verify a first order saddle point and IRC calculations or relaxed potential energy surface scans to verify that the transition state connects the appropriate intermediates. For multiply bound species, the B3LYP level of theory does an adequate job of estimating energetics, providing for a high-quality characterization of the overall surface.

### 3. Experimental results

Fig. 1 shows cross sections for the reaction of  $\text{CH}_4$  with  $\text{Hf}^+$ , which yields products listed in reactions (2)–(5).



We also looked for the  $\text{HfC}^+$  product, but its cross section could not be resolved from that of  $\text{HfCH}^+$ , indicating it must be at least an order of magnitude smaller. Cross sections for reactions (3) and (5) have been corrected for mass overlap with the much more intense  $\text{HfCH}_2^+$  cross section. The deuterated analogue of this system yields similar results with less mass overlap, providing for better measurement of product intensities over a broader energy range (Fig. 2).

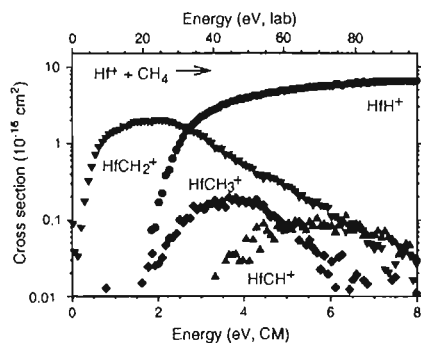


Fig. 1. Cross sections for reaction of  $\text{Hf}^+$  ( $^2\text{D}$ ) with  $\text{CH}_4$  as a function of kinetic energy in the laboratory (upper  $x$ -axis) and center of mass (lower  $x$ -axis) frames.

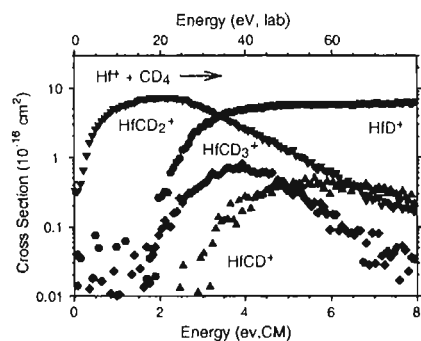


Fig. 2. Cross sections for reaction of  $\text{Hf}^+$  ( $^2\text{D}$ ) with  $\text{CD}_4$  as a function of kinetic energy in the laboratory (upper  $x$ -axis) and center of mass (lower  $x$ -axis) frames.

As illustrated in Figs. 1 and 2, all reactions with methane are endothermic. This is in agreement with previous FTICR studies done by Irikura and Beauchamp who observed no reaction at thermal energy with ground state ions [4]. As the kinetic energy is raised, dehydrogenation of methane to form  $\text{HfCH}_2^+$  (reaction (4)), is the only process observed at low energies. At higher energies, there is a marked decline in the cross section for  $\text{HfCH}_2^+$  that correlates with the apparent thresholds for the other products. Only the cross section for  $\text{HfH}^+$  is substantial enough to account for the initial drop in intensity of  $\text{HfCH}_2^+$ .

Because decomposition of  $\text{HfCH}_2^+$  to  $\text{HfH}^+$  +  $\text{CH}$  cannot occur until much higher energies, the cross sections must be coupled by competition between reactions (2) and (4), which implies that the two product channels share a common intermediate.

Figs. 1 and 2 show that reactions (2) and (5) and their deuterated analogues have similar apparent thresholds of about 1.5 eV, suggesting that the single bonds for  $\text{HfH}^+$  and  $\text{HfCH}_3^+$  are comparable in strength. Notwithstanding their similar bond strengths, the  $\text{HfH}^+$  cross section is more prevalent up to about 4 eV by a factor of about 3.5. Similarly, for the  $\text{CD}_4$  system, the  $\text{HfD}^+$  cross section exceeds that for  $\text{HfCD}_3^+$  up to about 4 eV by a factor of about 2. This preference can be attributed largely to angular momentum effects, as discussed further below. Above 4 eV, the  $\text{HfCH}_3^+$  ( $\text{HfCD}_3^+$ ) cross sections decline, which can be attributed partly to subsequent dehydrogenation to form  $\text{HfCH}^+$  ( $\text{HfCD}^+$ ) (reaction (3)). In addition, we find that the sums of the  $\text{HfCH}_3^+$  and  $\text{HfCH}^+$  ( $\text{HfCD}_3^+$  and  $\text{HfCD}^+$ ) cross sections also decline above 4 eV. This indicates that dissociation of  $\text{HfCH}_3^+$  to  $\text{Hf}^+$  +  $\text{CH}_3$ , which can begin at  $4.48 \text{ eV} = D(\text{H}-\text{CH}_3)$ , must also be occurring.

#### 4. Thermochemical and theoretical results

Data analysis of the cross sections is performed using Eq. (1). The optimal parameters for each product cross-section for the  $\text{CH}_4$  and  $\text{CD}_4$  systems are listed in Table 1. Because all sources of rotational, vibrational, and translational energy are included in the modeling, the  $E_0$  thresholds correspond to 0 K values. The BDEs at 0 K of the hafnium-ligand cations are calculated using Eq. (6):

$$D_0(\text{Hf}^+ - L) = D_0(R - L) - E_0 \quad (6)$$

where  $D_0(R - L)$  values can be calculated from heats of formation listed elsewhere [18]. It is assumed that there are no activation barriers other than the endothermicity of the reaction, which is generally the case for ion-molecule reactions because of the long-range attractive forces [25]. The potential energy surfaces calculated here verify this assumption in all cases.

In the following sections, details of our calculations for the products observed in reactions (2)–(5) are discussed. Energetics of these species are provided in Table 2, while Table 3 gives all structural information. BDEs for the likely ground states of the product ions calculated at several levels of theory are compared with experimental values in Table 4.

Table 1  
Optimized parameters for Eq. (1) for  $\text{Hf}^+$  +  $\text{CH}_4$  and  $\text{CD}_4$  systems

Reaction	$\sigma_0$	$n$	$E_0$ (eV)	$D_0(\text{Hf}^+ - L)$ (eV)
$\text{Hf}^+ + \text{CH}_4$	$\rightarrow \text{HfH}^+ + \text{CH}_3$	$9.05 \pm 0.57$	$0.9 \pm 0.1$	$2.51 \pm 0.13$
	$\rightarrow \text{HfCH}_3^+ + \text{H}$	$0.47 \pm 0.08$	$0.8 \pm 0.2$	$2.38 \pm 0.34$
	$\rightarrow \text{HfCH}_2^+ + \text{H}_2$	$2.54 \pm 0.15$	$1.0 \pm 0.1$	$0.44 \pm 0.04$
	$\rightarrow \text{HfCH}^+ + \text{H}_2 + \text{H}$	$0.48 \pm 0.16$	$0.5 \pm 0.3$	$3.96 \pm 0.04$
$\text{Hf}^+ + \text{CD}_4$	$\rightarrow \text{HfD}^+ + \text{CD}_3$	$18.2 \pm 6.1$	$0.9 \pm 0.2$	$2.60 \pm 0.22$
	$\rightarrow \text{HfCD}_3^+ + \text{D}$	$0.62 \pm 0.27$	$0.9 \pm 0.4$	$2.43 \pm 0.41$
	$\rightarrow \text{HfCD}_2^+ + \text{D}_2$	$10.5 \pm 1.8$	$1.2 \pm 0.1$	$0.33 \pm 0.04$
	$\rightarrow \text{HfCD}^+ + \text{D}_2 + \text{D}$	$2.32 \pm 0.70$	$0.7 \pm 0.3$	$4.16 \pm 0.39$

Table 2  
B3LYP/HW+6-311++G(3df,3p) theoretical energies of reactants and products<sup>a</sup>

Species	State	Energy ( $E_h$ )	Zero point energy ( $E_h$ ) <sup>b</sup>	$E_{rel}$ (eV) <sup>c</sup>
H	$^2S$	-0.502257		
H <sub>2</sub>	$^1\Sigma_g^+$	-1.180030	0.009953	
C	$^3P$	-37.857442		
CH	$^2\Pi$	-38.495898	0.006457	0.000
	$^4\Sigma^-$	-38.462172	0.006943	0.931
CH <sub>2</sub>	$^3B_1$	-39.167949	0.017169	
CH <sub>3</sub>	$^2A''$	-39.857664	0.029685	
CH <sub>4</sub>	$^1A_1$	-40.536527	0.044503	
Hf <sup>+</sup>	$^2D$	-48.497337		0.000
	$^4F$	-48.486389		0.298
	$^4F$	-48.420002		2.104
HfH <sup>+</sup>	$^3\Delta$	-49.103320	0.004206	0.000
	$^1\Sigma^+$	-49.098748	0.004404	0.130
	$^3\Pi$	-49.087363	0.004146	0.433
	$^1\Pi$	-49.083655	0.004101	0.533
	$^1\Delta$	-49.081523	0.004177	0.593
	$^3\Phi$	-49.062292	0.003889	1.108
	$^3\Sigma^-$	-49.051891	0.003801	1.389
	$^1\Phi$	-49.050365	0.003931	1.434
	$^1\Gamma$	-49.032709	0.004000	1.916
	$^1\Delta$	-49.009065	0.003896	2.556
HfCH <sup>+</sup>	$^1\Sigma^+$	-87.177045	0.012765	0.000
	$^3\Pi$	-87.172769	0.012193	0.101
	$^3\Sigma^-$	-87.144439	0.011391	0.850
	$^3\Phi$	-87.137549	0.011915	1.052
HfHC <sup>+</sup>	$^3A''$	-87.083378	0.007112	0.000 (2.397)
	$^3A''$	-87.076890	0.006601	0.163 (2.559)
	$^1A''$	-87.072754	0.007139	0.290 (2.686)
	$^1\Sigma^+$ ( $^1A'$ )	-87.061085	0.007319	0.612 (3.009)
	$^3A'$	-87.054698	0.006373	0.761 (3.157)
	$^3A'$	-87.034789	0.006315	1.301 (3.650)
HfCH <sub>2</sub> <sup>+</sup>	$^2A'$	-87.831733	0.021110	0.000
	$^2A_1$ (TS)	-87.829865	0.020314 (-204)	0.029
	$^2B_1$	-87.812945	0.020928	0.506
	$^4B_2$	-87.805013	0.021014	0.725
	$^4B_1$	-87.804947	0.020981	0.729
	$^2A_2$	-87.795142	0.020350	0.975
	$^2B_2$	-87.783332	0.021072	1.316
	$^4A_2$	-87.783319	0.021463	1.327
	$^4A_1$	-87.751197	0.021389	2.199
	$^2A_1$	-87.707169	0.021202	3.392
	$^4B_2$	-87.700530	0.031172	3.572
HfHfCH <sup>+</sup>	$^2A'$	-87.778978	0.017208	0.000 (1.331)
	$^2A''$	-87.769437	0.017334	0.263 (1.594)
	$^4A''$	-87.758773	0.016296	0.542 (1.873)
	$^4A'$	-87.735361	0.016081	1.157 (2.488)
HfCH <sub>3</sub> <sup>+</sup>	$^1A_1$ <sup>d</sup>	-88.471146	0.032216	0.000
	$^3E$	-88.468572	0.032626	0.081
	$^3A_2$	-88.420339	0.033072	1.406
	$^3A_1$	-88.368018	0.031424	2.785
HfHfCH <sub>2</sub> <sup>+</sup>	$^1A'$	-88.440676	0.027891	0.000 (0.713)
	$^1A'$	-88.438185	0.026881	0.041 (0.753)
	$^3A''$	-88.420940	0.026377	0.496 (1.209)
(H) <sub>2</sub> HfCH <sup>+</sup>	$^3A''$	-88.372489	0.022808	0.000 (2.432)
	$^1A_1$	-88.336447	0.023116	0.989 (3.420)

Table 2 (Continued)

Species	State	Energy ( $E_h$ )	Zero point energy ( $E_h$ ) <sup>b</sup>	$E_{rel}$ (eV) <sup>c</sup>
(H) <sub>2</sub> HfCH <sup>+</sup>	$^3A''$	-88.372573	0.027327	0.000 (2.551)
	$^1A''$	-88.369166	0.027269	0.091 (2.642)
	$^3A'$	-88.349986	0.026283	0.587 (3.138)
	$^1A_1$	-88.290278	0.023683	2.141 (4.692)

<sup>a</sup> All species exhibit  $s(s+1)$  values in agreement with the spin states shown (0.0 for singlet, 0.75 for doublet, 2.00 for triplet, and 3.75 for quartet) with the following exceptions: Hf<sup>+</sup> ( $^2D$ ),  $s(s+1) = 1.28$ ; HfCH<sub>2</sub><sup>+</sup> ( $^4B_1$ ),  $s(s+1) = 1.37$ ; and HfCH<sub>2</sub><sup>+</sup> ( $^2B_2$ ),  $s(s+1) = 1.75$ . For Hf<sup>+</sup> ( $^2D$ ,  $6s^25d^1$ ), an energy of -48.4900274  $E_h$  ( $E_{rel} = 0.199$  eV) is found for a level having no spin contamination.

<sup>b</sup> Imaginary frequencies ( $\text{cm}^{-1}$ ) in parentheses.

<sup>c</sup> Energy relative to the ground state species including zero point energies scaled by 0.989. Values in parentheses are relative to the lowest energy isomer.

<sup>d</sup> A spin contaminated,  $s(s+1) = 0.63$ , version of this state was also located at -88.476363  $E_h$ .

#### 4.1. HfH<sup>+</sup>

The bond energy of Hf<sup>+</sup>-H has recently been measured from the reaction of Hf<sup>+</sup> with H<sub>2</sub> and D<sub>2</sub>, yielding an average value of  $2.07 \pm 0.09$  eV [42]. From Eq. (6) with  $D_0(\text{CH}_4) = 4.48$  eV and our threshold of  $2.51 \pm 0.13$  eV (Table 1), we obtain a BDE for HfH<sup>+</sup> of  $1.97 \pm 0.13$  eV, within experimental uncertainty of the previous thermochemistry. Similarly, with  $D_0(\text{CD}_4) = 4.58$  eV, a threshold of  $2.60 \pm 0.22$  eV, and a calculated zero point energy difference between HfD<sup>+</sup> and HfH<sup>+</sup> of 0.033 eV, the BDE derived from the CD<sub>4</sub> system for HfH<sup>+</sup> is  $1.95 \pm 0.22$  eV, again in good agreement. Thus, the CH<sub>4</sub> and CD<sub>4</sub> systems behave similarly to each other and agree nicely with the thermodynamic results for the H<sub>2</sub> and D<sub>2</sub> systems. On average, the BDE obtained from the methane systems is lower by  $0.10 \pm 0.13$  eV, a minor discrepancy that may be attributed to a competitive shift with the lower energy dehydrogenation reaction.

Ohanessian et al. calculate that the ground state for HfH<sup>+</sup> is  $^3\Delta$  where the character of the bonding orbital on Hf is 35%  $6s$  and 64%  $5d$  [36]. This bonding can be thought of as stemming from a covalent bond between the  $1s$  orbital on H and a  $6s5d$  hybrid orbital on Hf<sup>+</sup>. This type of hybridization is quite efficient in the third-row transition metals because of the relativistic effects involved, making the  $6s$  orbital comparable in size to the  $5d$  orbitals. Such a singly occupied  $6s5d$  orbital is formed by a combination of the  $^2D$  ( $6s^25d^1$ ) and  $^4F$  ( $6s^15d^2$ ) states. Consequently, even though binding to the hybrid orbital of Hf<sup>+</sup> requires both promotion and the loss of exchange energy because the  $^4F$  state configuration is mixed in, the  $6s5d$  hybrid bonding orbital overlaps better with the  $1s$  orbital on H ( $^2S$ ) than pure  $6s$  or  $5d$  orbitals. The nonbonding valence orbitals that are occupied in the  $^3\Delta$  state are  $\sigma^1\delta^1$ , where the  $\sigma$  orbital is largely  $6s$  and the  $\delta$  orbital is pure  $5d$ . The bond length calculated by Ohanessian et al. is  $1.79 \text{ \AA}$  [36], which is in good agreement with the bond length calculated here of  $1.79 \text{ \AA}$ . We also calculated results for stable excited states (with nonbonding valence occupancies) of  $^1\Sigma^+(\sigma^2)$ ,  $^3\Pi(\sigma^1\pi^1)$ ,  $^1\Pi(\sigma^1\pi^1)$ ,  $^1\Delta(\sigma^1\delta^1)$ ,  $^1\Gamma(\delta^2)$ ,  $^3\Phi(\pi^1\delta^1)$ ,  $^3\Sigma^-(\pi^2, \delta^2)$ ,  $^1\Phi(\pi^1\delta^1)$ , and  $^1\Delta(\pi^2)$ , with relative energies listed in Table 2 and geometries in Table 3. Note that

Table 3  
B3LYP/HW + /6-311++G(3df,3p) theoretical structures of reactants and products<sup>a</sup>

Species	State	r(Hf–H)	r(Hf–C)	r(C–H)	∠HfCH	∠HCH	∠Dihedral <sup>b</sup>	
CH	<sup>2</sup> Π			1.122				
	<sup>4</sup> Σ <sup>-</sup>			1.093				
CH <sub>2</sub>	<sup>3</sup> B <sub>1</sub>			1.078(2)		135.1		
CH <sub>3</sub>	<sup>2</sup> A <sup>o</sup>			1.078(3)		120.0(3)	180.0	
CH <sub>4</sub>	<sup>1</sup> A <sub>1</sub>			1.088(4)		109.5(6)	120.0(6)	
HFH <sup>+</sup>	<sup>3</sup> Δ	1.786						
	<sup>1</sup> Σ <sup>+</sup>	1.746						
	<sup>3</sup> Π	1.776						
	<sup>1</sup> Π	1.781						
	<sup>1</sup> Δ	1.787						
	<sup>3</sup> Φ	1.826						
	<sup>3</sup> Σ <sup>-</sup>	1.824						
	<sup>1</sup> Φ	1.821						
	<sup>1</sup> Γ	1.824						
	<sup>1</sup> Δ	1.814						
HfCH <sup>+</sup>	<sup>1</sup> Σ <sup>+</sup>		1.801	1.085	180.0			
	<sup>3</sup> Π		1.896	1.086	180.0			
	<sup>3</sup> Σ <sup>-</sup>		2.036	1.088	180.0			
	<sup>3</sup> Φ		1.916	1.085	180.0			
HHfC <sup>+</sup>	<sup>3</sup> A <sup>o</sup>	1.792	1.909		96.9 <sup>c</sup>			
	<sup>5</sup> A <sup>o</sup>	1.783	2.084		98.5 <sup>c</sup>			
	<sup>1</sup> A <sup>o</sup>	1.792	1.906		96.9 <sup>c</sup>			
	<sup>1</sup> Σ <sup>+</sup> ( <sup>1</sup> A')	1.817	1.795		180.0 <sup>c</sup>			
	<sup>5</sup> A <sup>o</sup>	1.803	2.102		107.2 <sup>c</sup>			
	<sup>3</sup> A <sup>o</sup>	1.779	2.260		95.4 <sup>c</sup>			
HfCH <sub>2</sub> <sup>+</sup>	<sup>2</sup> A'		1.883	1.082, 1.130	86.6, 161.0	112.4	180.0	
	<sup>2</sup> A <sub>1</sub> (TS)		1.915	1.093(2)	123.2(2)	113.5	180.0	
	<sup>2</sup> B <sub>1</sub>		2.080	1.092(2)	123.6(2)	112.8	180.0	
	<sup>4</sup> B <sub>2</sub>		2.103	1.091(2)	123.7(2)	112.6	180.0	
	<sup>4</sup> B <sub>1</sub>		2.102	1.091(2)	123.7(2)	112.7	180.0	
	<sup>2</sup> A <sub>2</sub>		1.940	1.092(2)	123.4(2)	113.2	180.0	
	<sup>2</sup> B <sub>2</sub>		2.103	1.091(2)	123.7(2)	112.6	180.0	
	<sup>4</sup> A <sub>2</sub>		2.124	1.092(2)	124.6(2)	110.8	180.0	
	<sup>4</sup> A <sub>1</sub>		2.160	1.091(2)	124.4(2)	111.2	180.0	
	<sup>2</sup> A <sub>1</sub>		2.445	1.097(2)	125.0(2)	110.0	180.0	
	<sup>4</sup> B <sub>2</sub>		2.485	1.098(2)	126.0(2)	108.1	180.0	
	HHfCH <sup>+</sup>	<sup>2</sup> A'	1.801	1.904	1.086	97.4, <sup>c</sup> 176.0		0.0
		<sup>2</sup> A <sup>o</sup>	1.797	1.904	1.085	97.0, <sup>c</sup> 174.0		0.0
		<sup>4</sup> A <sup>o</sup>	1.785	2.063	1.087	98.9, <sup>c</sup> 176.8		0.0
<sup>4</sup> A'		1.805	2.080	1.086	105.8, <sup>c</sup> 176.5		0.0	
HfCH <sub>3</sub> <sup>+</sup>	<sup>1</sup> A <sub>1</sub>		2.072	1.096(3)	109.2(3)	109.7(3)	120.0(3)	
	<sup>3</sup> E		2.120	1.096(3)	109.5(3)	109.4(3)	120.0(3)	
	<sup>3</sup> A <sub>2</sub>		2.194	1.095(3)	109.7(3)	109.3(3)	120.0(3)	
	<sup>3</sup> A <sub>1</sub>		2.229	1.098(3)	111.3(3)	107.6(3)	120.0(3)	
HHfCH <sub>2</sub> <sup>+</sup>	<sup>1</sup> A'	1.803	1.889	1.083, 1.131	85.2, 98.5, <sup>c</sup> 162.3,	112.5	0.0, 180.0	
	<sup>1</sup> A'	1.803	1.902	1.083, 1.116	97.0, 98.8, <sup>c</sup> 149.8,	113.2	0.0, 180.0	
	<sup>3</sup> A <sup>o</sup>	1.788	2.095	1.091, 1.092	100.7, <sup>c</sup> 120.8, 126.8	112.4	0.0, 180.0	
(H <sub>2</sub> )HfCH <sup>+</sup>	<sup>3</sup> A <sup>o</sup>	1.785(2)	2.066	1.087	99.0(2), <sup>c</sup> 175.7	101.0 <sup>d</sup>	±51.4	
	<sup>1</sup> A <sub>1</sub>	1.809(2)	2.031	1.089	121.9(2), <sup>c</sup> 180.0	116.3 <sup>d</sup>	0.0(2)	
(H <sub>2</sub> )HHfCH <sup>+</sup>	<sup>3</sup> A <sup>o</sup>	2.026, 2.056	1.926	1.086	68.5, <sup>c</sup> 91.6, <sup>c</sup> 179.8	23.1 <sup>d</sup>	0.0(2)	
	<sup>1</sup> A <sup>o</sup>	2.028, 2.056	1.929	1.086	69.0, <sup>c</sup> 92.1, <sup>c</sup> 179.9	23.1 <sup>d</sup>	0.0(2)	
	<sup>3</sup> A <sup>o</sup>	1.971, 1.996	1.941	1.086	66.4, <sup>c</sup> 90.6, <sup>c</sup> 179.7	24.1 <sup>d</sup>	180.0(2)	
	<sup>1</sup> A <sub>1</sub>	2.538(2)	2.063	1.088	171.5(2), <sup>c</sup> 180.0	17.1 <sup>d</sup>	0.0, 180.0	

<sup>a</sup> Bond lengths are in Å. Bond angles are in degrees. Degeneracies are listed in parentheses.

<sup>b</sup> Generally, ∠HHfCH except for the CH<sub>3</sub> species where it is ∠HCHH.

<sup>c</sup> ∠HHfC.

<sup>d</sup> ∠HHfH.

Table 4  
Experimental and theoretical bond energies for  $\text{Hf}^x\text{-H}$  and  $\text{Hf}^x\text{-CH}_x$ , ( $x = 1\text{--}3$ )<sup>a</sup>

Species	State	Exp	B3LYP		BHLYP		QCISD(T) <sup>b</sup>
			HW+	SD	HW+	SD	HW+
$\text{Hf}^x\text{-H}$	$^3\Delta^c$	$2.07 \pm 0.09$	2.71 (2.44)	2.63 (2.35)	2.59 (2.31)	2.54 (2.22)	2.34 (2.55)
	$^1\Sigma^+$		2.58	2.44	<b>2.42</b>	<b>2.30</b>	<b>2.74</b>
$\text{Hf}^x\text{-CH}_3$	$^1A_1$	$2.12 \pm 0.26$	3.09	2.88	<b>2.76</b>	<b>2.57</b>	<b>3.54</b>
	$^3E^c$		3.01 (2.74)	2.87 (2.59)	2.73 (2.45)	2.63 (2.31)	2.93 (3.14)
	$^3E^c$						
$\text{Hf}^x\text{-CH}_2$	$^2A'$	$4.37 \pm 0.07$	4.42	4.21	3.85	3.66	4.56
$\text{Hf}^x\text{-CH}$	$^1\Sigma^+$	$5.10 \pm 0.15$	4.83	4.63	4.13	3.97	4.97

<sup>a</sup> All theoretical values may need to be decreased by the average spin-orbit energy of the  $\text{Hf}^x$  ( $^2D$ ) state, 0.227 eV [11], in which case corrections for the spin-orbit levels of the  $\text{HfH}^+$  and  $\text{HfCH}_x^+$  species would also be needed, but these are unknown.

<sup>b</sup> Geometries calculated at the B3LYP/HW+ level of theory.

<sup>c</sup> Values in parentheses are referenced to the  $\text{Hf}^x$  ( $^4F$ ) asymptote and adjusted by the experimental excitation energy for this state, 0.563 eV [11].

the excitation energy of the  $^1\Sigma^+$  state (0.13 eV) is sufficiently low that there is the possibility that this is the true ground state. This state is relatively low in energy because it can be formed directly from the  $\text{Hf}^x$  ( $^2D$ ,  $6s^25d^1$ ) state (thereby avoiding promotion and exchange energy costs) by coupling the  $\text{H}(1s)$  electron with the  $5d$  electron. Ohanessian et al. examined the triplet excited states (but no singlet states) finding the  $^3\Pi(\sigma^1\pi^1)$  at 0.49 eV, a  $^3\Phi(\pi^1\delta^1)$  at 1.01 eV, and the  $^3\Sigma^-(\pi^2, \delta^2)$  at 1.10 eV, all with bond lengths comparable to the present calculations [36].

As noted above, the  $^1\Sigma^+$  state is only 0.13 eV above the  $^3\Delta$  state at the B3LYP/HW+ level of theory. Other levels of theory agree that the  $^3\Delta$  state is the ground state, with excitation energies for the  $^1\Sigma^+$  state of 0.19 (B3LYP/SD), 0.17 (BHLYP/HW+), and 0.24 (BHLYP/SD) eV. However, at the QCISD(T)/HW+/B3LYP/HW+ level of theory, the  $^1\Sigma^+$  is calculated to have a BDE of 2.74 eV, 0.40 eV more than the  $^3\Delta$  state. Complicating the assignment of the true ground state is the fact that whereas the  $^1\Sigma^+$  state can be derived from pure  $\text{Hf}^x$  ( $^2D$ ), the  $^1\Delta$  state mixes in  $\text{Hf}^x$  ( $^4F$ ) character such that errors in the excitation energy of this state (see above) may propagate to the relative energies of the  $^3\Delta$  and  $^1\Sigma^+$  states. Indeed if the errors in the  $^4F$  excitation energies noted above are included in full (yielding the BDEs listed in parentheses in Table 4), the  $^1\Sigma^+$  state becomes the ground state in all cases, with  $^3\Delta$  excitation energies of 0.14, 0.09, 0.11, 0.08, and 0.19 eV for the B3LYP/HW+, B3LYP/SD, BHLYP/HW+, BHLYP/SD, and QCISD(T)/HW+ calculations, respectively (Table 4).

Ohanessian et al. calculated a BDE for the  $^3\Delta$  state of  $\text{HfH}^+$  of 2.38 eV using generalized valence bond theory (GVB) [36], a value somewhat above our experimental BDE. Theoretical BDEs for this state calculated here at all levels of theory greatly exceed the experimental BDE if the values are referenced to the  $\text{Hf}^x$  ( $^2D$ ) state. If referenced to the  $^4F$  state of  $\text{Hf}^x$  and corrected by the experimental excitation energy, the  $^3\Delta$  is no longer the ground state (see above) (Table 4). Likewise the BDEs calculated for the  $^1\Sigma^+$  state exceed the experimental value at all levels of theory. One possible reason for the discrepancy is to realize that the calculations are referenced to the average of the spin-orbit levels of  $\text{Hf}^x$  ( $^2D$ ), which experimentally lies 0.227 eV above the  $^2D_{3/2}$  level, the experimental ground level [11]. If the BDEs for the  $^1\Sigma^+$  state in Table 4 are reduced by this amount, it can

be seen that the BHLYP values agree with experiment within the uncertainties, 2.19 (HW+) and 2.07 (SD) eV compared to  $2.07 \pm 0.09$  eV. The B3LYP values remain high even with this correction, 2.35 (HW+) and 2.21 (SD) eV, consistent with the observations of Holthausen et al. for metal–ligand single bonds [37].

#### 4.2. $\text{HfCH}_3^+$

The BDE of  $\text{Hf}^x\text{-CH}_3$  derived from the  $\text{CH}_4$  system is  $2.10 \pm 0.34$  eV and the BDE of  $\text{Hf}^x\text{-CD}_3$  derived from the  $\text{CD}_4$  system is  $2.15 \pm 0.41$  eV (Table 1). After correcting for the zero point energy differences in these two values (0.012 eV), their weighted average is  $2.12 \pm 0.26$  eV for the BDE of  $\text{Hf}^x\text{-CH}_3$ . This value is similar to the value obtained for  $\text{HfH}^+$ ,  $D_0 = 2.07 \pm 0.09$  eV, as expected for a single covalent bond to  $\text{Hf}^x$ .

The experimental BDE derived for  $\text{HfCH}_3^+$  can be compared to calculations made by Holthausen et al., who have performed studies on first- and third-row transition metal methyl cations [37]. These calculations were performed using the B3LYP, BHLYP, QCISD, and QCISD(T) levels of theory, yielding values for the  $\text{Hf}^x\text{-CH}_3$  BDEs of 3.10, 2.80, 2.65, and 2.68 eV, respectively. Comparison of the theoretical calculations and experimentally derived values for the first-row transition metal methyl cations leads to an empirical correction for the BHLYP and QCISD(T) methods of  $-0.22$  and  $+0.16$  eV, yielding corrected values of 2.58 and 2.84 eV with estimated errors of  $\pm 0.22$  eV. All these values are well above our experimental value of  $2.12 \pm 0.26$  eV.

Our calculations find that the ground state for  $\text{HfCH}_3^+$  is  $^1A_1$ , in which the bonding involves the interaction of the singly occupied  $sp^3$  hybridized orbital on  $\text{CH}_3$  and the singly occupied  $5d\sigma$  orbital on  $\text{Hf}^x$  ( $^2D$ ,  $6s^25d^1$ ). This state, the equivalent of  $\text{HfH}^+$  ( $^1\Sigma^+$ ), requires no promotion energy or loss of exchange energy for binding to  $\text{Hf}^x$  ( $^2D$ ). The two nonbonding valence electrons in this state occupy an  $a_1$  orbital that is essentially the  $6s$  orbital of  $\text{Hf}$  hybridized with some  $5d$  character. The equivalent of the  $\text{HfH}^+$  ( $^3\Delta$ ) ground state is now the  $^3E$  ( $a_1e^1$ ), which lies only 0.08 eV higher in energy and therefore could be the true ground state. The switch in the ground state character

between the  $\text{HfH}^+$  and  $\text{HfCH}_3^+$  molecules indicates the subtle nature of the hybridization and promotion energies in these systems. Indeed, in their calculations, Holthausen et al. report that  $\text{HfCH}_3^+$  has a  $^3\text{E}$  state, although it is unclear whether a singlet state was explicitly considered [37]. Our calculated bond length for Hf–C is 2.07 Å in the  $^1\text{A}_1$  state and 2.12 Å in the  $^3\text{E}$  state, where the latter value is in good agreement with the bond length of 2.11 Å calculated by Holthausen et al. at the QCISD(T) level [37]. We also calculated energies for stable excited states (with nonbonding valence occupancies) of  $^3\text{A}_2$  ( $e^2$ ) and  $^3\text{A}_1$  ( $a_1^1 a_1^1$ ), with relative energies listed in Table 2 and geometries in Table 3. (The  $^3\text{A}_2$  state is misidentified in the Gaussian code as  $^3\text{A}_1$ . As discussed elsewhere [43], the properly antisymmetrized wavefunctions for an ( $e^2$ ) configuration lead to  $^1\text{A}_1$ ,  $^1\text{E}$ , and  $^3\text{A}_2$  states.)

As noted above, the excitation energy for the  $^3\text{E}$  state at the B3LYP/HW<sup>+</sup> level of theory is only 0.08 eV. B3LYP/SD, B3LYP/HW+, and QCISD(T)/HW+/B3LYP/HW+ levels of theory also find a  $^1\text{A}_1$  ground state, with  $^3\text{E}$  state excitation energies of 0.01, 0.03, and 0.61 eV, respectively. The B3LYP/SD combination reverses the order of the states such that the  $^3\text{E}$  state has a BDE of 2.63 eV, with an excitation energy for the  $^1\text{A}_1$  state of 0.06 eV. If the BDEs of the triplet state are referenced to the  $\text{Hf}^+$  ( $^4\text{F}$ ) asymptote instead and then corrected by the experimental excitation energy of this state, the BDEs fall to 2.74, 2.59, 2.45, 2.31, and 3.14 eV, respectively (Table 4).

For our B3LYP/HW<sup>+</sup> theoretical calculations, we obtain  $D_0(\text{Hf}^+-\text{CH}_3) = 3.09$  eV for the  $^1\text{A}_1$  state and 3.01 eV for the  $^3\text{E}$  state. The latter value compares favorably with the B3LYP calculations made by Holthausen et al.,  $D_0 = 3.03$  eV [37]. Using the SD ECP on  $\text{Hf}^+$ , a value of 2.88 eV was obtained for the  $^1\text{A}_1$  state. Again, to offset the overbinding of the B3LYP functional for single covalent metal–ligand bonds, we carried out calculations using the B3LYP functional to provide a better estimate of  $D_0(\text{Hf}^+-\text{CH}_3, ^1\text{A}_1)$ . Using this level of theory, we obtain lower values of 2.76 (HW+) and 2.57 (SD) eV, which are in better agreement but still exceed our experimental value of  $2.12 \pm 0.26$  eV. If these values are corrected for the 0.227 eV average spin–orbit state implicit in the theoretical calculations (see discussion above), the agreement is better, 2.53 and 2.34 eV, respectively. Our B3LYP/HW+ value for the  $^3\text{E}$  state of 2.73 eV matches the B3LYP value from Holthausen et al. of  $D_0 = 2.72$  eV [37]. At the QCISD(T) level of theory, we calculate a BDE of 3.54 eV for  $D_0(\text{Hf}^+-\text{CH}_3, ^1\text{A}_1)$  and 2.93 eV for the  $^3\text{E}$  state, whereas Holthausen et al. get  $D_0 = 2.60$  eV for the latter [37]. In accordance with  $\text{HfH}^+$  and  $\text{HfCH}_3^+$  having similar single covalent metal–ligand bonds and similar experimental BDEs, theoretical results obtained for these two species are comparable with one another.

We also examined alternate isomers of  $\text{HfCH}_3^+$ , namely  $\text{HHfCH}_2^+$  and  $(\text{H})_2\text{HfCH}^+$ . The lowest-lying hafnium hydrido methylidene isomer has a  $^1\text{A}'$  state and lies 0.71 eV above the hafnium methyl isomer. This planar molecule has Hf–H and Hf–C bond lengths comparable to those of  $\text{HfH}^+$  and  $\text{HfCH}_2^+$ , with a HHfC bond angle of  $99^\circ$  (Table 3). The triplet state of this isomer is similar in structure but has an elongated Hf–C bond. The hafnium dihydride methylidyne structure is still higher in

energy, 2.43 eV, and has a triplet as its lowest energy state. This species has Hf–H bond lengths characteristic of  $\text{HfH}^+$  ( $^3\Delta$ ), but the HfC bond is quite long, 2.07 Å compared to 1.90 Å for  $\text{HfCH}^+$  ( $^3\Pi$ ). The three covalent bonds in this molecule are essentially perpendicular to one another, indicating the use of  $5d$  orbitals for bonding on Hf. Notably, several calculations of  $(\text{H})_2\text{HfCH}^+$  species collapsed to a  $(\text{H}_2)\text{HfCH}^+$  geometry in which dihydrogen is electrostatically bound to  $\text{HfCH}^+$ . The lowest of these isomers is a  $^3\text{A}''$ , lying 2.55 eV above the  $\text{HfCH}_3^+$  ground state (Table 2).

#### 4.3. $\text{HfCH}_2^+$

The thresholds for dehydrogenation (reaction (4)), in the  $\text{CH}_4$  and  $\text{CD}_4$  systems are  $0.44 \pm 0.04$  and  $0.33 \pm 0.04$  eV. Combined with a ZPE correction of 0.015 eV, these results yield BDEs for  $\text{Hf}^+-\text{CH}_2$  derived from the  $\text{CH}_4$  and  $\text{CD}_4$  systems of  $4.27 \pm 0.05$  and  $4.47 \pm 0.05$  eV, respectively. The weighted mean for these two values of  $D_0(\text{Hf}^+-\text{CH}_2)$  is  $4.37 \pm 0.07$  eV. This value is in good agreement with the results of Irikura and Beauchamp [4] who determined that  $4.0 \text{ eV} < D_0(\text{Hf}^+-\text{CH}_2) < 4.8 \text{ eV}$  using FTICR mass spectrometry. These limits were obtained by bracketing the formation of  $\text{HfCH}_2^+$  in reactions of  $\text{Hf}^+$  with cyclopropane, which is exothermic, and that with methane, which is endothermic. Irikura and Goddard calculated a bond energy ( $D_e$ ) of 3.99 eV, but empirically correct this by 0.52 eV to yield a recommended bond energy ( $D_0$ ) of  $4.51 \pm 0.22$  eV [44]. For our B3LYP theoretical calculations, we obtain BDEs for  $\text{Hf}^+-\text{CH}_2$  of 4.42 (HW+) and 4.21 (SD) eV, which are in good agreement with our experimental results. At the B3LYP level of theory, we calculate values of 3.85 (HW+) and 3.66 (SD) eV for  $D_0(\text{Hf}^+-\text{CH}_2)$ , which are below the experimental results. At the QCISD(T) level of theory, a value of 4.56 eV for  $D_0(\text{Hf}^+-\text{CH}_2)$  was obtained, slightly higher than experiment.

The ground state of  $\text{HfCH}_2^+$  was found to be  $^2\text{A}'$ , whereas Irikura and Goddard reported a  $^2\text{A}_1$  ground state because they constrained their GVB calculations to  $\text{C}_{2v}$  symmetry [44]. Indeed, we find that this  $^2\text{A}_1$  state is a transition state that lies 0.029 eV (0.051 eV before zero point energy corrections) above the ground state of the hafnium methylidene cation. The imaginary frequency of  $204 \text{ cm}^{-1}$  corresponds to an in-plane, wagging motion that leads to the distorted  $^2\text{A}'$  ground state. Because the zero point energy of this molecule (0.57 eV) is much greater than the barrier, the hafnium methylidene cation effectively has  $\text{C}_{2v}$  symmetry. Our calculations find that the  $^2\text{A}_1$  state has  $r(\text{Hf}-\text{C}) = 1.92$  Å,  $r(\text{C}-\text{H}) = 1.09$  Å and  $\angle\text{HfCH} = 123^\circ$ , whereas the GVB results find values of 2.00 Å, 1.09 Å, and  $123^\circ$ , respectively. The electronic configuration is  $(1a_{1b})^2(1b_{1b})^2(2a_1)^1$ , where the  $1a_{1b}$  and  $1b_{1b}$  orbitals are the Hf–C  $\sigma$  and  $\pi$  bonding orbitals. Nonbonding orbitals on the hafnium include the  $2a_1$  ( $6s-5d_{z^2}$ ),  $3a_1$  ( $5d_{x^2-y^2}$ ),  $1a_2$  ( $5d_{xy}$ ), and  $1b_2$  ( $5d_{yz}$ ) given that the molecule lies in the  $yz$ -plane with the Hf–C bond along the  $z$ -axis [44]. Excited states identified by Irikura and Goddard include  $^2\text{A}_2$  [ $(1a_{1b})^2(1b_{1b})^2(1a_2)^1$ ] and  $^4\text{A}_1$  [ $(1a_{1b})^2(1b_{1b})^1(2a_1)^1(2b_1^*)^1$ ] lying 0.97 and 1.47 eV, respectively, above the ground state. Our calculations find

excited states of  ${}^2B_1[(1a_{1b})^2(1b_{1b})^1(2a_1)^2]$ ,  ${}^4B_2[(1a_{1b})^2(1b_{1b})^1(2a_1)^1(1a_2)^1]$ ,  ${}^4B_1[(1a_{1b})^2(1b_{1b})^1(2a_1)^1(3a_1)^1]$ ,  ${}^2A_2[(1a_{1b})^2(1b_{1b})^2(1a_2)^1]$ ,  ${}^2B_2[(1a_{1b})^2(1b_{1b})^1(2a_1)^1(1a_2)^1]$ ,  ${}^4A_2[(1a_{1b})^2(1b_{1b})^1(2a_1)^1(1b_2)^1]$ ,  ${}^4A_1[(1a_{1b})^2(1b_{1b})^1(1a_2)^1(1b_2)^1]$ ,  ${}^2A_1[(1a_{1b})^2(2a_1)^2(3a_1)^1]$ , and  ${}^4B_2[(1a_{1b})^2(2a_1)^1(3a_1)^1(1b_2)^1]$ , with relative energies listed in Table 2 and geometries in Table 3. Note that our excitation energy for the  ${}^2A_2$  state agrees well with that of Irikura and Goddard, but that we find a lower-lying doublet state at 0.51 eV,  ${}^2B_1$ , as well as a lower-lying quartet state at 0.72 eV,  ${}^4B_2$ .

We also examined the alternate isomer of  $HfCH_2^+$ , namely  $HHfCH^+$ . The lowest state of this isomer,  ${}^2A'$ , lies 1.33 eV above the  $HfCH_2^+$  ( ${}^2A'$ ) ground state. In all cases, the  $HfCH$  part of the molecule is nearly linear (bond angles of  $\sim 175^\circ$ , Table 3), whereas the  $HHfC$  bond angle is close to  $100^\circ$ , indicating that  $6s$ – $5d$  hybrids are used to form the two covalent bonds to Hf. Excited states,  ${}^2A''$ ,  ${}^4A''$ , and  ${}^4A'$ , were found lying 1.59, 1.87, and 2.49 eV higher in energy, respectively (Table 2).

#### 4.4. $HfCH^+$

Experimental cross sections for the formation of  $HfCH^+$  and  $HfCD^+$  were analyzed to yield thresholds of  $3.96 \pm 0.15$  and  $4.16 \pm 0.39$  eV, respectively. This corresponds to BDEs of  $5.11 \pm 0.16$  and  $5.08 \pm 0.39$  eV for the perprotio methane and perdeuterated methane systems. After correcting for a zero-point energy difference in the BDEs of 0.028 eV, we obtain a weighted mean for these two values of  $D_0(Hf^+-CH) = 5.10 \pm 0.15$  eV. This value is deemed a lower limit to the true thermodynamic value because of the possibility of competition with other channels.

The ground state configuration of  $HfCH^+$  is calculated to be  ${}^1\Sigma^+$ , having a  $1\sigma_g^2 1\pi_g^4$  valence electron configuration in which a triple bond is formed between hafnium and carbon. For our theoretical calculations, we obtain  $D_0(Hf^+-CH)$  of 4.83 (HW+) and 4.63 (SD) eV using B3LYP, somewhat below experiment. Using BHLYP, values are 4.13 (HW+) and 3.97 (SD) eV, which are well below the experimental results. At the QCISD(T) level of theory, we calculate a value of 4.97 eV for  $D_0(Hf^+-CH)$ , in reasonable agreement with experiment. Irikura and Goddard estimated a much higher value for  $D_0(Hf^+-CH)$  of 6.2 eV, derived from an intrinsic bond energy model [44] and well above our experimental value. The  $Hf$ – $C$  bond length and  $HfCH$  bond angle (Table 3) in the ground state are calculated to be 1.80 Å and  $180^\circ$ . The lowest lying excited state is  ${}^3\Pi$ , which lies 0.10 eV higher in energy and corresponds to excitation of a  $\pi$ -bonding electron into a  $\sigma$ -nonbonding (largely  $6s$ ) orbital. Thus, the  $Hf$ – $C$  bond length increases to 1.90 Å. Other excited states, all with longer  $Hf$ – $C$  bond lengths (Table 3), include  ${}^3\Sigma^-$  (0.85 eV, excitation of  $\sigma$ -bonding to  $\sigma$ -nonbonding orbitals) and  ${}^3\Phi$  (1.05 eV, excitation of  $\pi$ -bonding to  $\delta$ -nonbonding orbitals).

We also examined the alternate isomer of  $HfCH^+$ , namely  $HHfC^+$ . In all cases, these species are bent and lie well above the energy of the methylidyne isomer, with the lowest lying state,  ${}^3A''$ , being 2.40 eV higher in energy (Table 2).

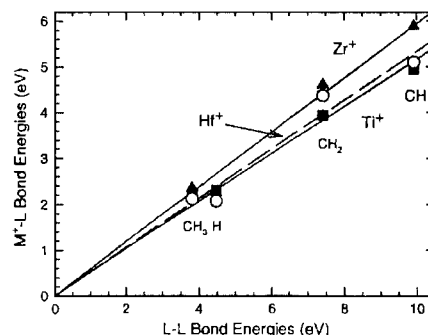


Fig. 3. Correlation of  $Hf^+$ – $L$  bond energies with those for the organic analogues,  $L$ – $L$ .  $Hf^+$ – $L$  values (open circles) are from Table 4. Data for  $Ti^+$  and  $Zr^+$  are listed in the text and shown by squares and triangles, respectively. The lines are linear regression fits to the experimental data constrained to pass through the origin to emphasize the bond-order correlations.

#### 4.5. Bond-energy bond-order correlation for $Hf^+-CH_x$ bonds

One interesting way of investigating the bond order of simple metal–ligand species is to compare with organic analogues, i.e.,  $D_0(Hf^+-L)$  versus  $D_0(L-L)$ . Such a plot is shown in Fig. 3. It can be seen that the correlation is remarkably good, which indicates that  $Hf^+-H$  and  $Hf^+-CH_3$  are single bonds,  $Hf^+=CH_2$  is a double bond, and  $Hf^+\equiv CH$  is a triple bond, as confirmed by theory. (The linear regression line in Fig. 3 is constrained to include the origin to emphasize the bond-order correlation of  $HfL^+$  versus  $L_2$  species.)

It is also interesting to compare these results to those for the first-row and second-row congeners,  $Ti^+$  and  $Zr^+$  (Fig. 3). BDEs for  $TiH^+$ ,  $TiCH^+$ ,  $TiCH_2^+$ , and  $TiCH_3^+$  are  $2.31 \pm 0.11$ ,  $4.95 \pm 0.05$ ,  $3.94 \pm 0.09$ , and  $2.22 \pm 0.03$  eV, respectively [45]. The analogous species for  $Zr$  have BDEs of  $2.26 \pm 0.08$ ,  $5.89 \pm 0.13$ ,  $4.61 \pm 0.05$ , and  $2.36 \pm 0.10$  eV, respectively [19,46]. From this comparison, we find that the first- and second-row transition-metal bonded species of  $Ti^+$  and  $Zr^+$  are quite comparable to those of  $Hf^+$ . On average, the linear regression lines indicate that the bonds to  $Zr^+$  are 10% stronger than those to  $Hf^+$ , and the multiply bonded Hf species are 8% stronger than those to  $Ti^+$ . This is in contrast to most other columns of the periodic table where the lanthanide contraction allows the third-row metals to form much stronger bonds than the first- and second-row congeners [31–34]. This difference in behavior can again be attributed to the unusual doubly occupied  $6s^2$  orbital of  $Hf^+$  ( ${}^2D$ ).

#### 4.6. Potential energy surfaces of $[HfC, 4H]^+$

Fig. 4 illustrates the potential energy surfaces (PESs) for the interaction of  $Hf^+$  with methane. The energies of all intermediates are provided in Table 5, while Table 6 shows geometric parameters these species. Our ab initio calculations indicate

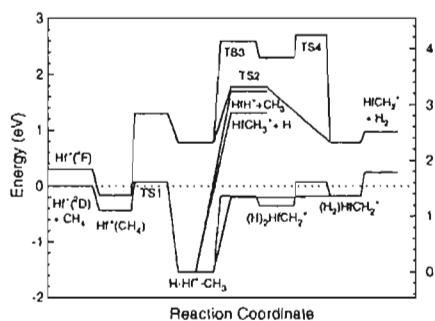


Fig. 4.  $[\text{Hf.C.4H}]^+$  potential energy surfaces derived from theoretical results. The energies of all species relative to the  $\text{Hf}^*(^2\text{D}) + \text{CH}_4$  ground state asymptote are based on ab initio calculations at the B3LYP/HW+6-311++G(3df,3p) level (see Table 5). Doublet surfaces are in green ( $^2\text{TS3}$  and  $^2\text{TS4}$ ) and blue ( $^2\text{TS2}$ ). Quartet surfaces are in pink ( $^4\text{TS3}$  and  $^4\text{TS4}$ ) and red ( $^4\text{TS2}$ ).

that the ground states of all intermediates and transition states leading from  $\text{Hf}^*(^2\text{D}) + \text{CH}_4$  to the  $\text{HfCH}_2^+ (^2\text{A}') + \text{H}_2 (^1\Sigma_g^+)$  products have doublet-spin ground states. Therefore, the dehydrogenation process is spin-allowed. The quartet surface remains higher in energy throughout the entire PES, such that coupling between the doublet and quartet surfaces is anticipated to be unimportant in the observed reactivity. It should also be noted that formation of the  $\text{HfH}^+ (^3\Delta, ^1\Sigma^+) + \text{CH}_3 (^2\text{A}'')$  and  $\text{HfCH}_3^+ (^1\text{A}_1, ^3\text{E}) + \text{H} (^2\text{S})$  products are spin-allowed from doublet intermediates.

#### 4.7. Doublet surface

On the doublet surface,  $\text{Hf}^*(^2\text{D}, 6s^25d^1)$  reacts with methane to form an  $\text{Hf}^*(\text{CH}_4)$  adduct in which the methane molecule remains intact and largely unperturbed (Fig. 5). The methane binds with  $C_s$  symmetry in a  $^2\text{A}'$  state and has a Hf–C bond distance of 2.66 Å. This species has a valence electron configuration on the metal that is  $(1a')^2(2a')^1$  in which the  $1a'$  orbital is mostly  $6s$  (nearly  $a_1$ ) and the  $2a'$  is a  $b_2(\pi)$ -like orbital with its lobes perpendicular to the plane defined by the H-atoms closest

Table 5  
B3LYP/HW+6-311++G(3df,3p) theoretical energies of  $[\text{Hf.C.4H}]^+$  intermediates and transition states

Species	State	$s(r+1)^3$	Energy ( $E_h$ )	Zero point energy ( $E_h$ ) <sup>b</sup>	$E_{\text{rel}}$ (eV) <sup>c</sup>
$\text{Hf}^*(^2\text{D}) + \text{CH}_4$	$^2\text{D}$	1.28*	-89.033864	0.044503	0.000
$\text{Hf}^*(\text{CH}_4)$	$^2\text{A}'$	1.25*	-89.050420	0.045022	-0.437
	$^4\text{A}$	3.75	-89.040310	0.044914	-0.164
	$^4\text{B}_2$	3.75	-89.040032	0.046340	-0.118
TS1	$^2\text{A}$	0.75	-89.023674	0.037030 (-1069)	0.076
	$^4\text{A}$	3.75	-88.978257	0.036636 (-445)	1.301
$\text{HHfCH}_3^+$	$^2\text{A}'$	0.75	-89.084072	0.038104	-1.538
	$^2\text{A}''$	0.76	-89.061408	0.038255	-0.918
	$^4\text{A}'$	3.76	-88.996956	0.036036	0.776
	$^4\text{A}''$	3.76	-88.996978	0.036190	0.780
	$^4\text{A}_2$	3.76	-88.955091	0.036632	1.932
TS2	$^2\text{A}'$	0.75	-89.032631	0.035860 (-330)	-0.199
	$^4\text{A}''$	3.76	-88.958576	0.034456 (-1263)	1.778
TS3	$^2\text{A}$	0.76	-89.028602	0.032822 (-644)	-0.171
	$^4\text{A}'$	3.76	-88.921983	0.027837 (-833)	2.596
$(\text{H}_2)\text{HfCH}_2^+$	$^2\text{A}'$	0.75	-89.035591	0.033191	-0.351
	$^4\text{A}_1$	3.76	-88.940595	0.029210	2.126
	$^4\text{A}''$	3.76	-88.934602	0.029184	2.289
	$^4\text{A}_1$	3.76	-88.922959	0.029810	2.622
TS4	$^2\text{A}$	0.75	-89.021080	0.034374 (-553)	0.075
	$^4\text{A}'$	3.76	-88.916988	0.026862 (-620)	2.706
$(\text{H}_2)\text{HfCH}_2^+$	$^2\text{A}'$	0.75	-89.032724	0.036813	-0.176
	$^2\text{A}$	0.75	-89.028202	0.037841	-0.025
	$^2\text{A}'$	0.75	-89.019558	0.034285	0.114
	$^2\text{A}''$	1.40*	-88.998800	0.033158	0.649
	$^4\text{A}'$	3.75	-88.995414	0.034566	0.779
	$^4\text{A}''$	3.75	-88.995377	0.034851	0.788
	$^4\text{A}_2$	3.75	-88.976940	0.036097	1.323
	$^2\text{A}_1$	0.75	-88.891713	0.033319	3.567

<sup>a</sup> Values indicating spin contamination are marked with an asterisk.

<sup>b</sup> Imaginary frequencies ( $\text{cm}^{-1}$ ) in parentheses.

<sup>c</sup> Energy relative to the ground state reactants including zero point energies scaled by 0.989.



Table 6  
 B3LYP/6-311++G(3d/3p) theoretical structures of  $[H_3C_2FH]^+$  intermediates and transition states<sup>a</sup>

Species	State	r(H–H)	r(H–C)	r(C–H)	r(H–H)	∠HCH	∠HCH	∠HHC	∠HHH	∠HHCH
HCHL <sup>+</sup>	<sup>2</sup> A'	2.319(2)	2.665	1.096, 1.090, 1.107(2)		60.0(2), 107.6, 141.0	104.9(2), 110.6(2), 111.3, 114.3			
	<sup>4</sup> A	2.247, 2.394	2.699	1.087, 1.098, 1.101, 1.112		54.7, 62.3, 118.3, 129.7	105.5, 106.9, 107.7, 108.9, 111.6, 116.3			
	<sup>4</sup> B <sub>2</sub>	2.293(2)	2.672	1.088(2), 1.108(2)		58.3(2), 124.2(2)	107.2(4), 111.3, 116.6			
TS1	<sup>2</sup> A	1.882	2.103	1.091(2), 1.199, 1.395		61.2, 70.6, 124.0, 124.2	101.3(2), 105.2(2), 111.0, 131.8	40.5		
	<sup>4</sup> A	1.808	2.549	1.082, 1.081, 1.092		84.7, 102.0, 105.2	117.5, 118.3, 119.2	85.0		
HHCHL <sup>+</sup>	<sup>1</sup> A'	1.785	2.106	1.097(2), 1.098		108.2, 110.6(2)	109.6, 108.9(2)	100.3		0.0, ±119.2
	<sup>2</sup> A'	1.802	2.125	1.097(2), 1.098		105.3, 112.4(2)	108.3, 109.2(2)	102.3		0.0, ±118.7
	<sup>4</sup> A'	1.868	2.385	1.089, 1.090(2)		99.2(2), 102.2	116.9(3)	164.1		±39.7, 180.0
	<sup>4</sup> A'	1.868	2.386	1.890, 1.090(2)		99.1, 100.6(2)	116.6, 117.0(2)	164.2		0.0, ±120.0
	<sup>1</sup> A <sub>2</sub>	1.889	2.484	1.087(2)		101.0(2)	116.5(3)	180.0		180.0(2)
TS2	<sup>2</sup> A'	1.930, 1.930	1.967	1.093(2), 1.902	0.902	123.7(2)	105.8(2), 112.5	58.4, 83.3	26.9	±89.4(2)
	<sup>4</sup> A'	1.888, 1.960	2.242	1.039(2), 1.227	1.310	60.7, 121.2(2)	113.1(2), 114.4	33.1, 72.8	39.8	±100.8
TS3	<sup>1</sup> A	1.794, 1.811	2.036	1.091, 1.093, 2.047		52.7, 119.8, 127.0	105.0, 107.1, 112.6	64.0, 100.3		9.8, -86.5, 87.6, 179.9
	<sup>4</sup> A'	1.837, 2.371	2.038	1.092(2), 1.937		55.0, 122.8(2)	103.1(2), 113.1	50.7, 138.7		±97.1, ±82.9
(H <sub>2</sub> )HCH <sup>+</sup>	<sup>2</sup> A'	1.787(2)	2.098	1.092(2)		123.8(2)	112.2	99.6(2)	102.6	±34.8, ±139.4
	<sup>4</sup> A <sub>1</sub>	1.937(2)	2.100	1.092(2)		123.9(2)	112.2	98.7(2)	162.6	±90.0(2)
	<sup>4</sup> A <sub>1</sub>	1.790, 2.003	2.181	1.089, 1.090		116.6, 121.5	121.9	97.8, 160.1	102.1	0.0(2), 180.0(2)
	<sup>4</sup> A <sub>1</sub>	1.927(2)	2.113	1.092(2)		123.9(2)	112.2	102.0(2)	136.0	0.0(2), 180.0(2)
TS4	<sup>2</sup> A	2.374, 2.375	1.892	1.082, 1.128	0.755	87.8, 159.7	112.5	93.5, 94.3	18.3	-80.4, 83.0, -98.8, 101.4
	<sup>4</sup> A'	1.968(2)	2.112	1.092(2)		121.6, 126.6	111.8	106.0(2)	87.1	±43.8, ±134.2
(H <sub>2</sub> )HCH <sub>2</sub> <sup>+</sup>	<sup>2</sup> A'	1.974, 1.999	1.958	1.093(2)	0.850	123.7(2)	112.5	60.1, 66.8	24.7	±89.9(2)
	<sup>1</sup> A	2.021, 2.053	1.907	1.085, 1.157	0.818	77.6, 180.0	102.4	68.4, 91.5	23.2	-1.1, -2.1, 92.8, 93.6
	<sup>1</sup> A'	2.457, 2.481	1.884	1.081, 1.138	0.755	83.5, 164.6	111.9	134.5, 152.1	17.6	0.0(2), 180.0(2)
	<sup>2</sup> A'	2.598, 2.748	2.088	1.090, 1.093	0.752	122.2, 125.7	112.1	146.7, 167.6	15.9	0.0(2), 180.0(2)
	<sup>4</sup> A'	2.173(2)	2.108	1.090, 1.093	0.781	122.4, 125.9	112.1	170.3(2)	20.7	±12.0, ±168.0
	<sup>4</sup> A'	2.141(2)	2.108	1.091(2)	0.787	123.8(2)	112.4	104.1(2)	21.2	±79.5, ±101.3
	<sup>4</sup> A <sub>2</sub>	2.306(2)	2.139	1.093(2)	0.783	125.3(2)	109.1	169.8(2)	20.4	0.0(2), 180.0(2)
	<sup>2</sup> A <sub>1</sub>	2.609(2)	2.418	1.096(2)	0.751	125.0(2)	110.0	171.7(2)	16.6	0.0(2), 180.0(2)

<sup>a</sup> Bond lengths are in Å. Bond angles are in degrees. Degeneracies are listed in parentheses.

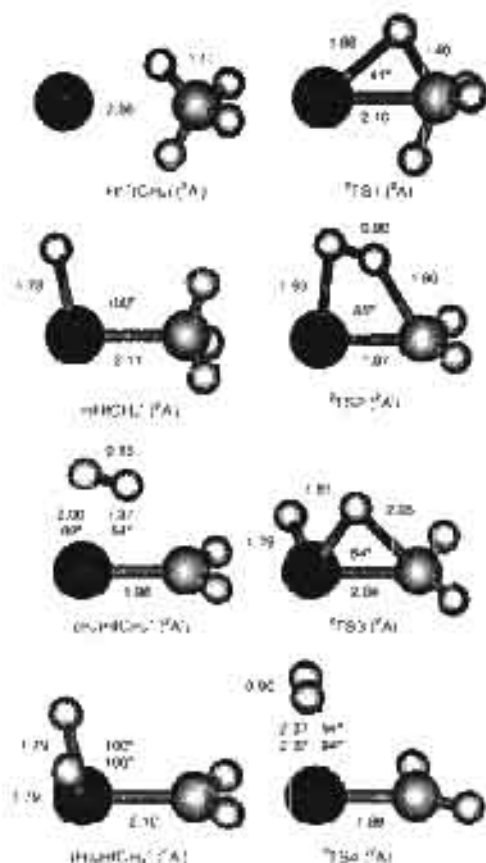


Fig. 3. Structures of several intermediates and transition states along the double surface of the  $\text{H}_2^+/\text{HCH}_2^+$  system calculated at the  $\text{RSH}/\text{STP}/\text{PW91}/6-311++(3,2)/\text{EPR}$  level of theory. Bond lengths shown are in Ångströms and HCH<sub>2</sub><sup>+</sup> bond angles are in degrees.

to  $\text{H}^+$  from this intermediate, or relative addition of a C–H bond to  $\text{H}^+$  forms an  $\text{H}_2\text{HCH}_2^+$  dihydride intermediate (Fig. 5); the global minimum on the PES. The transition state for the state addition,  $^2\text{TS}_1$ , has an  $C_s$  symmetry and a H–H–C bond angle of  $41^\circ$ . The H–H bond distance,  $1.88 \text{ \AA}$ , is longer than that of  $\text{H}_2^+(\text{H})_2^+$  ( $1.74 \text{ \AA}$ ), as is the H–C bond distance,  $2.10 \text{ \AA}$ , compared to that of  $\text{HCH}_2^+(\text{H})_2^+$  ( $1.81 \text{ \AA}$ ),  $2.07 \text{ \AA}$ . The energy of  $^2\text{TS}_1$  lies above the energy of the reactants by  $0.08 \text{ eV}$  (Fig. 4), consistent with the fact that the  $\sigma$ -acceptor orbital on  $\text{H}^+$  is doubly occupied in the  $^2\text{H}_2^+$  state. The  $\text{H}_2\text{HCH}_2^+$  dihydride intermediate has  $\nu(\text{H}-\text{H}) = 178 \text{ cm}^{-1}$ ,  $\nu(\text{H}-\text{C}) = 211 \text{ cm}^{-1}$ , and  $\nu(\text{HCH}_2^+) = 100 \text{ cm}^{-1}$  and a  $^2\text{A}'$  ground state. These bond lengths are comparable to those of  $\text{H}_2^+(\text{H})_2^+$  and  $\text{HCH}_2^+(\text{H})_2^+$ , indicating the covalent bonds to both H and  $\text{CH}_2$  are formed. The singly occupied molecular orbital (SOMO) in this molecule is essentially a  $\pi$ -orbital,

big orbital on hydrogen. A  $^2\text{A}'$  excited state of this dihydride was also located. It has a similar geometry (Table 6), but now the SOMO is a nonbonding  $5d$  (essentially one  $5d_{xy}$  orbital on hydrogen).

Continuing along the double surface, the  $\text{H}_2\text{HCH}_2^+$  intermediate can reductively eliminate  $\text{H}_2$  to form a  $(\text{H}_2)\text{HCH}_2^+$  intermediate by proceeding through a low-centered transition state,  $^2\text{TS}_2$ . This  $^2\text{A}'$  transition state has  $C_s$  symmetry and an H–C bond distance of  $1.97 \text{ \AA}$ . The  $(\text{H}_2)\text{HCH}_2^+$  intermediate looks very similar to the transition state, retaining the  $^2\text{A}'$  state and  $C_s$  symmetry. The H–C bond length is  $1.96 \text{ \AA}$ , longer than the bond length in  $\text{HCH}_2^+(\text{H})_2^+$  ( $1.88 \text{ \AA}$ ), indicating that the H–C double bond is not yet fully formed in this intermediate. Further, the  $\text{H}_2$  bond distance is  $0.85 \text{ \AA}$ , as compared to that of free  $\text{H}_2$ ,  $0.74 \text{ \AA}$ , indicating that molecular hydrogen is electrostatically bound to the  $\text{HCH}_2^+$  molecule. Other states of  $(\text{H}_2)\text{HCH}_2^+$  were also located, each of which retains a relatively short H–H bond distance. For the lowest lying excited state,  $^2\text{A}'$ , the main distinction is that the  $\text{CH}_2$  fragment has broken  $C_s$  symmetry by a rocking motion (see HCH bond angles, Table 6). Whereas the  $^2\text{A}'$  ground state has the center of the  $\text{H}_2$  loc used perpendicular to the plane of the  $\text{HCH}_2^+$  molecule, the  $^2\text{A}'$  state with an excitation energy of  $0.29 \text{ eV}$  has the  $\text{H}_2$  center in this plane, as does the  $^2\text{A}'$  state, which is heavily spin contaminated (Table 5). There is also a  $^2\text{A}_1$  state having  $C_2v$  symmetry where the  $\text{H}_2$  center lies along the H–C bond axis, but this lies well above the ground state ( $3.74 \text{ eV}$ ).

Decomposition of  $(\text{H}_2)\text{HCH}_2^+$  by loss of  $\text{H}_2$  results in the final dehydrogenation product,  $\text{HCH}_2^+$ . Importantly, although  $(\text{H}_2)\text{HCH}_2^+(\text{H})_2^+$  is a stable intermediate on the PES, zero point energy corrections are included, the energy of  $^2\text{TS}_2$  lies below that of the intermediate by  $0.02 \text{ eV}$  (Table 5). Thus, reductive elimination of  $\text{H}_2$  from  $\text{H}_2\text{HCH}_2^+$  is essentially a barrierless process to form products (Fig. 4).

An alternative mechanism for dehydrogenation of the  $\text{H}_2\text{HCH}_2^+$  intermediate involves sequential H atom transfers to form a  $(\text{H}_2)\text{HCH}_2^+(\text{H})_2^+$  dihydride intermediate (Fig. 5). This dihydride intermediate is relatively unstable because  $\text{H}^+$  cannot simultaneously form four covalent bonds. Consequently, although the two H–H bond lengths,  $1.79 \text{ \AA}$  each, are comparable to that of  $\text{H}_2^+(\text{H})_2^+$ ,  $1.74 \text{ \AA}$ , the H–C bond length of  $2.08 \text{ \AA}$  is indicative of a single covalent bond such as in  $\text{HCH}_2^+(\text{H})_2^+$  ( $1.81 \text{ \AA}$ ), rather than that of the double bond in  $\text{H}_2\text{H}_2^+(\text{H})_2^+$  ( $1.88 \text{ \AA}$ ). The dihydride intermediate is reached via  $^2\text{TS}_3$ , which lies  $0.13 \text{ eV}$  below the reactant energy. Reductive elimination of  $\text{H}_2$  from the dihydride intermediate occurs the molecule across  $^2\text{TS}_4$ , which lies  $0.08 \text{ eV}$  above the reactants. The imaginary frequency ( $55 \text{ cm}^{-1}$ ) in  $^2\text{TS}_4$  is essentially a rotation of the  $\text{H}_2$  molecule that moves the hydrogen so that they are parallel with the H–C bond, as in  $(\text{H}_2)\text{HCH}_2^+(\text{H})_2^+$ . Note that a lower energy pathway for transformation of  $(\text{H}_2)\text{HCH}_2^+(\text{H})_2^+$  to  $(\text{H}_2)\text{HCH}_2^+(\text{H})_2^+$  is actually to return to  $\text{H}_2\text{HCH}_2^+(\text{H})_2^+$  via  $^2\text{TS}_5$  followed by  $^2\text{TS}_2$  (Fig. 4). Overall, this alternative pathway for loss of  $\text{H}_2$  from the  $\text{H}_2\text{HCH}_2^+$  intermediate is less favorable energetically by  $0.27 \text{ eV}$  compared to the low-centered pathway of  $^2\text{TS}_2$ .

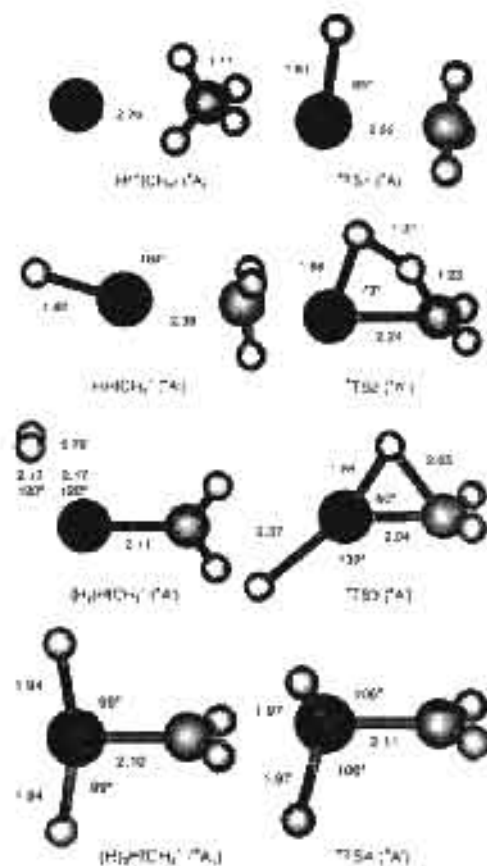


Fig. 3. Structures of various intermediates and transition states along the quartet surface of the  $\text{H}_2^+\text{CH}_2^+$  system computed at the  $\text{B3LYP}/6-31+G(3d,3p)$  level of theory. Bond lengths given are in Ångströms and HCH bond angles are in degrees.

#### 4.1. Quartet surface

On the quartet surface, the interaction of  $\text{H}^+$  with methylene leads to the formation of a  $\text{H}^+\text{CCH}_2^+$  adduct having no symmetry and a  $^4A_1$  state (Fig. 3). This intermediate lies 0.27 eV above its analogue on the doublet surface, directly reflecting the calculated excitation energy of the  $\text{H}^+$  ( $^4F$ ) state. It has a valence configuration in the equivalent  $C_2v$  designation of  $(1a_1)^2(1b_1)^2(2a_1)^1$  where the  $1a_1$  is largely  $2s$ , the  $1b_1$  is  $5d_{xy}$  and the  $2a_1$  is  $5d_{z^2-1}$ , where the  $z_2$  plane is defined by the H atoms closest to  $\text{H}^+$ . We also located a  $^2B_2$  state having  $C_{2v}$  symmetry, which lies 0.05 eV higher in energy and has a  $(1a_1)^2(1b_2)^2(2a_1)^2$  configuration. It seems likely that these two states are actually degenerate. Cleavage addition of a C–H bond to  $\text{H}^+$  leads to  $^4TS1$ , which then forms the hydroxymethyl

halomethyl cation intermediate,  $\text{HCH}_2^+$  ( $^4A_1$ ) (Fig. 4). The transition state has no symmetry and a H–H bond length comparable to that of  $\text{H}_2^+$  ( $^1\Delta_g$ ), 1.79 Å, but a very long H–C bond, 2.55 Å, and an HHC bond angle of 85°. The intermediate has  $C_1$  symmetry and a H–H–C bond angle of 164°. The H–H bond distance, 1.87 Å, is somewhat longer than that of  $\text{H}_2^+$  ( $^1\Delta_g$ ), 1.79 Å, but the H–C bond distance, 2.38 Å, is much larger than in  $\text{HCH}_2^+$  ( $^1A_1$ ), 2.07 Å. This observation indicates that the methyl molecule is loosely bound to  $\text{H}^+$  in this high spin state, consistent with the fact that two covalent bonds to  $\text{H}^+$  cannot be formed given this high spin. Thus, near  $^4TS1$  and  $\text{HCH}_2^+$  ( $^4A_1$ ) lie well above the analogous species on the doublet surface (Fig. 4). The  $^4A_1$  excited state of this intermediate differs from the  $^2A_1$  unity in the dihedral angle ( $0^\circ$  versus  $\pm 100^\circ$ ) and lies only 0.01 eV higher in energy. The  $^4A_1$  excited state lies much higher in energy (by 1.6 eV, Table 5). The geometry of this state has  $C_2v$  symmetry and an HHC bond angle of  $180^\circ$  (Table 6).

As in the doublet surface, dehydrogenation of the  $\text{HCH}_2^+$  ( $^4A_1$ ) intermediate occurs most readily over a four-centered transition state,  $^4TS2$  (Fig. 5). This  $^4A_1$  transition state has  $C_1$  symmetry and an H–C bond distance of 2.24 Å, much longer than the doublet analogue, again indicating the lack of a good covalent bond. This leads to the  $(\text{H}_2)\text{HCH}_2^+$  ( $^4A_1$ ) intermediate, which lies only 0.13 eV below the energy of the  $\text{HCH}_2^+$  ( $^2B_2$ )– $\text{H}_2$  product asymptote, consistent with a weakly bound  $\text{H}_2$  molecule. Indeed, the H–H and H–C bond lengths in  $(\text{H}_2)\text{HCH}_2^+$  ( $^4A_1$ ) are 0.78 and 2.11 Å, respectively, comparable to free  $\text{H}_2$  ( $0.74$  Å) and  $\text{HCH}_2^+$  ( $^2B_2$ ) ( $2.10$  Å). Low-lying excited states of  $(\text{H}_2)\text{HCH}_2^+$  were also located. The  $^4A_1$  state (only 0.01 eV higher in energy) is similar to the  $^4A_1$  state except for the location of the  $\text{H}_2$  molecule. In the  $^4A_1$  state, the center of the  $\text{H}_2$  molecule lies in the plane defined by  $\text{HCH}_2^+$ , whereas in the  $^4A_1$ , it lies perpendicular to this plane. The  $^4A_1$  excited state (0.54 eV higher in energy) has  $C_{2v}$  symmetry such that the center of the  $\text{H}_2$  molecule lies on the same axis as the H–C bond.

Alternatively, the  $\text{HCH}_2^+$  intermediate can transfer an  $\alpha$ -H to form a diatomic methyldene hafnium cation intermediate  $(\text{H})\text{HCH}_2^+$ . The transition state for this motion,  $^4TS3$  ( $^4A_1$ ), has  $C_1$  symmetry and lies 2.00 eV above ground state reactants. The dihydride intermediate has  $C_2v$  symmetry ( $^4A_1$  state) and lies high in energy, 2.14 eV above ground state reactants, because this high spin state cannot support the multiple bonds necessary. This is reflected in the H–C bond length of 2.10 Å, characteristic of a single covalent bond, and the H–H bond lengths of 1.94 Å, substantially longer than that of  $\text{H}_2^+$  ( $^1\Delta_g$ ), 1.79 Å. Excited states of the dihydride,  $^4A_1$  and  $^4A_1$ , lie only 0.16 and 0.50 eV, respectively, higher in energy (Table 5). The upper  $^4A_1$  state has a similar geometry to the lower  $^4A_1$  state but is planar, whereas the  $^4A_1$  state (also planar) has drastically changed one of the HHC bond angles (Table 6). The dihydride converts to the  $(\text{H}_2)\text{HCH}_2^+$  intermediate through  $^4TS4$  ( $^4A_1$ ), lying 0.58 eV higher than the dihydride in energy. Clearly this alternate pathway is again less favorable compared to the four-centered path way involving  $^4TS2$ , by 0.91 eV along the quartet surface.

## 5. Discussion

The dehydrogenation of methane by  $\text{Hf}^+$  ( $^2\text{D}$ ) (reaction (4)), is endothermic (Fig. 1). Reasonable agreement between theoretical and experimental BDEs indicates the  $\text{HfCH}_2^+$  product is formed in its  $^2\text{A}'$  ( $^2\text{A}_1$ ) ground state at threshold. This process must occur without activation in energy in excess of the endothermicity of the reaction because Irikura and Beauchamp observed that the reverse of reaction (4) occurs at thermal energies [4]. Experimental evidence that this reaction occurs through a  $\text{HHfCH}_3^+$  intermediate comes from the strong competition evident between the formation of  $\text{HfCH}_2^+ + \text{H}_2$  and  $\text{HfH}^+ + \text{CH}_3$ .

### 5.1. $\sigma$ -Bond activation

Even with a detailed PES in hand, it is useful to consider the qualitative aspects involved in understanding  $\sigma$ -bond activation by atomic metal ions. A simple donor–acceptor model predicts that  $\sigma$ -bond activation requires an electronic configuration on the metal in which there is an acceptor orbital into which the electrons of the bond to be broken can be donated. Concomitantly, metal electrons in orbitals with  $\pi$ -like symmetry backdonate into the antibonding orbital of the bond to be broken [7,10]. For hafnium, the  $6s$  acceptor orbital is doubly occupied in the  $^2\text{D}$  ground state and a repulsive interaction takes place at TS1 on the PES, leading to an inefficient reaction. This can explain the relatively low reactivity of the hafnium metal cation.

This qualitative picture can also be used to understand why the back reaction of  $\text{HfCH}_2^+$  ( $^2\text{A}'$ ,  $^2\text{A}_1$ ) adds  $\text{H}_2$  in a barrierless process to form  $\text{HHfCH}_3^+$ . The valence orbitals of the hafnium methylenide cation are  $(1a'_b)^2(1a''_b)^2(2a')^1$ , where the  $1a'_b$  and  $1a''_b$  orbitals are the  $\sigma(a_1)$  and  $\pi(b_1)$  Hf–C bonding orbitals, and the  $2a'$  is a  $6s$ – $5d_{z^2}$  nonbonding hybrid orbital on Hf. The lowest-lying unoccupied molecular orbitals include  $3a'$  ( $a_1$ ,  $5d_{x^2-y^2}$ ),  $2a''$  ( $a_2$ ,  $5d_{xy}$ ),  $4a'$  ( $b_2$ ,  $5d_{xz}$ ), and  $3a''$  ( $\pi^*$ ,  $b_1^*$ ). In this case, the acceptor orbital on  $\text{HfCH}_2^+$  is probably the empty  $3a'$ , whereas the donor orbital is the  $1a''_b$ . As  $\text{H}_2$  adds to  $\text{Hf}^+$  along the Hf–C bond, the  $\pi$  backdonation has the right symmetry to break the  $\text{H}_2$  bond and lead to formation of Hf–H and C–H covalent bonds. The availability of the empty  $3a'$  orbital on Hf allows a close approach, although there is undoubtedly mixing with the other  $a'$  orbitals as well.

### 5.2. Mechanism for higher energy products

Simple bond cleavages of the H–Hf $^+$ –CH $_3$  intermediate at energies beginning near 2.5 eV lead to  $\text{HfH}^+$  and  $\text{HfCH}_3^+$  products. These processes deplete the population of this intermediate, leading to a corresponding decline in the cross section for the dehydrogenation process. Because the formation of  $\text{HfCH}_2^+ + \text{H}_2$  is thermodynamically preferred by about 2.1 eV (Table 1), this competition indicates that formation of  $\text{HfH}^+ + \text{CH}_3$  is kinetically preferred, consistent with a simple bond cleavage compared to the more complex dehydrogenation process.

In the reaction of  $\text{Hf}^+$  with  $\text{CH}_4$  ( $\text{CD}_4$ ), the  $\text{HfH}^+$  ( $\text{HfD}^+$ ) cross section is dominant at energies above about 3 eV (Fig. 1). This is characteristic behavior for the reaction of bare metal ions with hydrogen-containing polyatomic molecules [9,45,47,48]. The fact that the  $\text{HfH}^+ + \text{CH}_3$  ( $\text{HfD}^+ + \text{CD}_3^+$ ) channel dominates the  $\text{HfCH}_3^+ + \text{H}$  ( $\text{HfCD}_3^+ + \text{D}$ ) channel is a result of angular momentum constraints [9,45,49,50]. Because the  $\text{HfCH}_3^+ + \text{H}$  ( $\text{HfCD}_3^+ + \text{D}$ ) channel has a reduced mass of 1.0 (2.0) amu as compared to the reactants 14.7 (18.0) amu, it is only formed by reactants that come together with small orbital angular momenta, i.e., at small impact parameters. In contrast, the  $\text{HfH}^+ + \text{CH}_3$  ( $\text{HfD}^+ + \text{CD}_3$ ) has a reduced mass of 13.9 (16.4) amu, much closer to that of the reactants, such that most impact parameters leading to strong interactions between the  $\text{Hf}^+$  and methane can form these products and still conserve angular momentum.

## 6. Conclusion

Ground state  $\text{Hf}^+$  ( $^2\text{D}$ ) ions react with methane yielding products over a broad range of kinetic energies. At low energies,  $\text{HfCH}_2^+$  dominates the product spectrum but is formed in an endothermic reaction pathway. At higher energies,  $\text{HfH}^+$  is the predominant species. Although the  $\text{HfCH}_3^+$  channel shares a common energy threshold with the  $\text{HfH}^+$  species, the latter product is favored because of angular momentum constraints. Dehydrogenation of  $\text{HfCH}_3^+$ , resulting in the  $\text{HfCH}^+$  product, reduces its cross section at higher energies.

Ab initio calculations verify that all transition states and intermediates have doublet ground states, guaranteeing that the dehydrogenation reaction pathway is spin allowed. The PES shows that  $\text{Hf}^+$  reacts with methane by oxidative addition of a C–H bond resulting in a hydrido-methyl hafnium intermediate,  $\text{HHfCH}_3^+$ . This is shown to be the global minimum on the PES. At elevated energies, simple bond cleavage from this intermediate yields the  $\text{HfH}^+ + \text{CH}_3$  and  $\text{HfCH}_3^+ + \text{H}$  products. The activation of a second C–H bond occurs through a four-centered transition state,  $^2\text{TS}_2$ , forming a  $(\text{H}_2)\text{HfCH}_2^+$  intermediate, in which molecular hydrogen is electrostatically bound to the hafnium methylenide cation. Elimination of  $\text{H}_2$  from this latter intermediate forms the metal methylenide ion product. Once zero point energies are included, it is found that the reductive elimination of  $\text{H}_2$  from the  $\text{HHfCH}_3^+$  intermediate occurs directly with no barriers in excess of the endothermicity.

The low relative reactivity of  $\text{Hf}^+$  ( $^2\text{D}$ ) compared with other third-row transition metal cations can be traced to its  $6s^2 5d^1$  electronic configuration, as originally suggested by Irikura and Beauchamp [4] over a decade ago. The present study reveals that the doubly occupied  $6s$  orbital results in a relatively high barrier for the oxidative addition of a CH bond to  $\text{Hf}^+$  ( $^2\text{D}$ ) and to a relatively weak  $\text{Hf}^+$ –CH $_2$  bond. Indeed,  $\text{Hf}^+$ –CH $_x$  BDEs are actually slightly weaker than those of the second-row congener,  $\text{Zr}^+$ –CH $_x$ , and only slightly stronger than those of the first-row congener,  $\text{Ti}^+$ –CH $_x$ . In addition, our calculations indicate that coupling to a  $^4\text{F}$  state having a  $6s^1 5d^2$  electronic configuration is not efficient as the high spin of this state results in a potential energy surface for reaction with methane that remains well above

the ground state doublet PES throughout the course of the reaction. Nevertheless, we find that the reactivity of methane with  $\text{Hf}^+$  ( $^2\text{D}$ ,  $6s^25d^1$ ) is still greater than that of  $\text{Lu}^+$  ( $^1\text{S}$ ,  $6s^2$ ) [9], which is probably related to the relative abilities to mix in some  $6s^15d^{n+1}$  character. For  $\text{Hf}^+$ , the  $^4\text{F}$  ( $6s^15d^2$ ) and  $^2\text{F}$  ( $6s^15d^2$ ) states lie only 0.563 and 1.483 eV, respectively, above the  $^2\text{D}$  ground state, whereas for  $\text{Lu}^+$ , the  $^3\text{D}$  ( $6s^15d^1$ ) and  $^1\text{D}$  ( $6s^15d^1$ ) states lie 1.628 and 2.149 eV, respectively, above the  $^1\text{S}$  ground state [11], making such mixing much more difficult.

### Acknowledgement

This work is supported by the National Science Foundation, Grant No. CHE-0451477.

### References

- [1] J. Haggin, Chem. Eng. News 71 (1993) 27.
- [2] B.K. Warren, S.T. Oyama, Heterogeneous Hydrocarbon Oxidation, ACS, Washington, DC, 1996.
- [3] K.K. Irikura, J.L. Beauchamp, J. Am. Chem. Soc. 113 (1991) 2769.
- [4] K.K. Irikura, J.L. Beauchamp, J. Phys. Chem. 95 (1991) 8344.
- [5] Y.A. Ranasinghe, T.J. MacMahon, B.S. Freiser, J. Phys. Chem. 94 (1991) 7721.
- [6] P.B. Armentrout, M.R. Sievers, J. Phys. Chem. A 107 (2003) 4396.
- [7] P.B. Armentrout, J.L. Beauchamp, Acc. Chem. Res. 22 (1989) 315.
- [8] L.S. Sunderlin, P.B. Armentrout, J. Phys. Chem. 92 (1988) 1209.
- [9] L.S. Sunderlin, P.B. Armentrout, J. Am. Chem. Soc. 111 (1989) 3845.
- [10] P.B. Armentrout, Organometallic Bonding and Reactivity, in: J.M. Brown, P. Hofmann (Eds.), Topics in Organometallic Chemistry, 4, Springer-Verlag, Berlin, 1999, p. 1.
- [11] C.E. Moore, Atomic Energy Levels, III, NSRDS-NBS, 35, 1971, p. 1.
- [12] S.K. Loh, D.A. Hales, L. Lian, P.B. Armentrout, J. Chem. Phys. 90 (1989) 5466.
- [13] R.H. Schultz, P.B. Armentrout, Int. J. Mass Spectrom. Ion Processes 107 (1991) 29.
- [14] E. Teloy, D. Gerlich, Chem. Phys. 4 (1974) 417.
- [15] D. Gerlich, Adv. Chem. Phys. 82 (1992) 1.
- [16] K.M. Ervin, P.B. Armentrout, J. Chem. Phys. 83 (1985) 166.
- [17] P.J. Chantry, J. Chem. Phys. 55 (1971) 2746.
- [18] C.L. Haynes, P.B. Armentrout, Organometallics 13 (1994) 3480.
- [19] M.R. Sievers, Y.-M. Chen, J.L. Elkind, P.B. Armentrout, J. Phys. Chem. 100 (1996) 54.
- [20] B.L. Kicket, P.B. Armentrout, J. Am. Chem. Soc. 117 (1995) 4057.
- [21] B.L. Kicket, P.B. Armentrout, J. Am. Chem. Soc. 117 (1995) 764.
- [22] D.E. Clemmer, Y.-M. Chen, F.A. Khan, P.B. Armentrout, J. Phys. Chem. 98 (1994) 6522.
- [23] W.J. Chesnavich, M.T. Bowers, J. Phys. Chem. 83 (1979) 900.
- [24] N. Aristov, P.B. Armentrout, J. Am. Chem. Soc. 108 (1986) 1806.
- [25] P.B. Armentrout, in: N.G. Adams, L.M. Babcock (Eds.), Advances in Gas-Phase Ion Chemistry, 1, JAI, Greenwich, CT, 1992, p. 83.
- [26] T. Shimanouchi, Tables of Molecular Vibrational Frequencies, consolidated I, NSRDS-NBS39, Washington, DC, 1972, p. 1.
- [27] M.T. Rodgers, P.B. Armentrout, J. Chem. Phys. 109 (1998) 1787.
- [28] A.D. Becke, J. Chem. Phys. 98 (1993) 5648.
- [29] C. Lee, W. Yang, R.G. Parr, Phys. Rev. B 37 (1988) 785.
- [30] M.J. Frisch, G.W. Trucks, H.B. Schlegel, G.E. Scuseria, M.A. Robb, J.R. Cheeseman, J.A. Montgomery, T. Vreven, K.N. Kudin, J.C. Burant, J.M. Millam, S.S. Iyengar, J. Tomasi, V. Barone, B. Mennucci, M. Cossi, G. Scalmani, N. Rega, G.A. Petersson, H. Nakatsuji, M. Hada, M. Ehara, K. Toyota, R. Fukuda, J. Hasegawa, M. Ishida, T. Nakajima, Y. Honda, O. Kitao, H. Nakai, M. Klene, X. Li, J.E. Knox, H.P. Hratchian, J.B. Cross, C. Adamo, J. Jaramillo, R. Gomperts, R.E. Stratmann, O. Yazyev, A.J. Austin, R. Cammi, C. Pomelli, J.W. Ochterski, P.Y. Ayala, K. Morokuma, G.A. Voth, P. Salvador, J.J. Dannenberg, V.G. Zakrzewski, S. Dapprich, A.D. Daniels, M.C. Strain, O. Farkas, D.K. Malick, A.D. Rabuck, K. Raghavachari, J.B. Foresman, J.V. Ortiz, Q. Cui, A.G. Baboul, S. Clifford, J. Cioslowski, B.B. Stefanov, G. Liu, A. Liashenko, P. Piskorz, I. Komaromi, R.L. Martin, D.J. Fox, T. Keith, M.A. Al-Laham, C.Y. Peng, A. Nanayakkara, M. Challacombe, P.M.W. Gill, B. Johnson, W. Chen, M.W. Wong, C. Gonzalez, J.A. Pople, Gaussian 03, Revision B. 02, Gaussian, Inc., Pittsburgh, PA, 2003.
- [31] X.-G. Zhang, R. Liyanage, P.B. Armentrout, J. Am. Chem. Soc. 123 (2001) 5563.
- [32] M.M. Armentrout, F.-X. Li, P.B. Armentrout, J. Am. Chem. Soc. 108 (2004) 9660.
- [33] P.B. Armentrout, S. Shin, R. Liyanage, J. Phys. Chem. A 110 (2006) 1242.
- [34] F.-X. Li, X.-G. Zhang, P.B. Armentrout, Int. J. Mass Spectrom., accepted for publication.
- [35] P.J. Hay, W.R. Wadt, J. Chem. Phys. 82 (1985) 299.
- [36] G. Ohanessian, M.J. Brusich, W.A. Goddard III, J. Am. Chem. Soc. 112 (1990) 7182.
- [37] M.C. Holthausen, C. Heinemann, H.H. Cornehl, W. Koch, H. Schwarz, J. Chem. Phys. 102 (1995) 4931.
- [38] M.C. Holthausen, M. Mohr, W. Koch, Chem. Phys. Lett. 240 (1995) 245.
- [39] D. Andrae, U. Haeussermann, M. Dolg, H. Stoll, H. Preuss, Theor. Chim. Acta 77 (1990) 123.
- [40] C. Peng, H.B. Schlegel, Isr. J. Chem. 33 (1994) 449.
- [41] C. Peng, P.Y. Ayala, H.B. Schlegel, M.J. Frisch, J. Comput. Chem. 17 (1996) 49.
- [42] C. Hinton, P.B. Armentrout, work in progress.
- [43] J. Simons, J. Nichols, Quantum Mechanics in Chemistry, Oxford University Press, New York, NY, 1997, p. 219.
- [44] K.K. Irikura, W.A. Goddard III, J. Am. Chem. Soc. 116 (1994) 8733.
- [45] P.B. Armentrout, B.L. Kicket, in: B.S. Freiser (Ed.), Organometallic Ion Chemistry, Kluwer, Dordrecht, The Netherlands, 1996, p. 1.
- [46] M.R. Sievers, P.B. Armentrout, Organometallics 22 (2003) 2599.
- [47] N. Aristov, P.B. Armentrout, J. Phys. Chem. 91 (1987) 6178.
- [48] Y.-M. Chen, M.R. Sievers, P.B. Armentrout, Int. J. Mass Spectrom. Ion Processes 167/168 (1997) 195.
- [49] L.S. Sunderlin, P.B. Armentrout, J. Phys. Chem. 92 (1988) 1209.
- [50] Y.-M. Chen, P.B. Armentrout, J. Phys. Chem. 99 (1995) 10775.

## CHAPTER 4

### EXPERIMENTAL AND THEORETICAL STUDIES OF THE ACTIVATION OF METHANE BY $\text{TA}^+$

Laura G. Parke, Christopher S. Hinton, P. B. Armentrout

Reproduced with permission from [Parke, L. G.; Hinton, C. S.; Armentrout P. B. *J. Phys. Chem. C* **2007**, *111*, 17773-177787.] Copyright [2007] American Chemical Society.

## Experimental and Theoretical Studies of the Activation of Methane by Ta<sup>+</sup>

Laura G. Parke, Chris S. Hinton, and P. B. Armentrout\*

Department of Chemistry, University of Utah, Salt Lake City, Utah 84112

Received: January 31, 2007; In Final Form: March 23, 2007

A guided-ion-beam tandem mass spectrometer is used to study atomic tantalum cations reacting with CH<sub>4</sub> and CD<sub>4</sub>. Like other third-row transition metal ions, W<sup>+</sup>, Os<sup>+</sup>, Ir<sup>+</sup>, and Pt<sup>+</sup>, the dehydrogenation reaction to form TaCH<sub>2</sub><sup>+</sup> + H<sub>2</sub> is exothermic. At higher energies, other products, TaH<sup>+</sup>, TaCH<sup>+</sup>, and TaCH<sub>3</sub><sup>+</sup>, are observed with TaH<sup>+</sup> dominating the product spectrum. Modeling of the endothermic cross sections provides the 0 K bond dissociation energies (in eV) of  $D_0(\text{Ta}^+-\text{CH}) = 5.82 \pm 0.16$  and  $D_0(\text{Ta}^+-\text{CH}_3) = 2.69 \pm 0.14$  eV. We also examined the reverse reaction, TaCH<sub>2</sub><sup>+</sup> + H<sub>2</sub> → Ta<sup>+</sup> + CH<sub>4</sub>, and its isotopic equivalent, TaCH<sub>2</sub><sup>+</sup> + D<sub>2</sub>. By combining the cross sections for the forward and reverse processes, an equilibrium constant for this reaction is derived, from which  $D_0(\text{Ta}^+-\text{CH}_2) = 4.81 \pm 0.03$  eV is obtained. The Ta<sup>+</sup>-H and Ta<sup>+</sup>-CH<sub>3</sub> experimental bond energies are in reasonable agreement with density functional calculations at the B3LYP/HW+/6-311++G(3df,3p) level of theory, whereas the Ta<sup>+</sup>-CH and Ta<sup>+</sup>-CH<sub>2</sub> bond energies are predicted well by B3LYP/HW+/6-311++G(3df,3p) calculations. Theoretical calculations at this latter level of theory reveal that these reactions proceed through a H-Ta<sup>+</sup>-CH<sub>3</sub> intermediate and provide details of the various intermediates and transition states.

### 1. Introduction

Third-row transition metal cations have been found to be much more reactive than the comparable first- and second-row transition metal cations in the gas phase but have been studied less extensively. Although none of the first- and second-row transition metals react exothermally with methane, Irikura and Beauchamp<sup>1</sup> report that several of the third-row transition metal ions (Ta<sup>+</sup>, W<sup>+</sup>, Os<sup>+</sup>, Ir<sup>+</sup>, and Pt<sup>+</sup>) dehydrogenate methane at thermal energies. The reaction with Ta<sup>+</sup>, one of the more reactive of these elements, has been studied using ion cyclotron resonance (ICR) mass spectrometry by Irikura and Beauchamp,<sup>1,2</sup> Buckner et al.,<sup>3</sup> and Wesendrup and Schwarz.<sup>4</sup> It has been found that Ta<sup>+</sup> reacts four times with methane by sequential dehydrogenations at thermal energies to form TaCH<sub>2</sub><sup>+</sup> initially, followed by TaC<sub>2</sub>H<sub>4</sub><sup>+</sup> and TaC<sub>3</sub>H<sub>6</sub><sup>+</sup>, eventually forming TaC<sub>4</sub>H<sub>8</sub><sup>+</sup>.<sup>1–3</sup> Irikura and Goddard<sup>5</sup> calculated the low-lying states of TaCH<sub>2</sub><sup>+</sup> using multireference configuration interaction methods and recommended a binding energy of 4.99 eV, consistent with the exothermic dehydrogenation reaction. Sandig and Koch<sup>6</sup> have computationally investigated the mechanistic details of the potential energy surface using density functional theory.

In the present work, we use guided ion beam tandem mass spectrometry to examine the Ta<sup>+</sup> + methane system at energies greater than room temperature for the first time. This provides quantitative thermochemical and mechanistic information that augments our ongoing effort to provide insight into the periodic trends in the reactivity of the third-row transition metal cations.<sup>7,8</sup> We find that Ta<sup>+</sup>, which has a <sup>3</sup>F ground electronic state with a 6s<sup>1</sup>5d<sup>3</sup> configuration, reacts much more like W<sup>+</sup> (<sup>6</sup>D, 6s<sup>1</sup>5d<sup>4</sup>)<sup>9</sup> than Hf<sup>+</sup> (<sup>2</sup>D, 6s<sup>2</sup>5d<sup>1</sup>)<sup>10</sup> because of the open valence shell. The quantitative thermochemistry obtained allows an assessment of theoretical approaches to evaluate these heavy metal species. For this reason, a complete theoretical

investigation of all product ions and the intermediates and transition states along the potential energy surfaces accessible are also pursued.

### 2. Experimental and Theoretical Methods

**2.1. General Procedures.** These experiments were performed using a guided ion beam tandem mass spectrometer described in detail elsewhere.<sup>11</sup> Ions are created in a direct current discharge flow tube source described below, extracted from the source, and then accelerated and focused into a magnetic sector momentum analyzer for mass analysis. Reactant ions containing the <sup>181</sup>Ta isotope (99.99% natural abundance) are selected, decelerated to a desired kinetic energy, and focused into an octopole ion guide that traps the ions in the radial direction using radio frequency electric fields.<sup>12,13</sup> The octopole passes through a static gas cell that contains the neutral collision/reaction partner at a pressure of less than ~0.4 mTorr. The product and unreacted parent ions are confined in the radial direction in the guide until they drift to the end of the octopole where they are extracted, focused, and passed through a quadrupole mass filter for mass analysis. Ions are then detected with a secondary electron scintillation ion detector,<sup>14</sup> and the signal is processed using standard pulse counting techniques. After correction for background signals, reaction cross sections are calculated from product ion intensities.<sup>15</sup> The uncertainties in the absolute cross sections are estimated as ±20%.

The kinetic energy is varied in the laboratory frame by scanning the direct current (dc) bias on the octopole rods with respect to the potential of the ion source region. Laboratory (lab) ion energies are converted to the center-of-mass (CM) frame using the formula  $E_{\text{CM}} = E_{\text{lab}}m/(m + M)$ , where  $m$  and  $M$  are the neutral and ionic reactant masses, respectively. The kinetic energy distribution of the reactant ion and the thermal motion of the neutral reactant gas (Doppler broadening) both contribute to broaden the cross sections.<sup>16</sup> By use of the octopole beam guide as a retarding potential analyzer, as described

\* Part of the special issue "Richard E. Smalley Memorial Issue".

previously,<sup>15</sup> both the absolute zero and the full width at half-maximum (fwhm) of the kinetic energy distribution of the ions are determined. The distributions of ion kinetic energies are nearly Gaussian, independent of energy, and have a typical fwhm of 0.3–0.6 eV (lab) in these studies. Uncertainties in the absolute energy scale are  $\pm 0.05$  eV (lab).

**2.2. Ion Source.** Ta<sup>+</sup> ions are produced in a dc discharge flow tube (DC/FT) source.<sup>17</sup> This source consists of a cathode held at high negative voltage (0.7–1.5 kV) over which a flow of approximately 90% He and 10% Ar passes at a total pressure of 0.3–0.4 Torr and ambient temperature. For this study, the cathode is made of tantalum. Ar<sup>+</sup> ions created in the discharge are accelerated toward the cathode, thereby creating Ta<sup>+</sup> ions. Ta<sup>+</sup> ions then drift with the buffer gases down a 1 m long flow tube, undergoing  $\sim 10^3$  collisions with He and  $\sim 10^4$  collisions with Ar before entering the guided ion beam apparatus. No evidence for low-lying excited states of Ta<sup>+</sup> (within about 1% sensitivity) is observed under these flow conditions. When compared to a surface ionization source, the DC/FT source has been found to generate Sc<sup>+</sup>,<sup>18</sup> Fe<sup>+</sup>,<sup>19</sup> Co<sup>+</sup>,<sup>20</sup> Ni<sup>+</sup>,<sup>21</sup> Ru<sup>+</sup>,<sup>22</sup> Rh<sup>+</sup>,<sup>22</sup> and Pd<sup>+</sup><sup>22</sup> ions with an average electronic temperature of 700  $\pm$  400 K and Y<sup>+</sup>, Zr<sup>+</sup>, Nb<sup>+</sup>, and Mo<sup>+</sup> ions with an average electronic temperature of 300  $\pm$  100 K.<sup>23</sup> Even at the maximum electronic temperature of 1100 K, the Ta<sup>+</sup> ion beam produced has a distribution of 64.9% <sup>3</sup>F<sub>1</sub> (0.000 eV), 28.0% <sup>3</sup>F<sub>2</sub> (0.128 eV), 4.8% <sup>5</sup>F<sub>3</sub> (0.328 eV), 1.7% <sup>3</sup>F<sub>2</sub> (0.394 eV), and 0.6% <sup>5</sup>F<sub>4</sub> (0.547 eV), with all other spin-orbit levels having populations less than 0.01%.<sup>24</sup> At 700 K, the populations are 82.4, 16.5, 0.8, 0.2, and 0.03%, respectively, and at 300 K, they are 98.8, 1.2, and <0.001%, respectively. Conservatively, the average electronic energy of the Ta<sup>+</sup> ions is estimated to be 0.025<sup>+0.039</sup>/<sub>-0.023</sub> eV.

TaCH<sub>3</sub><sup>+</sup> ions are produced by the introducing CH<sub>4</sub> into the flow tube  $\sim 15$  cm downstream of the discharge zone at a pressure of  $\sim 2$  mTorr. Three-body collisions with the He/Ar flow gas both thermalize and stabilize the ions rotationally and vibrationally. It is assumed that the ions are in their ground electronic state and that the internal energy of these complexes is described by a Maxwell-Boltzmann distribution of rotational and vibrational states corresponding to 300  $\pm$  100 K. Previous studies from our laboratory have shown that this is generally the case for molecular species.<sup>25,26</sup>

**2.3. Data Analysis.** Analysis of the kinetic energy dependence of product cross sections is performed to determine  $E_0$ , the energy threshold for product formation at 0 K. The apparent threshold observed under laboratory conditions differs from  $E_0$  because of the internal and kinetic energy distributions of the reactant ions and neutrals. These contributions allow for reactions to take place at energies below  $E_0$ . Previous theoretical and experimental work has shown that endothermic cross sections can be modeled using eq 1<sup>27,28</sup>

$$\sigma(E) = \sigma_0 \sum g_i (E + E_i + E_{el} - E_0)^n / E \quad (1)$$

where  $\sigma_0$  is an energy-independent scaling parameter,  $E$  is the relative kinetic (translational) energy of the reactants, and  $n$  is an adjustable parameter that determines the shape of the cross section. The summation is over all possible rovibrational states of the neutral reactant with energies  $E_i$  and populations  $g_i$ , where  $\sum g_i = 1$ . The various sets of vibrational frequencies and rotational constants used to determine  $E_i$  in this study are taken from the literature for H<sub>2</sub>, D<sub>2</sub>, CH<sub>4</sub>, and CD<sub>4</sub>.<sup>29</sup> As noted above, the electronic energy of the Ta<sup>+</sup> reactant,  $E_{el}$ , is 0.025<sup>+0.039</sup>/<sub>-0.023</sub> eV. Equation 1 is convoluted over the neutral and ion kinetic energy distribu-

tions prior to comparison with the data. The adjustable parameters,  $E_0$ ,  $\sigma_0$ , and  $n$ , are then optimized using a non-linear least-squares analysis to give the best reproduction of the data.<sup>28,30</sup> Values reported for these parameters are the average values obtained for each parameter over a range of best fits to several independent data sets. The resultant uncertainties are 1 standard deviation. Uncertainties in the absolute energy scale ( $\pm 0.05$  eV, lab) and in the electronic energy of Ta<sup>+</sup> are included in the uncertainties reported for  $E_0$ .

**2.4. Theoretical Calculations.** In the present study, quantum chemistry calculations are generally computed with the B3LYP hybrid density functional method<sup>31,32</sup> and performed with the Gaussian 03 suite of programs.<sup>33</sup> For most calculations done here, the B3LYP functional was used because it provides reasonable results for analogous reactions of methane with Pt<sup>+</sup>,<sup>34</sup> Re<sup>+</sup>,<sup>35</sup> W<sup>+</sup>,<sup>9</sup> Ir<sup>+</sup>,<sup>36</sup> Hf<sup>+</sup>,<sup>10</sup> and Au<sup>+</sup>.<sup>8</sup> The rather large 6-311++G(3df,3p) basis set is used for carbon and hydrogen because of the bridging hydrogens that occur for many of the transition states of interest. This basis set yields bond energies for the hydrocarbon species that reproduce experimental results within 0.08 eV: H-CH<sub>3</sub> (4.406 vs 4.480 eV), H<sub>2</sub>-CH<sub>2</sub> (4.666 vs 4.713 eV), H-CH (4.332 vs 4.360 eV), C-H (3.532 vs 3.465 eV), and H-H (4.505 vs 4.478 eV). (See refs 34 and 37 for thermochemistry used for all H, D, CH<sub>x</sub>, and CD<sub>x</sub> species.) The relativistic effective core potential (ECP) of Hay-Wadt (HW)<sup>38</sup> describes the 60 core electrons of tantalum and the Los Alamos double- $\zeta$  basis set (LANL2DZ) describes the valence electrons. This basis set is optimized for neutral atoms, whereas the charge on Ta<sup>+</sup> differentially contracts the 6s orbitals compared to the 5d orbitals. This is taken into account by using an altered valence basis set as described by Ohanessian et al.,<sup>39</sup> denoted by HW+ and is used for most of our calculations for Ta<sup>+</sup>. We determined the harmonic frequencies of normal modes and evaluated zero-point vibrational energies at the B3LYP/HW+/6-311++G(3df,3p) level of theory. The thermochemistry reported here is corrected for zero-point energies after scaling the calculated frequencies by 0.989.<sup>40</sup>

The most relevant choice for a level of theory for the first- and third-row transition metal methyl cations has been investigated by Holthausen et al.<sup>41</sup> and for first-row metal methylene cations by Holthausen, Mohr, and Koch.<sup>42</sup> In the first study, these authors used B3LYP, Becke-half-and-half-LYP (BHLYP), and QCISD(T) methods with a basis set consisting of a polarized double- $\zeta$  basis on C and H and the HW relativistic ECP with valence electrons added. The symmetries of the MCH<sub>3</sub><sup>+</sup> molecules were constrained to C<sub>3v</sub>. It was concluded that for the first-row MCH<sub>3</sub><sup>+</sup> species (M = Sc-Cu), where experimental results are available for all metals,<sup>43,44</sup> that the B3LYP functional overbinds, with a mean absolute deviation (MAD) from experiment of 0.41 eV. In contrast, the BHLYP functional and the QCISD(T) method gave better comparisons to experimental work, with MADs of 0.18 and 0.20 eV, respectively. For the metal methylene cation complexes,<sup>41</sup> the B3LYP functional predicts bond energies in good agreement with experimental data, whereas the performance of the BHLYP functional predicts bond energies consistently below experimental data. On the basis of these results, the present study includes calculations for the various product ions using the BHLYP functional and the Stuttgart-Dresden (SD) ECP<sup>45</sup> for Ta<sup>+</sup>, as well as QCISD(T) calculations using the HW+ ECP. Generally, our results will refer to the B3LYP/HW+/6-311++G(3df,3p) level of theory, unless otherwise noted.



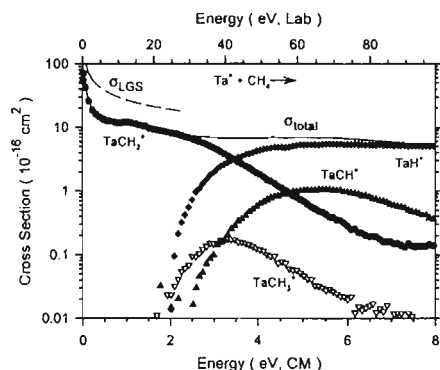
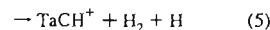
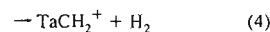
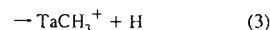
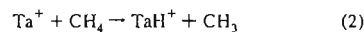


Figure 1. Cross sections for reaction of Ta<sup>+</sup> (<sup>5</sup>F) with CH<sub>4</sub> as a function of kinetic energy in the center-of-mass frame (lower axis) and laboratory frame (upper axis). The full line shows the sum of all product cross sections. The LGS collision cross section is indicated by the dashed line at low energies.

We calculated a <sup>5</sup>F (6s<sup>1</sup>5d<sup>3</sup>) ground state for Ta<sup>+</sup>, with the first two excited states (<sup>3</sup>P and <sup>3</sup>F, both 6s<sup>2</sup>5d<sup>2</sup>) at 0.402 and 0.626 eV, respectively, and a singlet state (<sup>1</sup>D, 6s<sup>2</sup>5d<sup>2</sup>) at 1.900 eV, using the HW<sup>+</sup> basis set and B3LYP level of theory. These values are comparable to those of Sandig and Koch<sup>6</sup> who calculated a <sup>5</sup>F ground state with <sup>3</sup>F and <sup>1</sup>D excited states at 0.806 and 1.743 eV, respectively, using the B3LYP level of theory and their BS1 basis set.<sup>6</sup> For the B3LYP/SD, B3LYP/HW<sup>+</sup>, and B3LYP/SD combinations of functional/basis set, we found excitation to the lowest lying state (<sup>3</sup>P) to be 0.427, 0.455, and 0.496 eV, demonstrating that the atomic excitations are largely independent of the functional and basis set used. However, for the QCISD(T) level of theory, we found a much lower excitation level of 0.194 eV. Similarly, we found excitation to the <sup>3</sup>F state to be 0.675 eV for B3LYP/SD and 0.247 eV for the QCISD(T) level of theory. No spin contamination was found for the different combinations of functional/basis set. The quintet–triplet excitation energies can be compared to experimental values (average of the spin–orbit levels) of 0.201 eV for the <sup>3</sup>P excited state and 0.428 eV for the <sup>3</sup>F excited state,<sup>24</sup> such that the density functional theoretical values are slightly too high (by about 0.2 eV). The quintet–singlet excitation energy has an experimental value of 1.216 eV,<sup>24</sup> much lower than the B3LYP/HW<sup>+</sup> theoretical value. Other experimentally determined excited states include <sup>5</sup>P (5d<sup>3</sup>(<sup>4</sup>P)6s), <sup>3</sup>G (5d<sup>3</sup>(<sup>2</sup>G)6s), <sup>3</sup>F (5d<sup>3</sup>(<sup>4</sup>F)6s), and <sup>3</sup>D (5d<sup>4</sup>), with average excitation energies of 1.010, 1.086, 1.406, and 1.472 eV, respectively.<sup>24</sup>

### 3. Experimental Results

**3.1. Reaction of Ta<sup>+</sup> with Methane.** The reaction of Ta<sup>+</sup> with CH<sub>4</sub> yields the product ions shown in reactions 2–5. The cross sections as a function of kinetic energy for these reactions are shown in Figure 1. Similar studies were performed for Ta<sup>+</sup> and CD<sub>4</sub>. The CD<sub>4</sub> results are comparable to those of Figure 1 both in cross section magnitudes and energy dependences for all products. The most notable difference is that the cross section for TaCD<sub>2</sub><sup>+</sup> declines somewhat less rapidly above 3 eV compared to that for TaCH<sub>2</sub><sup>+</sup> reaching a magnitude of ~0.5 × 10<sup>-16</sup> cm<sup>2</sup> at 8 eV.



As can be seen from Figure 1, the reactions to form TaH<sup>+</sup>, TaCH<sub>3</sub><sup>+</sup>, and TaCH<sup>+</sup> are all endothermic, whereas formation of TaCH<sub>2</sub><sup>+</sup> is exothermic. It is also the only product that is observed at low energies, which agrees with previous ICR studies of both Irikura and Beauchamp<sup>1,2</sup> and Buckner et al.<sup>3</sup> The cross section for this reaction declines as  $E^{-0.54 \pm 0.04}$  below 0.5 eV, comparable to the estimate of the Langevin–Gioumousis–Stevenson (LGS) collision cross section,<sup>46</sup> which has an  $E^{-0.5}$  energy dependence.

The magnitudes of our experimental cross sections are 30 ± 12% and 23 ± 8% of the LGS limit for the CH<sub>4</sub> and CD<sub>4</sub> reactions, respectively. To quantitatively compare our results to the literature, we convert our cross section to a rate constant using eq 6

$$k(E) = \nu \sigma(E) \quad (6)$$

where  $\nu = (2E/\mu)^{1/2}$  and  $\mu = mM/(m + M)$ , the reduced mass of the reactants. This rate constant is dependent on the mean energy of the reactants, which includes the average thermal motion of the neutral, eq 7

$$\langle E \rangle = E + (3/2)\gamma k_B T \quad (7)$$

where  $\gamma = M/(m + M)$ ,  $k_B$  is Boltzmann's constant, and  $T$  is the temperature of the reactant gas (298 K). Using this equation, we obtain  $k = (2.9 \pm 1.2) \times 10^{-10}$  cm<sup>3</sup>/s for reaction with CH<sub>4</sub> and  $k = (2.0 \pm 0.7) \times 10^{-10}$  cm<sup>3</sup>/s for reaction with CD<sub>4</sub> as compared to the LGS rates of  $9.8 \times 10^{-10}$  and  $8.8 \times 10^{-10}$  cm<sup>3</sup>/s, respectively. Our experimental values are comparable to the rate constants obtained by ICR mass spectrometry of  $k = (3.4 \pm 0.9) \times 10^{-10}$  cm<sup>3</sup>/s for CH<sub>4</sub> and  $k = (2.4 \pm 0.6) \times 10^{-10}$  cm<sup>3</sup>/s for CD<sub>4</sub>,<sup>1</sup> lying within experimental errors. The ICR results give reaction efficiencies of 35 ± 9% and 27 ± 7%, respectively, well within the experimental error of our results, 30 ± 12% and 23 ± 8%, respectively.

At higher energies (>2 eV), the TaCH<sub>2</sub><sup>+</sup> cross section begins to decline rapidly, Figure 1. The onset of this decrease corresponds well with the apparent thresholds of the other products observed. However, the only other cross section that is large enough to account for this decline is TaH<sup>+</sup>. From this, we can draw one of two conclusions: TaCH<sub>2</sub><sup>+</sup> decomposes to TaH<sup>+</sup> + CH or the formation of TaH<sup>+</sup> + CH<sub>3</sub> competes with the formation of TaCH<sub>2</sub><sup>+</sup> + H<sub>2</sub>. Because decomposition of TaCH<sub>2</sub><sup>+</sup> to TaH<sup>+</sup> + CH cannot occur until much higher energies (~6.7 eV), it can be concluded that formation of TaH<sup>+</sup> and TaCH<sub>2</sub><sup>+</sup> must compete with one another. This competition can best be explained if these two products share a common intermediate, as discussed further below.

The TaH<sup>+</sup> cross section rises from an apparent threshold near 2 eV and plateaus above 4 eV. The TaCH<sub>3</sub><sup>+</sup> cross section rises from a similar threshold but reaches a maximum magnitude near 3 eV. This behavior cannot be explained by dissociation to Ta<sup>+</sup> + CH<sub>3</sub>, which cannot begin until 4.48 eV =  $D_0(\text{H}-\text{CH}_3)$ . Instead, the cross section of TaCH<sub>3</sub><sup>+</sup> is limited by the subsequent elimination of molecular hydrogen to form TaCH<sup>+</sup> + H<sub>2</sub>, a pathway that requires little energy. TaCH<sub>3</sub><sup>+</sup> can also lose an H

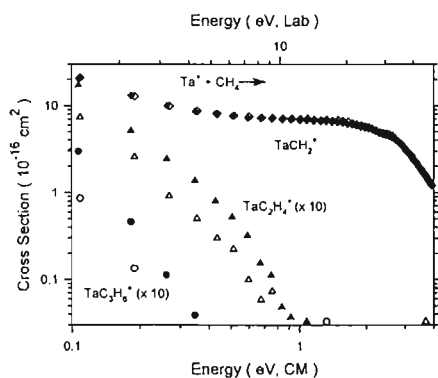


Figure 2. Cross sections for multiple reactions of  $\text{Ta}^+$  ( $^3\text{F}$ ) with  $\text{CH}_4$  as a function of kinetic energy in the center-of-mass frame (lower axis) and laboratory frame (upper axis). Open and closed symbols show results taken at methane pressures of 0.20 and 0.41 mTorr, respectively.

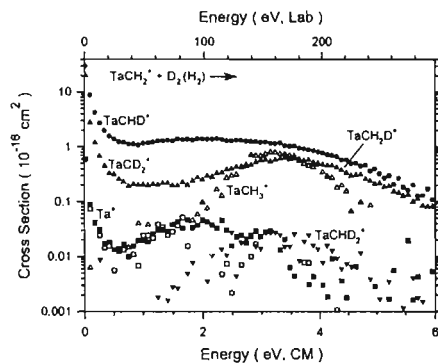


Figure 3. Cross sections for reaction of  $\text{TaCH}_2^+$  with  $\text{H}_2$  (open symbols) and  $\text{D}_2$  (closed symbols) as a function of kinetic energy in the center-of-mass frame (lower axis) and laboratory frame (upper axis).

atom to form  $\text{TaCH}_2^+$  at higher energies. Evidence for the latter pathway can be seen as the slight increase in the cross section of  $\text{TaCH}_2^+$  above 7 eV. Overall, this process corresponds to the formation of  $\text{TaCH}_2^+ + 2\text{H}$ .

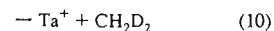
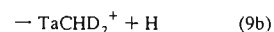
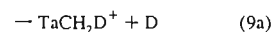
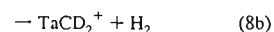
**3.2. Multiple Collision Dehydrogenation Reactions.** The primary  $\text{TaCH}_2^+$  products formed in reaction 4 react further with methane. In our experiments, we observe that  $\text{Ta}^+$  successively dehydrogenates three methane molecules to form  $\text{TaC}_2\text{H}_4^+$  and  $\text{TaC}_3\text{H}_6^+$  product ions, Figure 2. The cross sections for these product ions display a distinct dependence on methane pressure over a range of 0.1 (where the higher order products are very small) to 0.4 mTorr, verifying that they result from higher order reactions. The energy dependences for formation of these products indicate that each of these subsequent reactions is exothermic and has no barriers in excess of the reactant energies, Figure 2. These results are in good agreement with observations of Irikura and Beauchamp,<sup>1</sup> who observed that  $\text{Ta}^+$  reacts rapidly four times with methane with rates of 3.4, 2.0, 2.0, and  $1.4 \times 10^{-10} \text{ cm}^3 \text{ s}^{-1}$  to form  $\text{TaCH}_2^+$ ,  $\text{TaC}_2\text{H}_4^+$ ,  $\text{TaC}_3\text{H}_6^+$ , and  $\text{TaC}_4\text{H}_8^+$ . Because of the relatively low pressures used in our experiments, only the first three of these products are observed.

The higher order reactivity of  $\text{Ta}^+$  with  $\text{CD}_4$  observed here is less extensive than that seen for  $\text{Ta}^+ + \text{CH}_4$ . The formation

of secondary products is not as rapid, forming only  $\text{TaC}_2\text{D}_4^+$  and not  $\text{TaC}_3\text{D}_6^+$ . This is in qualitative agreement with Irikura and Beauchamp<sup>1</sup> observations that  $\text{Ta}^+$  reacts four times with  $\text{CD}_4$ , but with slower rates of 2.4, 0.6, 1.4 and  $1.3 \times 10^{-10} \text{ cm}^3 \text{ s}^{-1}$ .

For both the  $\text{CH}_4$  and  $\text{CD}_4$  system, the cross sections for the primary  $\text{TaCH}_2^+$  and  $\text{TaCD}_2^+$  products are essentially identical at all methane pressures examined (0.1, 0.2, and 0.4 mTorr), Figure 2. Thus, the cross section shown in Figure 1 for this product accurately represents the reaction probability under single collision conditions.

**3.3. Reaction of  $\text{TaCH}_2^+$  with  $\text{D}_2$ .** Figure 3 shows cross sections for reaction of  $\text{TaCH}_2^+$  with  $\text{D}_2$ , which yields five product ions, as shown in reactions 8–10.



Observation of reactions 8 has been previously reported in the ICR MS studies of Wesendrup and Schwarz, but no details have been provided.<sup>47</sup> In our work, because the  $\text{TaCH}_2\text{D}^+$  and  $\text{TaCD}_2^+$  products have the same mass, their cross sections cannot be measured independently. Although kinetic isotope effects can influence the energy dependence of isotopic variants of product ions, the overall shape of a cross section is primarily determined by the energetics, which differ by only zero point effects among isotopic variants of chemically identical species. Therefore, we expect that the cross section for  $\text{TaCD}_2^+$ , formed in reaction 8b, should have a roughly similar kinetic energy dependence to that of  $\text{TaCHD}^+$ , formed in reaction 8a. Likewise, the cross sections for  $\text{TaCH}_2\text{D}^+$  and  $\text{TaCHD}_2^+$ , formed in reactions 9a and 9b, should be roughly similar. Therefore, the exothermic part of this cross section, below 0.5 eV, is attributed to  $\text{TaCD}_2^+$  only, whereas contributions from both ions are anticipated above about 1.0 eV, Figure 3. Reactions 8a and 8b are exothermic because of zero point energy differences, specifically by  $-0.012$  and  $-0.051$  eV, respectively, using the B3LYP/HW+/6-311++G(3df,3p) frequencies. We find that these reaction cross sections decline approximately as  $E^{-1.0 \pm 0.1}$  and  $E^{-1.1 \pm 0.1}$ , respectively, below 0.5 eV. The rate constants for these two reactions at thermal energy (0.04 eV) are  $(4.3 \pm 0.9) \times 10^{-10}$  and  $(1.2 \pm 0.5) \times 10^{-10} \text{ cm}^3/\text{s}$ , respectively, compared to a collision (LGS) rate constant of  $10.5 \times 10^{-10} \text{ cm}^3/\text{s}$ . Thus, the combined efficiency of the observed reactions is  $52 \pm 13\%$ , which means that the return to reactants accounts for the other  $48 \pm 13\%$  of the reactivity. If dehydrogenation of a transiently formed  $\text{TaCH}_2\text{D}_2^+$  intermediate were statistically controlled, then the expected ratio of  $\text{TaCH}_2^+/\text{TaCHD}^+/\text{TaCD}_2^+$  products would be 1:4:1, whereas the observed ratio is approximately 4.2:3.6:1 at thermal energies. As the collision energy is increased, the ratio increases in favor of re-forming  $\text{TaCH}_2^+$  and  $\text{TaCD}_2^+$  formation declines compared to  $\text{TaCHD}^+$  formation.

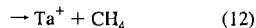
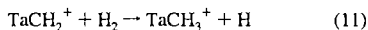
We find that reaction 10 exhibits no apparent energy barrier. The magnitude of this cross section is only about  $0.59 \pm 0.12 \text{ \AA}^2$  near thermal energies, falling to about  $0.022 \pm 0.005 \text{ \AA}^2$  by 0.4 eV. Using eq 6, we obtain a thermal rate constant of  $k = (5.9 \pm 1.5) \times 10^{-12} \text{ cm}^3/\text{s}$  for the reverse reaction of  $\text{TaCH}_2^+$

**TABLE 1: Optimized Parameters for Equation 1 for Ta<sup>+</sup> + CH<sub>4</sub> and CD<sub>4</sub> System**

reaction	$a_0$	$n$	$E_0$ (eV)	$D_0(\text{Ta}^+-\text{L})$ (eV)
Ta <sup>+</sup> + CH <sub>4</sub>	→ TaH <sup>+</sup> + CH <sub>3</sub>	10.44 ± 1.50	2.55 ± 0.14	1.93 ± 0.14
	→ TaCH <sub>3</sub> <sup>+</sup> + H	0.47 ± 0.03	2.23 ± 0.10	2.25 ± 0.10
	→ TaCH <sub>2</sub> <sup>+</sup> + H <sub>2</sub>		<0	>4.71
Ta <sup>+</sup> + CD <sub>4</sub>	→ TaCH <sup>+</sup> + H <sub>2</sub> + H	2.88 ± 0.51	3.24 ± 0.08	5.83 ± 0.08
	→ TaD <sup>+</sup> + CD <sub>3</sub>	8.41 ± 1.66	2.56 ± 0.03	2.02 ± 0.03
	→ TaCD <sub>3</sub> <sup>+</sup> + D	0.29 ± 0.11	2.31 ± 0.16	2.27 ± 0.16
	→ TaCD <sub>2</sub> <sup>+</sup> + D <sub>2</sub>		<0	>4.82
	→ TaCD <sup>+</sup> + D <sub>2</sub> + D	1.77 ± 0.56	0.9 ± 0.1	3.48 ± 0.35

+ D<sub>2</sub> → Ta<sup>+</sup> + CD<sub>2</sub>H<sub>2</sub>. This is only 0.56 ± 0.14% of the LGS collision rate. The Ta<sup>+</sup> cross section exhibits a cross section that rises near 0.6 eV and reaches a peak around 2.0 eV. Similar behavior was observed in the reaction of PtCH<sub>2</sub><sup>+</sup> with D<sub>2</sub>, where again formation of Pt<sup>+</sup> exhibits both exothermic and endothermic features.<sup>34</sup> In contrast, production of W<sup>+</sup> in the reaction of WCH<sub>2</sub><sup>+</sup> with D<sub>2</sub> exhibits only an exothermic feature.<sup>9</sup> Because of the complexity of the isotope exchange process, discussed further below, the origins of the endothermic feature are unclear; however, one intriguing possibility in this system is the formation of an excited electronic state of Ta<sup>+</sup>, discussed further below.

**3.4. Reaction of TaCH<sub>2</sub><sup>+</sup> with H<sub>2</sub>.** Figure 3 also shows cross sections for reaction of TaCH<sub>2</sub><sup>+</sup> with H<sub>2</sub>, which yields two product ions formed in reactions 11 and 12.



The cross section for reaction 11 has an energy dependence similar to that for reaction 9b and a magnitude similar to the second feature in the TaCD<sub>2</sub><sup>+</sup>/TaCH<sub>2</sub>D<sup>+</sup> cross section. This is further confirmation that this cross section is indeed a composite of both product ions. As for reaction 10, we find that reaction 12 exhibits no apparent energy barrier. The magnitude of this cross section is only 0.13 ± 0.03 Å<sup>2</sup> near thermal energies, falling to about 0.018 ± 0.007 Å<sup>2</sup> by 0.4 eV. Using eq 6, we obtain a thermal rate constant of (2.7 ± 0.5) × 10<sup>-12</sup> cm<sup>3</sup>/s for the reverse reaction of TaCH<sub>2</sub><sup>+</sup> + H<sub>2</sub> → Ta<sup>+</sup> + CH<sub>4</sub>. This is only 0.18 ± 0.04% of the LGS collision rate.

#### 4. Thermochemical and Theoretical Results

The endothermic cross sections for TaH<sup>+</sup>, TaCH<sup>+</sup>, and TaCH<sub>3</sub><sup>+</sup> are analyzed using eq 1, and the optimum values of the parameters are listed in Table 1. Because the rotational, translational, and vibrational energy distributions are included in the modeling, all  $E_0$  thresholds determined by eq 1 correspond to 0 K values. The BDEs of these species are calculated from the measured thresholds using eq 13

$$D_0(\text{Ta}^+-\text{L}) = D_0(\text{R}-\text{L}) - E_0 \quad (13)$$

where the  $D_0(\text{R}-\text{L})$  values can be calculated using the heats of formation summarized previously.<sup>20,34</sup> This equation assumes that there are no activation barriers in excess of the endothermicity of a given reaction. This assumption is generally the case for ion-molecule reactions because of the long-range attractive forces that are present.<sup>28,43</sup>

In the following sections, each product ion is evaluated both experimentally and theoretically. A summary of the B3LYP/HW+/6-311++G(3df,3p) theoretical results for the energies of the ground and low-lying excited states of each product is given in Table 2. Table S1 provides a complete listing of this

**TABLE 2: B3LYP/HW+/6-311++G(3df,3p) Theoretical Energies of Reactants and Products<sup>a</sup>**

species	state	energy ( $E_h$ )	zero point energy ( $E_0$ ) <sup>b</sup>	$E_{\text{rel}}$ (eV) <sup>c</sup>
H	<sup>2</sup> S	-0.502257		
H <sub>2</sub>	<sup>1</sup> Σ <sub>g</sub> <sup>+</sup>	-1.180030	0.009953	
C	<sup>3</sup> P	-37.857442		
CH	<sup>2</sup> Π	-38.495898	0.006369	0.000
	<sup>4</sup> Σ <sup>-</sup>	-38.462172	0.006867	0.931
CH <sub>2</sub>	<sup>3</sup> B <sub>1</sub>	-39.167949	0.016980	
CH <sub>3</sub>	<sup>2</sup> A''	-39.857664	0.029358	
CH <sub>4</sub>	<sup>1</sup> A <sub>1</sub>	-40.536527	0.044035	
Ta <sup>+</sup>	<sup>2</sup> F	-57.362276		0.000
	<sup>3</sup> P	-57.347518		0.402
	<sup>3</sup> F	-57.339272		0.626
	<sup>1</sup> D	-57.292467		1.900
TaH <sup>+</sup>	<sup>4</sup> Σ <sup>-</sup>	-57.971161	0.004395	0.000
	<sup>4</sup> Φ	-57.967063	0.004378	0.111
	<sup>2</sup> Φ	-57.958129	0.004471	0.357
	<sup>2</sup> Σ <sup>-</sup>	-96.077404	0.012996	0.000
TaCH <sup>+</sup>	<sup>2</sup> Δ	-96.061952	0.012745	0.414
	<sup>4</sup> Φ	-96.052780	0.012177	0.648
HTaC <sup>+</sup>	<sup>2</sup> A'	-95.996759	0.008048	0.000 (2.060)
	<sup>4</sup> A''	-95.975406	0.007929	0.578
TaCH <sub>2</sub> <sup>+</sup>	<sup>3</sup> A''	-96.710327	0.020874	0.000
	<sup>3</sup> A <sub>2</sub> (TS)	-96.708765	0.020142 (132i)	0.023
	<sup>3</sup> A'	-96.709213	0.020936	0.032
HTaCH <sup>+</sup>	<sup>3</sup> A'	-96.696699	0.021301	0.382
	<sup>1</sup> A'	-96.688717	0.018668	0.000 (0.528)
TaCH <sub>3</sub> <sup>+</sup>	<sup>3</sup> A''	-96.666937	0.017858	0.571
	<sup>4</sup> A <sub>1</sub>	-97.339794	0.032209	0.000
HTaCH <sub>2</sub> <sup>+</sup>	<sup>2</sup> A''	-97.329705	0.031980	0.272
	<sup>2</sup> A	-97.325410	0.027201	0.000 (0.255)
(H <sub>2</sub> )TaCH <sup>+</sup>	<sup>4</sup> A	-97.289492	0.027057	0.973
	<sup>2</sup> A''	-97.281554	0.024500	0.000 (1.375)
	<sup>3</sup> A'	-97.278011	0.026433	0.149
(H <sub>2</sub> )TaCH <sup>+</sup>	<sup>4</sup> A''	-97.241870	0.023796	1.061
	<sup>2</sup> A'	-97.264123	0.024925	0.000 (1.861)
	<sup>4</sup> A'	-97.256173	0.026686	0.264

<sup>a</sup> All species exhibit  $s(s+1)$  values in agreement with the spin states shown (0.0 for singlet, 0.75 for doublet, 2.00 for triplet, 3.75 for quartet, 6.00 for quintet, and 8.75 for sextet) with the following exceptions: Ta<sup>+</sup> (<sup>3</sup>F), 2.83; TaCH<sub>3</sub><sup>+</sup> (<sup>2</sup>A''), 1.55. <sup>b</sup> Zero point energies scaled by 0.989. Numbers in parentheses are imaginary frequencies in cm<sup>-1</sup>. <sup>c</sup> Energy relative to the ground state species for each isomer including zero point energies scaled by 0.989. Numbers in parentheses indicate the energy relative to the lowest energy isomer.

information for all stationary states located for all species, and Table S2 summarizes the structural details of these species obtained at this level of theory. Table 3 summarizes the comparison of the experimental thermochemistry with theoretical results, both from this study at multiple levels of theory and from the literature.

**4.1. Ta<sup>+</sup>-H.** The bond energy for TaH<sup>+</sup> has been measured in our lab from the reaction of Ta<sup>+</sup> with H<sub>2</sub> and D<sub>2</sub>,<sup>48</sup> yielding a value of 2.39 ± 0.08 eV. For the methane system, using eq 13 with  $D_0(\text{H}-\text{CH}_3) = 4.48$  eV and our threshold value of 2.55 ± 0.14 eV (Table 1), we obtain a BDE for TaH<sup>+</sup> of 1.93 ± 0.14 eV, well below the previous value and outside experimental uncertainties in the combined measurements. Similarly, with

**TABLE 3: Experimental and Theoretical Bond Energies for Ta<sup>+</sup>-H and Ta<sup>+</sup>-CH<sub>x</sub> (x = 1-3)**

species	statc	exp	B3LYP		BHLYP		QCISD(T) <sup>a</sup>	literature
			HW+	SD	HW+	SD	HW+	
Ta <sup>+</sup> -H	<sup>4</sup> Σ <sup>-</sup>	2.39 ± 0.08 <sup>b</sup>	2.78	2.71	2.61	2.55	2.71	2.34 <sup>c</sup>
Ta <sup>+</sup> -CH <sub>3</sub>	<sup>4</sup> A <sub>1</sub>	2.69 ± 0.14	3.19	3.07	2.83	2.73	3.43	2.79-3.41 <sup>d</sup>
Ta <sup>+</sup> -CH <sub>2</sub>	<sup>3</sup> A''	4.81 ± 0.03	4.79	4.63	4.13	3.97	5.13	4.99 ± 0.22 <sup>e</sup> 5.18 <sup>f</sup>
Ta <sup>+</sup> -CH	<sup>1</sup> Σ <sup>+</sup>	5.82 ± 0.16	5.79	5.57	4.93	4.72	6.33	

<sup>a</sup> Geometries calculated at the B3LYP/HW+ level of theory. <sup>b</sup> Reference 51. <sup>c</sup> Reference 42. <sup>d</sup> Reference 44, see text. <sup>e</sup> Reference 5. <sup>f</sup> Reference 6.

$D_0(\text{D}-\text{CD}_3) = 4.58$  eV, a threshold of  $2.56 \pm 0.06$  eV, and a calculated zero point energy difference between TaD<sup>+</sup> and TaH<sup>+</sup> of 0.033 eV, the bond energy derived from the CD<sub>4</sub> system for TaH<sup>+</sup> is  $1.99 \pm 0.03$  eV, again outside of experimental uncertainty of the previous thermochemistry. Thus, the CH<sub>4</sub> and CD<sub>4</sub> systems behave similarly to each other but have derived bond energies too low compared to the thermodynamic results from the H<sub>2</sub> and D<sub>2</sub> systems. On average, the bond energies obtained from the methane systems are lower by  $0.43 \pm 0.09$  eV, a discrepancy that may be attributed to a competitive shift with the much more efficient and lower energy dehydrogenation reaction 4. At threshold, the dehydrogenation reaction strongly competes with reaction 2, whereas there are no competing channels in the reaction of Ta<sup>+</sup> with H<sub>2</sub> and D<sub>2</sub>. This competition can delay the onset for formation of TaH<sup>+</sup> (TaD<sup>+</sup>) in the methane systems, providing for the higher thresholds that are observed. Although the complexity of this reaction system prevents quantitative analyses of these data that include this competition, simple phase space calculations performed previously for the Re<sup>+</sup> + CH<sub>4</sub> system confirm that such a competitive shift can occur in the methane reactions with a magnitude comparable to that observed experimentally.<sup>35</sup>

Ohanessian et al.<sup>39</sup> calculated a value of 2.34 eV for  $D_0(\text{Ta}^+-\text{H})$ , in good agreement with our experimental value of  $2.39 \pm 0.08$  eV. We calculate a BDE for Ta<sup>+</sup>-H of 2.78 eV when using the B3LYP functional and HW+ ECP. A slightly lower value of 2.71 eV was obtained when using the SD ECP on Ta and at the QCISD(T)/HW+ level of theory. Holthausen et al.<sup>41</sup> have previously characterized the overbinding of the B3LYP functional for the comparable third-row transition metal ion methyl cations, which involves a single covalent metal-ligand bond. As an alternative, these authors suggest using the BHLYP functional, and indeed, we obtain lower bond energies of 2.61 (HW+) and 2.55 (SD) eV, in better agreement with our experimental results (Table 3).

The ground state for TaH<sup>+</sup> is <sup>4</sup>Σ<sup>-</sup>, resulting from a covalent bond between the H (1s) orbital and a 6s5d hybrid orbital on Ta<sup>+</sup>. In this molecule, the singly occupied nonbonding metal valence orbitals are  $\delta^2\sigma$ ,<sup>1</sup> where the  $\sigma$  orbital is the other 6s5d hybrid. At the B3LYP level of theory, we determined a bond length of 1.729 Å (HW+) and 1.742 (SD) Å for Ta<sup>+</sup>-H. This compares favorably with the 1.741 Å bond length calculated by Ohanessian et al. using a GVB level of theory.<sup>39</sup> At the BHLYP level of theory, we determined bond lengths of 1.724 Å (HW+) and 1.736 Å (SD). We also determined the excitation energies and geometries for a number of excited states (Tables S1 and S2). We have previously discussed most of these results.<sup>48</sup>

**4.2. Ta<sup>+</sup>-CH<sub>3</sub>.** The BDE of Ta<sup>+</sup>-CH<sub>3</sub> derived from the CH<sub>4</sub> system is  $2.25 \pm 0.10$  eV and the BDE of Ta<sup>+</sup>-CD<sub>3</sub> from the CD<sub>4</sub> system is  $2.27 \pm 0.16$  eV, Table 1. After correcting for zero point energy differences in these two values (0.002 eV), we obtain a weighted average value of  $2.26 \pm 0.17$  eV for the

BDE of Ta<sup>+</sup>-CH<sub>3</sub> (where the uncertainty is 2 standard deviations of the mean). However, because of the competition with the efficient dehydrogenation channel, these thresholds are probably shifted to higher energies, as they were for formation of TaH<sup>+</sup>. To obtain a more accurate BDE for TaCH<sub>3</sub><sup>+</sup>, we note that the difference in the thresholds for reactions 2 and 3 is  $0.32 \pm 0.17$  eV (and  $0.25 \pm 0.16$  eV for the perdeuterated analogue). After correcting for the zero point energy differences (0.035 eV), these values have a weighted average of  $0.30 \pm 0.12$  eV. Thus, we assign the BDE for TaCH<sub>3</sub><sup>+</sup> as being higher than that for Ta<sup>+</sup>-H by this amount, namely,  $D_0(\text{Ta}^+-\text{CH}_3) = 2.69 \pm 0.14$  eV.

Using B3LYP, BHLYP, and QCISD(T) levels of theory, Holthausen et al. have carried out a detailed theoretical examination of first- and third-row transition metal methyl cations.<sup>41</sup> For these three methods, bond energies for Ta<sup>+</sup>-CH<sub>3</sub> were calculated to be 3.41, 3.01, and 2.97 eV, respectively. An empirical correction of -0.22 and +0.16 eV was made for the BHLYP and QCISD(T) methods, leading to final suggested bond energies of 2.79 and 3.13 eV, with estimated errors of  $\pm 0.22$  eV. These adjusted values were based on results for first-row metal methyl cations as compared to experiment. The adjusted BHLYP value is in reasonable agreement with our experimental value of  $2.69 \pm 0.14$  eV.

For our B3LYP theoretical calculations, we calculated  $D_0(\text{Ta}^+-\text{CH}_3) = 3.19$  eV, which is comparable with the B3LYP value obtained by Holthausen et al.<sup>41</sup> Using the SD ECP, our predicted bond energy drops by only 0.12 eV. With the BHLYP functional, however, there is a more substantial drop in bond energy to 2.83 (HW+) and 2.73 (SD) eV. The QCISD(T) calculations give us our highest predicted value, 3.43 eV. The BHLYP method is closest to experiment, Table 3, as also seen for the TaH<sup>+</sup> species.

The ground state of TaCH<sub>3</sub><sup>+</sup> was found to be <sup>4</sup>A<sub>1</sub> with C<sub>3v</sub> symmetry. The Ta-C and C-H bond lengths, and TaCH bond angle (2.057 Å, 1.098 Å, and 108.8°, B3LYP) are similar to those calculated by Holthausen et al. (2.039 Å, 1.104 Å, and 109.4°, B3LYP).<sup>41</sup> The first excited state, <sup>2</sup>A'', is found lying 0.27 eV higher in energy (Table 2), and distorts from C<sub>3v</sub> symmetry by bending one H atom toward the Ta ( $\angle\text{TaCH} = 105.4^\circ$ ). <sup>4</sup>A' and <sup>2</sup>A' states lie 0.35 and 0.49 eV, respectively, above the ground state and are also distorted from C<sub>3v</sub> symmetry, Table S2. <sup>6</sup>E and <sup>4</sup>E states, both having C<sub>3v</sub> symmetry, were found at 2.42 and 3.35 eV, respectively.

The <sup>4</sup>A<sub>1</sub> ground state of TaCH<sub>3</sub><sup>+</sup> has a valence electronic configuration of  $(1a_{1g})^2(2a_1)^1(1e)$ ,<sup>2</sup> where the  $1a_{1g}$  is the Ta-C  $\sigma$  bonding orbital, the  $2a_1$  orbital is a nonbonding 6s5d hybrid orbital on Ta, the  $1e$  and  $2e$  orbitals are the 5d ( $\delta$ - and  $\pi$ -like, respectively) nonbonding orbitals on Ta. The low-lying <sup>2</sup>A'', <sup>4</sup>A', <sup>2</sup>A', <sup>6</sup>E, and <sup>4</sup>E excited states have valence electronic configurations of  $(1a_{1g})^2(2a_1)^2(1e)$ ,<sup>1</sup>  $(1a_{1g})^2(2a_1)^1(1e)^1(2e)$ ,<sup>1</sup>  $(1a_{1g})^2(2a_1)^1(1e)^1(2e)$ ,<sup>1</sup>  $(1a_{1g})^1(2a_1)^1(1e)^2(2e)$ ,<sup>1</sup> and  $(1a_{1g})^1(2a_1)^1(1e)^2(2e)$ ,<sup>1</sup>

Activation of Methane by Ta<sup>+</sup>

(2e),<sup>1</sup> respectively, where the C<sub>3v</sub> symmetry designations are used in all cases.

We also investigated a number of alternate isomers of the TaCH<sub>3</sub><sup>+</sup> molecule. The isomer having the lowest energy, 0.255 eV above TaCH<sub>3</sub><sup>+</sup> (<sup>4</sup>A<sub>1</sub>), is HTaCH<sub>2</sub><sup>+</sup>, having a <sup>2</sup>A ground state. The H-Ta and Ta-C bond lengths and HTaC bond angle are 1.725 Å, 1.833 Å, and 93.8°, respectively, indicating that the Ta-H bond is a covalent single bond and the Ta-C bond is a covalent double bond. The bond angle suggests that the σ bonds utilize separate 6s5d hybridized orbitals on Ta<sup>+</sup>. The (H)<sub>2</sub>TaCH<sup>+</sup> isomer was also located, 1.375 eV above TaCH<sub>3</sub><sup>+</sup> (<sup>4</sup>A<sub>1</sub>). The <sup>2</sup>A'' ground state of this isomer has Ta-H bond lengths of 1.729 Å, suggesting covalent single bonds, and a Ta-C bond length of 1.853 Å, slightly longer than that of TaCH<sub>2</sub><sup>+</sup> and much longer than that in TaCH<sup>+</sup>. Finally, there is also the (H<sub>2</sub>)TaCH<sup>+</sup> isomer, which has a <sup>2</sup>A' ground state, with a short Ta-C bond, 1.762 Å, comparable to that of TaCH<sup>+</sup> (<sup>2</sup>Σ<sup>+</sup>), long Ta-H bonds, 2.607 Å, and a short H-H bond, 0.752 Å. This geometry is consistent with a weakly bound dihydrogen molecule bound to ground state TaCH<sup>+</sup>. Excited states of each of these isomers were also characterized, Tables S1 and S2.

**4.3. Ta<sup>+</sup>-CH<sub>2</sub>.** Reaction 4 and its deuterated analogue are exothermic. This indicates that D<sub>0</sub>(Ta<sup>+</sup>-CH<sub>2</sub>) > 4.71 eV and D<sub>0</sub>(Ta<sup>+</sup>-CD<sub>2</sub>) > 4.82 eV, as previously concluded by Irikura and Beauchamp.<sup>1</sup> There is no obvious threshold for formation of Ta<sup>+</sup> in the reaction TaCH<sub>2</sub><sup>+</sup> + H<sub>2</sub> → Ta<sup>+</sup> + CH<sub>4</sub>, Figure 3. As this process is the reverse of the dehydrogenation reaction Ta<sup>+</sup> + CH<sub>4</sub> → TaCH<sub>2</sub><sup>+</sup> + H<sub>2</sub>, this observation indicates that the dehydrogenation of methane by Ta<sup>+</sup> must be close to thermoneutral. From the rate constants for the forward (reaction 4) and reverse (reaction 12) reactions at the lowest kinetic energy in our experiments, we calculate an equilibrium constant *K* of 107 ± 52. From Δ*G* = -*RT* ln *K*, the free energy of the reaction is calculated to be -0.12 ± 0.02 eV at 298 K. This free energy can be converted to an enthalpy of reaction at 298 K, Δ<sub>r</sub>H<sub>298</sub>, of -0.06 ± 0.02 eV by using an entropic correction of 0.06 eV as determined using molecular parameters calculated here. These parameters are also used to determine the H<sub>0</sub> - H<sub>298</sub> values for reactants and products (-0.04 eV overall), leading to an enthalpy of reaction at 0 K of -0.10 ± 0.02 eV. Combining this value with D<sub>0</sub>(CH<sub>2</sub>-H<sub>2</sub>) = 4.71 ± 0.026 eV,<sup>34,37</sup> we obtain a BDE of 4.81 ± 0.03 eV for Ta<sup>+</sup>-CH<sub>2</sub>.

Irikura and Goddard<sup>5</sup> previously calculated a <sup>3</sup>A<sub>2</sub> ground state for TaCH<sub>2</sub><sup>+</sup> because they constrained their GVB calculations to C<sub>2v</sub> symmetry. They calculated a D<sub>e</sub> of 4.47 eV, which was empirically corrected by 0.52 ± 0.22 eV, leading to their final recommended 0 K bond energy of 4.99 ± 0.22 eV, consistent with our experimental result. Sandig and Koch determined a bond energy of 5.18 eV, which they believed was too large.<sup>6</sup> These values are similar to the results of the present calculations, B3LYP/HW+(SD) and QCISD(T), which find a Ta<sup>+</sup>-CH<sub>2</sub> bond energy of 4.79 (4.63) and 5.13 eV, respectively. These various theoretical values are generally in reasonable agreement with our experimental value. The BHLYP/HW+(SD) values calculated here, 4.13 (3.97) eV, are much too low.

Both Irikura and Goddard<sup>5</sup> and Sandig and Koch<sup>6</sup> found a <sup>3</sup>A<sub>2</sub> ground state for TaCH<sub>2</sub><sup>+</sup>. In contrast, we find a <sup>3</sup>A'' ground state in which the molecule distorts from C<sub>2v</sub> symmetry by bending in the plane of the molecule such that one C-H bond interacts with the metal ion, in essence, an agostic interaction that allows the CH<sub>2</sub>(1b<sub>1</sub>) doubly occupied orbital to donate into the empty Ta(5d<sub>z<sup>2</sup>) orbital. Our B3LYP calculations find that the <sup>3</sup>A<sub>2</sub> state having C<sub>2v</sub> symmetry lies only 0.023 eV after ZPE corrections (0.043 eV before) higher in energy than the <sup>3</sup>A''</sub>

ground state but has an imaginary frequency of 132 cm<sup>-1</sup> that converts it to the <sup>3</sup>A'' state. This difference in theoretical results could be a subtle reflection of the difference in basis set size. Because the geometries are determined here using a basis set having diffuse functions and extensive polarization functions on H, the present calculations may be able to better characterize the relative energies of the agostic interaction. Because of the distortion, our ground-state geometry of r(Ta-C) = 1.838 Å, r(C-H) = 1.082 and 1.138 Å, and ∠TaCH = 161.3° and 84.8° (Table S2) does not compare well to those calculated by Irikura and Goddard<sup>5</sup> or Sandig and Koch.<sup>6</sup> However, for the <sup>3</sup>A<sub>2</sub> state, the present calculations obtain a geometry that has r(Ta-C) = 1.877 Å, r(C-H) = 1.093 Å, and ∠TaCH = 122.5° compared to values of 1.951 Å, 1.085 Å, and 122.4°, respectively, from Irikura and Goddard and 1.877 Å, 1.101 Å, and 123.6°, respectively, from Sandig and Koch.

The first six excited states, <sup>3</sup>A', <sup>1</sup>A', <sup>1</sup>A'', <sup>1</sup>A', and <sup>5</sup>B<sub>2</sub>, lie 0.03, 0.38, 0.57, 0.58, and 0.98 eV higher in energy, respectively. These values are comparable to those found by Irikura and Goddard who located <sup>3</sup>A<sub>1</sub> (the same as our <sup>3</sup>A') and <sup>3</sup>A<sub>2</sub> (comparable to our <sup>5</sup>B<sub>2</sub>) states at 0.10 and 1.29 eV, respectively, whereas Sandig and Koch found a <sup>1</sup>A' state with an excitation energy of 0.49 eV. Our B3LYP calculations find that a <sup>1</sup>A<sub>1</sub> state having C<sub>2v</sub> symmetry was found to lie 0.14 eV higher in energy than the lower <sup>1</sup>A' state but has an imaginary frequency (in-plane CH<sub>2</sub> wag) of 260 cm<sup>-1</sup> that converts it to the <sup>1</sup>A' state. Our calculations also locate a number of other higher lying excited states as detailed in Tables S1 and S2.

The <sup>3</sup>A'' ground state of TaCH<sub>2</sub><sup>+</sup> has a valence electronic configuration (using the analogous C<sub>2v</sub> symmetry designations) of (1a<sub>1b</sub>)<sup>2</sup>(1b<sub>1b</sub>)<sup>2</sup>(2a<sub>1</sub>)<sup>1</sup>(1a<sub>2</sub>),<sup>1</sup> where the 1a<sub>1b</sub> and 1b<sub>1b</sub> orbitals are the Ta-C σ and π bonding orbitals, the 1a<sub>2</sub> is a 5d nonbonding orbital on Ta, and the 2a<sub>1</sub> orbital is a nonbonding 6s5d hybrid orbital on Ta. Thus there is a covalent double bond between Ta<sup>+</sup> and CH<sub>2</sub>. The low-lying <sup>3</sup>A', <sup>1</sup>A', <sup>1</sup>A'', <sup>1</sup>A', and <sup>5</sup>B<sub>2</sub> excited states have valence electronic configurations of (1a<sub>1b</sub>)<sup>2</sup>(1b<sub>1b</sub>)<sup>2</sup>(2a<sub>1</sub>)<sup>1</sup>(3a<sub>1</sub>),<sup>1</sup> (1a<sub>1b</sub>)<sup>2</sup>(1b<sub>1b</sub>)<sup>2</sup>(2a<sub>1</sub>)<sup>2</sup> (1a<sub>1b</sub>)<sup>2</sup>(1b<sub>1b</sub>)<sup>2</sup>(2a<sub>1</sub>)<sup>1</sup>(1a<sub>2</sub>),<sup>1</sup> (1a<sub>1b</sub>)<sup>2</sup>(1b<sub>1b</sub>)<sup>2</sup>(2a<sub>1</sub>)<sup>1</sup>(3a<sub>1</sub>),<sup>1</sup> and (1a<sub>1b</sub>)<sup>2</sup>(1b<sub>1b</sub>)<sup>1</sup>(2a<sub>1</sub>)<sup>1</sup>(1a<sub>2</sub>)<sup>1</sup>(3a<sub>1</sub>),<sup>1</sup> respectively, where the 3a<sub>1</sub> orbital is a 5d nonbonding orbital (essentially 5d<sub>x<sup>2</sup>-y<sup>2</sup>) on Ta.</sub>

It was verified that the TaCH<sub>2</sub><sup>+</sup> isomer was the lowest energy arrangement of atoms. The HTaCH<sup>+</sup> isomer lies 0.528 eV higher in energy and has a <sup>1</sup>A' ground state. The TaCH part of this molecule is similar to TaCH<sup>+</sup> (<sup>2</sup>Σ<sup>+</sup>). It has a short Ta-H bond with a HTaC bond angle of 91.5°, indicating that the hydrogen atom has covalently bound to the 2σ orbital of TaCH<sup>+</sup> (<sup>2</sup>Σ<sup>+</sup>).

**4.4. Ta<sup>+</sup>-CH.** Cross sections from the perprotio methane and perdeuterated methane experiments provide thresholds of 3.24 ± 0.08 and 3.48 ± 0.35 eV for formation of TaCH<sup>+</sup> and TaCD<sup>+</sup>, respectively. These thresholds correspond to BDEs for Ta<sup>+</sup>-CH of 5.83 ± 0.08 eV and for Ta<sup>+</sup>-CD of 5.77 ± 0.35 eV (Table 1). After correcting for zero-point energy effects (0.072 eV), we calculate a weighted mean of these two values of 5.82 ± 0.16 eV, where the uncertainty is 2 standard deviations of the mean. This value is deemed a lower limit to the true thermodynamic value, because of the possibility of competition with other channels.

Our present calculations, B3LYP/HW+(SD) and QCISD(T), find Ta<sup>+</sup>-CH bond energies of 5.79 (5.57) and 6.33 eV, respectively. These various theoretical values are in reasonable agreement with our experimental value. The BHLYP/HW+(SD) values calculated here, 4.93 (4.72) eV, are much too low.

The ground state of TaCH<sup>+</sup> is calculated to be a <sup>2</sup>Σ<sup>+</sup>, in which a Ta<sup>+</sup>≡C triple bond is formed. The valence electron orbital

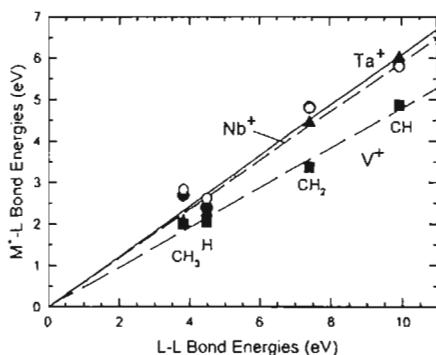


Figure 4. Correlation of Ta<sup>+</sup>-L bond energies with those for the organic analogues, L-L. Ta<sup>+</sup>-L values are from Table 3 and include both experiment (closed circles) and theory (open circles, B3LYP/HW+6-311++G(3df,3p) for TaH<sup>+</sup> and TaCH<sub>3</sub><sup>+</sup> and B3LYP/HW+6-311++G(3df,3p) for all others). The line is a linear regression fit to the experimental data, constrained to pass through the origin to emphasize the bond-order correlations. Data for VH<sup>+</sup>, VCH<sub>2</sub><sup>+</sup>, VCH<sub>3</sub><sup>+</sup>, and VCH<sup>+</sup> (taken from ref 43) are shown by squares, and data for NbH<sup>+</sup>, NbCH<sub>3</sub><sup>+</sup>, NbCH<sub>2</sub><sup>+</sup>, and NbCH<sup>+</sup> (taken from refs 23 and 49) are shown by triangles. The dashed lines are linear regression fits to these data.

occupation of this state is  $1\sigma_b^2 1\pi_b^4 2\sigma^1$ , where the  $1\sigma_b$  and  $1\pi_b$  orbitals are the bonding orbitals and  $2\sigma$  is a nonbonding  $6s5d$  hybrid on Ta. The lowest lying excited state is  $^2\Delta$ , lying 0.41 eV higher in energy and having a  $1\sigma_b^2 1\pi_b^4 1\delta^1$  configuration. Other stable excited states include  $^4\Phi$  (0.65 eV,  $1\sigma_b^2 1\pi_b^3 2\sigma^1 1\delta^1$ ),  $^2\Pi$  (0.76 eV,  $1\sigma_b^2 1\pi_b^3 2\sigma^2$ ),  $^6\Sigma^+$  (1.75 eV,  $1\sigma_b^2 1\pi_b^2 2\sigma^1 1\delta^2$ ),  $^4\Delta$  (2.05 eV,  $1\sigma_b^2 1\pi_b^2 2\sigma^1 1\delta^1$ ),  $^4\Sigma^+$  (2.22 eV,  $1\sigma_b^2 1\pi_b^2 2\sigma^1 1\delta^2$ ), and  $^6\Delta$  (3.60 eV,  $1\sigma_b^2 1\pi_b^2 2\sigma^1 1\delta^1 3\sigma^1$ ) (Table S1), where the  $1\delta$  orbital is a nonbonding  $5d$  orbital on Ta and the  $3\sigma$  orbital is an antibonding  $\sigma$  orbital.

The alternative isomer of HTaC<sup>+</sup> was also investigated and has a  $^2A'$  ground state located 2.06 eV above the TaCH<sup>+</sup> isomer. It has short Ta-H and Ta-C bond lengths, and a bond angle of 92°. Several excited states of this species were also located (Table S1), all with longer Ta-C bond lengths (Table S2).

**4.5. Bond-Energy Bond-Order Correlation for Ta<sup>+</sup>-CH<sub>n</sub> Bonds.** One way of investigating the bond order of simple metal-ligand species is to compare with organic analogues, i.e.,  $D_0(\text{Ta}^+-\text{L})$  versus  $D_0(\text{L}-\text{L})$ . Such a plot is shown in Figure 4. From the plot, it can be seen that the correlation is quite good, which indicates that Ta<sup>+</sup>-H and Ta<sup>+</sup>-CH<sub>3</sub> are single bonds, Ta<sup>+</sup>=CH<sub>2</sub> is a double bond, and Ta<sup>+</sup>≡CH is a triple bond. (The linear regression line in Figure 4 is constrained to include the origin to emphasize the bond-order correlation of TaL<sup>+</sup> vs L<sub>2</sub> species.) Also illustrated in Figure 4 is the relatively reasonable agreement between experiment and B3LYP/HW+ theory for multiple bonded species and B3LYP/HW+ for single bonded species.

It is also interesting to compare these results to those for the first-row and second-row congeners, V<sup>+</sup> and Nb<sup>+</sup>. Bond energies for VH<sup>+</sup>, VCH<sub>2</sub><sup>+</sup>, VCH<sub>3</sub><sup>+</sup>, and VCH<sup>+</sup> are  $2.05 \pm 0.06$ ,  $4.87 \pm 0.05$ ,  $3.37 \pm 0.06$ , and  $2.00 \pm 0.07$  eV, respectively.<sup>43</sup> The analogous species for Nb have bond energies of  $2.28 \pm 0.07$ ,<sup>23</sup>  $6.02 \pm 0.20$ ,  $4.44 \pm 0.09$ , and  $2.06 \pm 0.11$  eV,<sup>49</sup> respectively. From this comparison, we find that the first-row transition metal bonded species of V<sup>+</sup> are weaker than the corresponding third-row congener, Ta<sup>+</sup>, whereas the second-row transition metal bonded species of Nb<sup>+</sup> are comparable. The most noticeable

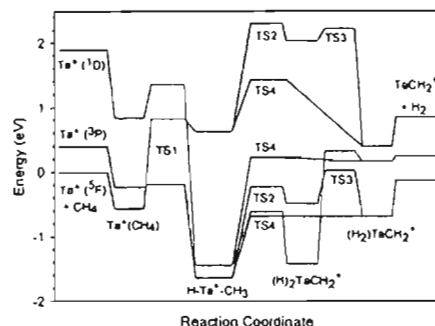


Figure 5. [Ta<sub>2</sub>C<sub>4</sub>H]<sup>+</sup> potential energy surfaces derived from theoretical results. The relative energies of all species are based on ab initio calculations. B3LYP/HW+6-311++G(3df,3p); see Table 4. The singlet surfaces are shown in green, the triplet surfaces in red, and the quintet surfaces in blue.

differences are for the multiple bonded species, MCH<sub>2</sub><sup>+</sup> and MCH<sup>+</sup>. The linear regression lines indicate that the bonds to Ta<sup>+</sup> are on average 27% greater than those to V<sup>+</sup> and only 3% greater than those to Nb<sup>+</sup>. The ground state of Ta<sup>+</sup> is  $^5F$  ( $6s^1 5d^3$ ), a configuration suitable for forming covalent bonds, having a singly occupied valence  $s$  orbital. To reach this same configuration, V<sup>+</sup> and Nb<sup>+</sup> have promotion energies from their  $^3D$  ( $d^4$ ) ground states to  $^5F$  ( $s^1 d^3$ ) excited states of 0.34 and 0.33 eV, respectively (1.08 and 0.89 eV to  $^3F$  ( $s^1 d^3$ )). In their theoretical evaluation of the periodic trends in metal hydride cations, Ohanessian, Brusich, and Goddard<sup>39</sup> find that the fraction of  $d$  character in the TaH<sup>+</sup> and NbH<sup>+</sup> molecules is identical (60%), whereas that for VH<sup>+</sup> is substantially less (40%). Ignoring exchange (which should be similar for the three group 5 ions) and promotion effects (which clearly do not have a large influence in this case), 60%  $d$  character leads to maximum bond stabilization. This helps explain why the heavier metals, Nb<sup>+</sup> and Ta<sup>+</sup>, have similar bond energies that are stronger than those of V<sup>+</sup>. Apparently, this correlation extends to the formation of stronger  $\pi$  bonds for the heavier metal ions as well.

**4.6. Potential Energy Surfaces of [Ta<sub>2</sub>C<sub>n</sub>AH]<sup>+</sup>.** The potential energy surfaces for the interaction of methane with Ta<sup>+</sup> in several spin states are shown in Figure 5. Calculations were performed at the B3LYP/HW+6-311++G(3df,3p) level of theory and include zero-point energy corrections (scaled by 0.989). For most cases under consideration, transition states were located using the synchronous transit-guided quasi-Newton method (QST3)<sup>50,51</sup> followed by geometry optimizations and frequency calculations to verify a first-order saddle point. As discussed above, the B3LYP level of theory provides adequately accurate bond energies for multiply bonded species but handles singly covalent bonds to Ta<sup>+</sup> poorly. Most species on these surfaces, however, involve multiple bonds to Ta<sup>+</sup>, such that B3LYP calculations should provide a qualitatively correct representation, if not quantitative. For our purposes, it is the qualitative characteristics that are of most interest. A summary of theoretical energies for each of the intermediates and transition states is provided in Table 4, and Table S3 lists the structures of these species.

Sandig and Koch (SK)<sup>6</sup> have conducted an extensive theoretical investigation of the potential energy surface for Ta<sup>+</sup> reacting with methane. They also used the B3LYP level of theory along with two basis sets, called BS1 (which uses the HW RECP on Ta and the D95 basis set on C and H) and BS2 (which uses an

TABLE 4: B3LYP/HW+/6-311++G(3df,3p) Theoretical Energies of [Ta<sub>2</sub>C<sub>2</sub>4H]<sup>+</sup> Intermediates and Transition States

species	state	s(s + 1) <sup>a</sup>	energy (E <sub>n</sub> )	zero point energy (E <sub>n</sub> ) <sup>b</sup>	E <sub>rel</sub> (eV) <sup>c</sup>
Ta <sup>+</sup> ( <sup>2</sup> F) + CH <sub>4</sub>	<sup>5</sup> F	6.00	-97.898803	0.044035	0.000
Ta <sup>+</sup> (CH <sub>4</sub> )	<sup>5</sup> A	6.00	-97.919881	0.044503	-0.561
	<sup>5</sup> A''	6.00	-97.915947	0.046039	-0.412
	<sup>3</sup> A	2.54*	-97.907293	0.044011	-0.232
	<sup>3</sup> A''	2.58*	-97.906682	0.045063	-0.186
	<sup>1</sup> A'	0.00	-97.868163	0.044257	0.840
	<sup>1</sup> A <sub>1</sub> (TS)	0.00	-97.868142	0.044083 (98i)	0.836
	<sup>3</sup> A''	2.00	-97.899496	0.037752 (969i)	-0.190
	<sup>5</sup> A''	6.01	-97.860919	0.036735 (327i)	0.832
	<sup>1</sup> A'	0.00	-97.844787	0.040025 (1307i)	1.361
	<sup>3</sup> A''	2.01	-97.953193	0.038285	-1.637
HTaCH <sub>3</sub> <sup>+</sup>	<sup>1</sup> A'	0.96*	-97.945916	0.038235	-1.440
	<sup>3</sup> A'	2.00	-97.941237	0.038142	-1.315
	<sup>1</sup> A'	0.91*	-97.936859	0.038227	-1.194
	<sup>5</sup> A''	6.00	-97.867709	0.036134	0.631
	<sup>1</sup> A'	0.00	-97.912036	0.034694 (492i)	-0.614
TS1	<sup>3</sup> A	2.01	-97.896139	0.033037 (863i)	-0.227
	<sup>5</sup> A''	6.01	-97.799819	0.029587 (862i)	2.300
	<sup>1</sup> A	0.00	-97.942135	0.035176	-1.420
(H) <sub>2</sub> TaCH <sub>2</sub> <sup>+</sup>	<sup>3</sup> A'	2.00	-97.906703	0.033986	-0.488
	<sup>1</sup> A''	1.01*	-97.903993	0.034166	-0.410
	<sup>5</sup> A <sub>2</sub>	6.01	-97.810395	0.030497	2.037
	<sup>1</sup> A <sub>2</sub>	1.00*	-97.811754	0.034233	2.102
	<sup>5</sup> A''	6.01	-97.801361	0.029958	2.268
	<sup>3</sup> A''	3.01	-97.796359	0.030896	2.430
	<sup>1</sup> A <sub>1</sub>	0.00	-97.799278	0.033988	2.435
	<sup>3</sup> A (est) <sup>d</sup>	2.00	-97.887888	0.032129 (1152i)	0.027
	<sup>1</sup> A	0.00	-97.877687	0.035023 (3995i)	0.329
	<sup>5</sup> A'	6.01	-97.801346	0.028308 (145i)	2.224
TS2	<sup>3</sup> A''	2.01	-97.915392	0.035429 (758i)	-0.686
	<sup>1</sup> A'	0.00	-97.882188	0.035609 (820i)	0.223
(H) <sub>2</sub> TaCH <sub>2</sub> <sup>+</sup>	<sup>5</sup> A	6.01	-97.836446	0.034271 (869i)	1.431
	<sup>3</sup> A''	2.01	-97.916933	0.036871	-0.688
	<sup>1</sup> A	0.00	-97.885674	0.037080	0.168
TS3	<sup>5</sup> A'	6.00	-97.875664	0.035646	0.401
	<sup>5</sup> A'	6.00	-97.866151	0.035534	0.657

<sup>a</sup> Values indicating spin contamination are marked with an asterisk. <sup>b</sup> Zero point energies scaled by 0.989. Imaginary frequencies (cm<sup>-1</sup>) in parentheses. <sup>c</sup> Energy relative to the ground state reactants including zero point energies scaled by 0.989. <sup>d</sup> Estimated values. See text.

expanded valence basis on Ta and the 6-31G\*\* basis set on C and H). Thus, their BS2 has a more flexible basis set on Ta than is used here but smaller basis sets on C and H. Their investigation includes geometries and structures of transition states for the lowest energy pathway as well as relative energies but did not explore the full potential energy surface for all spin states, quintet, triplet, and singlet. In our work, we examine all such species on all feasible spin states and, ultimately, find an alternative, lower energy pathway for reaction. Our results are compared to their BS2 results throughout the discussion below. As noted by SK, several species have structures slightly distorted from those of higher symmetry.

**4.7. Quintet Surface.** The interaction of Ta<sup>+</sup> (<sup>2</sup>F) with methane leads initially to the formation of a Ta<sup>+</sup>(CH<sub>4</sub>) adduct, Figure 5. The methane molecule binds with C<sub>1</sub> symmetry and is in a <sup>5</sup>A state. The Ta<sup>+</sup>(CH<sub>4</sub>) intermediate, shown in Figure 6, is calculated to lie 0.56 eV below the reactant asymptote, in good agreement with the 0.58 eV value found by SK for their <sup>5</sup>A'' state (the only species they characterized on the quintet surface). We also found a <sup>5</sup>A'' state having C<sub>s</sub> symmetry, lying only 0.15 eV higher in energy than the distorted <sup>5</sup>A ground state. Both species were characterized by all positive vibrational frequencies. These states are distinguished by the orbital populations: (sd<sub>z</sub>)<sup>2</sup>(d<sub>xy</sub>)<sup>2</sup>(d<sub>x<sup>2</sup>-y<sup>2</sup>)<sup>2</sup>(d<sub>xy</sub>)<sup>1</sup> for <sup>5</sup>A vs (sd<sub>z</sub>)<sup>2</sup>(d<sub>xy</sub>)<sup>2</sup>(d<sub>x<sup>2</sup>-y<sup>2</sup>)<sup>2</sup>(d<sub>xy</sub>)<sup>1</sup> for <sup>5</sup>A'' where the z-axis lies along the Ta-C bond and the xz plane is defined by the hydrogens closest to Ta. Our structures differ from that of SK in that we find much shorter Ta-C bonds, 2.626 (<sup>5</sup>A) or 2.478 (<sup>5</sup>A'') vs 3.199 Å.</sub></sub>

As the Ta-H bond distance reduces further, the system passes over a transition state, <sup>5</sup>TS1, leading to the H-Ta<sup>+</sup>-CH<sub>3</sub> insertion intermediate. This transition state has C<sub>s</sub> symmetry (<sup>5</sup>A''), a H-Ta-C bond angle of 82.1° (Figure 6), and an imaginary frequency of 327 cm<sup>-1</sup>. This frequency corresponds primarily to motion of the transferring H atom along with a rocking motion of the methyl group as it moves from pointing toward the H atom to Ta. On the quintet surface, the HTaCH<sub>3</sub><sup>+</sup> intermediate retains its <sup>5</sup>A'' symmetry with a H-Ta-C bond angle of 156.2°. The Ta-H bond distance is 1.805 Å, as compared to that of ground state TaH<sup>+</sup> (<sup>4</sup>Σ<sup>-</sup>), 1.729 Å. The Ta-C bond distance is 2.318 Å, as compared to the Ta-C bond distance in ground state TaCH<sub>3</sub><sup>+</sup> (<sup>4</sup>A<sub>1</sub>) of 2.057 Å. This observation indicates that the methyl group is loosely bound to the TaH<sup>+</sup> molecule in this intermediate, a consequence of the high-spin coupling between TaH<sup>+</sup> (<sup>4</sup>Σ<sup>-</sup>) and CH<sub>3</sub> (<sup>2</sup>A''). As a result, the HTa<sup>+</sup>-CH<sub>3</sub> bond energy is calculated to be only 0.99 eV.

From HTaCH<sub>3</sub><sup>+</sup> (<sup>5</sup>A''), the system can follow a stepwise pathway involving sequential H atom transfer to form a (H)<sub>2</sub>TaCH<sub>2</sub><sup>+</sup> (<sup>5</sup>A<sub>2</sub>) dihydride intermediate, Figure 6. The dihydride intermediate is reached via <sup>5</sup>TS2, which lies 2.30 eV above the reactants energy and has an imaginary frequency of 862 cm<sup>-1</sup> corresponding largely to motion of the transferring hydrogen. Continuing along the quintet surface, the dihydride intermediate can reductively eliminate the H<sub>2</sub> molecule, carrying the molecule across <sup>5</sup>TS3, which lies 2.22 eV above the reactants and has an imaginary frequency of 145 cm<sup>-1</sup> in which the two

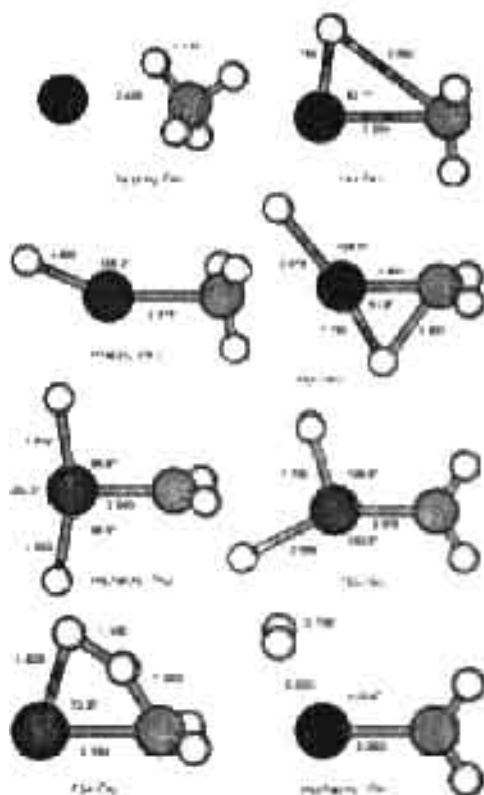


**Figure 6.** Structures of several intermediates and transition states along the reaction pathway of the  $[TaC]H^+$  system calculated at the B3LYP/6-311+G(d,p)/6-311+G(d,p) level of theory. Bond lengths are given in Å and angles in degrees.

hydrogen atoms were frozen. The  $(H_2)/[TaC]H^+$  intermediate has  $C_2$  symmetry. Figure 6 and 7 show the  $(H_2)/[TaC]H^+$  intermediate ( $H_2$  axis  $z$ - $z'$  and  $C_2$ - $C_2'$  bond distances of 2.061 (0.01) and 1.994 Å, respectively) compared to those of  $TaC_2H^+$  ( $H_2$ : 2.043 and 1.991 Å). The  $H_2$  bond distance of this intermediate is 0.796 Å, compared to 0.742 Å for free  $H_2$ . Thus, the dihydrogen molecule is loosely bound to  $TaC_2H^+$  compared with one 0.42 eV (measured in terms  $[TaC]H^+$ ,  $1.99_2 + 1.99_1$ ) kcal/mol ( $H_2$  axis  $z$ - $z'$ ) which the  $H_2$  group is rotated by 90° and also located 0.26 eV higher in energy.

Alternatively, the  $(H_2)/[TaC]H^+$  intermediate can proceed directly to the  $(H_2)/[TaC]H^+$  intermediate via a four-center transition state. This transition state has  $C_2$  symmetry in  $A'$  state (Figure 6), and it has a lower energy than the pathway involving sequential hydrogen addition (Figure 7). The imaginary frequency of 667 cm<sup>-1</sup> corresponds to the expected motion that brings the two hydrogens atoms together while breaking the  $TaC_2H$  moiety more slowly. The  $Ta-C$  bond distance is 2.164 Å between those of  $(H_2)/[TaC]H^+$  ( $A'$ ): 2.138 Å and  $(H_2)/[TaC]H^+$  ( $A'$ ): 2.081 Å.

**4.3. Triple Surface.** Reaction of methane with  $Ta^+$  ( $^3F$ ) leads directly to the formation of a  $Ta^+CH_4$  cation. The methanometalate binds with  $C_2$  symmetry in  $A'$  state (Figure 7) lying 0.63 eV below the reactant asymptote and 0.25 eV above

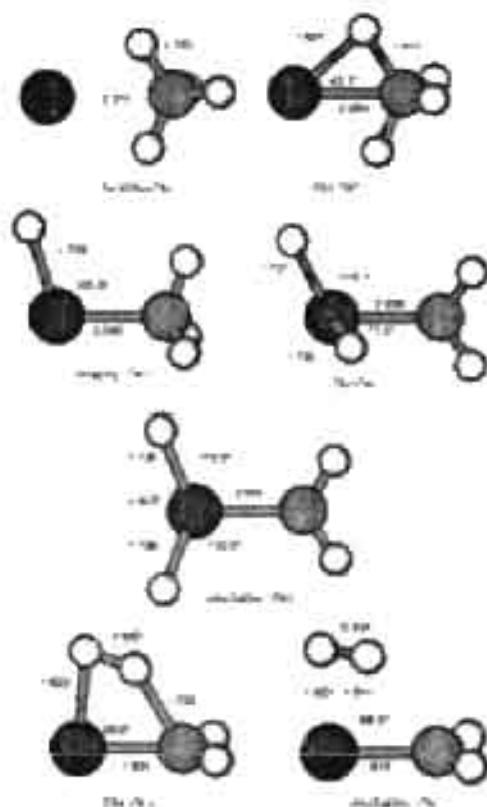


**Figure 7.** Structures of several intermediates and transition states along the reaction pathway of the  $[TaC]H^+$  system calculated at the B3LYP/6-311+G(d,p)/6-311+G(d,p) level of theory. Bond lengths are given in Å and angles in degrees.

$Ta^+CH_4$  ( $A'$ ). Comparison of ground state structures, the quadrupole-like  $0.21 \times 10^{24}$  esu of energy (calculated by the value of 0.42 eV lower obtained by SK). We also found a more symmetric  $A'$  state (ring size 0.07 eV) higher in energy than of these states which involve spin contamination. These states are distinguished by the orbital populations  $\langle d_{xy}^2 | d_{xy}^2 \rangle / \langle d_{xy}^2 | d_{xy}^2 \rangle$  for  $A'$  vs.  $\langle d_{xy}^2 | d_{xy}^2 \rangle / \langle d_{xy}^2 | d_{xy}^2 \rangle$  for  $A'$  where the latter lies along the  $Ta-C$  bond and the  $xy$  plane is defined by the hydrogen atoms by  $Ta$ .

As the  $Ta-H$  bond distance increases, the system passes over a transition state ( $TS$ ) leading to the  $(H_2)/[TaC]H^+$  methanometalate. We find the transition state lies slightly below the ground state structure, 0.018 eV, whereas SK find a slightly lower 0.017 eV. This difference may be a result of the larger basis set used in  $C$  and  $H$  here, which includes diffuse functions that may be useful in properly describing the character of such transition states. The transition state has  $C_2$  symmetry ( $A'$ ) and a  $H-Ta-C$  bond angle of 47.1° (Figure 7), indicating that it is much earlier on the potential energy surface compared to the quasi-antiperiplanar. The imaginary frequency of 969 cm<sup>-1</sup> has the same qualitative motion as the  $TS$ . The  $(H_2)/[TaC]H^+$  intermediate retains its symmetry as  $C_2$  ( $A'$ ) with a  $H-Ta-C$  bond angle of 67.0°. This is in good agreement with the  $H-Ta-C$  bond angle of 105.9° calculated by SK, who found



## Activation of Methane by Ta\*

bond lengths of  $r(\text{Ta}-\text{H}) = 1.741 \text{ \AA}$  and  $r(\text{Ta}-\text{C}) = 2.055 \text{ \AA}$ .<sup>6</sup> Our calculations find that the Ta-H bond distance in HTaCH<sub>3</sub><sup>\*</sup>, 1.729 Å, is the same as ground state TaH<sup>\*</sup> (<sup>4</sup>Σ<sup>-</sup>), and the Ta-C bond distance, 2.046 Å is also similar to the Ta-C bond distance in TaCH<sub>3</sub><sup>\*</sup> (<sup>4</sup>A<sub>1</sub>), 2.057 Å. This observation indicates that both the H atom and methyl group are covalently bound to Ta<sup>\*</sup>, consistent with a HTa<sup>\*</sup>-CH<sub>3</sub> bond energy of 3.26 eV. This triplet intermediate lies 1.64 eV below the reactant asymptote, in good agreement with SK's calculated value of 1.52 eV.<sup>6</sup> The electronic configuration of this state has the two nonbonding valence electrons on Ta in a *sd*<sub>z</sub> hybrid orbital and the *d*<sub>z</sub> orbital where the *z* axis is taken to point between the Ta-C and Ta-H bonds, with the *xz* plane defined by the plane of these bonds. We also located a <sup>3</sup>A'' version of this intermediate lying 0.32 eV higher in energy, where the key geometric difference is the HTaCH dihedral angle of 180.0° instead of 0.0° as for the <sup>3</sup>A' state. In this species, rotation of the methyl group by 60.0° costs only 0.02 eV but leads to a transition state with an imaginary torsional frequency of 87 cm<sup>-1</sup>. For the <sup>3</sup>A'' ground state, the equivalent rotation leads to a transition state only 0.10 eV higher, with the imaginary frequency being 332 cm<sup>-1</sup>. The electronic configuration of the <sup>3</sup>A' state moves the *d*<sub>z</sub> electron into a *d*<sub>xy</sub> orbital, which lies in the HTaC plane and forces the geometry change.

Continuing along the triplet surface, the (H<sub>2</sub>)TaCH<sub>2</sub><sup>\*</sup> dihydride intermediate is reached via <sup>3</sup>TS2 (Figure 5), lying 0.23 eV below ground state reactants, compared to SK's calculated value of 0.64 eV below<sup>4</sup> and 1.4 (0.88 SK) eV above the triplet HTaCH<sub>3</sub><sup>\*</sup> intermediate. The imaginary frequency of 863 cm<sup>-1</sup> corresponds to the expected motion of the transferring H atom along with motion of the existing TaH bond toward the geometry of the dihydride intermediate. The triplet dihydride methylene intermediate lies 0.49 (0.67 SK) eV below ground state reactants and has equal Ta-H bond distances of 1.736 Å and a Ta-C bond length of 2.045 Å, consistent with single covalent bonds to both H's and to CH<sub>2</sub>. A <sup>3</sup>A'' version of this intermediate in which the CH<sub>2</sub> group has rotated 90° and the HTaH bond angle has increased was also located.

The dihydride methylene intermediate converts to the (H<sub>2</sub>)TaCH<sub>2</sub><sup>\*</sup> intermediate via <sup>3</sup>TS3 (Figure 7), which we estimate lies 0.03 eV above the ground state reactants, as compared to SK's calculated value of 0.13 eV below the reactants. Repeated attempts to find an optimized version of <sup>3</sup>TS3 failed, generally because such calculations collapsed to the lower-lying <sup>3</sup>TS4 (see below). The energy and molecular parameters provided for <sup>3</sup>TS3 are taken from relaxed potential energy surface scans between (H<sub>2</sub>)TaCH<sub>2</sub><sup>\*</sup> and (H<sub>2</sub>)TaCH<sub>2</sub><sup>\*</sup> and correspond to a structure having a single imaginary frequency (1152 cm<sup>-1</sup>) of the anticipated motion. The (H<sub>2</sub>)TaCH<sub>2</sub><sup>\*</sup> intermediate has C<sub>v</sub> symmetry (<sup>3</sup>A'') with a H<sub>2</sub> bond distance of 0.834 (0.750 SK) Å compared to that of free H<sub>2</sub>, 0.742 Å. This is consistent with the dihydrogen molecule being weakly bound as it requires only 0.56 eV to form TaCH<sub>2</sub><sup>\*</sup> (<sup>3</sup>A'') + H<sub>2</sub>, the ground state products. The Ta-C and C-H bond distances are 1.910 and 1.093 Å (2) and the TaCH bond angle is 122.8°, compared to those from SK of 1.83 and 1.095 Å (2), and 121.3°. This is similar to the geometry of TaCH<sub>2</sub><sup>\*</sup> (<sup>2</sup>A<sub>1</sub>) where  $r(\text{Ta}-\text{C}) = 1.877 \text{ \AA}$ ,  $r(\text{C}-\text{H}) = 1.093 \text{ \AA}$  (2), and  $\angle\text{TaCH} = 122.5^\circ$ . Note that the longer TaC bond in the (H<sub>2</sub>)TaCH<sub>2</sub><sup>\*</sup> intermediate suggests that there is a considerable interaction between the H<sub>2</sub> and the π bond of TaCH<sub>2</sub><sup>\*</sup>. Indeed, this interaction is sufficient to induce the TaCH<sub>2</sub><sup>\*</sup> moiety in this intermediate to be symmetric, in contrast to the distorted

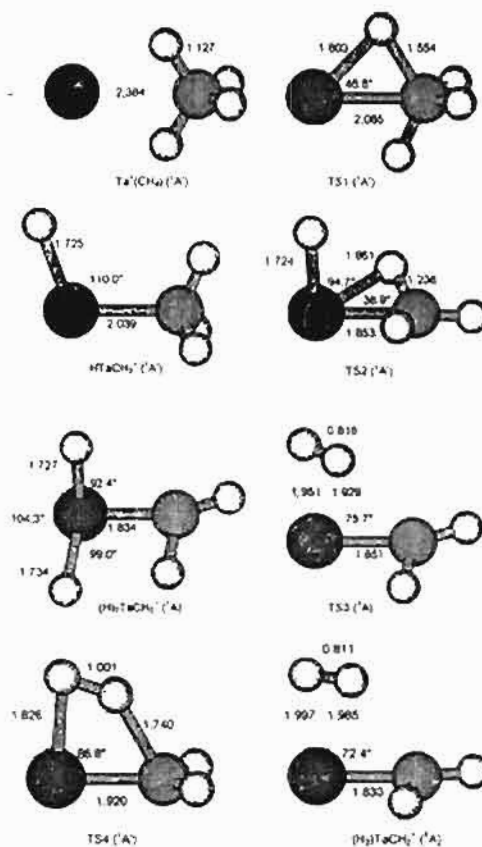


Figure 8. Structures of several intermediates and transition states along the singlet surface of the [Ta,C4H]<sup>\*</sup> system calculated at the B3LYP/HW+6-311++G(3df,3p) level of theory. Bond lengths are given in Å and HMOc bond angles in degrees.

geometry of TaCH<sub>2</sub><sup>\*</sup> (<sup>2</sup>A''). As noted above, this distortion requires very little energy (0.02 eV).

In a pathway not characterized by SK, we find that HTaCH<sub>3</sub><sup>\*</sup> (<sup>3</sup>A'') can proceed directly to a (H<sub>2</sub>)TaCH<sub>2</sub><sup>\*</sup> intermediate via a four-center transition state, <sup>3</sup>TS4. This transition state has C<sub>v</sub> symmetry and a <sup>3</sup>A'' state. The geometries of <sup>3</sup>TS4 and (H<sub>2</sub>)TaCH<sub>2</sub><sup>\*</sup> are quite similar, Figure 7, with a slightly longer Ta-C bond, 1.931 Å, in the former and slightly longer Ta-H bonds in the latter. This is consistent with their very similar energies, Figure 5, where <sup>3</sup>TS4 lies only 0.002 eV above the (H<sub>2</sub>)TaCH<sub>2</sub><sup>\*</sup> intermediate once zero point energies are included (0.042 eV before). Notably we find this alternate pathway to be considerably lower in energy than that involving sequential hydrogen atom transfer, which is limited by <sup>3</sup>TS3. <sup>3</sup>TS4 is lower in energy by 0.71 eV according to our estimate, and even if the energy of <sup>3</sup>TS3 found by SK is used, the difference is still 0.55 eV.

**4.9. Singlet Surface.** Reaction of methane with Ta<sup>\*</sup> (<sup>1</sup>D) leads initially to the formation of a Ta<sup>\*</sup>(CH<sub>4</sub>) adduct. The methane molecule binds with C<sub>v</sub> symmetry in a <sup>1</sup>A' state (Figure 8), lying 1.06 eV below the reactant asymptote (0.84 eV above ground state reactants). This does not agree well with SK's

calculated value for singlet  $\text{Ta}^+-\text{CH}_4$  of 0.58 eV. A more symmetric  ${}^1\text{A}'$  version of this singlet intermediate having  $\text{C}_{2v}$  symmetry was also located and has nearly the same energy and an imaginary frequency of  $98\text{ cm}^{-1}$  that converts it to the  ${}^1\text{A}'$  state. As the Ta-H bond distance decreases, the system passes over  ${}^1\text{TS1}$ , leading to the  $\text{H}-\text{Ta}^+-\text{CH}_3$  insertion intermediate. This transition state has  $\text{C}_s$  symmetry ( ${}^1\text{A}'$ ) and a H-Ta-C bond angle calculated to be  $46.8^\circ$  (Figure 8). The imaginary frequency of  $1307\text{ cm}^{-1}$  has a similar motion to  $\text{TS1}$  on the quintet and triplet surfaces. On the singlet surface, the  $\text{HTaCH}_3^+$  intermediate retains the  ${}^1\text{A}'$  state and has a H-Ta-C bond angle of  $110.0^\circ$ . The Ta-H bond distance,  $1.725\text{ \AA}$ , is similar to ground state  $\text{TaH}^+$  ( ${}^4\Sigma^-$ ),  $1.729\text{ \AA}$ . The Ta-C bond distance,  $2.039\text{ \AA}$ , is also similar to the Ta-C bond distance in  $\text{TaCH}_3^+$  ( ${}^4\text{A}_1$ ),  $2.058\text{ \AA}$ . This observation indicates that both the H atom and the methyl group are covalently bound to  $\text{Ta}^+$  in this state. The  $\text{HTa}^+-\text{CH}_3$  bond energy is calculated to be  $3.07\text{ eV}$  for dissociation to ground state products,  $\text{TaH}^+$  ( ${}^4\Sigma^-$ ) +  $\text{CH}_3$  ( ${}^2\text{A}''$ ), overall a spin-forbidden process. Alternatively, following a diabatic pathway,  $\text{HTa}^+-\text{CH}_3$  can dissociate to  $\text{TaH}^+$  ( ${}^2\Phi$ ) +  $\text{CH}_3$  ( ${}^2\text{A}''$ ), a process requiring  $3.42\text{ eV}$ . The singlet  $\text{HTaCH}_3^+$  intermediate lies  $1.44\text{ eV}$  below ground state reactants, compared to SK's calculated value of  $0.73\text{ eV}$  below ( $0.79\text{ eV}$  above the triplet). This difference could be a consequence of the spin contamination found in the present results. The singlet state of  $\text{HTaCH}_3^+$  lies only  $0.20\text{ eV}$  above the ground state triplet of this intermediate, consistent with the only difference being the coupling of the two nonbonding valence electrons on tantalum. Another  ${}^1\text{A}'$  state of  $\text{HTaCH}_3^+$  having a similar geometry was located only  $0.25\text{ eV}$  higher in energy. These two  ${}^1\text{A}'$  states are distinguished by the orbitals occupied by the two nonbonding valence electrons on Ta, as two of the Ta electrons are involved in covalent bonds to H and  $\text{CH}_3$ . The lower energy state has the electrons in  $s + d_{xy}$  and  $s - d_{xy}$  hybrid orbitals where the  $z$  axis is taken to lie along the Ta-C bond and the  $xz$  plane is defined by  $\text{HTaC}$ . In the higher lying state, an electron moves to the  $d_{xz}$  orbital, and the  $sd$  hybrids combine to form a  $sd^2$  hybrid (and thus is perpendicular to the  $xz$  plane). Note that the configuration for the higher  ${}^1\text{A}'$  state is the same as that for the lower-lying  ${}^3\text{A}''$  state, the only difference being the coupling of the two nonbonding valence electrons on tantalum.

Continuing along the singlet surface, the ground  $(\text{H}_2)\text{TaCH}_2^+$  intermediate is reached via  ${}^1\text{TS2}$  (Figure 5), lying  $0.61\text{ eV}$  below ground state reactants, comparable to SK's calculated value of  $0.52\text{ eV}$ . The singlet dihydride methylene intermediate lies  $1.42$  ( $1.30$  SK)  $\text{eV}$  below the ground state reactants and has  $\text{C}_1$  symmetry, Figure 8. It has Ta-H ( $1.727$  and  $1.734\text{ \AA}$ ) and Ta-C ( $1.834\text{ \AA}$ ) bond distances that are in good agreement with the Ta-H ( $1.737$  and  $1.744\text{ \AA}$ ) and Ta-C ( $1.846\text{ \AA}$ ) bond distances determined by SK. The dihydride methylene intermediate converts to the  $(\text{H}_2)\text{TaCH}_2^+$  intermediate via  ${}^1\text{TS3}$  (Figure 8), which lies  $0.33\text{ eV}$  above the ground state reactants after zero point energies are included, compared to SK's calculated value of  $0.31\text{ eV}$  below. The  $(\text{H}_2)\text{TaCH}_2^+$  intermediate is distorted from  $\text{C}_s$  symmetry with a  $\text{H}_2$  bond distance of  $0.811\text{ \AA}$ , compared to that of free  $\text{H}_2$ ,  $0.742\text{ \AA}$ , indicating a largely electrostatic bond. Indeed, loss of  $\text{H}_2$  to form  $\text{TaCH}_2^+$  ( ${}^1\text{A}'$ ) requires only  $0.09\text{ eV}$ . The Ta-C bond distance in this intermediate of  $1.833\text{ \AA}$  is slightly longer than the  $1.807\text{ \AA}$  bond length in the  $\text{TaCH}_2^+$  ( ${}^1\text{A}'$ ) product and both have distorted geometries. We also found more symmetric versions of the  $(\text{H}_2)\text{TaCH}_2^+$  intermediate (both  ${}^1\text{A}''$  and  ${}^1\text{A}'$  states), but they were spin contaminated,  $s(s+1) = 1.0$  instead of  $0.0$ , with geometries similar to the lower lying  ${}^3\text{A}''$  state.

$\text{HTaCH}_3^+$  ( ${}^1\text{A}'$ ) can also proceed directly to the  $(\text{H}_2)\text{TaCH}_2^+$  intermediate via a four-center transition state,  ${}^1\text{TS4}$ , a pathway not explored by SK. This transition state has  $\text{C}_s$  symmetry and a  ${}^1\text{A}'$  state. (A version of  ${}^1\text{TS4}$  having  ${}^1\text{A}''$  symmetry and a lower energy by  $0.51\text{ eV}$  was also located, but it is spin contaminated and has a geometry virtually identical to the  ${}^3\text{A}''$  state.) The imaginary frequency of  $820\text{ cm}^{-1}$  brings the two hydrogen atoms together. The energy of  ${}^1\text{TS4}$  is  $0.22\text{ eV}$  above the ground state reactants and, thus, lies below  ${}^1\text{TS3}$  by  $0.11\text{ eV}$ . As noted above, SK find  ${}^1\text{TS3}$  lies much lower in energy, such that it is unclear whether the sequential hydrogen transfer process or the four-centered elimination process is the most favorable pathway for  $\text{H}_2$  elimination on the singlet surface.

## 5. Discussion

As can be seen from Figure 1, the dehydrogenation reaction 4 to form  $\text{TaCH}_2^+ + \text{H}_2$  is the only process that is observed at low energies, consistent with previous ICR studies at thermal energies.<sup>1-4</sup> The cross section for dehydrogenation of  $\text{CH}_4$  to produce  $\text{TaCH}_2^+$  continues to decrease with increasing energy, indicating an exothermic reaction having no barrier in excess of the energy of the reactants. However, the reverse reaction 12 is also observed at low energies but with a much smaller cross section, indicating that reaction 4 is only slightly exothermic. These observations lead to a bond energy for  $\text{TaCH}_2^+$  that is in reasonable agreement with theory, Table 3, which indicates that this species is formed in its  ${}^3\text{A}''$  ground state at the lowest collision energies. Thus, the dehydrogenation of  $\text{CH}_4$  ( ${}^1\text{A}_1$ ) by reaction of  $\text{Ta}^+$  ( ${}^6\text{F}$ ) is spin-forbidden. In addition, the cross section for formation of  $\text{TaCH}_2^+ + \text{H}_2$  decreases once formation of  $\text{TaH}^+ + \text{CH}_3$  begins, indicating strong competition between these processes, which implies that these reactions share a common intermediate.

**5.1. Mechanism for Dehydrogenation of  $\text{Ta}^+$  with Methane.** On the quintet surface, the energies of  ${}^5\text{TS1}$ ,  ${}^5\text{TS2}$ ,  ${}^5\text{TS3}$ , and  ${}^5\text{TS4}$  are much higher than the energy of the  $\text{Ta}^+$  ( ${}^6\text{F}$ ) +  $\text{CH}_4$  reactants, because the high spin does not allow formation of the several covalent bonds needed to stabilize these four transition states. In particular, because ground state  $\text{Ta}^+$  ( ${}^6\text{F}$ ,  $6s^15d^3$ ) has a half-filled  $s$  orbital, there is no empty frontier orbital available to accept electron density from the methane molecule. Thus,  ${}^5\text{TS1}$  is much higher in energy than its counterpart on the triplet surface. Given the experimental observation that there are no barriers to formation of  $\text{TaCH}_2^+$  ( ${}^3\text{A}''$ ), it is clear that the reaction cannot proceed on the quintet surface past  $\text{Ta}^+(\text{CH}_4)$ . Rather, the initially formed  $\text{Ta}^+(\text{CH}_4)$  ( ${}^6\text{A}$ ) adduct molecule must couple to the triplet surface near  ${}^3\text{TS1}$ . From  ${}^3\text{TS1}$ , the dihydrido tantalum methyl cation intermediate,  $\text{H}-\text{Ta}^+-\text{CH}_3$  ( ${}^3\text{A}''$ ), is reached, forming two covalent bonds to tantalum using  $6s5d$  hybrid orbitals. This intermediate is the global minimum on the potential energy surface.

Next, the  $\text{H}-\text{Ta}^+-\text{CH}_3$  intermediate can follow one of two pathways for producing the  $(\text{H}_2)\text{TaCH}_2^+$  ( ${}^3\text{A}''$ ) intermediate that easily loses dihydrogen to form the ground-state  $\text{TaCH}_2^+$  ( ${}^3\text{A}''$ ) +  $\text{H}_2$  products. The lowest energy pathway involves a four-centered transition state,  ${}^3\text{TS4}$ , which leads directly between these two intermediates. The second pathway entails the activation of a second C-H bond ( $\alpha$ -H transfer), leading to the formation of a dihydrido methylene tantalum cation intermediate,  $(\text{H}_2)\text{Ta}^+\text{CH}_2$ . This pathway can occur on the triplet surface passing over  ${}^3\text{TS2}$  to form the  ${}^3\text{A}'$  state of  $(\text{H}_2)\text{TaCH}_2^+$ , followed by reductive elimination of dihydrogen to form  $(\text{H}_2)\text{TaCH}_2^+$  ( ${}^3\text{A}''$ ) by passing over  ${}^3\text{TS3}$ . Alternatively, because  ${}^1\text{TS2}$  and the  $(\text{H}_2)\text{Ta}^+\text{CH}_2$  ( ${}^1\text{A}$ ) intermediate are lower in energy than their

Activation of Methane by Ta<sup>+</sup>

triplet analogues, the sequential hydrogen transfer process can also occur by coupling with the singlet surface between H-Ta<sup>+</sup>-CH<sub>3</sub> (<sup>3</sup>A') and <sup>1</sup>TS2. However, because <sup>1</sup>TS3 lies higher in energy than <sup>3</sup>TS3 and leads to formation of the TaCH<sub>2</sub><sup>+</sup> (<sup>1</sup>A) excited state (endothermic by 0.25 eV), this second pathway must couple back to the triplet surface before <sup>3</sup>TS3. Thus, both pathways are ultimately limited by <sup>3</sup>TS3 whether the singlet or triplet (H<sub>2</sub>Ta<sup>+</sup>CH<sub>2</sub>) intermediate is formed. The energy of <sup>3</sup>TS3 is estimated at only 0.03 eV above the reactants (and SK put it 0.13 eV below), such that this pathway is consistent with experimental observations, but <sup>3</sup>TS4 lies much lower in energy (0.69 eV below the reactants). Thus, the concerted dihydrogen elimination pathway rate appears to be the energetically more favorable pathway.

This mechanism may also provide a rationale for the observation of the endothermic feature in the cross sections for the reverse reactions 10 and 12. Given the thermochemistry for TaCH<sub>2</sub><sup>+</sup> established above, the reverse reaction 12 forming ground state Ta<sup>+</sup> (<sup>5</sup>F<sub>1</sub>) + CH<sub>4</sub> (<sup>1</sup>A<sub>1</sub>) products is endothermic by only 0.10 ± 0.04 eV, such that the thermal energy content and kinetic energy distributions of the TaCH<sub>2</sub><sup>+</sup> (<sup>3</sup>A'') + H<sub>2</sub> (<sup>1</sup>Σ<sub>g</sub><sup>+</sup>) reactants allow observation with no apparent barrier. However, the reverse reaction forming Ta<sup>+</sup> (<sup>3</sup>P<sub>3/2</sub>) + CH<sub>4</sub> is endothermic by 0.49–1.30 eV (depending on which spin-orbit level is formed), consistent with the observed onset of the endothermic feature in the Ta<sup>+</sup> cross section near 0.5 eV, Figure 3. As this process is spin-allowed, it is possible that the efficiency of this reaction is higher, thereby allowing the excited-state production to be observed.

**5.2. Mechanism for Higher Energy Products.** As the energy available increases above about 1.5 eV, Ta<sup>+</sup>-H and Ta<sup>+</sup>-CH<sub>3</sub> products are formed by simple bond cleavages of the H-Ta<sup>+</sup>-CH<sub>3</sub> intermediate. These processes, in particular formation of TaH<sup>+</sup> + CH<sub>3</sub>, deplete the population of this intermediate such that there is a commensurate decline in the cross section for the dehydrogenation process. Because formation of TaCH<sub>2</sub><sup>+</sup> + H<sub>2</sub> is preferred by about 2.4 eV (Table 1), this competition suggests that formation of TaH<sup>+</sup> must be preferred kinetically. This is consistent with a simple bond cleavage of HTa<sup>+</sup>-CH<sub>3</sub> at increased kinetic energies, whereas elimination of H<sub>2</sub> occurs via the more restricted pathway discussed above.

In the reaction of Ta<sup>+</sup> with CH<sub>4</sub> (CD<sub>4</sub>), the TaH<sup>+</sup> (TaD<sup>+</sup>) cross section is dominant at energies above 2 eV (Figure 1). This is typical behavior for the reaction of bare metal ions with hydrogen containing polyatomic molecules.<sup>7,44,52–54</sup> The observation that the TaH<sup>+</sup> + CH<sub>3</sub> (TaD<sup>+</sup> + CD<sub>3</sub>) channel dominates is partly because the TaCH<sub>3</sub><sup>+</sup> (TaCD<sub>3</sub><sup>+</sup>) products decompose further by dehydrogenation to form TaCH<sup>+</sup> (TaCD<sup>+</sup>), a process that requires only 1.46 ± 0.21 eV. However, even once this dissociation process is included, the sum of the TaCH<sub>3</sub><sup>+</sup> and TaCH<sup>+</sup> cross sections is smaller than that for TaH<sup>+</sup>, which is largely a result of angular momentum constraints.<sup>52,53–55</sup> Briefly, because the TaCH<sub>3</sub><sup>+</sup> + H (TaCD<sub>3</sub><sup>+</sup> + D) channel has a reduced mass of 1.0 (2.0) amu, much smaller than that of reactants, 14.7 (18.1) amu, it can only be formed by the reactants that come together with smaller orbital angular momenta, i.e., at small impact parameters. In contrast, the TaH<sup>+</sup> + CH<sub>3</sub> (TaD<sup>+</sup> + CD<sub>3</sub>) channel has a reduced mass of 13.9 (16.4) amu, close to that of the reactants, such that most impact parameters leading to strong interactions between the Ta<sup>+</sup> and methane can form these products and still conserve angular momentum. We further note the branching ratio of  $\sigma(\text{TaH}^+)/[\sigma(\text{TaCH}_3^+) + \sigma(\text{TaCH}^+)]$  is about 5.9 ± 0.7 around the peak of the TaCH<sup>+</sup> cross section

(about 5.5 eV), consistent with the range of 4–20 suggested as appropriate for a statistical mechanism.<sup>30,54</sup>

**5.3. Mechanism for Hydrogen Exchange.** This potential energy surface also allows an understanding of the hydrogen exchange reactions 8a and 8b observed in the reaction of TaCH<sub>2</sub><sup>+</sup> with D<sub>2</sub>. First, we note that these exchange processes dominate the reaction profile compared to forming Ta<sup>+</sup> + CH<sub>2</sub>D<sub>2</sub>, reaction 10, even though all three reactions have similar energetics.

Because the observed H/D scrambling can only proceed via an intermediate in which the hydrogen and deuterium atoms have lost their identity as belonging to D<sub>2</sub> or TaCH<sub>2</sub><sup>+</sup>, a hydrido methyl intermediate must be involved.<sup>6</sup> If the reaction of TaCH<sub>2</sub><sup>+</sup> + D<sub>2</sub> starts and remains on the triplet surface, then D-Ta<sup>+</sup>-CH<sub>2</sub>D (<sup>3</sup>A) is easily formed and can obviously eliminate HD as well as D<sub>2</sub>. This explains formation of the dominant TaCHD<sup>+</sup> + HD product channel, whereas H<sub>2</sub> loss requires a more complicated process. The lowest energy process that further scrambles the hydrogen and deuterium atoms is the following sequence, D-Ta<sup>+</sup>-CH<sub>2</sub>D (<sup>3</sup>A) → (HD)TaCHD<sup>+</sup> (<sup>3</sup>A) → H-Ta<sup>+</sup>-CHD<sub>2</sub> (<sup>3</sup>A) → (H<sub>2</sub>)TaCD<sub>2</sub><sup>+</sup> (<sup>3</sup>A'') → TaCD<sub>2</sub><sup>+</sup> (<sup>3</sup>A'') + H<sub>2</sub>. Finally, we note that this scheme can explain why the branching ratio between HD and H<sub>2</sub> loss increasingly favors HD loss as the kinetic energy is increased, Figure 3. As the available energy increases, the lifetimes of the intermediates become shorter and the extent of exchange is limited by the need for multiple access to the hydrido methyl intermediate. It is also possible that hydrogen scrambling could involve a Ta<sup>+</sup>(CH<sub>2</sub>D<sub>2</sub>) intermediate, although this species and <sup>3</sup>TS1 do lie higher in energy than the isotopic variants of (H<sub>2</sub>)TaCH<sub>2</sub><sup>+</sup> and <sup>3</sup>TS4.

Competing with these dehydrogenation processes is the slightly more energetic loss of CH<sub>2</sub>D<sub>2</sub> to yield Ta<sup>+</sup>. The low abundance of this product ion correctly reflects the relative energetics of these processes. At higher energies, the D-Ta<sup>+</sup>-CH<sub>2</sub>D and H-Ta<sup>+</sup>-CHD<sub>2</sub> intermediates can decompose to form TaCH<sub>2</sub>D<sup>+</sup> + D and TaCHD<sub>2</sub><sup>+</sup> + H, respectively. The lower abundance of the latter, Figure 3, reflects the more complicated mechanism needed to form the required precursor intermediate. Also note that these intermediates should be able to decompose to form TaD<sup>+</sup> + CH<sub>2</sub>D and TaH<sup>+</sup> + CHD<sub>2</sub>, respectively. On the basis of analogous studies involving other third row metal ions, these product ions are probably near the limits of our sensitivity in this system. Nevertheless, it is clear that the tantalum methyl cation products are now much more abundant relative to the tantalum hydride cation products, in contrast to observations for the forward reaction, Figure 1. This is because the Ta<sup>+</sup>-CH<sub>3</sub> bond is stronger than the Ta<sup>+</sup>-H bond, Table 3, and the angular momentum effects discussed above are no longer restricting because the TaCH<sub>2</sub><sup>+</sup> + D<sub>2</sub> reactants have a much smaller reduced mass.

An acceptor-donor concept can be used to understand the activation of dihydrogen by TaCH<sub>2</sub><sup>+</sup>, and this provides more insight into the dehydrogenation reaction 4 as well. On the triplet surface, the <sup>3</sup>A'' ground state of TaCH<sub>2</sub><sup>+</sup> has an electron configuration (in C<sub>2v</sub> equivalent nomenclature) of (1a<sub>1g</sub>)<sup>2</sup>(1b<sub>1g</sub>)<sup>2</sup>(2a<sub>1g</sub>)(1a<sub>2g</sub>).<sup>1</sup> The orbital most likely to accept electron density from H<sub>2</sub> is the partially occupied 2a<sub>1</sub> orbital, largely a 6s orbital on Ta with some 6s5d hybridization. Accessible orbitals that are empty include the 1b<sub>2</sub> (5d<sub>xy</sub>) and 3a<sub>1</sub> (5d<sub>z<sup>2</sup></sub>), and it seems likely that the 2a<sub>1</sub> and 3a<sub>1</sub> mix to allow more efficient acceptance of the H<sub>2</sub> electrons. The donor orbital on TaCH<sub>2</sub><sup>+</sup> that interacts with the antibonding orbital of H<sub>2</sub> is either the 1a<sub>2</sub> (5d<sub>xy</sub>) orbital or the 1b<sub>1g</sub> bonding orbital. The former leads to H<sub>2</sub> addition to

the tantalum center, thereby forming <sup>3</sup>TS3 and the dihydride intermediate, whereas the latter leads to addition across the Ta–C π bond, leading to <sup>3</sup>TS4. The double occupation of the 1b<sub>1b</sub> orbital compared to the single occupation of the 1a<sub>2</sub> orbital leads to the former being energetically more favorable, Figure 5.

## 6. Conclusion

Ground-state Ta<sup>+</sup> ions are found to be highly reactive with methane over a wide range of kinetic energies. At low energies, dehydrogenation is efficient, exothermic, and a dominant process over the product spectrum. At high energies, the dominant process is formation of TaH<sup>+</sup> + CH<sub>3</sub>. At higher energies, the TaCH<sub>3</sub><sup>+</sup> product decomposes by dehydrogenation to form TaCH<sup>+</sup>. Finally, at still higher energies the TaCH<sub>3</sub><sup>+</sup> products undergo loss of a H atom to form TaCH<sub>2</sub><sup>+</sup>.

Analyses of the kinetic energy dependences of the reaction cross sections provide the BDEs of Ta<sup>+</sup>–CH<sub>3</sub> and Ta<sup>+</sup>–CH. The BDE for Ta<sup>+</sup>–CH<sub>2</sub> is determined from a measurement of the equilibrium constant for the forward and reverse dehydrogenation reactions. The singly bonded TaH<sup>+</sup> and TaCH<sub>3</sub><sup>+</sup> species have experimental BDEs that agree well with B3LYP calculations, whereas those for the multiply bonded TaCH<sub>2</sub><sup>+</sup> and TaCH<sup>+</sup> species are reproduced using the B3LYP density functional approach. No one theoretical approach yields good agreement for all species. Comparison of these experimental bond energies with the corresponding ones for the first-row and second-row transition metals (V and Nb) shows that they are stronger, but only slightly higher than those for Nb. The accessibility of the s<sup>1</sup>d<sup>3</sup> electronic configuration and the effectiveness of sd hybridization can be used to rationalize the trends.

Theoretical calculations also provide a detailed potential energy surface for the TaCH<sub>4</sub><sup>+</sup> system. The potential energy surface shows that the reaction of Ta<sup>+</sup> (<sup>3</sup>F) with methane couples rapidly with the triplet surface via <sup>3</sup>TS1 to oxidatively add one C–H bond to the metal center, yielding a hydrido-methyl tantalum cation intermediate, H–Ta<sup>+</sup>–CH<sub>3</sub> (<sup>3</sup>A''), the global minimum on the potential energy surface. TaH<sup>+</sup> and TaCH<sub>3</sub><sup>+</sup> can be formed by simple bond cleavages from this intermediate. The activation of a second C–H bond proceeds most readily through a four-centered transition state, <sup>3</sup>TS4, which forms the electrostatic complex, (H<sub>2</sub>)TaCH<sub>2</sub><sup>+</sup> (<sup>3</sup>A''). Finally, H<sub>2</sub> is eliminated from (H<sub>2</sub>)TaCH<sub>2</sub><sup>+</sup> (<sup>3</sup>A'') to form the metal carbene complex, TaCH<sub>2</sub><sup>+</sup> (<sup>3</sup>A'') + H<sub>2</sub>. Overall, dehydrogenation of methane by Ta<sup>+</sup> requires at least one spin change as it moves down the lowest energy pathway: Ta<sup>+</sup> (<sup>3</sup>F) + CH<sub>4</sub> (<sup>1</sup>A<sub>1</sub>) → H–Ta<sup>+</sup>–CH<sub>3</sub> (<sup>3</sup>A'') → (H<sub>2</sub>)TaCH<sub>2</sub><sup>+</sup> (<sup>3</sup>A'') → TaCH<sub>2</sub><sup>+</sup> (<sup>3</sup>A'') + H<sub>2</sub> (<sup>1</sup>Σ<sub>g</sub><sup>+</sup>). The spin-forbidden character of the reaction may help explain why the dehydrogenation reaction is found to occur with relatively low efficiency 18–44 (%). This conclusion is unlike that drawn in the Re<sup>+</sup> + CH<sub>4</sub> system, where the reaction efficiency is 86 ± 10% and requires three spin changes for dehydrogenation.<sup>35</sup> The differences in the reaction efficiencies of these systems may revolve around the subtleties of the crossing seams between the surfaces of different spin.

**Acknowledgment.** This work is supported by the National Science Foundation, Grant No. CHE-0451477. A grant of computer time from the Center for High Performance Computing in University of Utah is gratefully acknowledged.

**Supporting Information Available:** A summary of the B3LYP/6-311++G(3df,3p) theoretical results for the energies of the ground and excited states of each product (Table

S1), lists of the structural details of these species obtained at this level of theory (Table S2), and structural details of all intermediates and transition states listed in Table 4 (Table S3). This material is available free of charge via the Internet at <http://pubs.acs.org>.

## References and Notes

- (1) Irikura, K. K.; Beauchamp, J. L. *J. Phys. Chem.* **1991**, *95*, 8344–8351.
- (2) Irikura, K. K.; Beauchamp, J. L. *J. Am. Chem. Soc.* **1991**, *113*, 2769–2770.
- (3) Buckner, S. W.; MacMahon, T. J.; Byrd, G. D.; Freiser, B. S. *Inorg. Chem.* **1989**, *28*, 3511–3518.
- (4) Wesendrup, R.; Schwarz, H. *Angew. Chem., Int. Ed. Engl.* **1995**, *34*, 2033–2035.
- (5) Irikura, K. K.; Goddard, III, W. A. *J. Am. Chem. Soc.* **1994**, *116*, 8733–8740.
- (6) Sandig, N.; Koch, W. *Organometallics* **1997**, *16*, 5244–5251.
- (7) Sunderlin, L. S.; Armentrout, P. B. *J. Am. Chem. Soc.* **1989**, *111*, 3845–3855.
- (8) Li, F.-X.; Armentrout, P. B. *J. Chem. Phys.* **2006**, *125*, 133114–1–13.
- (9) Armentrout, P. B.; Shin, S.; Liyanage, R. *J. Phys. Chem. A* **2006**, *110*, 1242–1260.
- (10) Parke, L. G.; Hinton, C. S.; Armentrout, P. B. *Int. J. Mass Spectrom.* **2006**, *254*, 168–182.
- (11) Loh, S. K.; Hales, D. A.; Lian, L.; Armentrout, P. B. *J. Chem. Phys.* **1989**, *90*, 5466–5485.
- (12) Teloy, E.; Gerlich, D. *Chem. Phys.* **1974**, *4*, 417–427.
- (13) Gerlich, D. *Adv. Chem. Phys.* **1992**, *82*, 1–176.
- (14) Duly, N. R. *Rev. Sci. Instrum.* **1960**, *31*, 264–267.
- (15) Ervin, K. M.; Armentrout, P. B. *J. Chem. Phys.* **1985**, *83*, 166–189.
- (16) Chantry, P. J. *J. Chem. Phys.* **1971**, *55*, 2746–2759.
- (17) Schultz, R. H.; Armentrout, P. B. *Int. J. Mass Spectrom. Ion Processes* **1991**, *107*, 29–48.
- (18) Kickel, B. L.; Armentrout, P. B. *J. Am. Chem. Soc.* **1995**, *117*, 4057–4070.
- (19) Clemmer, D. E.; Chen, Y.-M.; Khan, F. A.; Armentrout, P. B. *J. Phys. Chem.* **1994**, *98*, 6522–6529.
- (20) Haynes, C. L.; Armentrout, P. B. *Organometallics* **1994**, *13*, 3480–3490.
- (21) Kickel, B. L.; Armentrout, P. B. *J. Am. Chem. Soc.* **1995**, *117*, 764–773.
- (22) Chen, Y.-M.; Elkind, J. L.; Armentrout, P. B. *J. Phys. Chem.* **1995**, *99*, 10438–10445.
- (23) Sievers, M. R.; Chen, Y.-M.; Elkind, J. L.; Armentrout, P. B. *J. Phys. Chem.* **1996**, *100*, 54–62.
- (24) Moore, C. E. *Atomic Energy Levels*; NSRDS-NBS 35; US Government Printing Office: Washington, DC, 1971; Vol. III.
- (25) Dalleska, N. F.; Honma, K.; Sunderlin, L. S.; Armentrout, P. B. *J. Am. Chem. Soc.* **1994**, *116*, 3519–3528.
- (26) Rodgers, M. T.; Armentrout, P. B. *J. Phys. Chem. A* **1997**, *101*, 1238–1249.
- (27) Chesnavich, W. J.; Bowers, M. T. *J. Phys. Chem.* **1979**, *83*, 900–905.
- (28) Armentrout, P. B. In *Advances in Gas Phase Ion Chemistry*; Adams, N. G., Babcock, L. M., Eds.; JAI Press: Greenwich, 1992; Vol. 1, pp 83–119.
- (29) Shimanouchi, T. *Tables of Molecular Vibrational Frequencies*; NSRDS-NBS 39; US Government Printing Office: Washington, DC, 1972; p 1.
- (30) Aristov, N.; Armentrout, P. B. *J. Am. Chem. Soc.* **1986**, *108*, 1806–1819.
- (31) Becke, A. D. *J. Chem. Phys.* **1993**, *98*, 5648–5652.
- (32) Lee, C.; Yang, W.; Parr, R. G. *Phys. Rev. B* **1988**, *37*, 785–789.
- (33) Frisch, M. J.; Trucks, G. W.; Schlegel, H. B.; Scuseria, G. E.; Robb, M. A.; Cheeseman, J. R.; Montgomery, J. J., Jr.; Vreven, T.; Kudin, K. N.; Burant, J. C.; Millam, J. M.; Iyengar, S. S.; Tomasi, J.; Barone, V.; Mennucci, B.; Cossi, M.; Scalmani, G.; Rega, N.; Petersson, G. A.; Nakatsuji, H.; Hada, M.; Ehara, M.; Toyota, K.; Fukuda, R.; Hasegawa, J.; Ishida, M.; Nakajima, T.; Honda, Y.; Kitao, O.; Nakai, H.; Klene, M.; Li, X.; Knox, J. E.; Hratchian, H. P.; Cross, J. B.; Adamo, C.; Jaramillo, J.; Gomperts, R.; Stratmann, R. E.; Yazyev, O.; Austin, A. J.; Cammi, R.; Pomelli, C.; Ochterski, J. W.; Ayala, P. Y.; Morokuma, K.; Voth, G. A.; Salvador, P.; Dannenberg, J. J.; Zakrzewski, V. G.; Dapprich, S.; Daniels, A. D.; Strain, M. C.; Farkas, O.; Malick, D. K.; Rabuck, A. D.; Raghavachari, K.; Foresman, J. B.; Ortiz, J. V.; Cui, Q.; Baboul, A. G.; Clifford, S.; Cioslowski, J.; Stefanov, B. B.; Liu, G.; Liashenko, A.; Piskorz, P.; Komaromi, I.; Martin, R. L.; Fox, D. J.; Keith, T.; Al-Laham, M. A.; Peng, C. Y.; Nanayakkara, A.; Challacombe, M.; Gill, P. M. W.; Johnson,

Activation of Methane by Ta<sup>+</sup>

- B.; Chen, W.; Wong, M. W.; Gonzalez, C.; Pople, J. A. *Gaussian 03*, Revision B.02; Gaussian, Inc.: Wallingford, CT, 2003.
- (34) Zhang, X.-G.; Liyanage, R.; Armentrout, P. B. *J. Am. Chem. Soc.* **2001**, *123*, 5563–5575.
- (35) Armentrout, M. M.; Li, F.-X.; Armentrout, P. B. *J. Phys. Chem. A* **2004**, *108*, 9660–9672.
- (36) Li, F.; Zhang, X.-G.; Armentrout, P. B. *Int. J. Mass Spectrom.* **2006**, *255–256*, 279–300.
- (37) Haynes, C. L.; Chen, Y.-M.; Armentrout, P. B. *J. Phys. Chem.* **1996**, *100*, 111–119.
- (38) Hay, P. J.; Wadt, W. R. *J. Chem. Phys.* **1985**, *82*, 299–310.
- (39) Ohanessian, G.; Brusich, M. J.; Goddard, W. A., III *J. Am. Chem. Soc.* **1990**, *112*, 7179–7189.
- (40) Foresman, J. B.; Frisch, A. E. *Exploring Chemistry with Electronic Structure Methods*, 2nd ed.; Gaussian, Inc.: Pittsburgh, PA, 1996.
- (41) Holthausen, M. C.; Heinemann, C.; Cornchl, H. H.; Koch, W.; Schwartz, H. *J. Chem. Phys.* **1995**, *102*, 4931.
- (42) Holthausen, M. C.; Mohr, M.; Koch, W. *Chem. Phys. Lett.* **1995**, *240*, 245.
- (43) Armentrout, P. B.; Kickel, B. L. In *Organometallic Ion Chemistry*; Freiser, B. S., Ed.; Kluwer: Dordrecht, 1996; pp 1–45.
- (44) Armentrout, P. B. In *Topics in Organometallic Chemistry*; Brown, J. M., Hofmann, P., Eds.; Springer-Verlag: Berlin, 1999; Vol. 4, pp 1–45.
- (45) Andrae, D.; Haeussermann, U.; Dolg, M.; Stoll, H.; Preuss, H. *Theor. Chim. Acta* **1990**, *77*, 123–141.
- (46) Gioumousis, G.; Stevenson, D. P. *J. Chem. Phys.* **1958**, *29*, 294–299.
- (47) Unpublished work of Wesendrup, R.; Schwarz, H., as reported in ref 6.
- (48) Zhang, X.-G.; Ruc, C.; Shin, S.-Y.; Armentrout, P. B. *J. Chem. Phys.* **2002**, *116*, 5574–5583.
- (49) Sievers, M. R.; Chen, Y.-M.; Haynes, C. L.; Armentrout, P. B. *Int. J. Mass Spectrom.* **2000**, *195/196*, 149–170.
- (50) Peng, C. Y.; Schlegel, H. B. *Isr. J. Chem.* **1994**, *33*, 449.
- (51) Peng, C. Y.; Ayala, P. Y.; Schlegel, H. B.; Frisch, M. J. *J. Comput. Chem.* **1996**, *17*, 49.
- (52) Aristov, N.; Armentrout, P. B. *J. Phys. Chem.* **1987**, *91*, 6178.
- (53) Chen, Y.-M.; Sievers, M. R.; Armentrout, P. B. *Int. J. Mass Spectrom. Ion Processes* **1997**, *167/168*, 195–212.
- (54) Sunderlin, L. S.; Armentrout, P. B. *Int. J. Mass Spectrom. Ion Processes* **1989**, *94*, 149–177.
- (55) Chen, Y.-M.; Armentrout, P. B. *J. Phys. Chem.* **1995**, *99*, 10775–10779.

CHAPTER 5

ENERGETICS AND MECHANISMS OF C-H BOND  
ACTIVATION BY A DOUBLY CHARGED METAL  
ION: GUIDED ION BEAM AND THEORETICAL  
STUDIES OF  $TA^{2+} + CH_4$

Laura G. Parke, Christopher S. Hinton, P. B. Armentrout

Reproduced with permission from [Parke, L. G.; Hinton, C. S.; Armentrout P. B. *J. Phys. Chem. C* **2008**, *112*, 10469-10480.] Copyright [2008] American Chemical Society.

## Energetics and Mechanisms of C–H Bond Activation by a Doubly Charged Metal Ion: Guided Ion Beam and Theoretical Studies of $\text{Ta}^{2+} + \text{CH}_4$

Laura G. Parke, Chris S. Hinton, and P. B. Armentrout\*

Department of Chemistry, University of Utah, Salt Lake City, Utah 84112

Received: June 13, 2008; Revised Manuscript Received: July 29, 2008

A guided ion beam tandem mass spectrometer is used to study the kinetic-energy dependence of doubly charged atomic tantalum cations ( $\text{Ta}^{2+}$ ) reacting with  $\text{CH}_4$  and  $\text{CD}_4$ . As for the analogous singly charged system, the dehydrogenation reaction to form  $\text{TaCH}_2^{2+} + \text{H}_2$  is exothermic. The charge-transfer reaction to form  $\text{Ta}^+ + \text{CH}_4^+$  and the charge-separation reaction to form  $\text{TaH}^+ + \text{CH}_3^+$  are also observed at low energies in exothermic processes, as is a secondary reaction of  $\text{TaCH}_2^{2+}$  to form  $\text{TaCH}_3^+ + \text{CH}_3^+$ . At higher energies, other doubly charged products,  $\text{TaC}^{2+}$  and  $\text{TaCH}_3^{2+}$ , are observed, although no formation of  $\text{TaH}^{2+}$  was observed. Modeling of the endothermic cross sections provides 0 K bond dissociation energies (in electronvolts) of  $D_0(\text{Ta}^{2+}-\text{C}) = 5.42 \pm 0.19$  and  $D_0(\text{Ta}^{2+}-\text{CH}_3) = 3.40 \pm 0.16$ . These experimental bond energies are in poor agreement with density functional calculations at the B3LYP/HW+/6-311++G(3df,3p) level of theory. However, the  $\text{Ta}^{2+}-\text{C}$  bond energy is in good agreement with calculations at the QCISD(T) level of theory, and the  $\text{Ta}^{2+}-\text{CH}_3$  bond energy is in good agreement with density functional calculations at the B3LYP level of theory. Theoretical calculations reveal the geometric and electronic structures of all product ions and are used to map the potential energy surface, which describes the mechanism of the reaction and key intermediates. Both experimental and theoretical results suggest that  $\text{TaH}^+$ ,  $\text{TaCH}_2^{2+}$ , and  $\text{TaCH}_3^{2+}$  are formed through a  $\text{H}-\text{Ta}^{2+}-\text{CH}_3$  intermediate.

### 1. Introduction

Relatively few studies of the reactivity of doubly charged atomic transition metal cations have been performed, although the mass spectrometric study of multiply charged complexes has become very active during the last two decades.<sup>1–4</sup> The dearth of atomic metal dication reactivity studies is partly a consequence of the difficulty in generating doubly charged atomic ions relative to singly charged ions. Further, it was generally believed that multiply ionized ions would undergo charge transfer reactions exclusively. Tonkyn and Weisshaar<sup>5</sup> were the first to report that the early transition metal  $\text{Ti}^{2+}$  undergoes a clustering reaction with methane at thermal energies, hydride transfer with ethane, and a simple charge transfer reaction with propane. This observation encouraged Freiser and co-workers to look at the behavior of other doubly charged early transition metals, using Fourier transform ion cyclotron resonance (FTICR) mass spectrometry. For  $\text{Nb}^{2+}$ , Freiser and co-workers found dehydrogenation to be the predominant pathways in the reaction with methane and ethane, whereas propane and butane reacted by charge transfer.<sup>6,7</sup> For  $\text{Zr}^{2+}$ , dehydrogenation of methane was again found to be the predominant pathway, with a small percentage (4%) of the hydride abstraction product,  $\text{ZrH}^+$ , and no charge transfer products,  $\text{Zr}^+ + \text{CH}_4^+$ .<sup>8</sup>  $\text{Zr}^{2+}$  undergoes dehydrogenation and demethanation reactions and hydride abstraction with ethane and propane. Propane also exhibits methide abstraction as well as charge transfer, which becomes the predominant reaction pathway with butane. For  $\text{Ta}^{2+}$  reacting with methane, dehydrogenation is the major pathway, but formation of the hydride abstraction product,  $\text{TaH}^+ + \text{CH}_3^+$ , along with charge transfer,  $\text{Ta}^+ + \text{CH}_4^+$  is also observed.<sup>8</sup> Freiser and co-workers report

that reactions of  $\text{Ta}^{2+}$  with longer chain alkanes result in exclusive charge transfer. In contrast,  $\text{La}^{2+}$  is unreactive with methane and ethane, but propane and butane yield dehydrogenation and alkane loss, as well as charge-separation reaction products in the case of butane.<sup>9</sup>

In the present study, we reexamine the reaction of  $\text{Ta}^{2+}$  with methane and its isotopologue,  $\text{CD}_4$ .  $\text{Ta}^{2+}$  is produced exclusively in its ground state,  $a^2F(5d^3)$ , using a dc discharge/flow tube ion source. In contrast to previous work that was limited to thermal reactions, our study is the first to examine the kinetic energy dependence of reactions of atomic multiply charged metal cations. Thus, this study provides quantitative thermochemical and mechanistic information that complements previous studies and allows an assessment of theoretical approaches for evaluating these highly charged heavy metal species. For this reason, a complete theoretical investigation of all product ions and the transition states and intermediates along the potential energy surfaces accessible are also pursued.

### 2. Experimental and Theoretical Methods

**2.1. General Procedures.** These experiments were performed using a guided ion beam tandem mass spectrometer described in detail elsewhere.<sup>10</sup> Ions are formed in a direct current discharge/flow tube (DC/FT) source described below, extracted from the source, then accelerated and passed through a magnetic sector momentum analyzer for mass analysis. Reactant ions containing the  $^{181}\text{Ta}$  isotope (99.99% natural abundance) are selected, decelerated to a desired kinetic energy, and focused into an octopole guide that radially traps the ions using radio frequency electric fields.<sup>11,12</sup> While in the octopole, the ions pass through a static gas cell that contains the neutral reaction partner at a pressure of less than  $\sim 0.3$  mTorr, to ensure that multiple ion–molecule collisions do not occur. This was verified by examining the pressure dependence of the reaction

\* Corresponding author.

cross sections. The remaining reactant and product ions are confined in the radial direction in the guide until they drift out of the gas cell and are focused into a quadrupole mass filter for mass analysis. The ions are then detected by a secondary electron scintillation ion detector, using standard pulse counting techniques. After correcting for background signals, ion intensities are converted to absolute cross sections, as described previously.<sup>13</sup> The uncertainties in absolute cross sections are estimated at  $\pm 20\%$ . The quadrupole is operated in a mode designed to optimize ion transmission to ensure accurate cross section magnitudes, such that product cross sections having adjacent masses have been corrected for mass overlap. Because the various product ions have distinct energy dependences, such corrections are unambiguous in the present case as verified by equivalent cross section determinations using both CH<sub>4</sub> and CD<sub>4</sub> reactants (see below).

The kinetic energy is varied in the laboratory frame by scanning the DC bias on the octopole rods with regard to the potential of the ion source region. The nominal potential difference between these regions ( $V_{\text{Laboratory}}$ ) is converted to the center-of-mass (CM) frame relative ion energy using the formula  $E_{\text{CM}} = 2 \times V_{\text{Laboratory}} m/(m + M)$ , where  $m$  and  $M$  are the neutral and ionic reactant masses, respectively. The kinetic energy distribution of the reactant ion and the thermal motion of the neutral reactant gas (Doppler broadening) both contribute to broaden the cross sections.<sup>14,15</sup> The octopole beam guide is used as a retarding potential analyzer, as described previously,<sup>13</sup> to determine both the absolute zero of the energy scale and the full width at half-maximum of the kinetic energy distribution of the ions. This distribution is nearly Gaussian and independent of energy. The full width at half-maximum is 0.2 – 0.6 eV (potential in the laboratory frame) in these studies (0.03–0.12 eV in the CM frame). Uncertainties in the absolute energy scale are  $\pm 0.01$  eV (CM).

**2.2. Ion Source.** Atomic Ta<sup>2+</sup> cations are formed in the DC/FT source, which utilizes a tantalum cathode held at high negative voltage (0.7–1.5 kV). A flow of approximately 90% He and 10% Ar passes over the cathode at a total pressure of 0.3–0.4 Torr and ambient temperature. Ar<sup>+</sup> ions created in the resultant discharge are accelerated toward the cathode, thereby creating Ta<sup>+</sup> and Ta<sup>2+</sup> ions. The ions then undergo  $\sim 10^5$  collisions with He and  $\sim 10^4$  collisions with Ar in the meter-long flow tube before entering into the guided ion beam apparatus. These source conditions are identical to those used previously to generate numerous singly charged transition metal cations, and it is anticipated that collisional cooling of the electronic states by the bath gases will be similar for both charge states. Previous work shows that, when compared to a surface ionization source, the DC/FT source generates Sc<sup>+</sup>,<sup>16</sup> Fe<sup>+</sup>,<sup>17</sup> Co<sup>+</sup>,<sup>18</sup> Ni<sup>+</sup>,<sup>19</sup> Ru<sup>+</sup>,<sup>20</sup> Rh<sup>+</sup>,<sup>20</sup> and Pd<sup>+</sup>,<sup>20</sup> ions with an average electronic temperature of  $700 \pm 400$  K, and Y<sup>+</sup>, Zr<sup>+</sup>, Nb<sup>+</sup>, and Mo<sup>+</sup> ions with an average electronic temperature of  $300 \pm 100$  K.<sup>21</sup> Even at an elevated electronic temperature (1100 K), a pure beam of <sup>4</sup>F ground-state Ta<sup>2+</sup> ions is produced, having a calculated distribution of 94.26% <sup>4</sup>F<sub>3/2</sub> (5d<sup>3</sup>, 0.000 eV), 5.29% <sup>4</sup>F<sub>5/2</sub> (5d<sup>3</sup>, 0.312 eV), 0.33% <sup>4</sup>F<sub>7/2</sub> (5d<sup>3</sup>, 0.602 eV), 0.07% <sup>4</sup>F<sub>3/2</sub> (6s5d<sup>2</sup>, 0.687 eV), and 0.03% <sup>4</sup>F<sub>9/2</sub> (5d<sup>3</sup>, 0.840 eV), with all other spin-orbit levels (with energies 0.891 eV and higher) having populations less than 0.01%. (All energies taken from ref 22). At 700 K, the populations are 99.14%, 0.85%, 0.01%, and <0.001%, respectively; and at 300 K, Ta<sup>2+</sup> ions are produced exclusively in their <sup>4</sup>F<sub>3/2</sub> ground state (<0.001% in

higher spin orbit states). Conservatively, the average electronic energy of the reactant Ta<sup>2+</sup> ions is estimated to be  $0.003 \pm 0.019/-0.003$  eV.

**2.3. Data Analysis.** To determine  $E_0$ , the energy threshold for product formation, the kinetic energy dependence of product cross sections is analyzed. The apparent threshold observed under laboratory conditions lies below  $E_0$  because of the Maxwell–Boltzmann velocity distribution, the internal energy of the neutral reactants, and the kinetic energy distribution of the reactant ions. Previous theoretical and experimental work has shown that endothermic cross sections can be modeled using eq 1<sup>23–25</sup>

$$\sigma(E) = \sigma_0 \sum g_i (E + E_i + E_{ei} - E_0)^n / E \quad (1)$$

where  $\sigma_0$  is an energy-independent scaling parameter,  $E$  is the relative kinetic energy of the reactants,  $E_i$  is the internal energy of the reactants,  $E_{ei}$  is the average electronic energy of the reactant ion,  $E_0$  is the reaction threshold at 0 K, and  $n$  is an adjustable parameter that determines the shape of the cross section. The summation is over all possible rovibrational states of the neutral reactant with energies  $E_i$  and relative populations  $g_i$ , where  $\sum g_i = 1$ . The various sets of vibrational frequencies and rotational constants used to determine  $E_i$  in this study are taken from the literature for CH<sub>4</sub> and CD<sub>4</sub>.<sup>26</sup> Equation 1 is convoluted over both the neutral and the ion kinetic energy distributions prior to comparison with the data. All adjustable parameters,  $E_0$ ,  $\sigma_0$ , and  $n$ , are then optimized to give the best reproduction of the data using a nonlinear least-squares analysis.<sup>24,25</sup> The average values obtained for each parameter over a range of best fits to several independent data sets are the values reported for  $E_0$ ,  $\sigma_0$ , and  $n$ . The resultant uncertainties are one standard deviation. The uncertainties reported for  $E_0$  also contain the uncertainty in the absolute energy scale ( $\pm 0.05$  eV, laboratory) and electronic energy,  $\pm 0.02$  eV.

**2.4. Theoretical Calculations.** In the present study, most quantum chemistry calculations are computed with the B3LYP hybrid density functional method<sup>27,28</sup> and performed with the Gaussian 03 suite of programs.<sup>29</sup> This level of theory was used because it provides reasonable results for analogous reactions of methane with other heavy transition metal atomic ions: Pt<sup>+</sup>,<sup>30</sup> Re<sup>+</sup>,<sup>31</sup> W<sup>+</sup>,<sup>32</sup> Ir<sup>+</sup>,<sup>33</sup> Hf<sup>+</sup>,<sup>34</sup> Au<sup>+</sup>,<sup>35</sup> and Ta<sup>+</sup>.<sup>36</sup> All thermochemistry reported here is corrected for zero-point energy effects. Because many of the transition states of interest have bridging hydrogens, the relatively large 6–311++G(3df,3p) basis set is used for carbon and hydrogen. This basis set provides bond energies for the hydrocarbon species that are comparable (within 0.08 eV) to experimental results: H–CH<sub>3</sub> (4.406 vs 4.480 eV), H<sub>2</sub>–CH<sub>2</sub> (4.666 vs 4.713 eV), H–CH (4.332 vs 4.360 eV), C–H (3.532 vs 3.465 eV), and H–H (4.505 vs 4.478 eV). (See Table 1 of ref 30 for thermochemistry used for all H, D, CH<sub>x</sub>, and CD<sub>x</sub> species.) The Los Alamos double- $\zeta$  basis set (LANL2DZ) describes the outer valence electrons and the relativistic effective core potential (ECP) of Hay–Wadt (HW)<sup>37</sup> describes the 60 core electrons of tantalum. Because this basis set is optimized for neutral atoms, whereas the charge on Ta<sup>2+</sup> differentially contracts the 6s orbitals compared to the 5d orbitals, an altered valence basis set as described by Ohanessian et al.,<sup>38</sup> denoted by HW+, is used throughout our calculations for Ta<sup>2+</sup>.

The most relevant choice for a level of theory for the first- and third-row transition metal methyl cations has been studied by Holthausen et al.<sup>39</sup> and for first-row transition metal methylene cations by Holthausen, Mohr, and Koch.<sup>40</sup> For the metal methyl complexes (constrained to C<sub>3v</sub> symmetry), these



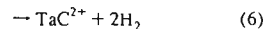
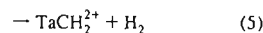
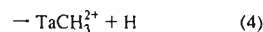
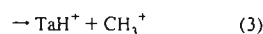
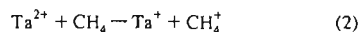
## Energetics and Mechanisms of C–H Bond Activation

authors used B3LYP and Becke-half-and-half-LYP (BHLYP) functionals and the QCISD(T) method with a basis set consisting of a polarized double- $\zeta$  basis on C and H and the Hay–Wadt relativistic ECP with valence electrons added. These authors concluded that, for the first-row  $MCH_3^+$  species ( $M = Sc-Cu$ ), where experimental results are available for all metals,<sup>41,42</sup> the B3LYP functional overbinds, with a mean absolute deviation (MAD) from experiment of 0.41 eV. In contrast, better comparison to experimental work was obtained with the BHLYP functional and the QCISD(T) method, with MADs of 0.18 and 0.20 eV, respectively. For the metal methylene cation complexes,<sup>40</sup> the B3LYP functional predicts bond energies in good agreement with experimental data, whereas the performance of the BHLYP functional predicts bond energies consistently below experimental data. On the basis of these results, the present study includes calculations for the various product ions using the BHLYP functional and the Stuttgart–Dresden (SD) ECP<sup>43</sup> for  $Ta^{2+}$ , as well as QCISD(T) calculations using the HW+ ECP. Unless otherwise noted, our theoretical results will refer to the B3LYP/HW+/6-311++G(3df,3p) level of theory.

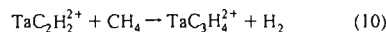
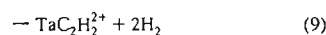
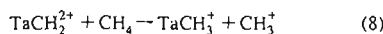
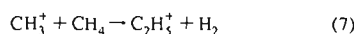
We calculated a  $4F(5d^3)$  ground state for  $Ta^{2+}$ , a  $2P(5d^3)$  excited state at 0.680 eV, and a  $4F(6s^15d^2)$  excited state at 0.895 eV, using the HW+ basis set and B3LYP level of theory. For the B3LYP/SD, BHLYP/HW+, and BHLYP/SD combinations of functional/basis set, we found excitation to the doublet state to be 0.666, 0.728, and 0.717 eV, respectively, and excitation to the quartet state to be 0.758, 0.985, and 0.911 eV, respectively, demonstrating that the atomic excitations are largely independent of the theoretical method chosen. For the QCISD(T)/HW+ level of theory, we found much lower excitation energies of 0.106 and 0.472 eV, respectively. No appreciable spin contamination was found for the different levels of theory for any of these states. The quartet-doublet excitation energies can be compared to experimental values (average of the spin-orbit levels for each state) of 0.381 eV for a  $2P(5d^3)$  excited state and 0.990 for a  $2D(5d^3)$  excited state,<sup>22</sup> such that the density functional theoretical values fall between these two values. The experimental excitation energy for the  $4F(6s^15d^2)$  state is 0.732 eV, in reasonable agreement with the theoretical values. The theoretically calculated IE of  $Ta^+$  is relatively insensitive to the level of theory used: 15.2, 15.2, 14.9, 14.8, and 14.6 eV using B3LYP/HW+, B3LYP/SD, BHLYP/HW+, BHLYP/SD, and QCISD(T)/HW+. In all cases, these values are low compared with the experimental value of  $16.2 \pm 0.5$  eV.<sup>44</sup>

## 3. Experimental Results

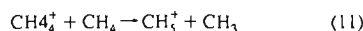
3.1. Reaction of  $Ta^{2+}$  with Methane. Reaction of  $CH_4$  with  $Ta^{2+}$  yields the primary products indicated in reactions 2–6.



In addition, several higher order products are observed as the pressure of methane is increased. These products, which are easily identified because their cross sections depend on the methane pressure, include reactions 7–10.



Reaction 8 is discussed further below and reactions 9 and 10 are explored more thoroughly in the next section. We anticipated that we should also observe the secondary reaction 11.



Because the intensity of the primary  $CH_4^+$  product is already small, the secondary  $CH_5^+$  product was not observed because it would be at least an order of magnitude smaller even at the highest methane pressures used. Reactions 7 and 11 deplete the primary  $CH_3^+$  and  $CH_4^+$  products at the lowest energies where the residence time of these products in the reaction chamber is the longest. This tends to scatter these products even further, such that collection of these secondary product ions is inefficient.

Figure 1 shows analogous results for  $Ta^{2+}$  reacting with  $CD_4$ , which provides cross sections consistent with those obtained for reaction with  $CH_4$ . This agreement verifies that the cross sections are accurately ascertained even though the mass-to-charge separation between some products is only 0.5  $m/z$  in the

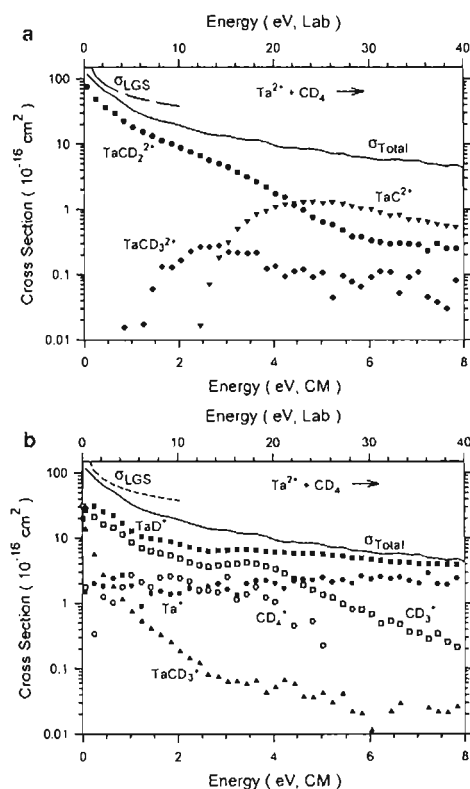


Figure 1. Cross sections for reaction of  $Ta^{2+}$  ( $4F$ ) with  $CD_4$  as a function of kinetic energy in the center-of-mass frame (lower axis) and laboratory frame (upper axis). Part a shows products retaining the 2+ charge, whereas part b shows products formed by charge transfer and charge separation. The  $TaCD_3^+$  cross section has a distinct pressure dependence, and the results shown here correspond to  $P(CD_4) = 0.4$  mTorr.

**TABLE 1: Rates ( $10^{-10} \text{ cm}^3 \text{ s}^{-1}$ ) and Reaction Efficiencies (% in Parentheses) for Reaction of  $\text{Ta}^{2+}$  with Methane**

product	this work		previous work <sup>a</sup>
	$\text{CH}_4$	$\text{CD}_4$	$\text{CH}_4$
$\text{Ta}^+$	$0.12 \pm 0.04$ (0.6 $\pm$ 0.2)	$0.17 \pm 0.03$ (1.0 $\pm$ 0.2)	$4.9 \pm 2.5$ (25 $\pm$ 13)
$\text{TaH}^+$	$3.5 \pm 0.7$ (18 $\pm$ 4)	$4.2 \pm 1.0$ (24 $\pm$ 6)	$4.5 \pm 2.3$ (23 $\pm$ 12)
$\text{CH}_3^+$	$4.9 \pm 1.8$ (25 $\pm$ 9)	$3.7 \pm 0.7$ (21 $\pm$ 4)	
$\text{TaCH}_2^{2+}$	$9.2 \pm 2.8$ (47 $\pm$ 14)	$8.0 \pm 1.6$ (45 $\pm$ 9)	$10.0 \pm 5.0$ (52 $\pm$ 27)
Total	$13.5 \pm 3.4$ (69 $\pm$ 17)	$12.1 \pm 2.4$ (69 $\pm$ 14)	$19.4 \pm 9.7$ (100 $\pm$ 50)
LGS <sup>b</sup>	19.5	17.6	19.5

<sup>a</sup> Reference 8. <sup>b</sup> Langevin–Gioumousis–Stevenson collision rate constant, ref 46.

$\text{CH}_4$  system (but at least 1.0  $m/z$  in the  $\text{CD}_4$  system). Only results for the perdeuterated species are shown here because use of  $\text{CD}_4$  reduces mass overlap, allowing for a more accurate measurement of product intensities over a greater energy range (in particular of  $\text{TaCH}_3^{2+}$ , which is much smaller than  $\text{TaCH}_2^{2+}$ , only 0.5  $m/z$  away). In the following discussion, the results will be generally described using perprotio species for both  $\text{CH}_4$  and  $\text{CD}_4$  systems.

As can be seen in Figure 1, formation of  $\text{Ta}^+ + \text{CH}_4^+$  (reaction 2),  $\text{TaH}^+ + \text{CH}_3^+$  (reaction 3), and  $\text{TaCH}_2^{2+} + \text{H}_2$  (reaction 5) exhibit no kinetic energy barriers to the overall reaction and hence must be exothermic. For the charge transfer reaction 2, this is consistent with fact that the ionization energy of  $\text{CH}_4$ ,  $12.61 \pm 0.01 \text{ eV}$ ,<sup>45</sup> is less than the second ionization energy of Ta,  $16.2 \pm 0.5 \text{ eV}$ .<sup>44</sup> For reaction 3, this observation is consistent with known thermochemical data:  $D_0(\text{CH}_3\text{--H}) = 4.480 \pm 0.006 \text{ eV}$ ,<sup>45</sup>  $\text{IE}(\text{CH}_3) = 9.84 \pm 0.01 \text{ eV}$ ,<sup>45</sup> and  $D_0(\text{Ta}^+\text{--H}) = 2.39 \pm 0.08$ ,<sup>36</sup> which indicate that this reaction is exothermic by  $4.26 \pm 0.51 \text{ eV}$ . As required by reactions 2 and 3, the magnitudes of the  $\text{CH}_4^+$  and  $\text{Ta}^+$  cross sections and those of  $\text{CH}_3^+$  and  $\text{TaH}^+$  are similar below about 3 and 4 eV, respectively (Figure 1b). This confirms that the collection of these products is quite good in our instrument, even with the high relative translational energy that presumably results from the Coulomb repulsion between these products (see below). At high energies (above about 4 eV for both reactions), the  $\text{CH}_4^+$  and  $\text{CH}_3^+$  cross sections decline, whereas the  $\text{Ta}^+$  and  $\text{TaH}^+$  cross sections stay relatively constant. This is attributable to the efficiency with which the product ions are transmitted through the quadrupole mass filter, although contributions from the transmission between the octopole and the quadrupole may also contribute. Because the  $\text{Ta}^+$  and  $\text{TaH}^+$  products retain the heavy tantalum nucleus, they retain most of the momentum in the laboratory frame associated with the reactant  $\text{Ta}^{2+}$  ion, and therefore are transmitted through the quadrupole filter efficiently at all collision energies. The lighter mass  $\text{CH}_4^+$  and  $\text{CH}_3^+$  products need not acquire much momentum in the laboratory frame, and therefore their transmission through the quadrupole is eventually limited once the DC bias on the octopole reaction region exceeds the DC bias voltage on the quadrupole mass filter, as verified by a rough correlation between the onset of the declines in the cross section in the laboratory frame with the DC bias voltage applied to the quadrupole. Exactly where this deviation occurs is dependent on the details of the dynamics of the reaction and is a rough measure of how forward scattered these products are in the laboratory frame.

The most probable reaction is formation of  $\text{TaCH}_2^{2+}$  in the dehydrogenation reaction 5. This product ion has a cross section that declines as  $E^{-0.5 \pm 0.1}$  below 1.5 eV, the same energy dependence as the Langevin–Gioumousis–Stevenson (LGS) collision cross section.<sup>46</sup> Likewise, the cross sections for formation of  $\text{TaH}^+$  and  $\text{CH}_3^+$  in reaction 3 decline as  $E^{-0.4 \pm 0.1}$  below 1.5 eV. In contrast, cross sections for the charge transfer

reaction 2, formation of  $\text{Ta}^+$  and  $\text{CH}_4^+$ , vary little with kinetic energy throughout the entire range examined. As noted above, the cross section for formation of  $\text{TaCH}_3^+$  shows a dependence on the reactant methane pressure, which is consistent with its energy dependence as it declines as  $E^{-1.0 \pm 0.1}$  below 1.5 eV. Such an energy dependence is consistent with sequential exothermic reactions that each follow the  $E^{-0.5}$  LGS energy dependence.

**3.2. Rate Constants.** To compare our results to the literature, we convert our cross sections to rate constants using eq 12,<sup>13</sup>

$$k(\langle E \rangle) = \nu \sigma(E) \quad (12)$$

where  $\nu = (2E/\mu)^{1/2}$  and  $\mu = mM/(m+M)$ , the reduced mass of the reactants. This rate constant depends on the mean energy of the reactants, which includes the average thermal motion of the neutral, eq 13,

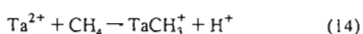
$$\langle E \rangle = E + (3/2)\gamma k_B T \quad (13)$$

where  $\gamma = M/(m+M)$ . Using this equation, we obtain the rates shown in Table 1 for reactions with  $\text{CH}_4$  and  $\text{CD}_4$ . Table 1 also lists the experimental reaction efficiencies compared with the LGS rates of  $19.5 \times 10^{-10} \text{ cm}^3/\text{s}$  ( $\text{CH}_4$ ) and  $17.6 \times 10^{-10} \text{ cm}^3/\text{s}$  ( $\text{CD}_4$ ), using a polarizability volume for methane of  $2.56 \text{ \AA}^3$ .<sup>47</sup> For the dominant reaction 5, the reaction efficiencies for the two systems agree nicely, and further, our result for  $\text{CH}_4$  agrees well with results obtained by FT ICR mass spectrometry.<sup>8</sup> Likewise, for reaction 3, the rates for both ionic products ( $\text{TaH}^+$  and  $\text{CH}_3^+$ ) agree within experimental uncertainty, and the efficiencies agree for both the  $\text{CH}_4$  and the  $\text{CD}_4$  systems. Again our values agree within experimental uncertainties with the rate constant obtained by FT ICR mass spectrometry, where only the  $\text{TaH}^+$  product was monitored.<sup>8</sup> For the charge transfer reaction 2, our rate constants for formation of  $\text{CH}_4^+$  and  $\text{CD}_4^+$  are not included in Table 1 because of poor collection efficiency at thermal energies for these two products. In comparison with the LGS collision rate, we find that reaction 2 occurs with efficiencies near 1%, which disagrees severely with the results obtained by FT ICR mass spectrometry, 25  $\pm$  13% efficiency, where only the  $\text{Ta}^+$  product was monitored.<sup>8</sup> However, Freiser and co-workers comment that the amount of  $\text{Ta}^+$  formed as a result of simple charge transfer observed in the FT ICR could be overestimated because of difficulties associated with multiple reactions between product ions and methane or between  $\text{Ta}^{2+}$  and residual gases in the FT ICR cell.<sup>8</sup> Furthermore, it is possible that the  $\text{Ta}^{2+}$  ions, which were generated with a Nd:YAG pulsed laser in the ICR experiments, could have had a population of excited electronic states that might undergo charge transfer more readily.

When the thermal rate constants for reactions 2, 3, and 5 are combined (taking the average rate for  $\text{TaH}^+$  and  $\text{CH}_3^+$ ), the total reaction rates are  $(13.5 \pm 3.4) \times 10^{-10} \text{ cm}^3/\text{s}$  for  $\text{CH}_4$  and  $(12.1 \pm 2.4) \times 10^{-10} \text{ cm}^3/\text{s}$  for  $\text{CD}_4$ , such that the overall reaction efficiencies are  $69 \pm 17\%$  and  $69 \pm 14\%$ , respectively.

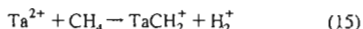
For the FT ICR results, the overall reaction efficiencies were quoted as  $100 \pm 50\%$  for the  $\text{CH}_4$  system, within the combined experimental errors. The agreement is improved once the overestimation of the charge transfer reaction,<sup>8</sup> noted above, is accounted for.

As noted above, formation of  $\text{TaCH}_3^+$  is observed as a secondary reaction and attributed to reaction 8. This reaction was not observed in the FT ICR study.<sup>8</sup> Reaction 8 is calculated to be exothermic by less than  $4.6 \pm 0.5$  eV, given thermochemical data above,  $D_0(\text{Ta}^+-\text{CH}_3) = 2.69 \pm 0.14$  eV<sup>36</sup> and  $D_0(\text{Ta}^{2+}-\text{CH}_2) > 4.7$  eV, which comes from the observation that reaction 5 is exothermic. Interestingly, formation of the  $\text{TaCH}_3^+$  product can conceivably occur in the primary reaction 14,



which is exothermic by  $0.81 \pm 0.52$  eV, given thermochemistry from above and  $\text{IE}(\text{H}) = 13.59844$  eV.<sup>45</sup> Nevertheless, this primary reaction does not appear to occur for reasons discussed further below. It might be thought that whether reaction 14 occurs or not could be verified by detecting the  $\text{H}^+$  product; however, because of its low mass, trapping of this species in the octopole is inefficient at the rf frequency used (about 7 MHz).

Finally, we note that neither we nor Freiser and co-workers observed a  $\text{TaCH}_2^+$  product, which could be formed in reaction 15.



Given  $D_0(\text{Ta}^+-\text{CH}_2) = 4.81 \pm 0.03$  eV,<sup>36</sup> this reaction is calculated to be exothermic by  $0.87 \pm 0.52$  eV. Ultimately, the failure to observe this process can be related to the relatively large ionization energy of  $\text{H}_2$ ,  $\text{IE} = 15.43$  eV,<sup>45</sup> as discussed further below.

**3.3. Multiple Collision Dehydrogenation Reactions.** As previously observed by Freiser and co-workers,<sup>8</sup> the primary  $\text{TaCH}_2^{2+}$  products formed in reaction 5 react further with methane (reactions 9 and 10). Indeed, the FT ICR study observed sequential dehydrogenation reactions with up to six methane molecules. In addition to the double dehydrogenation reaction 9, the single dehydrogenation reaction 16 was also observed in the FTICR study but with a branching ratio of only 10% compared with 90% for reaction 9.



Under our experimental conditions, we observe that  $\text{Ta}^{2+}$  successively dehydrogenates three methane molecules to form a sequence of  $\text{TaC}_x\text{H}_y^{2+}$ ,  $x = 1-3$ , product ions. (Reaction 16 was not observed, consistent with the low probability seen in the FTICR study.) The cross sections for these product ions (Figure 2) display a distinct dependence on methane pressure over the range examined, 0.1 to 0.4 mTorr. It can be seen that the cross section for the primary  $\text{TaCH}_2^{2+}$  product ion decreases as the methane pressure increases, verifying that it reacts away in subsequent collisions. In contrast, the cross sections for the  $\text{TaC}_2\text{H}_2^{2+}$  and  $\text{TaC}_3\text{H}_4^{2+}$  product ions increase with increasing methane pressure, showing that they result from higher order reactions. At the lowest energies, it is found that the  $\text{TaC}_2\text{H}_2^{2+}$  cross section doubles in magnitude for a two-fold increase in methane pressure, demonstrating that it is formed in a second order reaction, whereas the  $\text{TaC}_3\text{H}_4^{2+}$  cross section increases by a larger factor for the same pressure increase, showing that it is a third order reaction. The energy dependences of both of

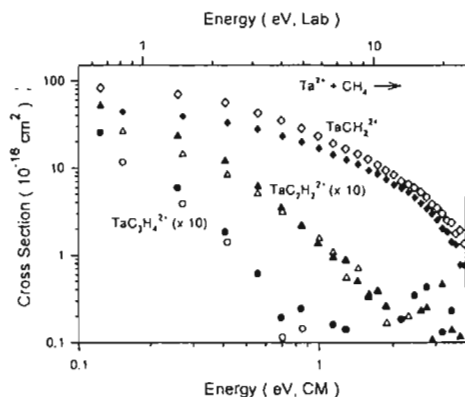


**Figure 2.** Cross sections for multiple reactions of  $\text{Ta}^{2+}$  ( $4F$ ) with  $\text{CH}_4$  as a function of kinetic energy in the center-of-mass frame (lower axis) and laboratory frame (upper axis). Open and closed symbols show results taken at methane pressures of 0.20 and 0.41 mTorr, respectively.

these product ions indicate that each of these subsequent reactions are exothermic, having no barriers in excess of the energy of the reactants.

#### 4. Thermochemical and Theoretical Results

The endothermic cross sections for  $\text{TaC}^{2+}$  and  $\text{TaCH}_3^{2+}$  are analyzed using eq 1 and the optimum values of the fitting parameters are listed in Table 2. Because the rotational, translational, and vibrational energy distributions are included in the modeling, all  $E_0$  thresholds determined by eq 1 correspond to 0 K values. The BDEs of these species are calculated from the measured thresholds using eq 17,

$$D_0(\text{Ta}^{2+}-\text{L}) = D_0(\text{R}-\text{L}) - E_0 \quad (17)$$

where the  $D_0(\text{R}-\text{L})$  values can be calculated using the heats of formation summarized previously.<sup>30</sup> This expression assumes that there are no activation barriers in excess of the endothermicity, which is generally the case for ion-molecule reactions because of the long-range attractive forces that are present.<sup>25</sup> A summary of the BDEs derived and a comparison to theoretical values are given in Table 3. A summary of the B3LYP theoretical results for the energies and structures of the product ions and their excited states is given in Supporting Information, Tables S1 and S2. The following sections discuss the results in detail for each of the species.

**4.1.  $\text{Ta}^{2+}-\text{H}$ .** The doubly charged  $\text{TaH}^{2+}$  species was not observed, however, for completeness, calculations were performed for this species and included here. For  $\text{Ta}^{2+}-\text{H}$ , we calculate a bond dissociation energy of 2.58 eV when using the B3LYP functional and HW+ ECP. A comparable value of 2.49 eV was obtained when using the SD ECP on  $\text{Ta}^{2+}$ . Holthausen et al.<sup>39</sup> have previously characterized the overbinding of the B3LYP functional for the comparable third-row transition metal ion methyl cations, which also involves a single covalent metal-ligand bond. These authors suggest using the BHLYP functional as an alternative, and indeed, we obtain lower bond energies of 2.30 (HW+) and 2.21 (SD) eV. At the QCISD(T) level of theory, we find a bond energy of 2.45 eV. Given this range of calculated BDEs, the formation of  $\text{TaH}^{2+} + \text{CH}_3$  should

TABLE 2. Optimized Parameters for Eq. 1 for Ta<sup>III</sup>-CH<sub>4</sub> and CD<sub>4</sub> Systems

	method	$\beta_0$	$\beta_1$	$E_{\text{Ta-CH}}$	$D_0(\text{Ta}^{III}\text{-CH}_4)$
Ta <sup>III</sup> -CH <sub>4</sub>	-1TaCH <sub>4</sub> <sup>III</sup> + H	0.11 ± 0.20	1.0 ± 0.1	1.30 ± 0.19 <sup>a</sup>	1.28 ± 0.19 <sup>b</sup>
	-1TaCH <sub>4</sub> <sup>III</sup> + H			0	1.23
	-Ta <sup>III</sup> + 2H	1.02 ± 0.72	0.9 ± 0.1	1.87 ± 0.30	1.79 ± 0.30
Ta <sup>III</sup> -CD <sub>4</sub>	-1TaCD <sub>4</sub> <sup>III</sup> + D	0.02 ± 0.11	0.9 ± 0.1	1.75 ± 0.27	1.67 ± 0.27 <sup>b</sup>
	-Ta <sup>III</sup> + 2D			0	1.62
	-1TaCD <sub>4</sub> <sup>III</sup> + D	1.13 ± 0.66	0.8 ± 0.1	1.77 ± 0.30	1.68 ± 0.30

TABLE 3. Experimental and Theoretical Bond Energies (eV) for Ta<sup>III</sup>-H and Ta<sup>III</sup>-CH<sub>4</sub> ( $\beta = 0.3$ )

method	type	exp	B3LYP				OCISONT	
			HF+V	SD	HF+V	SD	HF+V	SD
Ta <sup>III</sup> -H	<sup>3</sup> F		1.38	1.48	1.30	1.71	1.32	
Ta <sup>III</sup> -CH <sub>4</sub>	<sup>3</sup> A <sub>1</sub>	1.60 ± 0.16	1.71	1.99	1.34	1.34	1.25	
Ta <sup>III</sup> -CH <sub>4</sub>	<sup>1</sup> A <sub>1</sub>	1.12 <sup>c</sup>	1.26	1.41	1.02	1.09	1.12	
Ta <sup>III</sup> -CH <sub>3</sub>	<sup>2</sup> E		0.21	1.00	1.22	1.21	1.29	
Ta <sup>III</sup> -C	<sup>3</sup> F	1.43 ± 0.18	1.48	1.58	1.34	1.38	1.33	

<sup>a</sup> Calculated as discussed in the B3LYP/6-311++G(3d,3p) level of theory.

be understood by  $(\beta - 1) \text{ eV}$  whereas charge separation to yield Ta<sup>III</sup> + CH<sub>4</sub><sup>III</sup> is exothermic by over 1 eV. Hence, the Ta<sup>III</sup> product is not formed because, in these products system, an electron transfer can readily yield the lower energy Ta<sup>III</sup> + CH<sub>4</sub><sup>III</sup> product channel.

The ground state for Ta<sup>III</sup> is a <sup>3</sup>F. This maximum set of electronic configurations of  $(t_{2g})^3(e_g)^2$  is which there is a  $\pi$ -bonded bond,  $\pi_x$ , with two singly occupied nonbonding metal d-orbitals (calculated to have  $\pi$  and  $\delta$  symmetry). At the B3LYP level of theory, this state is determined to have a bond length of 1.72 (HF+V) and 1.73 (SD) Å, whereas at the B3LYP level of theory, the bond lengths are 1.30 (HF+V) and 1.26 (SD) Å. The lowest lying excited state of Ta<sup>III</sup> is <sup>1</sup>A<sub>1</sub>, lying 0.14 eV higher in energy and having a  $(t_{2g})^2(e_g)^3$  configuration. Other excited states include <sup>3</sup>A<sub>1</sub> ( $(t_{2g})^3(e_g)^2$ ), <sup>3</sup>E<sub>g</sub> ( $(t_{2g})^3(e_g)^2$ ), <sup>3</sup>E<sub>g</sub> ( $(t_{2g})^2(e_g)^3$ ), <sup>3</sup>F<sub>4</sub> ( $(t_{2g})^3(e_g)^2$ ), <sup>3</sup>F<sub>2</sub> ( $(t_{2g})^3(e_g)^2$ ), <sup>3</sup>F<sub>2</sub> ( $(t_{2g})^2(e_g)^3$ ), and <sup>3</sup>F<sub>4</sub> ( $(t_{2g})^2(e_g)^3$ ), where the higher lying  $\delta$  orbital is largely  $\delta$  on the Ta. Relative energies of these states are listed in Table 5 and their geometries are given in Table S1 (supporting information).

4.2. Ta<sup>III</sup>-CH<sub>4</sub>. For the methane system using eq. (1) with  $D_0(\text{Ta}^{III}\text{-CH}_4) = 0.41 \text{ eV}$  and our maximum value of  $1.10 \pm 0.19 \text{ eV}$  (Table 2), we obtain a BDE for TaCH<sub>4</sub><sup>III</sup> of  $1.38 \pm 0.19 \text{ eV}$ . Similarly, with  $D_0(\text{Ta}^{III}\text{-CD}_4) = 0.58 \text{ eV}$  and a threshold of  $1.13 \pm 0.27 \text{ eV}$ , the bond energy derived from the CD<sub>4</sub> system for TaCD<sub>4</sub><sup>III</sup> is  $1.43 \pm 0.27 \text{ eV}$ . After accounting for zero-point energy differences in these two values ( $-0.013 \text{ eV}$ ), we obtain a weighted average value of  $1.40 \pm 0.16 \text{ eV}$  for the BDE of Ta<sup>III</sup>-CH<sub>4</sub>.

For our theoretical calculations, Table 1, we find  $D_0(\text{Ta}^{III}\text{-CH}_4) = 1.23 \text{ eV}$  at the B3LYP (HF+V) level of theory using the SD BCP, and predicted bond energy drops by 0.22 eV, resulting a value of 1.09 eV. With the B3LYP truncated, however, there is a more substantial decrease in bond energy to 1.34 (HF+V) and 1.34 (SD) eV, a reasonable agreement with experiment. The OCISONT calculations give the highest predicted value, 1.25 eV.

The ground state of TaCH<sub>4</sub><sup>III</sup> is found to be <sup>3</sup>A<sub>1</sub> with  $C_{2v}$  symmetry (Figure 3) and has a valence electronic configuration using the anionic  $C_{2v}$  symmetry designations at  $(t_{2g})^2(e_g)^3$ , where the  $t_{2g}$  is the  $T_{2g}$   $\pi$  bonding orbital, the  $e_g$  orbital is a  $5d$  ( $\delta$ -like) nonbonding orbital on Ta, and the  $2a_1$  orbital is a nonbonding  $\delta$ -like hybrid orbital on Ta. The

Ta-C and C-H bond lengths are 1.92 ± 0.06 and 1.10(12) Å, and the TaCH bond angle is 86.0° (2) and 150.0° at compared with the ground state of TaCH<sub>4</sub><sup>III</sup>.  $T_{2g}$  is 0.58 eV, 0.98 Å (3), and 110.2° (2) for the excited state <sup>3</sup>A<sub>1</sub> is found to be only 0.04 eV higher in energy (Table S1), which is comparable with the  $(t_{2g})^3(e_g)^2$  configuration also differs from the ground state only in where the orbital is occupied in this state, the Ta-C bond length is slightly longer, 1.95 Å, whereas two of the C-H bond lengths are slightly shorter, 1.09 and 1.10(12) Å, with somewhat less accuracy from  $C_{2v}$  symmetry in the Ta-CH bond angle, i.e., 91.7° (2) and 138.4° (4).  $(t_{2g})^2(e_g)^3$  and  $(t_{2g})^3(e_g)^2$  states are 0.17 and 0.18 eV respectively above the ground state. Other excited states include <sup>3</sup>A<sub>1</sub> ( $(t_{2g})^3(e_g)^2$ ), <sup>3</sup>A<sub>1</sub> ( $(t_{2g})^2(e_g)^3$ ), <sup>3</sup>E<sub>g</sub> ( $(t_{2g})^3(e_g)^2$ ), <sup>3</sup>E<sub>g</sub> ( $(t_{2g})^2(e_g)^3$ ), and <sup>3</sup>F<sub>4</sub> ( $(t_{2g})^3(e_g)^2$ ) lying 0.19, 0.13, 0.22, 1.49, and 1.34 eV respectively above the ground state, where the  $C_{2v}$  symmetry designations of the valence orbitals are used in all cases.

Theoretical bond energies for Ta<sup>III</sup> and TaCH<sub>4</sub><sup>III</sup> indicate the state is bound more strongly by  $\sim 1.1 \text{ eV}$  (Table 3). For the hydride, the single H-atom on hydrogen can form only a single covalent bond to the theoretical bond energies for Ta<sup>III</sup> (2.30 eV) and Ta<sup>III</sup> (2.4 eV) at the B3LYP/6-311++G(3d,3p) level of theory are similar to the values to predict the bond energy for Ta<sup>III</sup>-H<sub>2</sub> (1.34 eV) is calculated to be much stronger than that for TaCH<sub>4</sub><sup>III</sup> (2.81 eV) (B3LYP/6-311++G(3d,3p) level of theory). This difference can be understood in an extension of the electronic state  $C_{2v}$  symmetry (Figure 3). By adding the methyl group, two C-H bonds begin to interact with the metal ion, resulting in

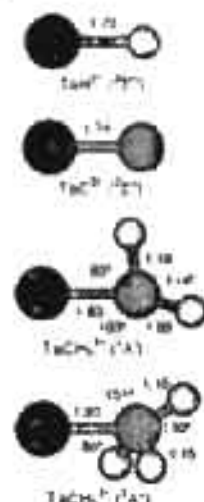


Figure 3. Structures of ground state products calculated at the B3LYP/6-311++G(3d,3p) level of theory. Bond lengths are given in Å, and H-Ta-C and H-C-H bond angles are given in degrees.

## Energetics and Mechanisms of C–H Bond Activation

an agostic interaction between the occupied  $\text{CH}_3$  ( $b_1$ ) bonding orbital and the empty in-plane  $5d_{xz}$  orbital on Ta.

We also investigated a number of alternate isomers of the  $\text{TaCH}_3^{2+}$  molecule. The isomer having the lowest energy, 0.45 eV above  $\text{TaCH}_3^{2+}$  ( $^3A''$ ), is  $\text{HTaCH}_2^{2+}$ , which has a  $^1A'$  ground state. The H–Ta and Ta–C bond lengths and HTaC bond angle are 1.726 Å, 1.822 Å, and  $99.0^\circ$ , respectively, indicating that the Ta–H bond is a covalent single bond and the Ta–C bond is a covalent double bond. The  $(\text{H}_2)\text{TaCH}_2^{2+}$  isomer was also located, 3.25 eV above  $\text{TaCH}_3^{2+}$  ( $^3A''$ ). The  $^1A'$  ground state of this isomer has Ta–H bond lengths of 1.741 Å, suggesting covalent single bonds, and a Ta–C bond length of 1.926 Å, slightly longer than that of  $\text{TaCH}_2^{2+}$  and much longer than that in  $\text{TaCH}^{2+}$  (see below). Finally, there is also the  $(\text{H}_2)\text{TaCH}^{2+}$  isomer, which has a  $^1A'$  ground state, with a short Ta–C bond, 1.773 Å, comparable to that of  $\text{TaCH}^{2+}$  ( $^1\Sigma^+$ ); short Ta–H bonds, 1.916 and 1.932 Å; and a short H–H bond, 0.858 Å. This geometry is consistent with a tightly bound dihydrogen molecule bound to ground state  $\text{TaCH}^{2+}$ . Excited states of each of these isomers were also characterized; see Tables S1 and S2.

**4.3.  $\text{Ta}^{2+}-\text{CH}_2$ .** Reaction 5 and its perdeuterio analogue are exothermic which gives a lower limit for the bond dissociation energy of  $\text{TaCH}_2^{2+}$  of  $4.71 \pm 0.03$  eV =  $D_0(\text{CH}_2-\text{H}_2)$  and  $\text{TaCD}_2^{2+}$  of  $4.82 \pm 0.03$  eV =  $D_0(\text{CD}_2-\text{D}_2)$ . Ranasinghe et al.<sup>8</sup> report a value of  $>4.81$  eV from the same observation, using 298 K thermodynamic values.

The present calculations, B3LYP/HW+ (SD) and QCISD(T), find a  $^2A'$  ground state with  $C_2$  symmetry (Figure 3) for  $\text{TaCH}_2^{2+}$  with a bond energy of 5.68 (5.47) and 5.83 eV, respectively. The B3LYP/HW+ (SD) functional yields lower values, 4.83 (4.64) eV. We find that the  $^2A'$  ground state of the  $\text{TaCH}_2^{2+}$  molecule distorts from  $C_{2v}$  symmetry by bending in the plane of the molecule such that one C–H bond interacts with the metal ion, in essence, an agostic interaction that allows the  $\text{CH}_2$  ( $1b_2$ ) doubly occupied bonding orbital in the plane of the molecule to donate into the empty Ta ( $5d_{yz}$ ) orbital, given that the molecule lies in the  $yz$  plane with the Ta–C bond along the  $z$  axis. For our ground-state geometry, we obtain  $r(\text{Ta}-\text{C}) = 1.830$  Å,  $r(\text{C}-\text{H}) = 1.094$  and 1.163 Å, and  $\angle\text{TaCH} = 163.0^\circ$  and  $83.4^\circ$  (Table S2). Our calculations also located several excited states (Table S1). The first four excited states,  $^2A''$ ,  $^4B_2$ ,  $^4B_1$ , and  $^2B_1$ , lie 0.13, 0.49, 0.52, and 0.76 eV higher in energy, respectively.

The  $^2A'$  ground state of  $\text{TaCH}_2^{2+}$  has a valence electronic configuration of (using the analogous  $C_{2v}$  symmetry designations)  $(1a_{1b})^2(1b_{1b})^2(2a_1)^1$ , where the  $1a_{1b}$  and  $1b_{1b}$  orbitals are the Ta–C  $\sigma$  and  $\pi$  bonding orbitals, and the  $2a_1$  orbital is a nonbonding  $6s-5d\sigma$  hybrid orbital on Ta. Thus, there is a covalent double bond between  $\text{Ta}^{2+}$  and  $\text{CH}_2$ . The  $^2A''$ ,  $^4B_2$ ,  $^4B_1$ , and  $^2B_1$  excited states have valence electronic configurations of  $(1a_{1b})^2(1b_{1b})^2(1a_2)^1$ ,  $(1a_{1b})^2(1b_{1b})^1(2a_1)^1(1a_2)^1$ ,  $(1a_{1b})^2(1b_{1b})^1(2a_1)^1(3a_1)^1$ , and  $(1a_{1b})^2(1b_{1b})^1(2a_1)^1(3a_1)^1$ , respectively, where the  $1a_2$  ( $5d_{xy}$ ) and  $3a_1$  ( $5d_{x^2-y^2}$ ) orbitals are nonbonding orbitals on the tantalum.

It was verified that the  $\text{TaCH}_2^{2+}$  isomer was the lowest energy arrangement of atoms. The lowest lying  $\text{HTaCH}_2^{2+}$  isomer lies 1.63 eV higher in energy and has a  $^2A''$  ground state. The Ta–C and C–H bond lengths in this molecule are 1.859 and 1.098 Å, respectively, with a HTaC bond angle of  $89.8^\circ$ . Other low lying states,  $^2A'$  and  $^6A'$ , were found lying 2.97 and 4.04 eV higher in energy than ground state  $\text{TaCH}_2^{2+}$ .

**4.4.  $\text{Ta}^{2+}-\text{CH}$ .** As for  $\text{TaH}^{2+}$ , doubly charged  $\text{TaCH}^{2+}$  was not observed experimentally, but theoretical results are included

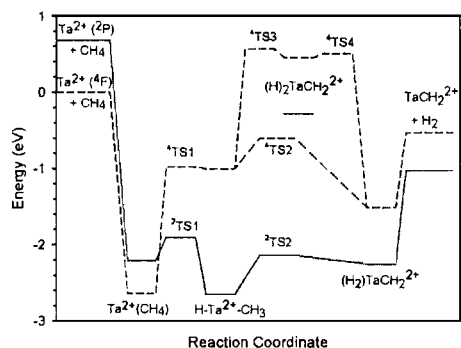


**Figure 4.**  $[\text{Ta,C,4H}]^{2+}$  potential energy surfaces derived from theoretical results. The relative energies of all species are based on ab initio calculations at the B3LYP/HW+6-311++G(3df,3p) level, Table S3, Supporting Information, relative to the  $\text{Ta}^{2+}$  ( $^4F$ ) +  $\text{CH}_4$  ground-state asymptote.

in Tables S1 and S2 for completeness. For  $\text{Ta}^{2+}-\text{CH}$ , we calculate bond dissociation energies of 5.3–7.0 eV at the various levels of theory considered; see Table 3. These values average about 15% greater than the calculated bond energies for  $\text{TaCH}_2^{2+}$ , consistent with an increase in the bond order. The ground state for  $\text{TaCH}^{2+}$  is  $^1\Sigma^+$ , having a bond order of 3.0 with a valence electron orbital occupation of  $1\sigma_b^2 1\pi_b^4$ , where the  $1\sigma_b$  and  $1\pi_b$  orbitals are the obvious Ta–C bonding orbitals. The molecule is linear with Ta–C and C–H bond lengths of 1.759 and 1.096 Å, respectively. Several excited states were also located lying 0.51 eV and higher in energy; see Table S1. The alternate  $\text{HTaC}^{2+}$  structure was also considered and found to lie 3.46 eV higher in energy than  $\text{TaCH}^{2+}$  ( $^1\Sigma^+$ ); see Table S1.

**4.5.  $\text{Ta}^{2+}-\text{C}$ .** Cross sections from the perdeuterated and perdeuterated methane experiments provide thresholds of  $2.87 \pm 0.20$  and  $2.72 \pm 0.10$  eV for formation of  $\text{TaC}^{2+}$ , respectively. These thresholds correspond to BDEs of  $5.19 \pm 0.20$  and  $5.48 \pm 0.10$  eV (Table 2). Our best experimental value for  $D_0(\text{Ta}^{2+}-\text{C})$  is the weighted average of these two values,  $5.42 \pm 0.19$  eV. This experimental value is in poor agreement with the results of the present calculations, 4.78 (B3LYP/HW+) and 4.59 (B3LYP/SD) eV; see Table 3. The B3LYP functional yields BDEs even further below experiment, 3.74 (HW+) and 3.56 (SD) eV, whereas the QCISD(T) performs better than the DFT methods, yielding a BDE of 5.13 eV.

We calculate the ground state for  $\text{TaC}^{2+}$  to be  $^2\Sigma^+$  (Figure 3), having a bond order of 2.5. The valence electron orbital occupation is  $1\sigma_b^1 1\pi_b^4$ , where the  $1\sigma_b$  and  $1\pi_b$  orbitals are the obvious bonding orbitals. The lowest lying excited state is a  $^4\Phi$ , lying 0.54 eV higher in energy and has a  $1\sigma_b^1 1\pi_b^3 1\delta^1$  configuration. Other stable excited states (no imaginary frequencies) include  $^2\Phi$  ( $1\sigma_b^1 1\pi_b^3 1\delta^1$ ),  $^6\Delta$  ( $1\sigma_b^1 1\pi_b^2 1\delta^1 2\sigma^1$ ),  $^4\Delta$  ( $1\sigma_b^1 1\pi_b^2 1\delta^1 2\sigma^1$ ),  $^1^2\Delta$  ( $1\sigma_b^1 1\pi_b^2 1\delta^1 2\sigma^1$ ),  $^6^1\Sigma^+$  ( $1\sigma_b^1 1\pi_b^2 1\delta^2$ ),  $^4^1\Sigma^+$  ( $1\sigma_b^1 1\pi_b^2 2\sigma^1$ ),  $^6\Phi$  ( $1\sigma_b^1 1\pi_b^2 1\delta^1 \pi^1$ ), and  $^4\Phi$  ( $1\sigma_b^1 1\pi_b^2 1\delta^1 2\pi^1$ ), Table S1, where the  $1\delta$  and  $2\sigma$  orbitals are nonbonding 5d and 6s5d hybrid orbitals, respectively, on Ta, and the  $2\pi$  is antibonding.

**4.6. Potential Energy Surfaces of  $[\text{Ta,C,4H}]^{2+}$ .** Figure 4 illustrates the potential energy surfaces (PES) for the interaction of  $\text{Ta}^{2+}$  with methane. The energies of all intermediates are listed in Table S3, and the geometric parameters of these species are provided in Table S4 and shown in Figures 5 (quartet states)

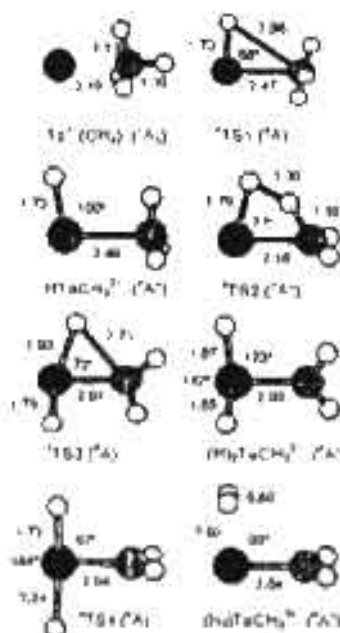


**Figure 5.** Structures of several intermediates and transition states along the reaction pathway of the  $\text{TaC}(\text{CH}_3)_3$  system calculated at the B3LYP/6-311++(2,3) level of theory. Bond lengths are given in Å and H-Ta-C angles are in degrees.

and 6 (doublets). Calculations were performed at the B3LYP level of theory and include zero-point energy corrections (calculated at 0.999). Transition states were located along the synchronous rearranged open-shell reaction method<sup>34</sup> followed by frequency calculations and geometry optimizations at nearly a first-order saddle point. Calculations were also carried out to verify energy of the reaction system but, in all cases, are found to be much higher in energy than the ground state reaction system.

**4.7. Doublet Surface.** On the potential energy surface for interaction of  $\text{Ta}^{II}(\text{Ta})$  with methane (Figure 4) a  $\text{Ta}^{II}(\text{Ta})\text{CH}_4$  adduct is formed in which the methane molecule remains intact and largely unperturbed ( $\text{C-H}$  is equally bonded). The methane molecule binds with  $C_{2v}$  symmetry and the complex has a  $^1A_1$  ground state (Figure 5). The  $\text{Ta}^{II}(\text{Ta})\text{CH}_4$  bond energy is 1.06 eV as compared with the  $\text{Ta}^{II}(\text{Ta})\text{CH}_4$  bond energy of 0.36 eV.<sup>35</sup> Likewise, the  $\text{Ta}-\text{C}$  bond distance in  $\text{Ta}^{II}(\text{Ta})\text{CH}_4$  of 2.148 Å is much shorter than that in  $\text{Ta}^{II}(\text{Ta})\text{CH}_4$  (2.25 Å)<sup>35</sup> and surprisingly, the extra charge on Ta promotes much tighter binding for this noncovalent complex.

As the  $\text{Ta}-\text{H}$  bond distance contracts, the system passes over a transition state (TS1) which lies 0.98 eV below the energy of the reactants leading to the  $\text{H-Ta}^{II}(\text{Ta})\text{CH}_3$  reaction intermediate. This transition state has  $C_{2v}$  symmetry ( $^1A_1$ ) and a  $\text{H-Ta}-\text{C}$  bond angle of 87.8° (Figure 5). On the quartet surface, the  $\text{HTaC}(\text{CH}_3)_2$  intermediate has  $C_{2v}$  symmetry ( $^1A_1$ ) and has a  $\text{H-Ta}-\text{C}$  bond angle of 99.8°. The  $\text{Ta}-\text{H}$  bond distance is 1.73 Å as compared with that of ground state  $\text{Ta}^{II}(\text{Ta})\text{CH}_4$  (1.72 Å). The  $\text{Ta}-\text{C}$  bond distance is relatively long (2.109 Å) compared with the  $\text{Ta}-\text{C}$  bond distance in ground state  $\text{TaC}(\text{CH}_3)_3$  (1.91 Å). Furthermore, the average H-Ta-H bond length

in the methyl group of  $\text{TaC}(\text{CH}_3)_3$  ( $^1A_1$ ) is 109° versus that for a free  $\text{CH}_4$  radical of 120°, whereas the  $\text{HTa}^{II}(\text{Ta})\text{CH}_3$  intermediate has an average HCH bond angle of 119° in the methyl group. These observations indicate that the methyl group is not covalently bound to the  $\text{TaC}^{II}$  molecule in this open state. From this intermediate,  $\text{HTa}^{II}(\text{Ta})\text{CH}_3$  and  $\text{CH}_3\text{Ta}^{II}(\text{Ta})\text{H}$  bond energies are theoretically determined to be 2.63 and 1.26 eV, respectively.

From  $\text{HTaC}(\text{CH}_3)_2$  ( $^1A_1$ ) the system can proceed directly to a  $(\text{H}_2)\text{TaC}(\text{CH}_3)_2$  intermediate via a four-center transition state (TS2) which lies 0.6 eV below the reactants energy. This transition state has  $C_{2v}$  symmetry ( $^1A_1$ ) and the  $\text{Ta}-\text{C}$  bond distance is 2.156 Å. The  $(\text{H}_2)\text{TaC}(\text{CH}_3)_2$  intermediate ( $^1A_1$ ) has a  $\text{Ta}-\text{C}$  bond distance of 2.042 Å, as compared to the  $\text{Ta}-\text{C}$  bond distance in the lowest lying quartet state  $\text{TaC}(\text{CH}_3)_3$  ( $^1B_2$ ) of 2.079 Å. The  $\text{C}-\text{H}$  bond distances are 1.100 (2) Å to  $(\text{H}_2)\text{TaC}(\text{CH}_3)_2$  ( $^1A_1$ ) and 1.103 (2) Å for  $\text{TaC}(\text{CH}_3)_3$  ( $^1B_2$ ). The  $\text{H}-\text{H}$  bond distance is 0.802 Å compared to free  $\text{H}_2$  at 0.742 Å. The  $\text{H}_2\text{C}(\text{Ta})-\text{H}_2$  bond energy is calculated to be 1.02 eV. Overall, formation of  $\text{TaC}(\text{CH}_3)_3 + \text{H}_2$  along this pathway is calculated to be exothermic by 0.54 eV with an activation energy in excess of the reactants (Figure 5) consistent with the experimental data for reaction 3.

Alternatively, the  $\text{HTaC}(\text{CH}_3)_2$  ( $^1A_1$ ) intermediate can follow a stepwise pathway involving sequential H atom transfer to form a  $(\text{H})\text{TaC}(\text{CH}_3)_2$  ( $^1A_1$ ) dihydro intermediate (Figure 5). The  $\text{Ta}-\text{C}$  bond distance is 2.030 Å, which is comparable to the  $\text{Ta}-\text{C}$  bond distance in the lowest lying quartet state of  $\text{TaC}(\text{CH}_3)_3$  ( $^1B_2$ ) (2.079 Å). The  $\text{Ta}-\text{H}$  bond distance, lying 0.45 eV above reactants, is reached via TS3 which lies 0.56 eV above the reactants. Continuing along the quartet surface, the dihydro intermediate can subsequently eliminate the  $\text{H}_2$  molecule carrying the molecule to the TS4 which lies 0.50 eV above the reactants. Clearly, this stepwise reaction pathway is not likely to be consistent with the observed exothermic and barrierless production of  $\text{TaC}(\text{CH}_3)_3 + \text{H}_2$  in reaction 1.

**4.8. Doublet Surface.** Reaction of methane with doublet state  $\text{Ta}^{II}(\text{Ta})$  leads initially to the formation of a  $\text{Ta}^{II}(\text{Ta})\text{CH}_4$  adduct in a  $^1A_1$  state ( $C_{2v}$  symmetry) (Figure 6). On the doublet surface,  $\text{Ta}^{II}(\text{Ta})\text{CH}_4$  lies 2.21 eV below the ground state quartet  $\text{TaC}(\text{CH}_3)_3$  and 0.43 eV above  $\text{Ta}^{II}(\text{Ta})\text{CH}_4$  ( $^1A_1$ ), somewhat less than the calculated  $^3B_1 - ^1A_1$  ground state reaction energy of 0.68 eV. As the  $\text{Ta}-\text{H}$  bond distance contracts, the system passes over TS1 leading to the  $\text{H-Ta}^{II}(\text{Ta})\text{CH}_3$  reaction intermediate. This transition state has  $C_{2v}$  symmetry ( $^1A_1$ ) and a  $\text{H-Ta}-\text{C}$  bond angle of 46.0° (Figure 6). The  $\text{HTaC}(\text{CH}_3)_2$  ( $^1A_1$ ) intermediate has a  $\text{H-Ta}-\text{C}$  bond angle of 98.2° with a  $\text{Ta}-\text{H}$  bond distance of 1.71 Å, this is similar to ground state  $\text{Ta}^{II}(\text{Ta})\text{CH}_4$  (1.71 Å). The  $\text{Ta}-\text{C}$  bond distance is 1.914 Å, it is also similar to the  $\text{Ta}-\text{C}$  bond distance in  $\text{TaC}(\text{CH}_3)_3$  (1.914 Å). This observation indicates that the hydrogens are not covalently bound to the  $\text{Ta}^{II}$  in the open state. The  $\text{HTa}^{II}(\text{Ta})\text{CH}_3$  and  $\text{H-TaC}(\text{CH}_3)_2$  bond energies are calculated to be 4.47 and 1.84 eV, respectively. This is consistent with the relative bond energies of  $\text{TaC}(\text{CH}_3)_3$  and  $\text{Ta}^{II}(\text{Ta})$  listed in Table 1.

Continuing along the doublet surface, the system can proceed from  $\text{HTaC}(\text{CH}_3)_2$  ( $^1A_1$ ) directly to a  $(\text{H}_2)\text{TaC}(\text{CH}_3)_2$  intermediate via a four-center transition state (TS2). This  $^1A_1$  transition state has  $C_{2v}$  symmetry with a  $\text{Ta}-\text{C}$  bond distance of 2.00 Å, indicating that the  $\text{CH}_3$  group is quite tightly bound. The  $\text{Ta}-\text{C}$  bond distance is slightly longer than that in ground state  $\text{TaC}(\text{CH}_3)_3$  ( $^1A_1$ ) (1.91 Å). TS2 leads to a  $(\text{H}_2)\text{TaC}(\text{CH}_3)_2$  intermediate ( $^1A_1$ ) that has a similar geometry to  $(\text{H}_2)\text{CH}(\text{Ta})$  ( $^1A_1$ ) with a  $\text{Ta}-\text{C}$  bond distance of 1.948 Å, slightly indicating a slightly looser bond. The  $\text{C}-\text{H}$  bond distances are 1.09 and 1.11 Å for

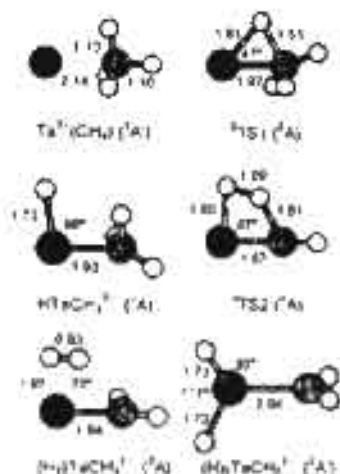


**Figure 6.** Structures of several intermediates and transition states along the double surface of the  $\text{TaC}_2\text{H}_6+\text{H}_2$  system calculated at the 6-311+P-MW4/6-311+AQ34//6-311+P level of theory. Bond lengths are given in Å and H-Ta-C and H-Ta-H bond angles in degrees.

$(\text{H})\text{TaC}_2\text{H}_5^+(1\text{A})$  compared with +0.94 and +1.13 Å for ground state  $\text{TaC}_2\text{H}_5^+(1\text{A})$ . The  $\text{Ta}-\text{H}$  bond dissociation energy is 1.21 eV and the H-H bond distance is 0.777 Å, significantly shorter than the calculated for free  $\text{H}_2$ , 0.743 Å. Overall ionization of  $\text{TaC}_2\text{H}_6^+(1\text{A}) \rightarrow \text{H}_2$  is exothermic by 1.61 eV from ground state  $\text{Ta}^+(1\text{D}) + \text{C}_2\text{H}_6$  reactants.

We carefully looked for a concerted pathway on the double surface and although a dihydrogen transition state does exist (intermediate and transition state) separating the two transition states on either side of the ground (TS1) and (TS2) always collapsed to the lowest energy double surface for the concerted pathway. This zero rate is not surprising given that the energy of this intermediate lies 2.71 eV above the global minimum (only 0.28 eV below ground state reactants).

### 1. Discussion

1.1.  $\sigma$ -Bond Activation, Concerted vs. Stepwise. The activation of methane by metal ions has been explained using a simple  $\sigma$ -bond acceptor model leading to an oxidative addition mechanism.<sup>14-16</sup>  $\sigma$ -Bond activation is a metal center approach to  $\text{C-H}$  bonds, coordination in which there is an energy increase related to the metal ion and where the activation of a bond to be broken is accompanied by a simultaneous decrease in energy by forming a new system's back donation into the antibonding orbital of the bond to be broken. If the acceptor orbital is sufficiently a sufficient interaction is established by effective overlap either by coordination of a barrier to the reaction or by more direct atom-atom pathways. For  $\text{Ta}^+$ , both the  $\pi$  and the  $\sigma$  orbitals have an unoccupied  $\text{d}_{xy}$  orbital. Oxidative addition of a C-H bond to  $\text{Ta}^+$  forms a  $\text{Ta}^+-\text{CH}_3$  intermediate in such a mechanism and products can be formed by the oxidative protonation of  $\text{H}_2$  or by hydrogen and by further dehydrogenation of primary products at still higher energies. For first-row transition metal ions, the oxidative addition process occurs through a five-coordinate transition state from the  $\text{H}-\text{M}^+-\text{CH}_3$  intermediate to a  $(\text{H}_2)\text{MCH}_3^+$  intermediate, in which molecular hydrogen is electrostatically bound to the  $\text{MCH}_3^+$  species.<sup>14-16</sup> The  $(\text{H}_2)\text{MCH}_3^+$  inter-

mediate then decomposes by expulsion of  $\text{H}_2$ . This pathway is also the lowest energy pathway for the analogous stepwise mechanism,  $\text{H}^+$  and  $\text{Ta}^+ \text{CH}_3$ . For other first-row transition metal ions,  $\text{M}^+ = \text{Re}^+, \text{Ir}^+, \text{Rh}^+$  and  $\text{Pt}^+$ ,<sup>14</sup> a different reaction mechanism involving a dihydrogen molecule intermediate has been demonstrated by calculations.

1.2. Mechanism for Dehydrogenation of Methane by  $\text{Ta}^+$ . Ground state  $\text{Ta}^+(1\text{D})$  forms a  $\text{TaC}_2\text{H}_6^+(1\text{A})$  adduct upon interaction with  $\text{CH}_4$ . This intermediate can then move along the double surface passing over (TS1) to form the hydrolytic transition methyl dihydrogen intermediate,  $\text{H-Ta}^+-\text{CH}_3(1\text{A})$ . Note that this transition state is quite low, such that its position and energy are similar to the transition dihydrogen methyl intermediate. See Figures 4 and 5. In the  $\text{H-Ta}^+-\text{CH}_3$  intermediate, can follow a concerted pathway for producing  $(\text{H}_2)\text{TaC}_2\text{H}_5^+(1\text{A})$  which easily loses dihydrogen to form  $(\text{H})\text{TaC}_2\text{H}_5^+(1\text{A}) + \text{H}_2$  product. This pathway involves a five-coordinate transition state, TS1, which leads directly between these two intermediates. The energy limiting step is the first expulsion of  $\text{H}_2$  and its transition state, and significantly below the energy of the reactants. Figure 6, consistent with the barrierless process observed experimentally.

Although the double surface is the lowest energy pathway for dehydrogenation, direct coupling to the double surface during the C-H bond activation step (see Figure 4) also forms TS1, which is a much earlier transition state than TS1 (see Figures 4 and 5). From TS1, the hydrolytic transition methyl dihydrogen intermediate,  $\text{H-Ta}^+-\text{CH}_3(1\text{A})$ , is reached because this step does not allow formation of two  $\sigma$ -bonds simultaneously. This intermediate is much lower in energy than its earlier ancestor and is the global minimum on the potential energy surface. From the  $\text{H-Ta}^+-\text{CH}_3$  intermediate, we can follow a concerted pathway for producing  $(\text{H}_2)\text{TaC}_2\text{H}_5^+(1\text{A})$  that involves a five-coordinate transition state, TS2. The  $(\text{H}_2)\text{TaC}_2\text{H}_5^+(1\text{A})$  intermediate easily loses dihydrogen and leads directly to ground state  $\text{TaC}_2\text{H}_5^+(1\text{A}) + \text{H}_2$  product.

To compare with other double-surface stepwise systems, we also looked for a second pathway involving the activation of a second C-H bond in  $\sigma$ - $\pi$  interaction, leading to the formation of dihydrogen molecule (whether diatomic or molecular). On the ground surface, activation of the second C-H bond occurs via TS3 and forms  $(\text{H}_2)\text{Ta}^+(\text{CH}_3)(1\text{A})$ . From this stepwise oxidative addition of the dihydrogen molecule, either via TS4 and leads again to  $(\text{H}_2)\text{Ta}^+(\text{CH}_3)(1\text{A})$ . All steps of these species are quite high in energy, with a rate-limiting transition state of TS3 at 8.26 eV above reactants (see Figure 4). Thus, this pathway is not experimentally viable. On the double surface, we could follow an analogous dihydrogen molecule intermediate,  $(\text{H}_2)\text{Ta}^+(\text{CH}_3)(1\text{A})$ , by the stepwise step  $\rightarrow \rightarrow \rightarrow$  high in energy, only 0.28 eV below reactants and well above the concerted pathway. In this case, separation by TS1 and TS2 always originated at the much lower energy concerted surface.

1.3. Mechanism for Other Product Channels. The most common of  $\text{Ta}^+ + \text{CH}_4$  and  $\text{TaC}_2\text{H}_6^+ + \text{H}_2$  product channels are easily explained by simple  $\sigma$ -bond donation from the  $\text{H-Ta}^+-\text{CH}_3$  intermediate. Instead, observation of other channels support the formation of a  $\text{H-Ta}^+-\text{CH}_3$  intermediate in the mechanism proposed above. Charge transfer to form  $\text{Ta}^+ + \text{CH}_3^+$  is an exothermic reaction that could potentially occur either in stepwise by electron transfer to the proceeding through an intermediate like the  $\text{Ta}^+(\text{CH}_3)$  complex.

A higher energy  $\text{Ta}^+ + \text{CH}_3^+$  and can be attributed to dehydrogenation of the  $\text{TaC}_2\text{H}_6^+$  primary product. The

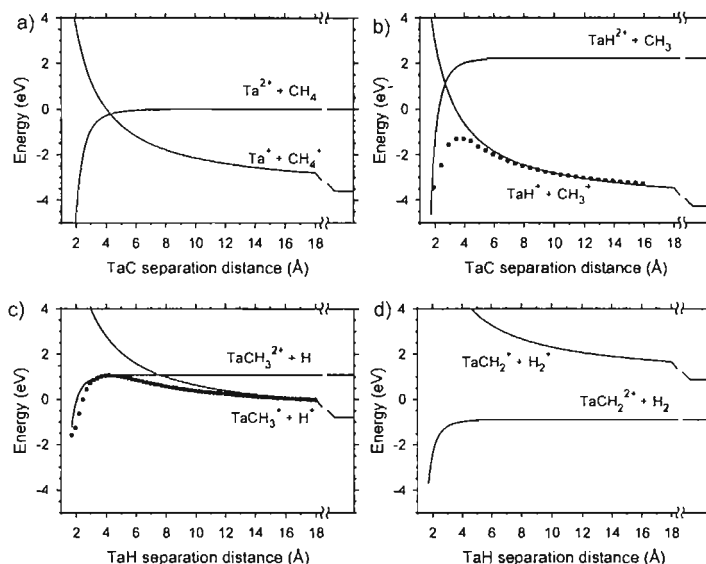


Figure 7. Curve crossing model derived from experimental data (full lines) and theoretical results calculated at a B3LYP/HW+6-311++G(3df,3p) level of theory (symbols). The relative energies of the  $\text{TaH}^+ + \text{CH}_3^+$  (part b) and  $\text{TaCH}_3^+ + \text{H}^+$  (part c) theoretical curves have been adjusted so that the asymptotic energies agree with experimental values, hence the potential wells do not match the theoretical value of  $-2.65$  eV.

coupling between these two products is demonstrated by the fact that the cross section for  $\text{TaCH}_2^{2+}$  decreases as that for  $\text{TaC}^{2+}$  rises. Finally, as noted above, the formation of the  $\text{TaCH}_3^+$  product ion can be attributed to hydride transfer between  $\text{TaCH}_2^{2+}$  and  $\text{CH}_4$  in a secondary collision.

**5.4. Curve Crossing Model.** Curve-crossing models have proven to provide considerable insight into the reaction of doubly charged metal cations with alkanes and help explain the branching between C–H bond activation, charge separation, and charge transfer reactions.<sup>5–8</sup> Figure 7 shows the potential energy surfaces involved in such a curve-crossing model for the case of  $\text{Ta}^{2+} + \text{CH}_4$ . In the entrance channel corresponding to  $\text{Ta}^{2+} + \text{CH}_4$  ( $\Delta H = 0$ ), Figure 7a, the potential energy surface exhibits an attractive ion-induced dipole potential,  $V(r) = -\alpha q^2/8\pi\epsilon_0 r^4 + \Delta H$ , where  $\alpha$  is the polarizability volume of the neutral reagent ( $2.56 \text{ \AA}^3$ ),<sup>47</sup>  $q = 2e$  is the charge on Ta,  $e$  is the charge of an electron,  $\epsilon_0$  is the permittivity of vacuum,  $r$  is the internuclear distance between Ta and C, and  $\Delta H$  is the reaction endothermicity. In the other parts of Figure 7, the surfaces for doubly charged products have similar potentials with variations in the polarizability volumes of the neutral ( $0.67 \text{ \AA}^3$  for H,<sup>58</sup>  $0.81 \text{ \AA}^3$  for  $\text{H}_2$ ,<sup>47</sup> and an estimate of  $2.0 \text{ \AA}^3$  for  $\text{CH}_3$ ), and the asymptotic energies ( $\Delta H$ ). Here, the reaction endothermicities are  $2.2$  eV for  $\text{TaH}^{2+} + \text{CH}_3$  using  $D_0(\text{Ta}^{2+}-\text{H}) = 2.3$  eV (from theory, Table 3),  $1.1 \pm 0.2$  eV for  $\text{TaCH}_3^{2+} + \text{H}$  using  $D_0(\text{Ta}^{2+}-\text{CH}_3) = 3.40 \pm 0.16$  eV (Table 3), and  $0.9$  eV for  $\text{TaCH}_2^{2+} + \text{H}_2$  using  $D_0(\text{Ta}^{2+}-\text{CH}_2) = 5.6$  eV (from theory, Table 3). (It might be noted that, in previous examinations of such curve crossing models,<sup>5–8</sup> the only doubly charged surface considered was that of the reactants, i.e., that in Figure 7a. Technically, this ignores the fact that all other reaction channels are located along different reaction coordinates of the overall potential energy surface. So for instance, the surface for  $\text{TaH}^+ + \text{CH}_3^+$  cannot possibly cross that for  $\text{Ta}^{2+} + \text{CH}_4$  as one hydrogen atom is not physically in

the same position.) For the charge transfer and charge separation products shown in Figure 7, the ion–ion repulsive potentials correspond to  $V(r) = q^2/4\pi\epsilon_0 r + \Delta H$ , where  $q = e$  is the charge on each product, and the  $\Delta H$  values are  $-3.6 \pm 0.5$  eV for reaction 2,  $-4.3 \pm 0.5$  eV for reaction 3,  $-0.8 \pm 0.5$  eV for reaction 14, and  $-0.9 \pm 0.5$  eV for reaction 15.

According to these surfaces, the attractive ion-induced dipole potential curve between the reactant ground state  $\text{Ta}^{2+}$  ion and the  $\text{CH}_4$  neutral is crossed by the Coulombic repulsive curve for the  $\text{Ta}^+ + \text{CH}_4^+$  products at  $4.3 \pm 0.6 \text{ \AA}$  at an energy of  $-0.2 \pm 0.4$  eV (Figure 7a). Thus, the rate limiting transition state for reaction 2, which occurs at the curve crossing, is nearly thermoneutral, which helps explain the relatively flat energy dependence observed for this reaction. An additional consideration is that the Franck–Condon factors for ionization of methane are small at the ground-state geometry of  $\text{CH}_4$ , such that  $\text{CH}_4^+$  is distorted significantly from this geometry. Consequently, the two curves shown in Figure 7a are displaced from one another along a distortion coordinate in another dimension. This moves the true crossing point between these two surfaces to larger TaC separations at energies even closer to zero. The relevant potential surfaces for reaction 3 are shown in Figure 7b. Here, the potential for the  $\text{TaH}^+ + \text{CH}_3^+$  products cross that for  $\text{TaH}^{2+} + \text{CH}_3$  at  $2.7 \pm 0.2 \text{ \AA}$  and an energy of  $1.1 \pm 0.3$  eV. Quantum chemical calculations of this surface at the B3LYP/HW+6-311++G(3df,3p) level (a relaxed potential energy surface scan of the HTa– $\text{CH}_3$  bond distance) are also shown in Figure 7b after normalizing the calculated energy to the correct asymptotic energy. These calculations indicate that the curve crossing is strongly avoided, leaving a transition state at about  $-1.31$  eV and  $r = 3.7 \text{ \AA}$ . Thus, this reaction occurs efficiently from the H– $\text{Ta}^{2+}$ – $\text{CH}_3$  intermediate upon cleavage of the Ta–C bond.

In contrast to the behavior of reactions 2 and 3, the potential for the  $\text{TaCH}_3^+ + \text{H}^+$  products (exothermic by  $0.8 \pm 0.5$  eV)



crosses that for  $\text{TaCH}_3^{2+} + \text{H}$  (endothermic by  $1.1 \pm 0.2$  eV) at a much larger distance of  $7.6 + 3.1/-1.7$  Å at an energy of  $1.1 \pm 0.5$  eV. Here, the surfaces are much more parallel, such that the avoided crossing does not drop the energy of the transition state appreciably. Indeed, quantum chemical calculations for this surface (a relaxed potential energy surface scan of the H–TaCH<sub>3</sub> bond distance) find the transition state lies at 1.13 eV and  $r = 4.1$  Å, essentially matching the energy of the  $\text{TaCH}_3^{2+} + \text{H}$  asymptote (Figure 7c). As a consequence, reaction 14 to form  $\text{TaCH}_3^+ + \text{H}^+$  is not observed, but reaction 4 yielding  $\text{TaCH}_3^{2+} + \text{H}$  is observed as an endothermic process (Figure 1a). This is presumably because the curve crossing occurs at a sufficiently long range that the electron transfer needed to move from the  $\text{TaCH}_3^{2+} + \text{H}$  surface to the  $\text{TaCH}_3^+ + \text{H}^+$  surface is inefficient.

For reaction 5, we note that the potential surface for  $\text{TaCH}_2^{2+} + \text{H}_2$  does not cross that for  $\text{TaCH}_2^+ + \text{H}_2^+$  because of the endothermicity of the latter channel (Figure 7d). Hence, there is no opportunity for the charge separation to occur along this reaction coordinate. Finally, we consider reaction 8, which could conceivably make  $\text{TaCH}_3^{2+} + \text{CH}_3$  instead. Here, the  $\text{TaCH}_3^+ + \text{CH}_3^+$  channel is exothermic by  $<4.6 \pm 0.5$  eV, whereas the charge retention channel is endothermic by more than  $1.1 \pm 0.2$  eV, such that the curve crossing between these surfaces occurs at  $2.9 \pm 0.3$  Å at an energy of  $0.3 \pm 1.0$  eV. These results are consistent with observation of reaction 8.

Overall, the behavior of the various possible reaction channels corresponds well to the “reaction window” proposed by Lindinger and co-workers.<sup>59</sup> They suggested that charge transfer and charge separation reactions that occur via a curve crossing are favored when the crossing point ranges from internuclear separations of 2–6 Å. As noted above, this is true for reactions 2 and 3 (Figure 7a,b) and reaction 8, where the singly charged product channels are observed, but not the doubly charged analogues. In contrast, for reactions 4 and 5, the curve crossings occur outside this window (Figure 7c,d), such that the doubly charged products are observed, but not the singly charged analogues.

## 6. Conclusion

Ground state  $\text{Ta}^{2+}$  ions are found to be highly reactive with methane over a wide range of kinetic energies. At low energies, dehydrogenation is efficient, exothermic, and a dominant process over the product spectrum. Formation of  $\text{TaH}^+ + \text{CH}_3^+$  and  $\text{Ta}^+ + \text{CH}_4^+$  are also observed at low energies in exothermic processes. At higher energies, the  $\text{TaCH}_2^{2+}$  product decomposes by loss of  $\text{H}_2$  to form  $\text{TaC}^{2+}$  and  $\text{TaCH}_3^{2+} + \text{H}$  is also formed. Several secondary processes (reactions 7–10) are also observed at low energies.

Analyses of the kinetic energy dependences of the reaction cross sections provide the BDEs of  $\text{Ta}^{2+}-\text{CH}_3$  and  $\text{Ta}^{2+}-\text{C}$ , the first covalent bond energies measured to a metal dication. Our experimental BDE for  $\text{Ta}^{2+}-\text{CH}_3$  is found to be in good agreement with ab initio calculations performed at the B3LYP/HW+/6-311++G(3df,3p) level of theory, and that for  $\text{Ta}^{2+}-\text{C}$  is found to be in reasonable agreement with ab initio calculations performed at the QCISD(T)/HW+ level of theory (Table 3).

Calculations also provide a detailed potential energy surface for the  $\text{TaCH}_4^{2+}$  system. When following the lowest energy pathway, the potential energy surface shows that the reaction of  $\text{Ta}^{2+}$  ( $^4\text{F}$ ) with methane couples to a doublet surface near  $^2\text{TS1}$ , followed by the oxidative addition of one C–H bond to yield a hydrido-methyl tantalum dication intermediate,  $\text{H}-\text{Ta}^{2+}-\text{CH}_3$  ( $^2\text{A}$ ), the global minimum on the potential energy

surface. In the dominant process observed experimentally, the  $\text{H}-\text{Ta}^{2+}-\text{CH}_3$  intermediate follows a concerted pathway involving a four-centered transition state ( $^2\text{TS2}$ ) to form the electrostatic complex,  $(\text{H}_2)\text{TaCH}_2^{2+}$  ( $^2\text{A}$ ). Finally,  $\text{H}_2$  is eliminated from  $(\text{H}_2)\text{TaCH}_2^{2+}$  ( $^2\text{A}$ ) to form the metal carbene complex,  $\text{TaCH}_2^{2+}$  ( $^2\text{A}'$ ) +  $\text{H}_2$ . The tantalum carbene retains the +2 charge as the separation to  $\text{TaCH}_2^+ + \text{H}_2^+$  requires too much energy (Figure 7d). Overall, dehydrogenation of methane by  $\text{Ta}^{2+}$  has one spin change as it moves along the lowest energy pathway:  $\text{Ta}^{2+}$  ( $^4\text{F}$ ) +  $\text{CH}_4$  ( $^1\text{A}_1$ )  $\rightarrow$   $\text{Ta}^{2+}(\text{CH}_4)$  ( $^4\text{A}_1$ )  $\rightarrow$   $\text{H}-\text{Ta}^{2+}-\text{CH}_3$  ( $^2\text{A}$ )  $\rightarrow$   $(\text{H}_2)\text{TaCH}_2^{2+}$  ( $^2\text{A}$ )  $\rightarrow$   $\text{TaCH}_2^{2+}$  ( $^2\text{A}'$ ) +  $\text{H}_2$  ( $^1\Sigma_g^+$ ). However, a comparable pathway on the quartet surface is available and also has no transition states in excess of the energy of the reactants, consistent with experimental observations.

The dehydrogenation reaction is found to occur with relatively high efficiency ( $47 \pm 14\%$ ). In the present system, the reaction efficiency is not higher because charge separation channels forming  $\text{TaH}^+ + \text{CH}_3^+$  account for another  $22 \pm 5\%$  of the overall reactivity. This product channel can be formed by simple bond cleavage from the  $\text{H}-\text{Ta}^{2+}-\text{CH}_3$  intermediate (doublet or quartet spin) and is an exothermic process with a low energy Coulombic barrier (Figure 7b). At higher energies, this intermediate can also decompose to form  $\text{TaCH}_2^{2+} + \text{H}$  in an endothermic process. Formation of  $\text{TaCH}_3^+ + \text{H}^+$ , although exothermic, is suppressed by the Coulombic barrier along this reaction pathway (Figure 7c). Instead, the observed formation of  $\text{TaCH}_3^+$  is attributed to the secondary reaction of  $\text{TaCH}_2^{2+}$  with methane, where charge separation into  $\text{TaCH}_3^+ + \text{CH}_3^+$  is facile. Exothermic charge transfer to form  $\text{Ta}^+ + \text{CH}_4^+$  is also observed but is relatively inefficient,  $\sim 1\%$  reactivity. This is consistent with a Coulombic barrier that is calculated to be near thermoneutral (Figure 7a).

**Acknowledgment.** Dedicated to Professor Helmut Schwarz on the occasion of his 65th birthday and in recognition of his many contributions to ion chemistry and understanding alkane bond activation by transition metals using mass spectrometric approaches. This work is supported by the National Science Foundation, Grant CHE-0748790. A grant of computer time from the Center for High Performance Computing in University of Utah is gratefully acknowledged. P.B.A. thanks Kent M. Ervin for reminding him about the interesting Franck–Condon aspects of Figure 7.

**Supporting Information Available:** Four tables (S1–S4) containing energies and structures of the various reactants, products, intermediates, and transition states in the  $[\text{Ta}_2\text{C}_4\text{H}]^{2+}$  system. These materials are available free of charge via the Internet at <http://pubs.acs.org>.

## References and Notes

- (1) Schröder, D.; Schwarz, H. *J. Phys. Chem. A* **1999**, *103*, 7385–7394.
- (2) Price, S. D. *Phys. Chem. Chem. Phys.* **2003**, *5*, 1717–1729.
- (3) Mathur, D. *Phys. Rep.* **2004**, *391*, 1–118.
- (4) Price, S. D. *Int. J. Mass Spectrom.* **2007**, *260*, 1–19.
- (5) Tonkyn, R.; Weisshaar, J. C. *J. Am. Chem. Soc.* **1986**, *108*, 7128–7130.
- (6) Buckner, S. W.; Freiser, B. S. *J. Am. Chem. Soc.* **1987**, *109*, 1247–1248.
- (7) Gord, J. R.; Freiser, B. S.; Buckner, S. W. *J. Chem. Phys.* **1989**, *91*, 7530–7536.
- (8) Ranasinghe, Y. A.; MacMahon, T. J.; Freiser, B. S. *J. Phys. Chem.* **1991**, *95*, 7721–7726.
- (9) Ranasinghe, Y. A.; MacMahon, T. J.; Freiser, B. S. *J. Am. Chem. Soc.* **1992**, *114*, 9112–9118.

- (10) Loh, S. K.; Hales, D. A.; Lian, L.; Armentrout, P. B. *J. Chem. Phys.* **1989**, *90*, 5466–5485.
- (11) Teloy, E.; Gerlich, D. *Chem. Phys.* **1974**, *4*, 417–427.
- (12) Gerlich, D. *Adv. Chem. Phys.* **1992**, *82*, 1–176.
- (13) Ervin, K. M.; Armentrout, P. B. *J. Chem. Phys.* **1985**, *83*, 166–189.
- (14) Chantry, P. J. *J. Chem. Phys.* **1971**, *55*, 2746–2759.
- (15) Lifshitz, C.; Wu, R. L. C.; Tieman, T. O.; Terwilliger, D. T. *J. Chem. Phys.* **1978**, *68*, 247–260.
- (16) Kickel, B. L.; Armentrout, P. B. *J. Am. Chem. Soc.* **1995**, *117*, 4057–4070.
- (17) Clemmer, D. E.; Chen, Y.-M.; Khan, F. A.; Armentrout, P. B. *J. Phys. Chem.* **1994**, *98*, 6522–6529.
- (18) Haynes, C. L.; Armentrout, P. B. *Organometallics* **1994**, *13*, 3480–3490.
- (19) Kickel, B. L.; Armentrout, P. B. *J. Am. Chem. Soc.* **1995**, *117*, 764–773.
- (20) Chen, Y.-M.; Elkind, J. L.; Armentrout, P. B. *J. Phys. Chem.* **1995**, *99*, 10438–10445.
- (21) Sievers, M. R.; Chen, Y.-M.; Elkind, J. L.; Armentrout, P. B. *J. Phys. Chem.* **1996**, *100*, 54–62.
- (22) Azarov, V. I.; Tchang-Brillet, W.-U. L.; Qyart, J.-F.; Meijer, F. G. *Phys. Scr.* **2003**, *67*, 190–207.
- (23) Chesnavich, W. J.; Bowers, M. T. *J. Phys. Chem.* **1979**, *83*, 900–905.
- (24) Aristov, N.; Armentrout, P. B. *J. Am. Chem. Soc.* **1986**, *108*, 1806–1819.
- (25) Armentrout, P. B. In *Advances in Gas Phase Ion Chemistry*; Adams, N. G., Babcock, L. M., Eds.; JAI Press: Greenwich, 1992; Vol. 1, pp 83–119.
- (26) Shimanouchi, T. *NSRDS-NBS* **1972**, *39*, 1.
- (27) Becke, A. D. *J. Chem. Phys.* **1993**, *98*, 5648–5652.
- (28) Lee, C.; Yang, W.; Parr, R. G. *Phys. Rev. B* **1988**, *37*, 785–789.
- (29) Frisch, M. J.; Trucks, G. W.; Schlegel, H. B.; Scuseria, G. E.; Robb, M. A.; Cheeseman, J. R.; Montgomery, J. J. A.; Vreven, T.; Kudin, K. N.; Burant, J. C.; Millam, J. M.; Iyengar, S. S.; Tomasi, J.; Barone, V.; Mennucci, B.; Cossi, M.; Scalmani, G.; Rega, N.; Petersson, G. A.; Nakatsuji, H.; Hada, M.; Ehara, M.; Toyota, K.; Fukuda, R.; Hasegawa, J.; Ishida, M.; Nakajima, T.; Honda, Y.; Kitao, O.; Nakai, H.; Klene, M.; Li, X.; Knox, J. E.; Hratchian, H. P.; Cross, J. B.; Adamo, C.; Jaramillo, J.; Gomperts, R.; Stratmann, R. E.; Yazyev, O.; Austin, A. J.; Cammi, R.; Pomelli, C.; Ochterski, J. W.; Ayala, P. Y.; Morokuma, K.; Voth, G. A.; Salvador, P.; Dannenberg, J. J.; Zakrzewski, V. G.; Dapprich, S.; Daniels, A. D.; Strain, M. C.; Farkas, O.; Malick, D. K.; Rabuck, A. D.; Raghavachari, K.; Foresman, J. B.; Ortiz, J. V.; Cui, Q.; Baboul, A. G.; Clifford, S.; Cioslowski, J.; Stefanov, B. B.; Liu, G.; Liashenko, A.; Piskorz, P.; Komaromi, I.; Martin, R. L.; Fox, D. J.; Keith, T.; Al-Laham, M. A.; Peng, C. Y.; Nanayakkara, A.; Challacombe, M.; Gill, P. M. W.; Johnson, B.; Chen, W.; Wong, M. W.; Gonzalez, C.; Pople, J. A. *Gaussian 03, Revision B.02*, Gaussian, Inc.: Pittsburgh, PA., 2003.
- (30) Zhang, X.-G.; Liyanage, R.; Armentrout, P. B. *J. Am. Chem. Soc.* **2001**, *123*, 5563–5575.
- (31) Armentrout, M. M.; Li, F.-X.; Armentrout, P. B. *J. Phys. Chem. A* **2004**, *108*, 9660–9672.
- (32) Armentrout, P. B.; Shin, S.; Liyanage, R. *J. Phys. Chem. A* **2006**, *110*, 1242–1260.
- (33) Li, F.-X.; Zhang, X.-G.; Armentrout, P. B. *J. Phys. Chem. A* **2005**, *109*, 8350–8357.
- (34) Parke, L. G.; Hinton, C. S.; Armentrout, P. B. *Int. J. Mass Spectrom.* **2006**, *254*, 168–182.
- (35) Li, F.-X.; Armentrout, P. B. *J. Chem. Phys.* **2006**, *125*, 133114.
- (36) Parke, L. G.; Hinton, C. S.; Armentrout, P. B. *J. Phys. Chem. C* **2007**, *111*, 17773–17787.
- (37) Hay, P. J.; Wadt, W. R. *J. Chem. Phys.* **1985**, *82*, 299–310.
- (38) Ohanessian, G.; Brusich, M. J.; Goddard III, W. A. *J. Am. Chem. Soc.* **1990**, *112*, 7179–7189.
- (39) Holthausen, M. C.; Heinemann, C.; Cornehl, H. H.; Koch, W.; Schwarz, H. *J. Chem. Phys.* **1995**, *102*, 4931.
- (40) Holthausen, M. C.; Mohr, M.; Koch, W. *Chem. Phys. Lett.* **1995**, *240*, 245.
- (41) Armentrout, P. B.; Kickel, B. L. In *Organometallic Ion Chemistry*; Freiser, B. S., Ed.; Kluwer: Dordrecht, 1996; pp 1–45.
- (42) Armentrout, P. B. In *Topics in Organometallic Chemistry*; Brown, J. M., Hofmann, P., Eds.; Springer-Verlag: Berlin, 1999; Vol. 4, pp 1–45.
- (43) Andrae, D.; Hauesermann, U.; Dolg, M.; Stoll, H.; Preuss, H. *Theor. Chim. Acta* **1990**, *77*, 123–141.
- (44) Moore, C. E. *Atomic Energy Levels, NSRDS-NBS 35*, Washington, D. C., 1971; Vol. III.
- (45) Lias, S. G.; Bartness, J. E. In *National Institute of Standards and Technology, Gaithersburg MD, 20899* (<http://webbook.nist.gov>) 2000; NIST Standard Reference Database Number 69.
- (46) Gioumousis, G.; Stevenson, D. P. *J. Chem. Phys.* **1958**, *29*, 294–299.
- (47) Rothe, E. W.; Bernstein, R. B. *J. Chem. Phys.* **1959**, *31*, 1619–1627.
- (48) Peng, C. Y.; Schlegel, H. B. *Israel J. Chem.* **1994**, *33*, 449.
- (49) Peng, C. Y.; Ayala, P. Y.; Schlegel, H. B.; Frisch, M. J. *J. Comput. Chem.* **1996**, *17*, 49.
- (50) Aristov, N.; Armentrout, P. B. *J. Phys. Chem.* **1987**, *91*, 6178.
- (51) Georgiadis, R.; Armentrout, P. B. *J. Phys. Chem.* **1988**, *92*, 7060–7067.
- (52) Haynes, C. L.; Armentrout, P. B.; Perry, J. K.; Goddard, W. A., III. *J. Phys. Chem.* **1995**, *99*, 6340–6346.
- (53) Haynes, C. L.; Chen, Y.-M.; Armentrout, P. B. *J. Phys. Chem.* **1996**, *100*, 111–119.
- (54) Chen, Y.-M.; Sievers, M. R.; Armentrout, P. B. *Int. J. Mass Spectrom. Ion Processes* **1997**, *167/168*, 195–212.
- (55) Sunderlin, L. S.; Armentrout, P. B. *J. Phys. Chem.* **1988**, *92*, 1209–1219.
- (56) Georgiadis, R.; Armentrout, P. B. *J. Phys. Chem.* **1988**, *92*, 7067–7074.
- (57) Li, F.-X.; Zhang, X.-G.; Armentrout, P. B. *Int. J. Mass Spectrom.* **2006**, *255/256*, 279–300.
- (58) Miller, T. M.; Bederson, B. *Adv. Atomic Molec. Phys.* **1977**, *13*, 1–55.
- (59) Smith, D.; Adams, N. G.; Alge, E.; Villinger, H.; Lindinger, W. *J. Phys. (France)* **1980**, *B13*, 2787.